

Precise Measurement of Rare Pion Decay

by

Saul Cuen-Rochin

B.Sc.E.E., Centro de Enseñanza Técnica y Superior, 2005
M.Phys., Universidad Autónoma de Sinaloa, 2012

A THESIS SUBMITTED IN PARTIAL FULFILLMENT OF
THE REQUIREMENTS FOR THE DEGREE OF
DOCTOR OF PHILOSOPHY

in

The Faculty of Graduate and Postdoctoral Studies
(Physics)

THE UNIVERSITY OF BRITISH COLUMBIA
(Vancouver)

April 2019

© Saul Cuen-Rochin 2019

The following individuals certify that they have read, and recommend to the Faculty of Graduate and Postdoctoral Studies for acceptance, a thesis/dissertation entitled:

Precise Measurement of Rare Pion Decay
submitted by Saul Cuen-Rochin in partial fulfillment of the requirements for
the degree of Doctor of Philosophy
in Physics

Examining Committee:

Omer Angel, Mathematics
Chair

Douglas Bryman, Physics
Research Supervisor

Christopher Hearty, Physics
Supervisory Committee Member

Michael Hasinoff, Physics
University Examiner

Takamasa Momose, Chemistry
University Examiner

Klaus Kirch, Physics - ETH Zürich
External Examiner

Additional Supervisory Committee Members:

Douglas Scott, Physics
Supervisory Committee Member

Oliver Stelzer-Chilton, Physics
Supervisory Committee Member

Hirohisa Tanaka, Physics
Supervisory Committee Member

Abstract

The PIENU¹ experiment at TRIUMF² aims to measure the pion decay branching ratio, defined as the relative rate of decay of pions into electrons over muons including associated neutrinos and radiative components (denoted R_π) to a precision level of $\mathcal{O}(0.1\%)$. This Standard Model (SM) observable provides a sensitive test of lepton universality, where weak coupling strengths are assumed to be equal for all leptons ($g = g_e = g_\mu = g_\tau$). Comparing the measured experimental (R_π^{exp}) and calculated SM (R_π^{SM}) ratios, the ratio of the coupling constants can be extracted and compared with the SM expectation $g_e/g_\mu = 1$ as follows $g_e/g_\mu = (R_\pi^{\text{exp}}/R_\pi^{\text{SM}})^{1/2}$.

The current theoretical calculation of the SM prediction $R_\pi^{\text{SM}} = (1.2352 \pm 0.0002) \times 10^{-4}$ with a precision of 0.016% is more precise than the measurements of previous generation experiments by a factor of 30; thus, there is scope for significant improvement. If the measurement is consistent with the SM, new constraints could be set on new physics scenarios for SM extensions, such as R-parity-violating super-symmetry, leptoquarks, and heavy neutrinos lighter than the pion. Most remarkably, a deviation from the SM could result from a new pseudo-scalar interaction with an energy scale of up to $\mathcal{O}(1000 \text{ TeV})$ which would enhance the branching ratio by $\mathcal{O}(0.1\%)$. In some instances, these constraints can far exceed the reach of direct searches at colliders.

Between 2009 and 2012 around 6.5 million $\pi^+ \rightarrow e^+ \nu_e$ events were gathered. The analysis of a subset of the 2010 data with 0.4 million events was published in 2015, giving $R_\pi^{\text{exp}} = (1.2344 \pm 0.0023(\text{stat.}) \pm 0.0019(\text{syst.})) \times 10^{-4}$, with a precision of 0.24%. This is in agreement with the SM, representing a 0.12% measurement of lepton universality at $g_e/g_\mu = 0.9996 \pm 0.0012$. The analysis presented in this thesis is blinded but includes the highest quality data portion available, around 3 million $\pi^+ \rightarrow e^+ \nu_e$ events. For this work, major experimental systematic problems have been solved allowing for increased precision up to 0.12% for R_π^{exp} and up to 0.06% for lepton universality.

¹Acronym for $\pi^+ \rightarrow e^+ \nu_e$ decay mode.

²Canada's particle accelerator centre.

Lay Summary

The Standard Model (SM) of particle physics is the best available theoretical framework to predict the subatomic interactions between the fundamental elements of known matter. The PIENU experiment at TRIUMF makes a precise measurement for one of the SM's best calculated predictions involving the force that governs radioactive decays. If a measurement is consistent with the SM, better constraints can be set on theories which extend the SM. In some instances, these constraints can far exceed the reach of direct searches at high energy colliding beam facilities like the Large Hadron Collider at CERN. Most remarkably, a deviation from the SM expectation could imply the presence of new physics effects not included in the SM. This thesis describes the analysis of a dataset including 3 million $\pi^+ \rightarrow e^+\nu_e$ events. Major experimental systematic problems have been solved, allowing for increased precision by a factor of two over PIENU's previous measurement from 2015.

Preface

The PIENU collaboration consists of a team of around 20 people from several countries. TRIUMF approved the experiment's proposal in 2005, and the PIENU detector was designed and prototyped the following years in TRIUMF's Meson Hall. The prototype had initial beam tests in 2007, and finally during 2008 the final version of the PIENU detector was installed at the end of M13-beam-line with most of the components assembled. After the assembly was completed, data-taking Run I and Run II and the main calorimeter's energy response test measurements were performed in 2009, culminating in the beam-line paper [1]. In 2010, Run III and Run IV were performed, and the calorimeter paper was published [2]. In 2011, the collaboration collected special data for beam-line studies and improved the calorimeters' energy response test measurement. Subsequently, Run V was completed and a heavy neutrino search analysis paper using runs just from 2009 was published [3].

The author joined the collaboration as a Ph.D. student in the summer of 2012, and took many shifts during Run VI, the most significant data taking period. In addition, the author participated in data monitoring and collection, and ensured quality data taking with onsite-online-offline beam-line-trigger-detector-computer maintenance. Later in the same year he participated in data taking of additional special runs for beam-line studies. Finally in 2013, the collaboration dismantled the experiment. From 2012 to 2015, the collaboration worked intensively to unravel all aspects of the detector performance and available data. In 2015, the collaboration published the detector design and performance [4] as well as an analysis of the Run IV data [5], setting a record for precision measurement of the branching ratio at a level of 0.24% and in the $e\text{-}\mu$ universality test at a level of 0.12%. Since 2012, the author has been responsible for the beam-line low-momenta particle contamination study (Section 6.1.2 and Appendix D), performing data analysis and simulations [6] to avoid uncertainty in the main corrections and sources of systematic uncertainties. The author also conducted studies on possible energy bias and or acceptance in the calorimeter ($\pi^+ \rightarrow e^+\nu_e$

over $\pi^+ \rightarrow \mu^+ \nu_\mu \rightarrow e^+ \nu_e \bar{\nu}_\mu$ or vice-versa) from multiple pulse elimination in scintillator T1 [7], the counter responsible for the positron timing after the pion-stopping target. The author was in charge of and compiled comprehensive documentation [8], including all aspects of the analysis and results used in the first PIENU paper [5].

In addition, the author inherited all the legacy code and frameworks for the analysis, and served as a system administrator for the local cluster and the PIENU web-page [9]. Furthermore, the author re-coded and reprocessed all raw data to the current version and pushed the entire dataset migration from the Westgrid-Bugaboo to the ComputeCanada-Cedar cluster. The author also compiled an extensive initial report [10] on the Run VI dataset, which was approximately five times larger than the Run IV dataset. The author participated in the collaboration's three-year effort to eliminate the primary source of systematic uncertainty, the calorimeter's radial acceptance in the branching ratio, in order to achieve the current level of precision. Finally, through this thesis, the author has been in charge of the comprehensive documentation for the current preliminary final result, including all aspects of the analysis for the upcoming final PIENU paper.

From 2016 to 2018, the collaboration was engaged in full analysis for all datasets. The group published a new improved heavy neutrino search paper [11] in 2018 using the full PIENU dataset, i.e., all runs from 2009 to 2012. The experiment is now in the last stage prior to unblinding the final branching ratio R_π^{exp} result, currently having an estimated precision level of up to 0.12% (0.06% for the e- μ universality test), using the highest quality data portion available, around 3 million $\pi^+ \rightarrow e^+ \nu_e$ events. Representing a factor of approximately 30 improvement from previous generation experiments [12] [13] and a factor of 2 from a subset of PIENU data (0.4 million events) published [5] in 2015. For the 2012 dataset (2 million events), this thesis presents the total reduced $\chi^2/\text{d.o.f.}$ (d.o.f. = 1557) of 1.19, and 1.13 for the pulse-height (PH) and charge-integration (Q) based time spectrum analysis, from which the raw branching ratio is extracted. For the 2011 dataset (0.5 million events) the $\chi^2/\text{d.o.f.}$ is 1.08, and 1.06 for the PH and Q based analysis. For the 2010-November dataset (0.4 million events) the $\chi^2/\text{d.o.f.}$ is 1.00, and 1.07 for the PH and Q based analysis. Since the SM branching ratio prediction R_π^{SM} is at a precision level of 0.016%, there is still scope for improvement in the next generation of experiments. In recent years, most PIENU collaborators have left TRIUMF, making the author the

last Ph.D. student working full time on the experiment. Through this thesis the author shares the latest breakthroughs and improvements in major systematic problems recently solved with the collective contributions from the collaboration; specifically (in order) D. Bryman, L. Doria, S. Ito, R. Mischke, T. Numao, A. Sher, and T. Sullivan.

The author gave a talk [14] in 2016 to promote the initial results from the PIENU experiments and holds co-authorship with the collaboration for three peer-reviewed articles ([4], [5], [11]), and six proceedings. In addition, the author produced four technical-notes ([6], [7], [8], [10]) and more than one-hundred documents for PIENU's internal archives, most of them presented across six years of weekly meetings. The PIENU collaboration plans to publish up to six more peer-reviewed articles in the near future: regarding massive neutrino searches in pion-stopping scintillator target $\pi^+ \rightarrow \mu^+ \nu$ energy spectra; Majorana neutrino searches in the calorimeter's $\pi^+ \rightarrow e^+ \nu_e$ energy spectrum; direct muon capture in Zirconium from a special set of muon runs; the calorimeter's energy response; and the final branching ratio analysis (both short and extended versions) for PIENU. The goals and milestones reached so far for the PIENU experiment are shown in Table 3.3. The author is indebted to the previous PIENU theses, which were the foundation of this dissertation: specially (and chronologically) those of, K. Yamada, Ph.D. 2010 [15], C. Malbrunot, Ph.D. 2012 [16], D. vom Bruch, M.Sc. 2013 [17], S. Ito, Ph.D. 2016 [18], T. Sullivan, Ph.D. 2017 [19], R. Nuttall, B.Sc. 2018 [20], and L. Doria's Habilitationsschrift (*in preparation*). Nevertheless, the writing of this thesis is from the author alone.

Table of Contents

Abstract	iii
Lay Summary	iv
Preface	v
Table of Contents	viii
List of Tables	xii
List of Figures	xiv
Algorithms	xxvii
Glossary	xxviii
Acknowledgements	xxxix
Dedication	xxxii
1 Introduction	1
1.1 Previous Measurements	3
1.2 Experimental Technique	5
1.2.1 Lessons from the E248 experiment	6
1.2.2 PIENU technique	8
1.3 Blind Analysis	11
1.4 Thesis Outline	13
2 Theory	14
2.1 The Standard Model of Particle Physics	14
2.1.1 Electroweak interactions	16
2.1.2 Strong interactions	16
2.2 Pion Decay Theory	17

Table of Contents

2.2.1	Vector-Axial-Vector (V-A) Weak Interaction	18
2.2.2	Helicity Suppression	21
2.2.3	Radiative Corrections	22
2.3	Motivation Beyond the Standard Model	26
2.3.1	Lepton Universality	26
2.3.2	New-Pseudo-scalar Interactions	30
2.3.3	Partial Compositeness	35
2.3.4	Heavy Neutrino	35
3	Experiment	39
3.1	Cyclotron and Beam-line	39
3.1.1	Beam-line Extension	42
3.2	Detector	44
3.2.1	Scintillators	46
3.2.2	Wire Chambers	47
3.2.3	Silicon Detectors	48
3.2.4	Bina	49
3.2.5	CsI	50
3.2.6	Tracking	51
3.3	Final Detector Assembly	55
3.4	Data Acquisition System	56
3.4.1	Trigger	56
3.4.2	Boards	60
3.4.3	Software	64
3.5	Data-taking History and Milestones	65
3.5.1	2009	65
3.5.2	2010	66
3.5.3	2011	66
3.5.4	2012	66
3.5.5	Full analysis	67
4	Analysis	69
4.1	Variable Extraction and Calibration	69
4.1.1	Run Selection	69
4.1.2	Scintillators	69
4.1.3	Silicon Detectors and Calorimeter	71
4.1.4	Wire-chambers	73
4.2	Event Selection	76
4.2.1	Pion Identification	76
4.2.2	Pileup T1, and T2	78

Table of Contents

4.2.3	Early Time	79
4.2.4	Calorimeter Acceptance Radius A_R	80
4.2.5	Summary of Event Selection	80
4.3	Energy Spectra	81
4.3.1	Monte-Carlo Calibration	81
5	Time Spectrum	94
5.1	Construction	94
5.2	Signal and Background	98
5.2.1	Signals	98
5.2.2	Pion Decay-In-Flight and Muon from Previous Event (Old-muon) in Target B3	99
5.2.3	T1 Double Pulse Resolution.	99
5.2.4	Muon from Previous Event (Old-muon) No-T1-Hit	105
5.2.5	Radiative Pion Decay	105
5.3	The Fitting Function	106
5.3.1	Time-Independent Addition of Energy	107
5.3.2	Low-Energy Components	108
5.3.3	High-Energy Components	108
5.3.4	Fit Parameters	109
5.3.5	Signal Overlay and Residuals	111
6	Corrections	124
6.1	Calorimeter's Low Energy Tail	124
6.1.1	Response Function Measurement	127
6.1.2	Beam-line's Intrinsic Tail	131
6.2	Acceptance	134
6.3	Muon Decay in Flight	137
6.4	t_0	138
7	Results	140
7.1	Stability and Systematic Errors	140
7.1.1	Fit Tests	141
7.1.2	LET tests	149
7.1.3	Charge- vs. Pulse-height-based R_π	150
7.2	Error Budget	153
7.3	Combination of Datasets	154
7.4	Future prospects	157
7.4.1	Current PIENU experiment	157
7.4.2	Next generation PIENU	157

Table of Contents

8	Limits on New Physics	159
8.1	The $\pi^+ \rightarrow e^+\nu_e$ branching ratio	159
8.2	Lepton Universality	160
8.3	New Pseudo-scalar Interactions	160
8.3.1	R-Parity violating SUSY	161
8.3.2	Charged Higgs Boson	161
8.4	Search for Massive Neutrinos in the $\pi^+ \rightarrow e^+\nu_e$ Decay	162
8.5	Summary and Forward-looking for SM deviation scenarios	163
	Bibliography	165
 Appendices		
A	Time spectrum for $\pi \rightarrow \mu \rightarrow e$	176
B	Cuts for Pion Data	177
C	Cuts for Positron Data	179
D	Beam-line Simulation	184
E	Trigger Diagram	191
F	Technical Drawings	192

List of Tables

2.1	Bosons (integer spin).	15
2.2	Fermions (spin 1/2 integers).	16
2.3	Measured pion decay modes [21]. The radiative energy ($E_{\gamma 1}$) restrictions are concerning the cited experiment, not the PIENU experiment.	18
2.4	Measured muon decay modes [21]. The radiative energy ($E_{\gamma 1}$) restrictions are concerning the cited experiment, not the PIENU experiment.	18
2.5	Summary of the electroweak corrections for R_0^{π}	25
2.6	Experimental results on lepton universality (LU) tests from studies of π , K , τ , μ and W decay. In some cases, μ and τ 's lifetime (τ_{μ} , and τ_{τ}) measurements were used in combination for LU tests. Here, \mathcal{B} represents the branching fraction of a particular decay mode.	28
3.1	Parameters for the PIENU detector [4].	45
3.2	Rates for all triggers [4].	60
3.3	Run history and milestones of the PIENU experiment.	68
4.1	Cut flow for event selection. The number of events before cuts is 2.027×10^9 for the 2012 dataset.	82

List of Tables

5.1	Results from the timing spectra for the three data-taking periods, presented for both integrated-charge (Q) and pulse-height (PH) calorimeter variables. The exact fit values are truncated for a more compact presentation. The errors are statistical only as obtained by the MINUIT [22] fit, and the parameters marked as fixed were kept fixed during the fit. The errors in the R_{π}^{raw} reflect the magnitude of the data samples collected in the three periods. The acceptance radius used was $R_A = 40$ mm, and the nominal range for our fitting function (FF) for both high- and low-energy time spectra is from -290 to 520 ns, excluding prompt events from -20 to 10 ns. Using 1 ns bins for the time spectrum, the total degrees of freedom (<i>d.o.f.</i>) are 1557	110
6.1	Low energy tail fraction (T) percentage for nominal pion beam configuration as a function of the maximum acceptance radius A_R with $E_{cut} = 52$ MeV, and as a function of E_{cut} with $A_R = 60$ mm.	129
6.2	Upper limit to beam-line's contribution to tail fraction (T_{beam}) percentage.	134
6.3	Acceptance correction C_{Acc} for different A_R values.	137
6.4	Muon decay in flight correction $C_{\mu DIF}$ for different E_{cut} and A_R values.	139
7.1	Stability tests and systematic errors from the fit, following standard methodology [23]. Non-negligible deviations are in red. See Section 7.1.1 for discussion. Units in the branching ratio change are ΔR [10^{-8}], with uncorrelated errors unless specified otherwise.	146
7.2	Error budget in [10^{-8}] branching ratio units.	153
7.3	Combination of 2010, 2011, and 2012 datasets for $A_R = 40$ mm. The branching ratios for all datasets are still blinded. See Section 7.3 and Table 7.2 for nomenclature. The PH version was chosen over the Q based branching ratio since the global systematic error is (marginally) better.	156
B.1	List of cuts.	177
B.2	Year dependent cut values.	178
D.1	Beam-line's settings for positron runs	185

List of Figures

1.1	History of the R_{π}^{exp} branching ratio measurements. Red line: SM calculation [24]. Black dashed line: PDG experimental average [21].	4
1.2	Schematic illustration of experimental technique: two pionic decays in a scintillator target; and decay positrons collected by the calorimeter.	5
1.3	(Top) Experimental setup of the E248 experiment at TRIUMF [25]. (Bottom) Positron energy spectrum obtained by suppressing $\pi^+ \rightarrow \mu^+ \nu_{\mu} \rightarrow e^+ \nu_e \bar{\nu}_{\mu}$ events, the x -axis is energy in ADC counts (channel 3400 corresponds to 56.4 MeV).	7
1.4	Energy deposited in the target B3 for $\pi^+ \rightarrow e^+ \nu_e$ (blue line) and $\pi^+ \rightarrow \mu^+ \nu_{\mu} \rightarrow e^+ \nu_e \bar{\nu}_{\mu}$ (red line) events from GEANT4.	9
1.5	(Left) Time spectra and (right) energy spectra in the calorimeters of $\pi^+ \rightarrow e^+ \nu_e$ and $\pi^+ \rightarrow \mu^+ \nu_{\mu} \rightarrow e^+ \nu_e \bar{\nu}_{\mu}$ decays obtained from simulations. The spectra are normalized to the same amplitude. Using an energy cut-off (E_{cut}) above the $\pi^+ \rightarrow \mu^+ \nu_{\mu} \rightarrow e^+ \nu_e \bar{\nu}_{\mu}$ energy spectrum edge (dashed line), we divide the energy spectrum into low-energy (LE) and high-energy (HE) parts The low energy tail (LET) from the $\pi^+ \rightarrow e^+ \nu_e$ energy spectrum is not visible due to scale and the pion decay in flight (π DIF) contribution was deactivated. The $\pi^+ \rightarrow e^+ \nu_e$ time distribution peaks near $t = 0$ because of the relatively short pion lifetime.	9
1.6	Evolution in time (years) of the neutron's lifetime experimental result [21].	12
1.7	PIENU's blinding technique. A smooth inefficiency function (unknown to the experimenters) removes events based on their energy deposited in the target, lowering (case a) or raising (case b) the branching ratio.	12
2.1	Feynman diagram for the $\pi^+ \rightarrow l^+ \nu_l$ decay, where $l = e, \mu$	19

List of Figures

2.2	Fermi-point-like interpretation for $\pi^+ \rightarrow l^+ \nu_l$ decay.	23
2.3	Feynman diagrams for the radiative corrections to pion decay, from real (a) and virtual (b) photons.	24
2.4	The limits on $\Delta_{\mu\tau}$ and $\Delta_{e\tau}$ from (a) W -decay, (b) τ -decay, (c) π and K -decay, and (d) all decays combined. The 1σ bands are shown for each coupling constant ratio, ignoring correlations. The shaded areas represent the 68% (dark grey) and 90% (light grey) confidence contours, including correlations (Figure from ref. [26]).	29
2.5	Comparison of measurements with SM predictions: The branching fraction B is $B^- \rightarrow \tau^- \bar{\nu}_\tau$ (left), the ratio $R(D)$ is $\bar{B} \rightarrow D\tau^- \bar{\nu}_\tau$ over $\bar{B} \rightarrow D e^- \bar{\nu}_e$ (center), and $R(D^*)$ is $\bar{B} \rightarrow D^* \tau^- \bar{\nu}_\tau$ over $\bar{B} \rightarrow D^* e^- \bar{\nu}_e$ (right) by BABAR, Belle, and LHCb. The data points indicate statistical and total uncertainties. ST and HT refer to the measurements with semileptonic and hadronic tags, respectively. The average values of the measurements and their combined uncertainties, obtained by the Heavy Flavor Averaging Group, are shown in red as vertical lines and bands, and the expectations from the SM calculations are shown in blue. Image and data from ref. [27].	30
2.6	Feynman diagrams for pseudo-scalar interactions induced at one loop including three classes of diagrams: scalar-dressed Z exchange box diagrams (top), scalar-dressed W exchange box diagrams (middle) and radiative corrections to the quark vertex (bottom).	32
2.7	Tree level RPV contributions to R^π [28].	33
2.8	Constraints on RPV parameters from R_π	34
2.9	The 90% C.L. upper limit on the heavy-neutrino mixing parameter, as a function of its mass. The dashed line shows the result from the previous PIENU experiment [29], and the circles and triangles are the limits from a subset of PIENU data, published in 2011 [3]. The circles indicate a restricted angular region was used when constructing the $\pi^+ \rightarrow e^+ \nu_e$ energy spectrum.	38
3.1	Schematic illustration of TRIUMF's cyclotron, primary beam-lines, and Meson Hall's secondary beam-lines [30].	40
3.2	M13 channel with the extension [1]	41

List of Figures

3.3	Left: Position distribution of π^+ , μ^+ , and e^+ at F3. The solid lines are Gaussian fits. Right: π^+ and e^+ rates at F4 as a function of the selected momentum [1]. The PIENU detector was placed at final focus point F4.	41
3.4	The end of the M13 beam-line, before (left) and after (right) the extension. Part of the detector was in place to measure the particle content of the beam.	42
3.5	Left: Fraction of beam positrons as a function of the selected momentum. Right: Fit of the delayed component of the positrons time-of-flight showing consistency with the pion decay time [1].	44
3.6	Schematic illustration of the PIENU detector [4]. The target region is magnified in the inset.	46
3.7	(Left) B1, (also B2, B3, and T1) plastic scintillator is read out with 4 PMTs (grey cylinders); Light was collected by four acrylic light guides (light green). (Right) Readout scheme with wavelength-shifting fibers of the T2 plastic scintillator. .	47
3.8	(Left) WC1/2 wire chamber plane and its preamplifier board. Each chamber consisted of three planes. (Right) WC1/2 after installation on the beam pipe [9].	48
3.9	(Left) Image of the wire chamber WC3 placed in front of the NaI(Tl) calorimeter. (Right) S1 and S2 assembly on their support structure [9] [31].	49
3.10	(Left) Back side of the NaI(Tl) crystal on the test bench. (Right) The NaI(Tl) crystal and the 97 CsI crystals while the calorimeter was under construction [9].	50
3.11	Schematic of the tracking devices, the $\pi^+ \rightarrow e^+ \nu_e$ signal, and the different decay-in-flight backgrounds (the sizes are not to scale). π DAR \rightarrow μ DIF: In $\pi^+ \rightarrow \mu^+ \nu_\mu \rightarrow e^+ \nu_e \bar{\nu}_\mu$ decay, the muon decays in flight in the target. π DIF upstream of target (“up.”) \rightarrow μ DAR: The pion decays in flight before entering the target. Part of these decays can be detected by tracking through the kink variable (K_θ). π DAR \rightarrow μ DAR: Both the pion and the muon in the $\pi^+ \rightarrow \mu^+ \nu_\mu \rightarrow e^+ \nu_e \bar{\nu}_\mu$ channel decay at rest in the target. π DIF inside target (“it.”) \rightarrow μ DAR: Pion decay-in-flight in the target and muon decay at rest. The “u” orientation of a WC plane corresponds to a rotation of $+60^\circ$ while “v”= -60°	52
3.12	Simulation of the kink angle K_θ for different pion decay modes.	53

List of Figures

3.13	Bottom: Beam goes from right \rightarrow left. The PIENU detector and beam-line after the last bending magnet, showing the steel wall used for radiation shielding. Top-Left: PIENU-1 assembly of scintillators, wire-chambers, and silicon detectors. Top-Right: PIENU-2 detector calorimeter assembly, image from [9].	57
3.14	Beam-line-Detector CAD drawing [9].	58
3.15	Schematic of the trigger diagram for the three physics triggers. The rates of the triggers are listed in Table 3.2. Image from [18].	59
3.16	Picture of main COPPER board mounted with four FINESSE modules.	61
3.17	A waveform digitized by COPPER. The red circles and blue crosses show the digitization of each 250 MHz ADCs, which produce a 500 MHz waveform.	62
3.18	Web interface of the MIDAS data acquisition system. All the VME modules were integrated and easily controlled via this interface.	64
4.1	COPPER's signals timing. Image from [18].	71
4.2	Comparison prior to calibration between data (black) taken with the cosmic ray trigger and an MC simulation (red) based on the CRY [32] simulation package. The spectra are relative to the 21 crystals in the inner-upstream CsI ring. Horizontal axes are ADC counts. The peak positions vary up to 20% in energy with the position of the crystal in the detector, but they are well emulated in MC. The energy deposited by minimum ionizing particles in a single CsI crystal is about 50 MeV. Image from [18].	75
4.3	Pion Cut: B1 (top) and B2 (bottom) energy distribution without cuts in black, energy distribution with all cuts in red (excluding cut being discussed), and cut values are shown in blue. No normalization. Peaks from left to right in B1 (and B2): positrons at 1.1 (0.5), muons at 3.2 (1.5), pions at 4.5 (2.5), and two pions arriving at the same time at 9 (4.7) MeV.	84
4.4	Acceptance for WC1 (top) and WC2 (bottom); beam halo is removed.	85

List of Figures

4.5	Charge (top) and time (bottom) distributions without cuts in black, distributions with all cuts in red (excluding cut being discussed), cut values are shown in blue. No normalization. Top: B1 short gate/wide gate integrated charge. Bottom: Trigger Consistency Cut.	86
4.6	Energy in the NaI (Bina) versus minimum energy loss in the downstream counters. Protons are above the red line indicating the cut position. The red blob represents $\pi^+ \rightarrow \mu^+ \nu_\mu \rightarrow e^+ \nu_e \bar{\nu}_\mu$ events and the small yellow blob $\pi^+ \rightarrow e^+ \nu_e$ events.	87
4.7	The ratio of integrated charge in the T1 PMTs to the fitted pulse height as a function of the fitted pulse height. The red line indicates the cut used to separate real pileup (above) from pileup due to fake hits (below).	87
4.8	The false trigger cut rejects events when positrons from π DIF make false trigger. The positrons are found at $(B3_t - B1_t) > 4$ ns and $B3_{charge} < 200$ ADC counts (~ 3 MeV). The three bands on the left represent pileup related to 4, 3, and 2 PMTs at 450, 300, and 150 ADC counts (10, 4, and 2 MeV), respectively. The main red blob in the center represents good beam pion events stopping in the center of target B3 and the blob's downward tail represents pions barely entering B3, while the upward tail is pions stopping at the end of B3.	88
4.9	Calorimeter's acceptance radius (A_R) cut distribution without cuts in black, radius distribution with all cuts in red (excluding the cut being discussed), and cut value is shown in blue.	89
4.10	Combined energy spectrum of the NaI plus CsI detectors for the 2012 dataset. The vertical red line indicates $E_{cut} = 52$ MeV. The composition of the high energy tail beyond 70 MeV is due to pileup events.	89

List of Figures

4.11	Alignment of scintillators and calorimeter’s energy scales to Monte-Carlo. a) E_{tot} ’s “suppressed” energy in black, E_{tot} ’s “late” energy in blue, and MC’s E_{tot} energy for $\pi^+ \rightarrow e^+\nu_e$ events only in red. b) Calorimeter’s “suppressed” energy in black, “late” energy in blue, and MC’s for $\pi^+ \rightarrow e^+\nu_e$ events only in red. c) Calorimeter’s “suppressed” and “late” energy with E_{tot} ’s cut to select $\pi^+ \rightarrow e^+\nu_e$ events. For all subplots the “suppressed” (black) energy distribution was normalized to the MC’s (red) $\pi^+ \rightarrow e^+\nu_e$ peak, for proper comparison such normalization was used for the “late” (blue) spectrum as well. The alignment coefficient between data and MC was done to match the $\pi^+ \rightarrow e^+\nu_e$ peak in the calorimeter (Bina+CsI). The resultant alignment uncertainty of the scintillators’ total energy and the calorimeter’s peak to MC is below the calibration’s uncertainty 0.1 MeV. The normalization for each subplot (left, center, and right) was done independently, thus the vertical axes between subplots don’t match, i.e., E_{tot} ’s plots were normalized to 1, and the calorimeter’s energies to the total number of events.	90
4.12	Early triggers for all years including charge-integration (Q) and pulse-height (PH) calorimeter (NaI+CaI) energy based variables defined by Eq. 4.5 and Eq. 4.6. The three datasets (2010, 2011, and 2012) make two groups in the tail above 70 MeV, in such region all three PH versions have less pileup than the Q version group.	91
4.13	Prescale triggers for all years including charge-integration (Q) and pulse-height (PH) calorimeter (NaI+CaI) energy based variables defined by Eq. 4.5 and Eq. 4.6. The three datasets (2010, 2011, and 2012) make two groups in the tail above 70 MeV, in such region all three PH versions have less pileup than the Q version group.	92
4.14	TIGC triggers for all years including charge-integration (Q) and pulse-height (PH) calorimeter (NaI+CaI) energy based variables defined by Eq. 4.5 and Eq. 4.6. The three datasets (2010, 2011, and 2012) make two groups in the tail above 70 MeV, in such region all three PH versions have less pileup than the Q version group.	93

List of Figures

5.1	2012 Dataset - Low-Energy (LE) Time-Spectrum (TS), T_{pos} for $E_{\text{NaI+CsI}} < E_{\text{cut}}$: Using the pulse-height “PH” $E_{\text{NaI+CsI}}^{\text{PH}}$ and charge-integrated “Q” $E_{\text{NaI+CsI}}^{\text{Q}}$ calorimeter based variable to construct the LE TS “tsL”. Overlaying TS with different levels of cuts: The “raw” (orange and black) spectrum (no cuts), “L1” (violet and red) with “Pion Identification” cuts, “L2” (light-blue and yellow) with “Pileup T1, and T2” cuts, and the final “clean” (dark-green and navy-blue) TS with “Early Time and Acceptance” (All) cuts. See Section 4.2 for discussion on cuts. The PH and Q versions overlap.	96
5.2	2012 Dataset - High-Energy (HE) Time-Spectrum (TS), T_{pos} for $E_{\text{NaI+CsI}} \geq E_{\text{cut}}$: Using the pulse-height “PH” $E_{\text{NaI+CsI}}^{\text{PH}}$ and charge-integrated “Q” $E_{\text{NaI+CsI}}^{\text{Q}}$ calorimeter based variable to construct the HE TS “tsH”. Overlaying TS with different levels of cuts: The “raw” (orange and black) spectrum (no cuts), “L1” (violet and red) with “Pion Identification” cuts, “L2” (light-blue and yellow) with “Pileup T1, and T2” cuts, and the final “clean” (dark-green and navy-blue) TS with “Early Time and Acceptance” (All) cuts. See Section 4.2 for discussion on cuts. The PH version is shown to be less sensitive to pileup compared to the Q based branching ratio.	97
5.3	The time difference between subsequent hits in each T1 PMT. The leading times are fitted with an error function. The peak around 30 ns is due to an after-pulse hit at a characteristic time after the real hit.	101
5.4	a) T1 resolution function $\mathcal{F}_{2A}(t)$ evaluated with $\Delta T = 15.7$ ns. b) T1 resolution pileup events with artificial $\Delta T = 100$ ns.	103
5.5	a, b, c, d, and e) Amplitudes of $\mathcal{F}_2(t)$ from 2012 dataset’s pileup events vs. artificial T1 double pulse resolutions (ΔT) for different pre-pileup windows; points fitted with a quadratic curve. If the double pulse resolution time ΔT was zero, the amount of pileup would not be negative below 15.7 ns. f) Each intercept at $\Delta T = 15.7$ ns from subplots a) to e) is correlated to the number of old-muon events from the LE time region. See Section 5.2.3 for discussion.	104
5.6	The shape used in the time spectrum fit from positrons entering the calorimeter, missing the T1-hit requirement. Integrated charge (Q) based in blue and pulse-height (PH) based in black.	106

List of Figures

5.7	The shape used in the time spectrum fit for $\pi^+ \rightarrow \mu^+ \nu_\mu \gamma$ events. contribution from NaI in red, CsI crystals in black, and the sum in blue.	107
5.8	Time Spectra for 2012 dataset pulse-height (PH) R_π based time fit. Left: LE time spectrum on a logarithmic scale (black line). Right: HE time spectrum on a logarithmic scale (black line).	112
5.9	Residuals (data - fit) for 2012 dataset pulse-height (PH) R_π based time fit. Top-Left: HE, negative times. Top-Right: HE, positive times. Bottom-Left: LE, negative times. Bottom-Right: LE, positive times.	113
5.10	Time Spectra for 2012 dataset integrated-charge (Q) R_π based time fit. Left: LE time spectrum on a logarithmic scale (black line). Right: HE time spectrum on a logarithmic scale (black line).	114
5.11	Residuals (data - fit) for 2012 dataset integrated-charge (Q) R_π based time fit. Top-Left: HE, negative times. Top-Right: HE, positive times. Bottom-Left: LE, negative times. Bottom-Right: LE, positive times.	115
5.12	Time Spectra for 2011 dataset pulse-height (PH) R_π based time fit. Left: LE time spectrum on a logarithmic scale (black line). Right: HE time spectrum on a logarithmic scale (black line).	116
5.13	Residuals (data - fit) for 2011 dataset pulse-height (PH) R_π based time fit. Top-Left: HE, negative times. Top-Right: HE, positive times. Bottom-Left: LE, negative times. Bottom-Right: LE, positive times.	117
5.14	Time Spectra for 2011 dataset integrated-charge (Q) R_π based time fit. Left: LE time spectrum on a logarithmic scale (black line). Right: HE time spectrum on a logarithmic scale (black line).	118
5.15	Residuals (data - fit) for 2011 dataset integrated-charge (Q) R_π based time fit. Top-Left: HE, negative times. Top-Right: HE, positive times. Bottom-Left: LE, negative times. Bottom-Right: LE, positive times.	119
5.16	Time Spectra for November 2010 dataset pulse-height (PH) R_π based time fit. Left: LE time spectrum on a logarithmic scale (black line). Right: HE time spectrum on a logarithmic scale (black line).	120

5.17	Residuals (data - fit) for November 2010 dataset pulse-height (PH) R_π based time fit. Top-Left: HE, negative times. Top-Right: HE, positive times. Bottom-Left: LE, negative times. Bottom-Right: LE, positive times.	121
5.18	Time Spectra for November 2010 dataset integrated-charge (Q) R_π based time fit. Left: LE time spectrum on a logarithmic scale (black line). Right: HE time spectrum on a logarithmic scale (black line).	122
5.19	Residuals (data - fit) for November 2010 dataset integrated-charge (Q) R_π based time fit. Top-Left: HE, negative times. Top-Right: HE, positive times. Bottom-Left: LE, negative times. Bottom-Right: LE, positive times.	123
6.1	Schematic drawing of the detector setup for special positron runs, showing rotating angle θ between the beam and calorimeter.	125
6.2	The energy spectrum from a 70 MeV positron beam parallel to the crystal axis. Data is shown in black and simulation is shown in red. The histograms are normalized to have the same total number of events.	126
6.3	Tail fraction below 53.7 MeV vs angle for the positron data (blue) and MC (red), equivalent to the 52 MeV cutoff in the $\pi^+ \rightarrow e^+\nu_e$ data. The 1σ error band for the tail fractions in data and MC overlap at all angles.	128
6.4	Simulated Bina+CsI spectrum from $\pi^+ \rightarrow e^+\nu_e$ decay including radiative components and events that underwent Bhabha scattering in the target.	129
6.5	The BINA spectrum for events with a late hit (450 to 670 ns) in CsI. Data in black, MC in red. The two photo-nuclear peaks are enhanced.	131
6.6	Positron momentum distribution at F4 (target B3), for the 75 MeV/c positron beam (run #54880).	132
6.7	Positron momentum vs. angle distribution at F4 (target B3), for the 75 MeV/c positron beam (run #54880).	133
6.8	Left: Sum of the energies in B1, B2, S1, S2, and B3. Right: Z-vertex for events with positron energy $E_{cut} < 52$ MeV (shaded histogram) and $E_{cut} > 52$ MeV (blue full line). The two distributions are normalized to the same number of events, and cuts applied are indicated by the red vertical dashed lines. Image from [11].	135

List of Figures

6.9	The pion stopping position Z_v distribution from data.	136
6.10	Acceptance correction C_{Acc} as a function of the A_R radius for the 2012 dataset. Error bars are only statistical.	137
6.11	Time and energy spectra for μ DIF.	139
7.1	Change in the branching ratio ΔR vs time resolution: The x -axis is the time resolution from the scintillators. The y -axis is in ΔR units, with zero change representing 2012(PH)'s nominal analysis (without time resolution effects). The uncorrelated statistical error is zero for all points since there is no change in statistics for this test. The blue solid line represents the 2012 dataset pulse-height (PH) based branching ratio. The blue dashed line represents the actual time resolution from the scintillators (B1 and T1) from which the timing signal is extracted. The change in the branching ratio ΔR is $< 1 [10^{-8}]$ for time resolutions < 2 ns. Since the time difference between B1 and T1 has the time resolution of $\sigma = (0.3 \pm 0.1)$ ns the time resolution effects are negligible for the branching ratio to our level of precision.	142
7.2	$\Delta R \pm \Delta e$ (Eq. 7.1) vs. PrePU: The x -axis is the PrePU window in ns units (Figure 4.1). The y -axis is in ΔR units, with zero change representing 2012(PH)'s nominal analysis (PrePU cut enabled), the error bars (Δe) on each point represent the uncorrelated statistical error between the point in question and the nominal point with the error bars going up, when there is a statistical increase, and down otherwise. The horizontal dashed black lines, both at the same distance from nominal, represent the raw statistical error from the 2012 dataset.	147
7.3	$\Delta R \pm \Delta e$ (Eq. 7.1) vs Bin size: The x -axis is the bin size in ns units. The y -axis is in ΔR units, with zero change representing 2012(PH)'s nominal analysis (binning 1 ns), the error bars (Δe) on each point represent the uncorrelated statistical error between the point in question and the nominal point with the error bars going up, when there is a statistical increase, and down otherwise. The horizontal dashed black lines, both at the same distance from nominal, represent the raw statistical error from the 2012 dataset.	148

7.4	$\Delta R \pm \Delta e$ (Eq. 7.1) vs. A_R , Charge Integration and Pulse-height: The x -axis is the A_R value in mm units. The y -axis is in ΔR (corrected) units, with zero change representing 2012(PH)'s analysis using anchor point with cuts $A_R = 60$ mm and $E_{\text{cut}} = 52$ MeV, the error bars (Δe) on each point represent the uncorrelated statistical error between the point in question and the anchor point with the error bars going up when there is an statistical increase and down otherwise. The horizontal dashed black lines both at the same distance from anchor represent the calorimeter's LET systematic error. The bottom part shows the total χ^2 from the fitting function for each point.	151
7.5	$\Delta R \pm \Delta e$ (Eq. 7.1) vs. E_{cut} , Charge Integration and Pulse-height: The x -axis is the E_{cut} value in MeV units. The y -axis is in ΔR units, with zero change representing 2012(PH)'s analysis using anchor point with cuts $A_R = 60$ mm and $E_{\text{cut}} = 52$ MeV, the error bars (Δe) on each point represent the uncorrelated statistical error between the point in question and the anchor point with the error bars going up when there is an statistical increase and down otherwise. The horizontal dashed black lines both at the same distance from anchor represent the calorimeter's LET systematic error. The bottom part shows the total χ^2 from the fitting function for each point.	152
8.1	The 95% C.L. upper limit on the heavy neutrino mixing parameter, as a function of its mass. The blue line shows the result from the derived branching ratio upper limit from a subset of data (Run IV) published in 2015 [5].	162
8.2	Background-suppressed $\pi^+ \rightarrow e^+ \nu_e$ positron energy spectrum (black histogram). Fitted components include muon decays in flight (thick blue line, from MC), $\pi^+ \rightarrow e^+ \nu_e$ (green, dot-dashed line, fit to MC), and $\pi^+ \rightarrow \mu^+ \nu_\mu \rightarrow e^+ \nu_e \bar{\nu}_\mu$ (red dashed line, from late-time data events). The insert shows the (rebinned) residuals (Data-Fit) with statistical error bars and the signal shape (massive neutrino search) in the case of $E_{e^+} = 40$ MeV and $ U_{ei} ^2 = 10^{-8}$ [11].	163

List of Figures

8.3	90% C.L. upper limits on the square of the mixing matrix elements $ U_{ei} ^2$ of heavy neutrinos coupled to electrons (thick red line) regarding the full PIENU dataset, , i.e., all runs from 2009 to 2012 [11]. The black dashed line shows the results from the previous generation PIENU experiment [29].	164
C.1	The 0 degree positron energy spectrum cleanse trough WC12 spatial and timing cuts.	180
C.2	The energy in Bina + CsI vs. the energy in T2. Blobs corresponding to positrons (~ 70 MeV), muons (~ 18 MeV), and pions (~ 14 MeV) can be clearly seen. There is also a structure around 30 MeV in Bina + CsI, with energy loss in T2 between positrons and beam muons. A similar structure appears in simulated pion events, from decays in flight.	181
C.3	The time of flight vs. the energy in BINA + CsI. Blobs corresponding to positrons and muons can be clearly seen. The region with essentially no events is due to the trigger condition excluding part of the RF window.	181
C.4	The energy spectrum of positrons in BINA + CsI, selected by time of flight.	182
C.5	The energy spectrum of muons in BINA + CsI, selected by time of flight.	182
D.1	T1 production target apparatus for M13 beam extension. . .	184
D.2	Beam input simulation	185
D.3	Beam low momenta cleaning sequentially through different beam components and the final beam spot at F4.	187
D.4	Position profiles from MC and from positron run #54880 at F4.	188
D.5	Position profiles from MC and from positron run #81633 at F4.	188
D.6	Focus point F1 slit simulation	189

List of Figures

D.7	Aerial view of beam-line simulation including all main components. Please refer to Figure 3.2 for blueprint. a) Right to Left: Starting from the T1 production target 75 MeV width ± 12 MeV positrons (red) are isotropically simulated and go through the first two focusing quadrupoles Q2 . Only a small solid angle is displayed. Positron passes horizontal slit (F0SL) and vertical jaws (F0JA) combo, then the first bending dipole steers the beam CW, then low momenta cleanse is done through F1SL/JA . Beam gets re-focused with three quads Q3 , Q4 , and Q5 , enters another F2SL/JA to then get bended CC and further focused by quads Q6 and Q7 . Positrons enter the beam-line extension and positrons bend CW through dipole B3 and final focusing is done with Q8 , Q9 and Q10 . b) Same configuration but in this case only pions (green) are produced initially. Muons (blue) and positrons are produced along each pion tree event but limited to one vertex. Additionally, a Lucite absorber is inserted after F1SL to separate the beam composition to enable magnetic selection of pions further downstream and finally a collimator at the beginning of the beam-line extension to filter the pions.	190
E.1	Complete trigger diagram of the PIENU Experiment [19].	191
F.1	Side view of the PIENU Detector. The pion beam comes from the right side.	192
F.2	Cross section of the PIENU Detector.	193
F.3	The PIENU detector mounted to TRIUMF's M13 beam-line.	194

Algorithms

5.1 Time Spectra Algorithm.	95
-------------------------------------	----

Glossary

Each entry is followed by “(G)” if it is a term in general use or “(E)” if it is specific to the experiment.

R_π (E)
 $\frac{\Gamma(\pi^+ \rightarrow e^+ \nu_e + \pi^+ \rightarrow e^+ \nu_e \gamma)}{\Gamma(\pi^+ \rightarrow \mu^+ \nu_\mu + \pi^+ \rightarrow \mu^+ \nu_\mu \gamma)}$ branching ratio.

SM (G)
Standard Model of particle physics.

π DIF (E)
Pion Decay in Flight.

π DAR (E)
Pion Decay at Rest.

LET (E)
Low Energy Tail.

LE (E)
Low Energy.

HE (E)
High Energy.

B1 (E)
Scintillator target for the beam.

NaI(Tl), NaI or Bina (E)
The main calorimeter, a monolith crystal made of thallium-doped sodium iodide.

CsI (E)
The 97 pure cesium iodide crystals surrounding Bina.

Bina+CsI (E)
The full PIENU calorimeter.

GEANT4 (E)

(for GEometry ANd Tracking) a platform for “the simulation of the passage of particles through matter,” using Monte Carlo methods.

Prescale (E)

One of the three physics triggers. Pre-scaled by 16 to save redundant data.

Early (E)

One of the three physics triggers. Selects events from an early time window.

TIGC or BinaHigh (E)

One of the three physics triggers. Selects events above an energy threshold.

QFT (G)

Quantum Field Theory.

EM (G)

Electro-Magnetic.

QCD (G)

Quantum Chromo Dynamics.

U(N) (G)

Unitary matrix of order N.

SU(N) (G)

Special Unitary matrix of order N.

QED (G)

Quantum Electro-Dynamics.

QFD (G)

Quantum Flavor-Dynamics.

EWT (G)

Electro-Weak Theory.

CKM (G)

CabibboKobayashiMaskawa matrix.

CMB (G)

Cosmic Microwave Background.

Λ CDM (G)

Lambda Cold Dark Matter model.

WIMPs (G)

Weakly-interacting massive particles.

ChPT (G)

Chiral Perturbation Theory.

BSM (G)

Beyond the Standard Model.

MSSM (G)

Minimal Super-symmetric Standard Model.

RPV (G)

R-Parity Violation.

Acknowledgements

To the entire PIENU collaboration and the Rare Decay Group at TRIUMF for their contributions, followed by guidance, and comradeship along the way from those who I met personally: alphabetically, Alexis A. Aguilar-Arevalo, Dorothea vom Bruch, Luca Doria*, Shintaro Ito, Matek Lewczuk, Richard Mischke*[†], Toshio Numao*[†], Rohan Nuttall, Yevgeniy Petrov, Aleksey Sher*, Tristan Sullivan*, Dima Vavilov, and Bob Velghe.

To my advisor Douglas Bryman*[†] for his trust, mentorship and financial support.

To [†] for writing reference letters to secure my next job with the T2K-Canada group.

To my committee, alphabetically, Omer Angel, Michael Hasinoff*, Christopher Hearty*, Klaus Kirch*, Takamasa Momose, Douglas Scott*, Oliver Stelzer-Chilton*[◇], Hirohisa Tanaka, also to faculty members, Gary Hinshaw, William McCutcheon, and Scott Oser, and fellow graduate students Terry Buck, Ricardo Chavez-Gonzalez, Joochun (Jason) Park, Itamar Reis, and Rodrigo A. Vargas-Hernandez for their assistance in achieving candidacy and graduation. To [◇] and Donald Witt for entrusting me with their lectures on several occasions, which provided me with invaluable teaching experience.

To * for giving critical comments on the draft stages for this thesis.

To UBC, TRIUMF, CONACYT, SEP-DGRI, Universidad Autonoma de Sinaloa, and Industrias Rochin SA de CV for their financial support. To members of the Brock Hall Ballers, and the Strathcona Stevedores for the good times throughout the years. To my family and friends for their unconditional support, especially Hernalda Felix-Avedaño, Maria J. Rochin-Uriarte, and Ernelda Ramos-Felix.

To Nelly, Sara, and Lucia.

Chapter 1

Introduction

The Prophecy. The pion is the lightest meson (quark-anti-quark bound state) with a mass of $139 \text{ MeV}/c^2$, and it was first predicted by Yukawa, when he published his theory of mesons in 1935 [33], as the carrier of a strong and short-range force that can bind nucleons in nuclei. In 1947, Powell and his collaborators discovered the pion [34] by exposing photographic plates to cosmic rays at a high altitude, i.e., at the tops of mountains. Yukawa and Powell received the Nobel Prize in Physics in 1949 and 1950, respectively [35]. Another light particle, the muon has a mass of $105.7 \text{ MeV}/c^2$; it was discovered in 1936, 10 years before the pion, and as it was in the same mass range, it was initially thought to be Yukawa's particle. The community had shared confusion for years before realizing that the muon was some heavy electron that was unable to interact with strong forces. Before the muon, the scientific community had only come across photons, protons, electrons, and neutrons. The particle physics revolution was still underway. Years later, Yukawa reflected on his seminal paper on particle interaction published in 1934:

"I felt like a traveler who rests himself at a small tea shop at the top of a mountain slope. At that time I was not thinking about whether there were any more mountains ahead." Tabibito [36].

Puzzles. The first puzzle was the observation of the $\pi^+ \rightarrow \mu^+ \nu_\mu \rightarrow e^+ \nu_e \bar{\nu}_\mu$ decay chain, but never the direct $\pi^+ \rightarrow e^+ \nu_e$ decay³. From pure phase space considerations, if the electron at $0.511 \text{ MeV}/c^2$ is two orders of magnitude smaller in mass than the muon, why do pions not decay directly into positrons or electrons? In 1955 and 1957, two experiments, one at Columbia University [37] and the other at the E. Fermi Institute [38], reported no direct electronic decay from pions, setting an upper limit on the branching ratio defined as the relative rate of decay of pions into electrons

³ $\pi^+ \rightarrow \mu^+ \nu_\mu \rightarrow e^+ \nu_e \bar{\nu}_\mu$ refers to a pion decaying to a muon and then to a positron with their respective neutrinos; $\pi^+ \rightarrow e^+ \nu_e$ refers to a pion decaying to a positron directly.

over muons (including associated neutrinos and radiative components),

$$R_\pi = \frac{\Gamma(\pi^+ \rightarrow e^+ \nu_e + \pi^+ \rightarrow e^+ \nu_e \gamma)}{\Gamma(\pi^+ \rightarrow \mu^+ \nu_\mu + \pi^+ \rightarrow \mu^+ \nu_\mu \gamma)}. \quad (1.1)$$

The upper limit was set to $R_{1957}^{\text{exp}} \sim 10^{-6}$. Another puzzle at the time was the evidence for parity violation in weak interactions; C. Wu *et al.* confirmed it with their beta-decay experiment in 1956 [39].

At the time, parity violation could only be explained by the contemporary vector-axial-vector (V-A) theory of weak interactions proposed by E.C.G. Sudarshan and R.E. Marshak [40]. In 1958, parity violation and the concept of a universal form of weak interaction were combined into one theory by R.P. Feynman and M. Gell-Mann [41]. The approach predicted a branching ratio of pions decaying directly to positrons over muons of the order of $R_{1958}^{(\text{V-A})} \sim 10^{-4}$ in contradiction with the experimental upper limit at that time. The V-A theory explains how the mass dependent helicity suppression (Section 2.2.2) favors the muonic decay over the positron by four orders of magnitude.

“These theoretical arguments seem to the authors to be strong enough to suggest that the disagreement with the He^6 recoil (a double focusing magnetic spectrometer used by Anderson *et. al.*) experiment and with some other less accurate experiments indicates that these experiments are wrong. The $\pi \rightarrow e + \bar{\nu}$ problem may have a more subtle solution.” - Feynman and Gell-Mann [41].

Redemption. Later in 1958, the $\pi^+ \rightarrow e^+ \nu_e$ decay mode was finally discovered at CERN [42] and Columbia University [43]. Later, in 1960, H.L. Anderson *et al.* obtained the first precise measurement [44] with $R_{1960}^{\text{exp}} = (1.21 \pm 0.07) \times 10^{-4}$, cementing and establishing the new V-A theory as the correct description of the weak interaction, which was subsequently adopted into the Standard Model (SM) of particle physics. Since pions were used to establish the SM, we can now use them to challenge it, measuring its properties with high precision and trying to detect deviations from predictions. Bryman *et al.* reported the latest theoretical ratio update in 2011 [24] at $R_{2011}^{\text{SM}} = (1.2352 \pm 0.0002) \times 10^{-4}$ which represents one of the most precisely calculated SM observable involving quarks.⁴ By contrast, the

⁴Discussed in Chapter 2.

1.1. Previous Measurements

current experimental value reported in 2015 by the PIENU experiment is $R_{2015}^{\text{exp}} = (1.2344 \pm 0.0023(\text{stat.}) \pm 0.0019(\text{syst.})) \times 10^{-4}$ [5], representing only about a tenth of our data, which is less precise than the theory by an order of magnitude. Therefore, further precision is required. The PIENU experiment at TRIUMF was planned with the aim of improving the precision level to 0.1%.

Motivation and Status. Deviations from the SM prediction may imply a violation of lepton universality, the SM hypothesis that electrons and muons have the same weak interactions; heavy neutrinos lighter than the pion [45]; and the presence of new physics beyond the SM, such as new pseudo-scalar interactions, i.e., R-parity violating super-symmetry pseudo-scalars [28], leptoquarks [46], and charged Higgs bosons [24]. In some instances, these indirect constraints can far exceed the reach of direct searches at colliders. Most remarkably, a deviation from SM could imply the existence of a new pseudo-scalar interaction with an energy scale up to $\mathcal{O}(1000 \text{ TeV})$, which would enhance the branching ratio by $\mathcal{O}(0.1\%)$ [47].

This dissertation represents the latest experimental measurement effort by the PIENU collaboration. The PIENU datasets contain four years of data, taken between 2009 and 2012, with 6.5 million (M) $\pi^+ \rightarrow e^+\nu_e$ events. The current analysis presented in this thesis is blinded, but includes the highest quality data portion available, 3 M $\pi^+ \rightarrow e^+\nu_e$ events. Moreover, major experimental systematic problems have been solved recently, allowing for increased precision up to 0.12% in R_{π}^{exp} .

1.1 Previous Measurements

The first precise measurement of the branching ratio was performed in 1960 by Anderson et al, using a magnetic spectrometer [44]. The experimental ratio $R_{1960}^{\text{exp}} = (1.21 \pm 0.07) \times 10^{-4}$ represents a precision level of 5%, and it was in complete agreement with the SM and the V-A structure of the weak interaction. The next milestone came in 1964, when Di Capua *et al.* [48] used a NaI (Tl) detector (length, 23 cm; diameter, 23 cm) sensitive to positrons as well as photons from radiative decays; the experiment collected around 11k $\pi^+ \rightarrow e^+\nu_e$ events at $R_{1964}^{\text{exp}} = (1.247 \pm 0.028) \times 10^{-4}$ representing a precision level of 2%. Di Capua's ratio was later revised to $R_{1975}^{\text{exp}} = (1.274 \pm 0.024) \times 10^{-4}$ [49], owing to a more accurate determination of the pion lifetime and remained within 2σ from the SM's theoretical

1.1. Previous Measurements

calculation ratio R_π^{SM} .

Another generation of experiments was initiated in 1983 at TRIUMF by Bryman *et al.* [50] using a larger NaI(Tl) crystal, measuring $R_{1983}^{\text{exp}} = (1.218 \pm 0.014) \times 10^{-4}$ from a sample of 0.032 M events. Such a ratio at a precision level of 1% was within 1σ of R_π^{SM} . In the 1990s, two subsequent experiments were carried out in TRIUMF [13] (experiment E248, see Section 1.2.1) and PSI [12], both collecting around 0.190 M events. The 1992 TRIUMF experiment used a NaI(Tl) crystal as the main calorimeter, while the 1993 PSI experiment used a 4π steradian BGO⁵ calorimeter; both achieved comparable levels of statistical and systematic uncertainties yielding as a combined result of $R_{\text{PDG1994}}^{\text{exp}} = (1.231 \pm 0.005) \times 10^{-4}$ [21]. This ratio, at a precision level of 0.5%, was again within 1σ from R_π^{SM} .

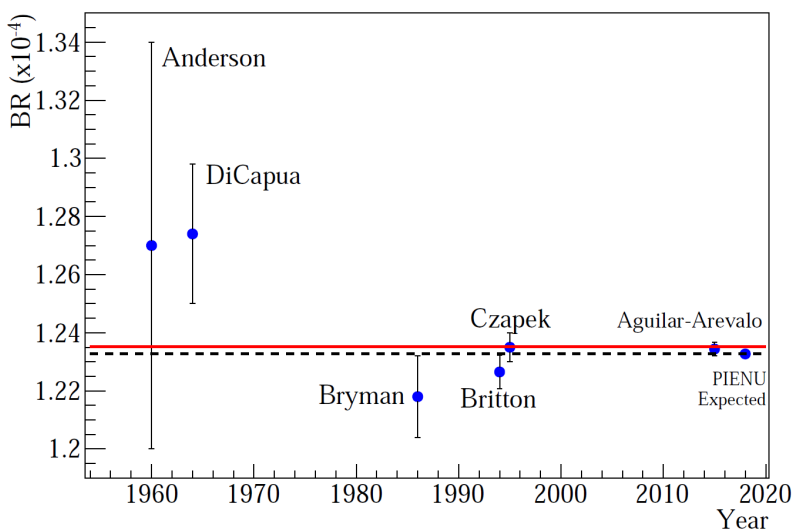


Figure 1.1: History of the R_π^{exp} branching ratio measurements. Red line: SM calculation [24]. Black dashed line: PDG experimental average [21].

The current generation of R_π^{exp} measurements is being performed at TRIUMF and PSI [51] with similar precision goals. Recently, in 2015, the PIENU experiment at TRIUMF reported a subset of its data resulting $R_{2015}^{\text{exp}} = (1.2344 \pm 0.0023(\text{stat.}) \pm 0.0019(\text{syst.})) \times 10^{-4}$ [5], with only 0.4 M events out of the 5 M available; this represents a 0.24% precision level,

⁵Bismuth germanium oxide.

1.2. Experimental Technique

and is in agreement with the SM. The current average reported by the Particle Data Group (PDG) is $R_{\text{PDG2018}}^{\text{exp}} = (1.2327 \pm 0.0023) \times 10^{-4}$ [21] with precision of 0.19%. This weighted average includes all measurements from 1986 to 2015. The PIENU experiment once finalized, will have an expected precision level of 0.1%. Figure 1.1 shows the experimental ratio time evolution.

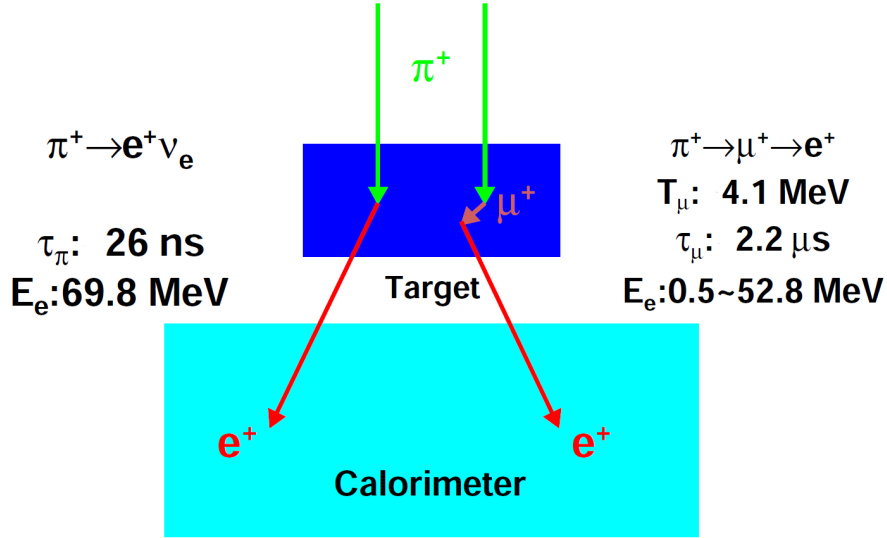


Figure 1.2: Schematic illustration of experimental technique: two pionic decays in a scintillator target; and decay positrons collected by the calorimeter.

1.2 Experimental Technique

Since 1964, following Di Capua's experiment [48], the same fundamental technique has been used for every branching ratio measurement. One stops a charged pion beam in a scintillator target, thick enough to allow the pion to decay within it to either the $\pi^+ \rightarrow \mu^+ \nu_\mu \rightarrow e^+ \nu_e \bar{\nu}_\mu$ decay chain or directly to $\pi^+ \rightarrow e^+ \nu_e$; then, a calorimeter measures positrons from both pion decays (Figure 1.2). Muons deposit $T_\mu = 4.12 \text{ MeV}$ of kinetic energy in the scintillator and decay within the target. $\pi^+ \rightarrow \mu^+ \nu_\mu \rightarrow e^+ \nu_e \bar{\nu}_\mu$ positrons, produce a broad energy distribution (referred to as muon spectrum) between its rest mass 0.511 MeV and a sharp endpoint at half the muon's mass of 52.8 MeV. The $\pi^+ \rightarrow e^+ \nu_e$ positrons give rise to a mono-energetic peak at 69.8 MeV. Most positrons ($E_{e^+} > 5 \text{ MeV}$) from both decay channels, traverse

half of target, and the rest of the remaining detector components traversing about 8 cm upstream of the front of the calorimeter’s face. Positrons on the beam’s axis traverse plastic scintillator, silicon, and aluminum depositing about 3.7 MeV on average before entering the calorimeter. Time-wise, the pion lifetime at $\tau_\pi = 26.0$ ns is two orders of magnitude shorter than that of the muon at $\tau_\mu = 2.197$ μ s. Different energies and timings allow for distinction between the two decay modes.

1.2.1 Lessons from the E248 experiment

The setup of the previous TRIUMF experiment E248 for the pion branching ratio measurement is shown in Figure 1.3. Pions were stopped in a scintillator target, and the decay positrons were detected in a cylindrical NaI(Tl) crystal named “Tina”, whose axis of rotation was orientated at 90° with respect to the beam to avoid beam-related backgrounds. Although the solid angle was only 2% of 4π steradians, 0.190 M $\pi^+ \rightarrow e^+\nu_e$ events were collected during six months of data-taking, resulting in $R_{1992}^{\text{exp}} = (1.2265 \pm 0.0034(\text{stat.}) \pm 0.0044(\text{syst.})) \times 10^{-4}$ [25]. The main systematic uncertainty came from the estimation of the $\pi^+ \rightarrow e^+\nu_e$ low energy tail (LET) “buried” under the broad $\pi^+ \rightarrow \mu^+\nu_\mu \rightarrow e^+\nu_e\bar{\nu}_\mu$ energy spectrum. The LET comes mainly due to energy loss in the calorimeter (Section 6.1).

The LET needs to be estimated precisely in order to correct the branching ratio for those misidentified low energy positrons. In order to suppress the $\pi^+ \rightarrow \mu^+\nu_\mu \rightarrow e^+\nu_e\bar{\nu}_\mu$ events and estimate the size of this tail, tight cuts were used on the target energy to reject the muonic decay. The calorimeter’s “suppressed spectrum” is shown in Figure 1.3 (right). Clearly, a $\pi^+ \rightarrow \mu^+\nu_\mu \rightarrow e^+\nu_e\bar{\nu}_\mu$ component is still visible; these were mostly events where the pion decayed in flight (π DIF) before the target. The π DIF component was identified with the slightly higher energy deposit in target by the muon due to the Lorentz boost effect, thus through this mechanism the event is misidentified as a $\pi^+ \rightarrow e^+\nu_e$ event and is carried over to the “suppressed spectrum” shown in Figure 1.3 (right).

The calorimeter energy threshold was set at 56.4 MeV (3400 channel in Figure 1.3). The fraction of events below the energy threshold compared to the total number of $\pi^+ \rightarrow e^+\nu_e$ events was around 20% and was dominated by these π DIF events. The large remaining tail and the low statistics were limiting factors for precise estimation of the low energy tail (LET),

1.2. Experimental Technique

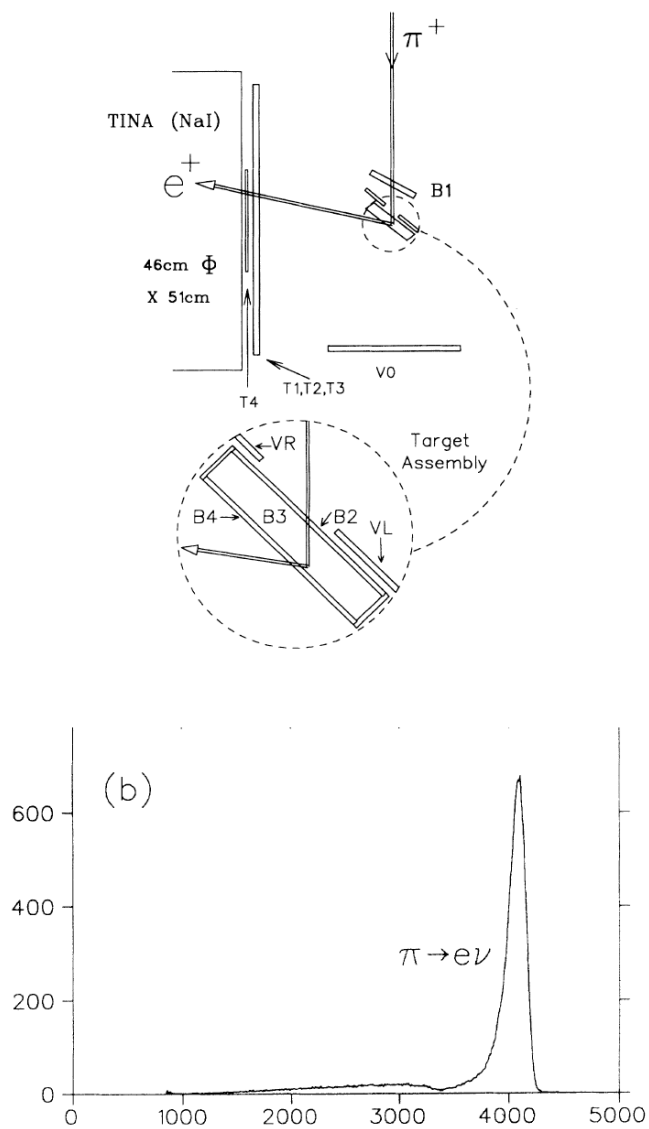


Figure 1.3: (Top) Experimental setup of the E248 experiment at TRIUMF [25]. (Bottom) Positron energy spectrum obtained by suppressing $\pi^+ \rightarrow \mu^+ \nu_\mu \rightarrow e^+ \nu_e \bar{\nu}_\mu$ events, the x -axis is energy in ADC counts (channel 3400 corresponds to 56.4 MeV).

which is the main correction for the branching ratio and therefore a leading contributor to the final error. The LET arises because of energy losses due to electromagnetic shower⁶ leakage in the calorimeter measuring the positron energy and from radiative decays ([25], and [13]). To increase the statistics in the new PIENU experiment, the calorimeter was placed directly downstream following the target scintillator, thereby increasing the angular acceptance of the isotropic positron tracks. Particle tracking hardware was added before the target to identify π DIF in order to reduce the uncertainty in the LET. Also, the new PIENU detector was designed with the ability to rotate the calorimeter setup relative to the beam angle to help characterize the calorimeters response to a direct positron beam to further reduce the experiment’s main correction and source of systematics for the branching ratio.

1.2.2 PIENU technique

In the PIENU experiment 520 MeV protons from TRIUMF’s cyclotron primary beam-line BL1 strike a Beryllium production target to generate pions that are subsequently collected by a secondary beam-line. Pions are selected with a momentum of 75 ± 1 MeV/c [1]; then, the beam is aimed at PIENU’s 8-mm-thick plastic scintillator target named “B3”. The beam momentum is tuned so that the pions will stop in the middle of target B3. Muons from π DAR have a penetration range of 1 mm within B3. Therefore, there is sufficient material to contain the decay vertex from both decays $\pi^+ \rightarrow \mu^+ \nu_\mu \rightarrow e^+ \nu_e \bar{\nu}_\mu$ and $\pi^+ \rightarrow e^+ \nu_e$. Figure 1.4 shows a GEANT4⁷ energy distribution in the target for both pion decay modes. Positrons from both decays enter the 48 cm \times 48 cm (19 radiation-length long) single crystal PIENU calorimeter named “Bina”, made of Thallium-doped sodium iodide NaI(Tl) loaned from Brookhaven National Laboratory. To further contain the radiative shower energy leakage and reduce uncertainty in the LET, Bina is surrounded by 97 pure CsI crystals. The PIENU calorimeter is named “Bina+CsI”. Figure 1.5(left) shows GEANT4 energy distributions for both

⁶ An electromagnetic shower begins when a high-energy electron, positron or photon enters a material. At high energies (above a few MeV), photons interact with matter primarily via pair production (electron-positron) by interacting with an atomic nucleus or electron in order to conserve momentum. High-energy electrons and positrons primarily emit photons, a process called bremsstrahlung. When photons fall below the pair production threshold, then energy losses of electrons (and positrons) from photoelectric effects and Compton scattering start to dominate.

⁷For GEometry ANd Tracking is a platform for “the simulation of the passage of particles through matter,” using Monte Carlo method [52].

1.2. Experimental Technique

signals.

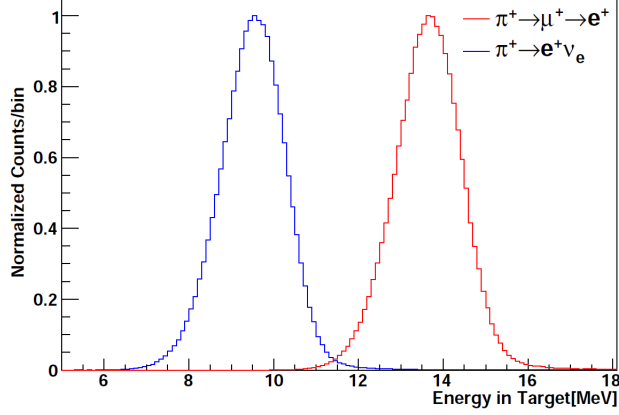


Figure 1.4: Energy deposited in the target B3 for $\pi^+ \rightarrow e^+\nu_e$ (blue line) and $\pi^+ \rightarrow \mu^+\nu_\mu \rightarrow e^+\nu_e\bar{\nu}_\mu$ (red line) events from GEANT4.

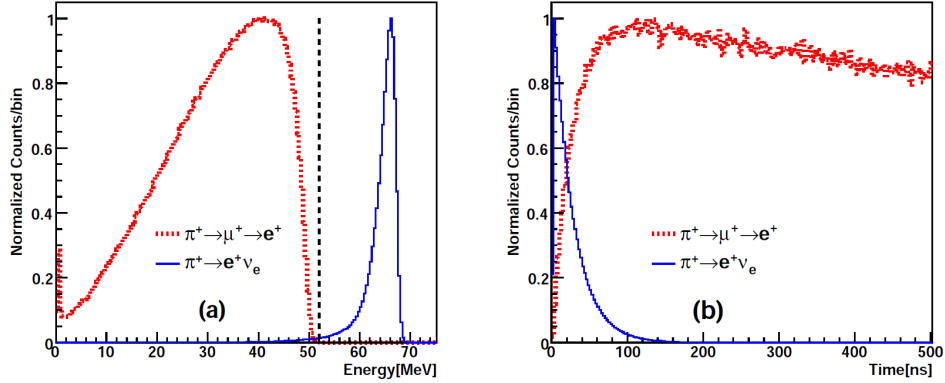


Figure 1.5: (Left) Time spectra and (right) energy spectra in the calorimeters of $\pi^+ \rightarrow e^+\nu_e$ and $\pi^+ \rightarrow \mu^+\nu_\mu \rightarrow e^+\nu_e\bar{\nu}_\mu$ decays obtained from simulations. The spectra are normalized to the same amplitude. Using an energy cut-off (E_{cut}) above the $\pi^+ \rightarrow \mu^+\nu_\mu \rightarrow e^+\nu_e\bar{\nu}_\mu$ energy spectrum edge (dashed line), we divide the energy spectrum into low-energy (LE) and high-energy (HE) parts. The low energy tail (LET) from the $\pi^+ \rightarrow e^+\nu_e$ energy spectrum is not visible due to scale and the pion decay in flight (π DIF) contribution was deactivated. The $\pi^+ \rightarrow e^+\nu_e$ time distribution peaks near $t = 0$ because of the relatively short pion lifetime.

1.2. Experimental Technique

If the two decay modes and the various backgrounds are known precisely, then counting the number of events above and below the $\pi^+ \rightarrow \mu^+ \nu_\mu \rightarrow e^+ \nu_e \bar{\nu}_\mu$ energy spectrum edge can provide an estimate of the branching ratio. Such an estimate would ignore the background due to pile-up effects (Chapter 4) and the dominant correction of the LET (Section 6.1). The main sources of background in the PIENU experiment are the beam-related background, pileup of muons from previous pion decays, pileup of neutral particles, and photons emitted during the decay chains that could shift energies in the detector leading to misidentification of events. Chapter 4 will address all backgrounds. As the exact energy distribution from the two main decay modes and backgrounds cannot be known with sufficient accuracy, we extract the number of events from the time spectrum distributions, most of which are analytically well known. Figure 1.5(right) shows GEANT4 simulations of time distributions for both decays. The $\pi^+ \rightarrow e^+ \nu_e$ decay time distribution is an exponential with the pion lifetime $\propto e^{-t/\tau_\pi}$. The $\pi^+ \rightarrow \mu^+ \nu_\mu \rightarrow e^+ \nu_e \bar{\nu}_\mu$ decay chain time distribution (derived in Appendix A) rises up to around 100 ns, and then falls with the muon lifetime $\propto (e^{-t/\tau_\pi} - e^{-t/\tau_\mu})$. Using an energy cut-off (E_{cut}) above the $\pi^+ \rightarrow \mu^+ \nu_\mu \rightarrow e^+ \nu_e \bar{\nu}_\mu$ energy spectrum edge (dashed line in Figure 1.5(Left)), we divide the energy spectrum into low-energy (LE) and high-energy (HE) parts, and we then build the two separate time spectra. The LE time spectrum contains mainly $\pi^+ \rightarrow \mu^+ \nu_\mu \rightarrow e^+ \nu_e \bar{\nu}_\mu$ and the HE time spectrum mainly $\pi^+ \rightarrow e^+ \nu_e$ events.

The raw branching ratio can be extracted by performing a simultaneous fit of signal and background shapes from both the LE and HE time spectra. The raw ratio is corrected by the amount of LET calculated (the LET shape is not included in the time spectrum analysis) plus other corrections related to the detector's acceptance and the pion stopping position within the target. Chapter 6 describes the calculation of the corrections and the separate experiment for LET calculation involving the rotation of Bina+CsI against a direct positron beam to obtain the energy response. Measuring the ratio of the decay rates or the energy distributions does not require knowledge of the total number of incoming pions, as positrons from both decay chains are measured regardless of the mode. Most efficiencies of the cuts and triggers cancel in the measured ratio of decay, thus reducing the systematic uncertainty. The geometrical acceptance and its correction are due

to energy-dependent multiple scattering, Bhabha scattering⁸, and pair production⁹. The time spectrum analysis (Chapter 4) is chosen over the energy analysis, as it eliminates or reduces most sources of systematic error.

1.3 Blind Analysis

A blind analysis is recognized as an important tool to reduce the impact of human conscious or unconscious bias, especially in a high precision measurement that will then be compared with a precise theoretical prediction. A well-known example of possible bias would be the experimental results of the neutron lifetime through the years as shown in Figure 1.6 [21]; the good agreement of the central value for sets of consecutive experiments may be interpreted as bias. Several scenarios for blind analysis in particle physics have been executed, as discussed in many papers (e.g., [53] [54]). However, the blinding technique is fully dependent on the experiment and can sometimes be difficult to implement. The blinding procedure should not artificially hide or create new systematic effects that would sabotage the analysis.

In the PIENU experiment, the energy information in the target was used to blind the branching ratio (R_π). The R_π value was changed without distorting the time spectrum in which the fitting was performed. Figure 1.7 shows the schematic of the blinding method in the PIENU experiment. A smooth rectangular function (red line in Figure 1.7) with hidden efficiency was used to remove $\pi^+ \rightarrow e^+\nu_e$ events. As $\pi^+ \rightarrow e^+\nu_e$ events were randomly rejected, R_π was changed without distortion of the time spectrum or the calorimeter's energy spectrum. This inefficiency factor was produced by a uniform random number between 0 and 0.5%. The same procedure was applied uniformly to all datasets so that they can be compared in systematic tests such as R_π vs. acceptance, energy cut-off (E_{cut}) for the HE/LE regime, and pileup. The position of the edge of the rectangular function was aligned to the position of valley between $\pi^+ \rightarrow e^+\nu_e$ and $\pi^+ \rightarrow \mu^+\nu_\mu$ peaks so that the edge would be hidden under the statistical fluctuation of the low statistics region. The blinded events will be included in the analysis once all the event selection cuts, shapes used in the time spectrum fit, and branching

⁸ In quantum electrodynamics, Bhabha scattering is the electron-positron scattering process mediated by the photon. The Bhabha scattering rate is used as a luminosity monitor in electron-positron colliders.

⁹The creation of a subatomic particle and its antiparticle from a neutral boson. Examples include creating an electron and a positron, a muon and an antimuon, or a proton and an antiproton.

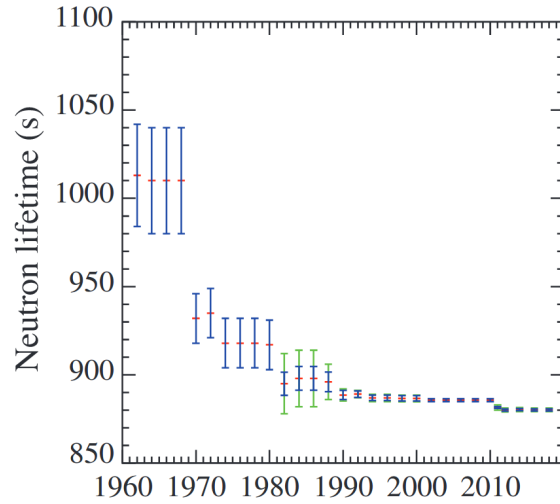


Figure 1.6: Evolution in time (years) of the neutron's lifetime experimental result [21].

ratio corrections are finalized. Moreover, the blinded branching ratio must be stable as we vary the parameters in the analysis, and all systematic errors must be assigned before unblinding the result. The current analysis presented in this thesis is blinded.

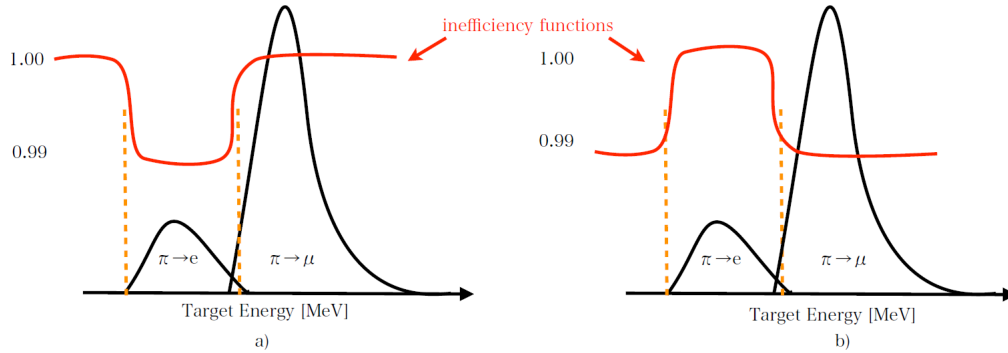


Figure 1.7: PIENU's blinding technique. A smooth inefficiency function (unknown to the experimenters) removes events based on their energy deposited in the target, lowering (case a) or raising (case b) the branching ratio.

1.4 Thesis Outline

In Section 1.1, previous pion decay measurements are listed, and in Section 1.2, an overview of PIENU's experimental technique is provided. Chapter 2 briefly explains the Standard Model (SM), i.e., the main theoretical background for our experiment, provides a historical review of the current branching ratio calculation, beyond SM candidates for deviations and parameter space limits linked to the experimental value. Chapter 3 provides a comprehensive description of the experimental setup with regard to the beam-line, instrumentation, detectors, and software architecture involved. Chapter 4 briefly describes the variable extraction procedures, event selection, and the energy spectra for the calorimeter. Chapter 5 outlines the time spectrum analysis procedure for obtaining the first-order or raw branching ratio. Chapter 6 explains the main corrections for the raw ratio. Chapter 7 presents the results for the branching ratio, including systematic stability tests, total error budget, the dataset combination procedure, and future prospects for further precision measurement improvement. Finally, Chapter 8 presents the final *blinded* branching ratio, and the new physics limits reached assuming the central value from the branching ratio published by the PIENU experiment in 2015 [5].

Chapter 2

Theory

The Standard Model (SM) is the theoretical framework for describing the $\pi^+ \rightarrow e^+ \nu_e$ decay. A brief description is given in Section 2.1. Section 2.2 deals with the electroweak theory for pion decay, and Section 2.3 presents the motivation beyond the Standard Model for the $\pi^+ \rightarrow e^+ \nu_e$ measurement.

2.1 The Standard Model of Particle Physics

The SM is a relativistic *Quantum Field Theory* (QFT) for particle physics. The SM was developed in the 20th century with ideas for unification, symmetries, and gauge theories to describe the basic structure of matter and vacuum. The SM considers the fundamental particles (or fields) as indivisible entities and their interactions are governed by known forces in the universe, i.e., *Electromagnetic* (EM), *Weak*, *Strong*, but not including *Gravity*. Table 2.1 shows the force mediators, called bosons. Topologically, the SM is a gauge theory based on the group

$$\underbrace{SU(3)}_{\text{strong}} \times \underbrace{SU(2) \times U(1)}_{\text{electroweak}}. \quad (2.1)$$

The model unifies the weak and electromagnetic force (“electroweak” force) within the $SU(2) \times U(1)$ groups, respectively. Mass is provided by a spontaneous symmetry-breaking mechanism driven by the presence of a scalar Higgs field. The Higgs mechanism has four degrees of freedom and after spontaneous symmetry breaking three of them are “eaten up” by 3 of the 4 $SU(2) \times U(1)$ generators, leading to 3 new massive particles W^\pm and Z^0 , while leaving the fourth massless particle identified with the photon (γ) of the electromagnetic interaction and their respective coupling constants g and α [55] [56] [57] [58].

All known fundamental particles and some of their properties are summarized in Table 2.1 for full-integer spin bosons, and Table 2.2 for half-integer

2.1. The Standard Model of Particle Physics

spin fermions. Fermions are the building blocks of all known nuclei, thus responsible for all known elements. The SM bosons and fermions are massive, with the exception of the massless photons (γ) and neutrinos (ν). Nevertheless, current experimental observations indicate ν do have mass. Each column in the Table 2.2 represents a *generation*¹⁰. Each particle has its own antiparticle; in theory, they should have the same mass as one another but opposite electric charges and differences in other quantum numbers. For example, an electron (e^-) has a positive partner, the positron (e^+). Other neutral charged entities, such as the electron neutrino (ν_e), has a counterpart electron anti-neutrino ($\bar{\nu}_e$), and they differ by having opposite signs of lepton number¹¹ and chirality¹². A detailed historical and theoretical description and the limits of the SM can be found in [55], [56], [57], and [58].

Table 2.1: Bosons (integer spin).

Mediator	Coupling at $\sim 100\text{MeV}$	Range	Behaviour
gluon (massless)	$\alpha_s = 1.7$ (energy dependent)	10^{-15}m	$\sim r$ (confinement)
$\gamma < 1 \times 10^{-18} \text{ eV}$	$\alpha = 1/137$	∞	$1/r^2$
$W^\pm = 80.38(1) \text{ GeV}/c^2$	$G_{\text{Fermi}} \sim g^2/m_W^2$		
$Z^0 = 91.1876(21) \text{ GeV}/c^2$	$G_{\text{Fermi}} \approx 10^{-5} \text{ GeV}^{-2}$		
$H = 125 \text{ GeV}/c^2$			

¹⁰ Between generations, particles differ by their flavour quantum number and mass, but their interactions are identical.

¹¹ Lepton number is a conserved quantum number representing the difference between the number of leptons and the number of anti-leptons in an elementary particle reaction

¹² Chirality is a fundamental property of a particle; particles which differ in terms of chirality can be viewed as an entirely different type of particle. It refers to how a particle's quantum mechanical wave function behaves when a particle is rotated (or looked at from a different angle). For example, a spin 1/2 (fermion) particle's wavefunction will gain a minus sign under a 360 degree rotation, as the rotation changes the complex phase of the wavefunction. The particle's chirality determines in a sense which way around the complex plane this phase travels to reach the -1, traveling in either a left handed way from 1 to -1, or a right handed way from 1 to -1. A massive particle can have either left- or right-handed helicity dependent on the reference frame, but can only have one chirality either left- or right-handed. A massless particle helicity and chirality is the same for all frames. Only left-handed fermions and right-handed antifermions interact with the weak force.

2.1. The Standard Model of Particle Physics

Table 2.2: Fermions (spin 1/2 integers).

	Generations			Charge (Q/ e)
	I	II	III	
Leptons	$e = 0.511 \text{ MeV}/c^2$	$\mu = 105.658 \text{ MeV}/c^2$	$\tau = 1.77686(12) \text{ GeV}/c^2$	-1
	$\nu_e < 2 \text{ eV}/c^2$	$\nu_\mu < 0.17 \text{ MeV}/c^2$	$\nu_\tau < 18.2 \text{ MeV}/c^2$	0
Quarks	$u = 2.2(5) \text{ MeV}/c^2$	$c = 1.275(35) \text{ GeV}/c^2$	$t = 173.0(4) \text{ GeV}/c^2$	+2/3
	$d = 4.7(5) \text{ MeV}/c^2$	$s = 95(9) \text{ MeV}/c^2$	$b = 4.18(4) \text{ GeV}/c^2$	-1/3

2.1.1 Electroweak interactions

Weak interactions are less familiar in everyday life than EM and act through a mediator W^\pm for a charged current decay channel or Z^0 boson for a neutral-current decay channel on all known particles. *Quantum flavour-dynamics* (QFD) is the fundamental framework for the weak force with the $SU(2)$ group; however, the *electroweak theory* (EWT) is used over QFD as it provides the best understanding of the weak processes under the $SU(2) \times U(1)$ groups. The weak interaction is responsible for radioactive decay, such as beta decay, $n \rightarrow p + e^- + \bar{\nu}_e$. Characteristics of the weak interaction are *flavour-changing*¹³ of quarks, parity-symmetry **P** violation, and charge-parity **CP** violation [55] [56] [57] [58].

The electromagnetic (EM) force acts using the photon (γ) boson as the mediator between electric charge particles such as protons, electrons, muons (μ), and charged pions. The EM force is best described with *quantum electrodynamics* (QED) theory using the $U(1)$ group. The EM force explains the structure of atoms, crystals, molecules, and chemistry in general, as well as EM radiation or light. QED gives exceptionally accurate predictions for quantities such as the magnetic moment of the electron and the Lamb shift of the hydrogen energy level [59].

2.1.2 Strong interactions

Strong interactions act using a *gauge boson* called a *gluon* as the mediator on some subset of the particles, i.e., hadrons, or anything made of quarks (q), such as protons (p), neutrons (n), and pions (π^0 or π^\pm). The strong interaction is described with *Quantum Chromo-Dynamics* (QCD) using the

¹³ Flavour refers to the species of an elementary particle. The Standard Model counts six flavours of quarks and three flavours of leptons. They are conventionally parameterized with flavour quantum numbers that are assigned to all subatomic particles.

$SU(3)$ Lie groups. The role of the strong interaction in nature results in nuclear binding or fusion, i.e., allowing the variety of nuclei to be formed in the stars, indispensable for their life cycle, and representing their main source of energy. The strong interaction is also responsible for nuclear fission, which is the ultimate source of energy of nuclear reactors, and weapons.

An important feature of QCD is “asymptotic freedom”, meaning that the strong coupling becomes smaller with increasing momentum transfer in particle interactions. One of the consequences of the QCD running coupling is that at low energies quarks are confined in uncoloured bound states (baryons and mesons). In the low energy regime the QCD coupling constant cannot be considered small and this implies that a perturbative treatment is not possible. Non-perturbative methods such as Chiral Perturbation Theory (ChPT) and Lattice QCD have been used for strong interaction calculations in the low energy regime, allowing for an expansion of the decay rates in powers of the pion mass (Section 2.2.3) and the electromagnetic coupling, through which the uncertainty on the ratio can be tightly constrained.

2.2 Pion Decay Theory

Mesons are quark-anti-quark pairs bound together by strong forces. Pions are mesons of the first generation; π^+ is made of an *up* (u) and *anti-down* (\bar{d}) quark; π^- is made of a *down* (d) and *anti-up* (\bar{u}) quark; and π^0 is a combination of a u with \bar{u} or d with an \bar{d} quark. As pions are the lightest particles made of quarks, they can only decay via weak interactions. The π^\pm has mass $139.57 \text{ MeV}/c^2$ and a mean lifetime of 26.033 ns . It only decays into lighter leptons, i.e., either a muon or an electron and a neutrino. Muons (μ) have mass of $105.658 \text{ MeV}/c^2$ and a mean lifetime of $2.2 \mu\text{s}$. They decay through weak interactions principally to electrons and neutrino-anti-neutrino pairs.

According to [21], the measured π^+ and μ^+ decay modes are shown in Table 2.3 and 2.4, respectively. The PIENU experiment is sensible to $\pi^+ \rightarrow \mu^+ \nu_\mu$ (Γ_1^π), $\pi^+ \rightarrow \mu^+ \nu_\mu \gamma$ (Γ_2^π), $\pi^+ \rightarrow e^+ \nu_e$ (Γ_3^π), and $\pi^+ \rightarrow e^+ \nu_e \gamma$ (Γ_4^π). All other pion decay rate channels are below 10^{-7} , negligible for our 0.1% level of precision and thus can be ignored here. Section 2.2.1 explains the decay mode theory for Γ_1^π and Γ_3^π . Section 2.2.2 discusses *helicity suppression*, which shows why the $\pi^+ \rightarrow \mu^+ \nu_\mu \rightarrow e^+ \nu_e \bar{\nu}_\mu$ decay is preferred over

2.2. Pion Decay Theory

Table 2.3: Measured pion decay modes [21]. The radiative energy (E_γ) restrictions are concerning the cited experiment, not the PIENU experiment.

	Decay mode	Fraction (Γ_i^π/Γ^π)
Γ_1^π	$\pi^+ \rightarrow \mu^+ \nu_\mu$	0.9998770 ± 0.00004
Γ_2^π	$\pi^+ \rightarrow \mu^+ \nu_\mu \gamma$	$(2.00 \pm 0.25) \times 10^{-4}$ ($E_\gamma > 1$ MeV)
Γ_3^π	$\pi^+ \rightarrow e^+ \nu_e$	$(1.230 \pm 0.004) \times 10^{-4}$
Γ_4^π	$\pi^+ \rightarrow e^+ \nu_e \gamma$	$(7.39 \pm 0.05) \times 10^{-7}$ ($E_\gamma > 10$ MeV)
Γ_5^π	$\pi^+ \rightarrow \pi^0 e^+ \nu_e$	$(1.036 \pm 0.006) \times 10^{-8}$
Γ_6^π	$\pi^+ \rightarrow e^+ \nu_e e^+ e^-$	$(3.2 \pm 0.5) \times 10^{-9}$

Table 2.4: Measured muon decay modes [21]. The radiative energy (E_γ) restrictions are concerning the cited experiment, not the PIENU experiment.

	Decay mode	Fraction (Γ_i^μ/Γ^μ)
Γ_1^μ	$\mu^+ \rightarrow e^+ \nu_e \bar{\nu}_\mu$	$\approx 100\%$
Γ_2^μ	$\mu^+ \rightarrow e^+ \nu_e \bar{\nu}_\mu \gamma$	$(1.4 \pm 0.4)\%$ ($E_\gamma > 10$ MeV)
Γ_3^μ	$\mu^+ \rightarrow e^+ \nu_e \bar{\nu}_\mu e^+ e^-$	$(3.4 \pm 0.4) \times 10^{-5}$

the $\pi^+ \rightarrow e^+ \nu_e$ one, and Section 2.2.3 comments on the radiative correction calculations concerning the Γ_2^π and Γ_4^π decay modes.

2.2.1 Vector-Axial-Vector (V-A) Weak Interaction

The π^+ decay is described with the *Feynman diagram* [55] shown in Figure 2.1. It illustrates the scattering process of π^+ , $u + \bar{d} \rightarrow l^+ + \nu_l$ decay, where $l = e, \mu$. The internal wavy line represents the W^+ boson as the intermediate particle and the flavour changing processes, q , p_l , and p_ν are the four-momenta for W^+ , anti-lepton l^+ , and ν , as indicated in Figure 2.1. Each vertex has 4-momentum conservation using delta functions, $-ig(2\pi)^4 \delta^4(p_u - p_d - q)$ on the left and $-ig(2\pi)^4 \delta^4(q + p_l - p_\nu)$ on the right. 4-momenta entering the vertex are positive, while those leaving are negative. The factors at each vertex and internal line are multiplied by the amplitude integral. The direction of time goes from negative left to positive right. The arrows going right are particles and arrows going left are anti-particles. The weak interaction coupling constant (g), is expected to be the same for all leptons in the SM.

2.2. Pion Decay Theory

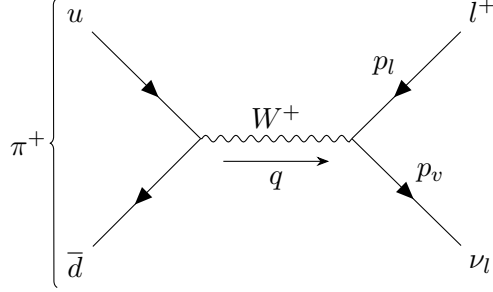


Figure 2.1: Feynman diagram for the $\pi^+ \rightarrow l^+ \nu_l$ decay, where $l = e, \mu$. The TikZ-Feynman package [60] was used.

Expressing Fermi's golden rule [55], the differential decay rate for $\pi^+ \rightarrow l^+ \nu_l$ (where $l = e$ or μ) can be written as

$$d\Gamma = \frac{1}{2m_\pi} |\mathcal{M}|^2 \frac{1}{E_l E_\nu} \frac{d^3 p_l}{(2\pi)^3} \frac{d^3 p_\nu}{(2\pi)^3} (2\pi)^4 \delta^4(q - p_l - p_\nu), \quad (2.2)$$

where m_π is the mass of a pion. The matrix element \mathcal{M} is the product of the propagator and the leptonic and hadronic currents, where the pion and lepton vertex currents $\mathcal{J}_{\mu\pi}$ and $\mathcal{J}_{l\nu}$ are products of the particles' wavefunctions (Ψ) with 4-vector operators (\mathcal{O}):

$$\mathcal{M} = \frac{ig^{\mu\nu}}{M_W^2 - q^2} \mathcal{J}_{\mu\pi} \mathcal{J}_{l\nu} \sim (\bar{\Psi}_b \mathcal{O} \Psi_b) (\bar{\Psi}_l \mathcal{O} \Psi_l). \quad (2.3)$$

However, in our case, the momentum transfer is small compared to the mass of the W boson so that the momentum transfer q in the propagator's denominator can be ignored. This is equivalent to assuming a Fermi point-like interaction, and the matrix element is $\mathcal{M} = \langle l^+ \nu_l | \mathcal{L} | \pi^+ \rangle$ and \mathcal{L} is the charged current Lagrangian [55]:

$$\mathcal{L}_{W^+} = \frac{ig}{2\sqrt{2}} W_\mu^+ (\bar{\nu}_m \gamma^\mu (1 - \gamma^5) e_m + V_{mn} \bar{u}'_m \gamma^\mu (1 - \gamma^5) d'_m). \quad (2.4)$$

Dirac gamma matrices are γ^μ , where the summation index μ goes from zero to three and $\gamma^5 = i\gamma^0\gamma^1\gamma^2\gamma^3$. The index m goes from one to three, representing the particle generation with $e_1 = e$, $e_2 = \mu$, and $e_3 = \tau$, as in the case of neutrinos ν_m . The term $V_{mn} \bar{u}'_m \gamma^\mu (1 - \gamma^5) d'_m = \bar{u}_m \gamma^\mu (1 - \gamma^5) d_m$ represents the flavor quark change due to the weak interaction and

2.2. Pion Decay Theory

V_{mn} comes from the Cabbibo-Kobayashi-Maskawa (CKM) matrix in the following manner:

$$\begin{bmatrix} d' \\ s' \\ b' \end{bmatrix} = \begin{bmatrix} V_{ud} & V_{us} & V_{ub} \\ V_{cd} & V_{cs} & V_{cb} \\ V_{td} & V_{ts} & V_{tb} \end{bmatrix} \begin{bmatrix} d \\ s \\ b \end{bmatrix}. \quad (2.5)$$

The primes indicate particles in the interaction basis, while the unprimed vector represents particles in the mass basis. The *operator* $(1-\gamma^5)$ is responsible for the parity-violating nature of the weak interaction. Parity violation is most easily seen by writing γ^5 and the spinor representing a fermion in the Weyl or chiral basis [61]:

$$\gamma^5 = \begin{bmatrix} 1 & 0 & 0 & 0 \\ 0 & 1 & 0 & 0 \\ 0 & 0 & -1 & 0 \\ 0 & 0 & 0 & -1 \end{bmatrix}, \psi = \begin{bmatrix} \psi_L \\ \psi_R \end{bmatrix}. \quad (2.6)$$

Here, ψ_L and ψ_R are two-component objects, where the components represent the two possible spin states of a spin 1/2 particle. The operator $\frac{1-\gamma^5}{2}$ when multiplied against a spinor selects left-handed chiral particles and right-handed chiral anti-particles as components.

Expanding the matrix element into a hadronic and leptonic part with Eq. 2.3 and Eq. 2.4, respectively. Together with the Fermi *coupling constant* relation $\frac{G_F}{\sqrt{2}} = \frac{g_l^2}{8M_W^2}$ gives [55],

$$\mathcal{M} = \frac{iG_F V_{ud}}{\sqrt{2}} \langle 0 | \bar{d}(\gamma^\mu - \gamma^\mu \gamma^5) u | \pi^+ \rangle \bar{l}(p_l) \gamma^\mu (1 - \gamma^5) \nu(p_\nu), \quad (2.7)$$

where p_l and p_ν are the momenta carried by the outgoing anti-lepton and neutrino, respectively. The first part of the brackets in Eq. 2.7 connects the pseudo-scalar pion to the scalar vacuum. The vector part of the weak interaction becomes an expression with odd parity and therefore vanishes when the integral is completed. The remaining hadronic part in the bracket is the axial-vector component of the weak interaction. This term is not easy to calculate as it involves the *strong interaction*. In any case, we know this term should be a Lorentz 4-vector and the only one available is momentum transfer q^μ to the virtual W^+ boson shown in Figure 2.1. The bracket is then

2.2. Pion Decay Theory

$$\langle 0 | \bar{d} \gamma^\mu \gamma^5 u | \pi^+ \rangle = i F_\pi q^\mu \quad (2.8)$$

The term F_π is the constant that parameterizes the strong interaction, i.e., the so-called pion decay constant. Then, the matrix element squared after summation over the spin states, and integrating Eq. 2.2 over outgoing particle energies gives an expression for the decay rate:

$$\Gamma_{\pi \rightarrow l}^0 = \frac{G_F^2 V_{ud}^2 m_\pi F_\pi^2 m_l^2}{4\pi} \left(1 - \frac{m_l^2}{m_\pi^2} \right)^2. \quad (2.9)$$

To first order, the pion branching ratio R_π^0 is the ratio of decay rates from pions to positrons and muons, which can be calculated using Eq. 2.9 as follows:

$$R_\pi^0 = \frac{\Gamma_{\pi \rightarrow e}}{\Gamma_{\pi \rightarrow \mu}} = \frac{g_e^2 m_e^2}{g_\mu^2 m_\mu^2} \left(\frac{m_\pi^2 - m_e^2}{m_\pi^2 - m_\mu^2} \right)^2. \quad (2.10)$$

The strong interaction coefficients are canceled in the branching ratio, leaving the final equation as a ratio of lepton masses and the weak interaction couplings g_e^2/g_μ^2 . As the SM assumes “lepton universality”, i.e., $g_e = g_\mu$, then,

$$R_\pi^0 = (1.28336 \pm 0.00002) \times 10^{-4} \quad (2.11)$$

The error in the first-order branching ratio R_π^0 not including the radiative (QED) corrections, comes from the uncertainty in the muon and positron masses.

2.2.2 Helicity Suppression

This section explains how the charged pion decay plays the role of helicity in the weak interaction. As the muon is two orders of magnitude larger in mass, naively, we could say that the $\pi^+ \rightarrow l^+ \nu_l$ decay illustrated in Figure 2.1 should have electronic mode dominance from pure phase-space considerations. However, the opposite happens because helicity suppresses electron decay. Experiments have verified the establishment of the V-A form of the weak interaction. The operator $\frac{1-\gamma^5}{2}$ (2.4) selects only left-handed chiral particles and right-handed chiral antiparticles, ultimately explaining *parity violation* at a fundamental level.

2.2. Pion Decay Theory

The *helicity* of a particle is right-handed if the direction of its spin is the same as the direction of its motion and left-handed if the directions are opposite; e.g., if a standard clock is tossed with its face facing forwards with its hands rotating as the spin vector, it has left-handed helicity. Formally, helicity is the sign of the projection of the spin vector onto the momentum vector: left is negative, right is positive. For massless spin 1/2 particles or antiparticles, helicity is equivalent to chirality. For massive particles, distinct chirality states have both right-handed and left-handed helicity components proportional to the mass of the particle.

Considering the kinematics of positively charged pion decay at rest, as shown in Figure 2.2, the following can be deduced.

- As the π^+ spin is zero, the spins from the anti-lepton l^+ and associated neutrino ν_l must be opposite. Their momenta are anti-parallel or back-to-back.
- The neutrino mass is very small $m_\nu \approx 0$ and our energy framework gives the condition $E \gg m_\nu$. We can approximate neutrinos as massless. Therefore, the associated neutrino ν_l must have left-handed helicity and chirality.
- Angular momentum (helicity) must be conserved. Therefore, the anti-lepton l^+ must have left-handed helicity.
- Weak interaction restrictions force anti-lepton l^+ to have right-handed chirality.
- The matrix element given by Eq. 2.7 is proportional to the right-handed chiral component and left-handed helicity for the anti-lepton l^+ spinor, $\mathcal{M} \propto \frac{m_l}{m_\pi + m_l}$.
- Hence, as the positron mass is much smaller than the muon mass, the $\pi^+ \rightarrow e^+ \nu_e$ decay suffers heavily from “helicity suppression”, leading to the 10^{-4} factor coming from the positron mass squared $\sim m_e^2$, as shown in Eq. 2.10 and Eq. 2.11.

2.2.3 Radiative Corrections

The first-order branching ratio R_π^0 calculated in Section 2.2.1 does not include radiative corrections. In leading order, radiative decay Feynman

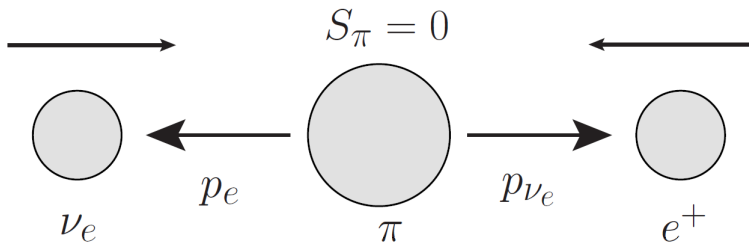


Figure 2.2: Fermi-point-like interpretation for $\pi^+ \rightarrow l^+ \nu_l$ decay: pion (middle); anti-lepton (right); and neutrino (left). The helicity suppression mechanism in the pion (spin zero) decay is illustrated: p_l and p_{ν_l} are the particles' momenta; the black arrows over the decay particles describe their spin state, which according to angular momentum conservation are opposite; and the helicity states (in the case of massless neutrinos) both forced to be left-handed by the chiral V-A structure of the weak interactions (see text). This mechanism leads to the suppression of the positron mode relative to the muon.

diagrams based on to the emission of real photons are named Inner Bremsstrahlung (IB γ), as shown in Figure 2.3(a). Decays from the emission and re-absorption of virtual photons (ER γ) are shown in Figure 2.3(b). The first attempt in the late 1950s to calculate the IB γ and ER γ radiative corrections for the branching ratio assuming a point-like pion were made by Kinoshita [62] and Berman [63]. Although the calculation of these diagrams requires both infrared and ultraviolet cutoffs¹⁴ to be imposed, their effect on R_π can still be rigorously computed. The term involving the infrared cutoff cancels exactly for IB γ and ER γ processes, and the ultraviolet cutoff cancels in the branching ratio (equal contributions from both $\pi^+ \rightarrow e^+ \nu_e$ and $\pi^+ \rightarrow \mu^+ \nu_\mu$ decays were assumed), although it affects the individual decay rates. Ultimately, a correction of -3.929% to R_π was obtained.

In the late 1970s, the pion was well known to have a structure, leading to attempts at the calculation using proper gauge theories. First, Goldman and Wilson [64] and later, Marciano and Sirlin [65], expanded the pion decay in a power series and found that structure-dependent contributions

¹⁴ An infrared cutoff is the minimal value of energy or equivalently, the maximal wavelength that will be taken into account in a calculation, typically an integral.

At the opposite end of the energy scale, an ultraviolet cutoff is the maximal allowed energy or the shortest wavelength.

2.2. Pion Decay Theory

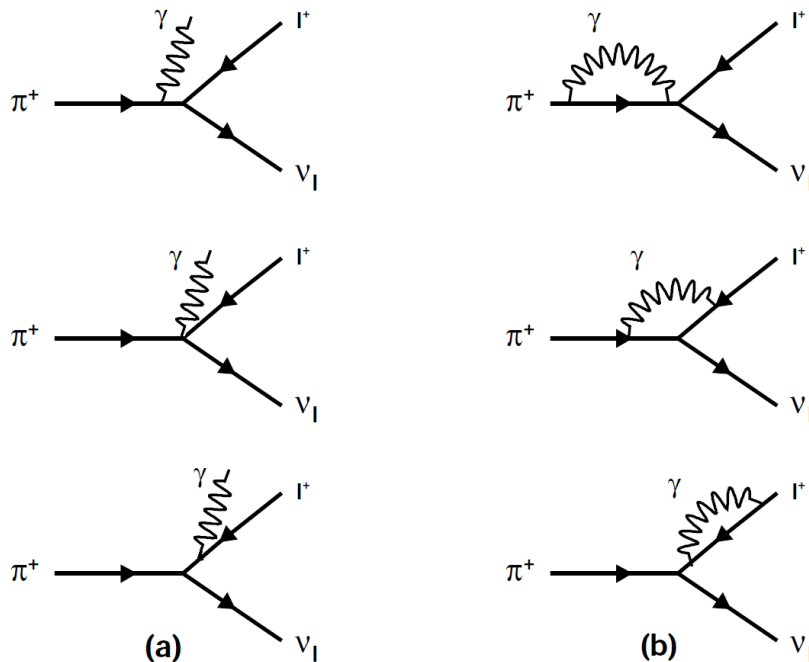


Figure 2.3: Feynman diagrams for the radiative corrections to pion decay, from real (a) and virtual (b) photons.

from $ER\gamma$ and common interference $IB\gamma$ components canceled each other; this allowed for a high precision calculation. It was also found that the leading lepton mass term is independent of strong interactions. Such a term is in agreement with the Kinoshita and Berman calculations. In 1993, Marciano and Sirlin repeated the prediction with a proper assessment for the uncertainty; the radiative correction constrained the branching ratio to $R_\pi = (1.2352 \pm 0.0005) \times 10^{-4}$ [66].

In 2007, Cirigliano and Rosell [47] recalculated the corrections using Chiral Perturbation Theory (ChPT). ChPT uses a low-energy effective field theory for QCD, allowing for strong interaction calculations. ChPT enabled a power series solution for the radiative corrections,

$$R_\pi = R_\pi^0 [1 + \Delta_{e^2 p^2} + \Delta_{e^2 p^4} + \Delta_{e^2 p^6} + \dots] [1 + \Delta_{LL}]. \quad (2.12)$$

The terms $\Delta_{e^2 p^n}$ represent decay-rate expansions in powers of p proportional to the pion mass and electromagnetic coupling constant e . The

2.2. Pion Decay Theory

pion point-like calculation is equivalent to the leading electromagnetic term $\Delta_{e^2p^2}$; the next term $\Delta_{e^2p^4}$ represents the structure-dependent correction with prominent uncertainty in the prediction. The $\Delta_{e^2p^6}$ term arises from the emission of a photon by the decaying pion, which evades the helicity suppression and must thus be taken into account despite being of higher order. Photons emitted at any other part of the pion decay diagram, such as real bremsstrahlung from the decay lepton or a loop starting on the W line, do not affect the helicity suppression. Finally, Δ_{LL} represents the lepton mass corrections of order $\alpha^n \ln^n(m_\mu/m_e)$. Table 2.5 lists the values for Eq. 2.12 and the branching ratio sums up to $R_\pi = (1.2352 \pm 0.0001) \times 10^{-4}$ [47].

Table 2.5: Summary of the electroweak corrections for R_0^π

Power counting	Corrections (%) from [47]
$\Delta_{e^2p^2}$	-3.929
$\Delta_{e^2p^4}$	0.053 ± 0.011
$\Delta_{e^2p^6}$	0.073
Δ_{LL}	0.054^a

^a The original correction in [47] is 0.055%, but because of a shift in the pion's mass, it has become 0.054% [24].

In 2011, Bryman *et al.* [24] reported an additional 0.01% uncertainty from two-loop diagrams contributions from $\mathcal{O}(\alpha^2)$ terms. After including the point-like ($\Delta_{e^2p^2}$) and structure-dependent ($\Delta_{e^2p^4}$) radiative corrections terms, together with the higher order final state photon ($\Delta_{e^2p^4}$), and lepton mass corrections (Δ_{LL}) to the vector-axial first-order branching ratio and adding their respective uncertainties in quadrature, the final branching ratio takes the value [24]

$$R_\pi = (1.2352 \pm 0.0002) \times 10^{-4}, \quad (2.13)$$

which is in agreement with all previous calculations. The theoretical uncertainty prediction of R_π is 0.016%. Such a level of precision in a hadronic decay is possible because the strong interaction dynamics cancels out the branching ratio and the structure dependence appears only through electroweak radiative corrections. The next section will explain the new physics

that can be found if a measurement deviates from the R_π calculation (Eq. 2.13); if it is in agreement, then new constraints could be set on SM extensions.

2.3 Motivation Beyond the Standard Model

The Standard Model (SM) has been extremely successful at describing interactions among the known particles. However, there are still unsolved mysteries, e.g., the three generations and different mixing in the lepton and quark sector, the nature of neutrinos and their masses, the large range of particle masses from $<eV$ to GeV, and the relative small mass of the Higgs boson. The SM does not provide sufficient CP violation to explain the matter/antimatter asymmetry in the observed universe. There is no explanation for the presence of dark matter and dark energy, which ultimately affects the structure and fate of the universe over SM matter-energy. Thus, the SM is believed to be an effective low energy approximation of a more fundamental theory. Beyond Standard Model (BSM) theory could be discovered by producing new particles at high-energy colliders. Moreover, BSM theory can also be manifest through SM predictions by the presence of virtual effects of new particles [55] [56] [57] [58].

BSM or new physics (NP) effects at the weak TeV scale could be found at the precision level of 0.1%. If the R_π measurement is consistent with the SM, new constraints could be set for new physics scenarios on SM extensions. Examples include, lepton universality violation (section 2.3.1), and new pseudo-scalar interactions (section 2.3.2), including R-parity violating super-symmetry, lepto-quarks, and charged Higgs (non-SM coupling). Other BSM possibilities are partial compositeness (section 2.3.3), and massive neutrinos lighter than the pion (section 2.3.4). In some instances, these constraints can far exceed the reach of direct searches at colliders; under the assumption that a deviation from the SM is found, a new pseudo-scalar interaction with an energy scale up to $\mathcal{O}(1000 \text{ TeV})$ could enhance the branching ratio by $\mathcal{O}(0.1\%)$ [47]. More recently, an analysis of renormalization-group evolution has denied that the current precision measurement and calculation of meson decays (i.e., $\pi^+ \rightarrow e^+\nu_e$) sets a scale for BSM at $\mathcal{O}(500 \text{ TeV})$ [67].

2.3.1 Lepton Universality

The assumption that the W boson couples with equal strength with every lepton generation, i.e., the coupling is flavour independent, was used to

2.3. Motivation Beyond the Standard Model

derive R_π^0 . Such an assumption is known as *lepton universality*. The SM leptons differ only by their mass, and their electroweak coupling constant is the same. Going back to Eq. 2.10, we could introduce the hypothesis that the coupling constants are different for each generation ($g = g_e = g_\mu = g_\tau$) and then the branching ratio expression becomes

$$R_\pi^{\text{SM}} = \left(\frac{g_\mu}{g_e}\right)^2 R_\pi^{\text{exp}}. \quad (2.14)$$

Hence, using the measured R_π^{exp} and calculated R_π^{SM} branching ratio, the coupling constants ratio for the electron-muon universality test becomes accessible to the PIENU experiment. Constraints on the ratios of the coupling constants come from many different types of precision measurement experiments using W bosons, τ -lepton, or π and K meson decays; examples are $W \rightarrow l\nu$, $\pi \rightarrow l\nu$, $W \rightarrow l\nu$ and $\tau \rightarrow l\nu_\tau\nu_l$ decays. Lepton universality tests with π and τ decays give comparable precision, but complementary aspects: $\pi^+ \rightarrow e^+\nu_e$ currently provides the most precise test of electron-muon universality, although the branching ratio of τ -lepton decays to muons and electrons is close. These tests are not exactly equivalent; since the pion is spin zero while the tau is spin 1/2, the mediating W boson in the π case must be in the spin zero state, whereas in the τ case all spin states contribute. Table 2.6 summarizes the most recent results.

Loinaz *et al.* [26] parameterized the couplings g_l to quantify the current bounds as

$$g_l \rightarrow g \left(1 - \frac{\varepsilon_l}{2}\right). \quad (2.15)$$

The linear combinations of ε_l constrained by W , τ , π , and K decay measurements are given by

$$\frac{g_\mu}{g_e} = 1 + \frac{\varepsilon_e - \varepsilon_\mu}{2}, \quad \frac{g_\tau}{g_\mu} = 1 + \frac{\varepsilon_\mu - \varepsilon_\tau}{2}, \quad \text{and} \quad \frac{g_\tau}{g_e} = 1 + \frac{\varepsilon_e - \varepsilon_\tau}{2}. \quad (2.16)$$

Setting $\Delta_{e\mu} \equiv \varepsilon_e - \varepsilon_\mu$, $\Delta_{\mu\tau} \equiv \varepsilon_\mu - \varepsilon_\tau$, and $\Delta_{e\tau} \equiv \varepsilon_e - \varepsilon_\tau$, the experimental bounds can be evaluated in the parameter space of lepton universality constraints, as shown in Figure 2.4. The PIENU experiment aims to restrict BSM theories with a measurement of the $\pi^+ \rightarrow e^+\nu_e$ branching ratio within 1.0 to 0.01% precision.

2.3. Motivation Beyond the Standard Model

Table 2.6: Experimental results on lepton universality (LU) tests from studies of π , K , τ , μ and W decay. In some cases, μ and τ 's lifetime (τ_μ , and τ_τ) measurements were used in combination for LU tests. Here, \mathcal{B} represents the branching fraction of a particular decay mode.

Decay mode, and lifetimes	g_μ/g_e
$\Gamma_{\pi\rightarrow\mu}/\Gamma_{\pi\rightarrow e}$	1.0004 ± 0.0012 [5]
$\mathcal{B}_{\tau\rightarrow\mu}/\mathcal{B}_{\tau\rightarrow e}$	1.0018 ± 0.0014 [68]
$\mathcal{B}_{K\rightarrow\mu}/\mathcal{B}_{K\rightarrow e}$	0.996 ± 0.005 [69]
$\mathcal{B}_{K\rightarrow\pi\mu}/\mathcal{B}_{K\rightarrow\pi e}$	1.002 ± 0.002 [70]
$\mathcal{B}_{W\rightarrow\mu}/\mathcal{B}_{W\rightarrow e}$	0.997 ± 0.010 [70]
	g_τ/g_μ
$\mathcal{B}_{\tau\rightarrow e}, \tau_\mu, \tau_\tau$	1.0011 ± 0.0015 [68]
$\mathcal{B}_{\tau\rightarrow\pi}/\mathcal{B}_{\pi\rightarrow\mu}$	0.9963 ± 0.0027 [68]
$\mathcal{B}_{\tau\rightarrow K}/\mathcal{B}_{K\rightarrow\mu}$	0.9858 ± 0.0071 [68]
$\mathcal{B}_{W\rightarrow\tau}/\mathcal{B}_{W\rightarrow\mu}$	1.039 ± 0.013 [70]
	g_τ/g_e
$\mathcal{B}_{\tau\rightarrow\mu}, \tau_\mu, \tau_\tau$	1.0029 ± 0.0015 [68]
$\mathcal{B}_{W\rightarrow\tau}/\mathcal{B}_{W\rightarrow e}$	1.036 ± 0.014 [70]

Recently, charged current (CC) second-order weak interactions have been measured, pointing towards *lepton universality violation*. LHCb reported flavour-changing neutral-current processes $B^+ \rightarrow K^+ l^+ l^-$ [71], where $l = e, \mu$, and the charged-current processes $\bar{B}^0 \rightarrow D^{*+} l^- \bar{\nu}_l$ [72], where $l = \mu, \tau$. The first process yielded an excess of 2.8σ in the electron mode, and the second gave a surplus of 2.1σ in the τ mode. The BaBar collaboration also reported a 2.7σ excess in this mode and a 2.0σ excess in the similar $\bar{B}^0 \rightarrow D^+ \tau^- \bar{\nu}_\tau$ [73]. On the other hand, the latest test of flavour universality through measurement of the $\bar{B}^0 \rightarrow D^{*-} \tau^+ \nu_\tau$ [74] branching ratio to the muon channel is in agreement with the SM prediction and with previous measurements. Alternatively, the latest test of lepton universality with the $B^0 \rightarrow K^{*0} l^+ l^-$ [75] branching ratio (where $l = \mu, e$), is compatible with the SM expectations. A comparison of second-order measurements with SM predictions [27] is shown in Figure 2.5. A comprehensive review of lepton universality tests in B decays can be found in ref. [76].

2.3. Motivation Beyond the Standard Model

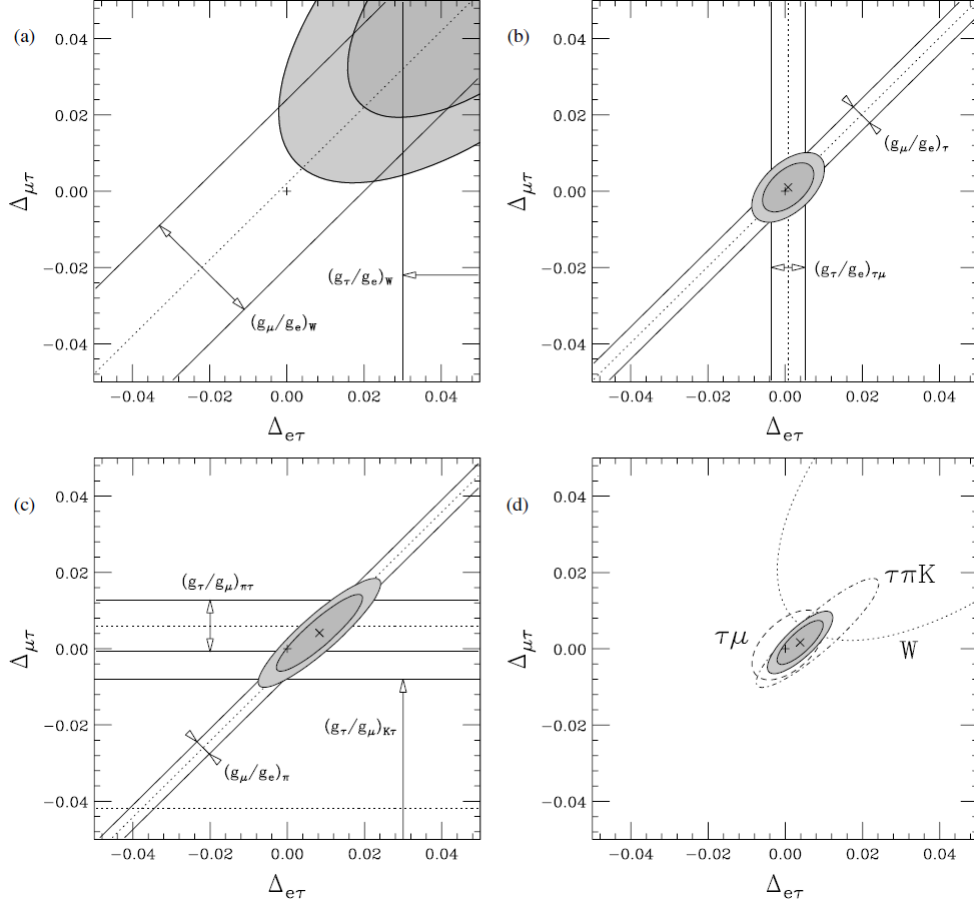


Figure 2.4: The limits on $\Delta_{\mu\tau}$ and $\Delta_{e\tau}$ from (a) W -decay, (b) τ -decay, (c) π and K -decay, and (d) all decays combined. The 1σ bands are shown for each coupling constant ratio, ignoring correlations. The shaded areas represent the 68% (dark grey) and 90% (light grey) confidence contours, including correlations (Figure from ref. [26]).

The LHCb and BaBar second-order weak interaction deviations from universality, required to explain these measurements, are extensive compared to the uncertainties stated in Table 2.6. To interpret these results concerning new physics, while remaining consistent with other measurements, generally requires the new physics to couple preferentially to the third generation of particles [77]. Beyond SM theories have proposed solutions such as new vector bosons W' , similar to the electroweak ones but more massive, which

2.3. Motivation Beyond the Standard Model

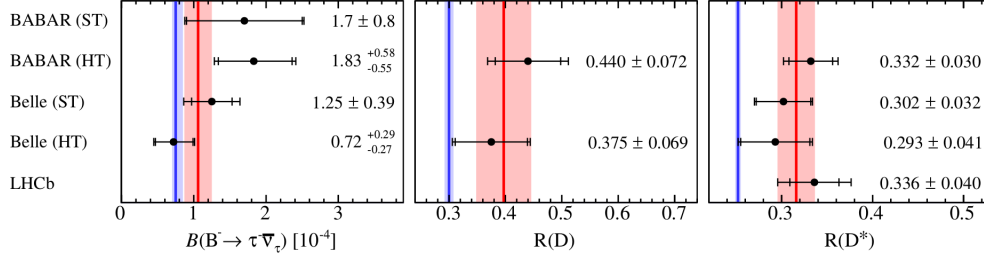


Figure 2.5: Comparison of measurements with SM predictions: The branching fraction B is $B^- \rightarrow \tau^- \bar{\nu}_\tau$ (left), the ratio $R(D)$ is $\bar{B} \rightarrow D\tau^- \bar{\nu}_\tau$ over $\bar{B} \rightarrow D e^- \bar{\nu}_e$ (center), and $R(D^*)$ is $\bar{B} \rightarrow D^*\tau^- \bar{\nu}_\tau$ over $\bar{B} \rightarrow D^* e^- \bar{\nu}_e$ (right) by BABAR, Belle, and LHCb. The data points indicate statistical and total uncertainties. ST and HT refer to the measurements with semileptonic and hadronic tags, respectively. The average values of the measurements and their combined uncertainties, obtained by the Heavy Flavor Averaging Group, are shown in red as vertical lines and bands, and the expectations from the SM calculations are shown in blue. Image and data from ref. [27].

couple differently among generations for quarks and leptons. Another possibility is a new charged spin-0 Higgs boson. Lastly, SUSY theories generically predict the presence of charged Higgs particles [78] [79].

2.3.2 New-Pseudo-scalar Interactions

Measurements of pseudo-scalar meson (pion) decay can provide high precision in searches for new pseudo-scalar interactions for beyond SM theories, as such decays are highly helicity suppressed. Electroweak renormalization effects or loop corrections can generate new-pseudo-scalars such as lepto-quarks, super-symmetric (SUSY) particles at loop level, and charged Higgs bosons [78] [79]. Taking the pion decay matrix element for leptonic and hadronic currents from Eq. 2.7,

$$\mathcal{M} = \frac{iG}{\sqrt{2}} \langle 0|(V - A)u|\pi^+ \rangle \bar{l}(p_l)\gamma^\mu(1 - \gamma^5)\nu(p_\nu). \quad (2.17)$$

Here, the bracket $\langle 0|(V - A)|\pi^+ \rangle$ connects the pseudo-scalar particle to vacuum. As explained in Section 2.2.1, the vector part vanishes, leaving only the vector-axial-vector contribution.

2.3. Motivation Beyond the Standard Model

Instead, a general bracket $\langle 0|\mathcal{O}|\pi^+\rangle$ is proposed, allowing beyond SM physics, where \mathcal{O} can be a scalar (\mathcal{S}), pseudo-scalar (\mathcal{P}), vector (\mathcal{V}), or axial-vector (\mathcal{A}) operator. The pion is \mathcal{P} , and since only \mathcal{P} and \mathcal{A} terms give non-vanishing contributions, the transition amplitude is [79]

$$\langle 0|\bar{u}\gamma^5 d|\pi\rangle = i\sqrt{2}\frac{f_\pi m_\pi^2}{m_u + m_d} = i\sqrt{2}\tilde{f}_\pi. \quad (2.18)$$

The effective Fermi pseudo-scalar contact Lagrangian assuming only left-handed neutrinos, is

$$\mathcal{L}_P = -i\frac{\rho}{2\Lambda^2} [\bar{l}(1 - \gamma^5)\nu_l] [\bar{u}\gamma^5 d], \quad (2.19)$$

where ρ is the coupling constant for the new pseudo-scalar and Λ is its mass scale. The Lagrangian \mathcal{L}_P leads to a new pseudo-scalar matrix element \mathcal{M}_P . The final matrix element \mathcal{M}_{BSM} will be a coherent sum of \mathcal{M}_P and \mathcal{M} , the SM (V-A) matrix element from Eq. 2.17. After squaring the BSM total matrix element and summing over final states, assuming that lepton universality holds for the new interaction, the branching ratio becomes accessible [79],

$$1 - \frac{R_\pi^{\text{exp}}}{R_\pi^{\text{SM}}} \sim \pm \frac{\sqrt{2\pi}}{G} \frac{1}{\Lambda^2} \frac{\tilde{f}_\pi}{m_e} \sim \left(\frac{1\text{TeV}}{\Lambda}\right)^2 \times 10^3. \quad (2.20)$$

Considering real coupling of approximately the same strength as the weak interaction, the most significant contribution from the BSM matrix comes from the interference term proportional to $\frac{1}{\Lambda^2}$. The PIENU experiment aims to reach a 0.1% precision measurement; thus, we are sensitive to a new pseudo-scalar interaction at the 1000 TeV mass scale, well beyond the reach of any present direct searches at colliders. The pseudoscalar interaction can potentially be induced at one loop through three classes of diagrams: scalar-dressed Z exchange box diagrams, scalar-dressed W exchange box diagrams and radiative corrections to the quark vertex (Figure 2.6). The weak interactions do not respect parity and the scalar interactions change chirality, thus diagrams of this form can potentially induce a pseudoscalar interaction. Pseudo-scalar BSM candidates include leptoquarks, SUSY particles, and charged Higgs bosons. In the following section these candidates will be described briefly.

R-Parity Violation SUSY

The Minimal Super-symmetric Standard Model (MSSM) is an extension of the SM. It has been shown that the MSSM can induce non-universal

2.3. Motivation Beyond the Standard Model

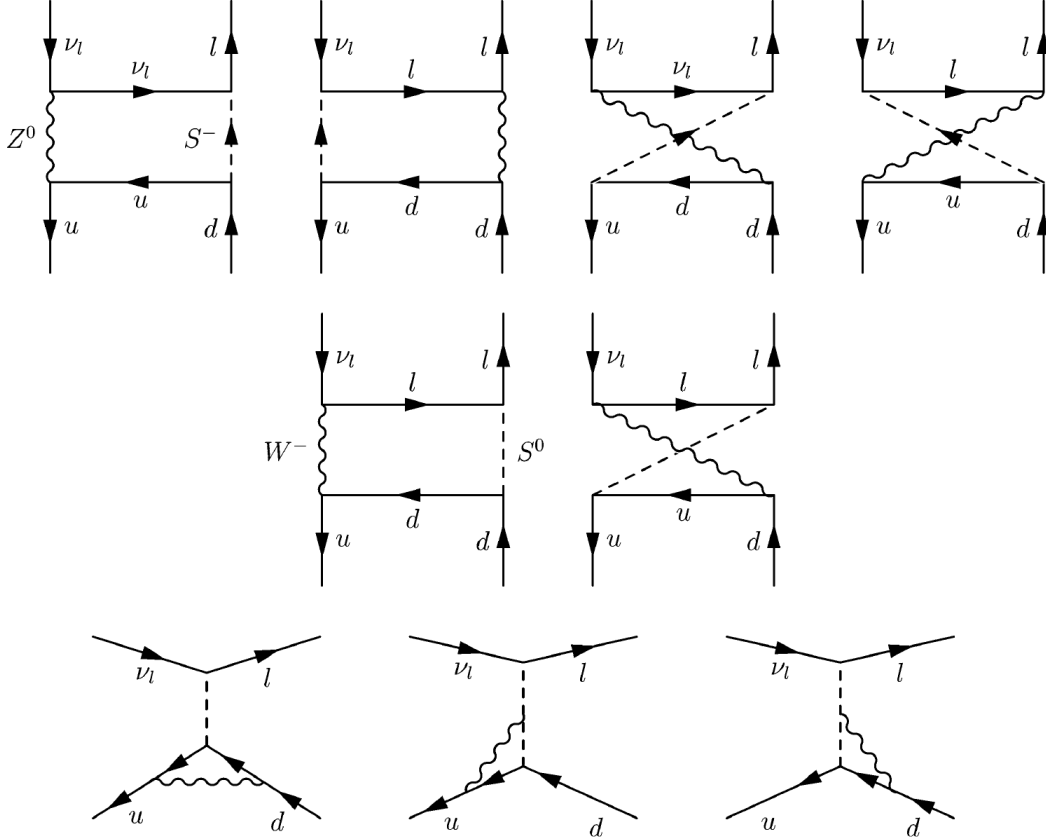
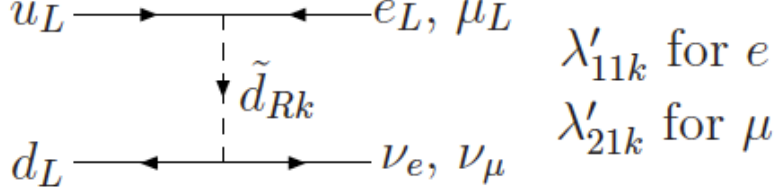


Figure 2.6: Feynman diagrams for pseudo-scalar interactions induced at one loop including three classes of diagrams: scalar-dressed Z exchange box diagrams (top), scalar-dressed W exchange box diagrams (middle) and radiative corrections to the quark vertex (bottom).

contributions and modify the branching ratio calculation R_π^{SM} by a quantity $\delta R_\pi^{\text{SUSY}}$, which can arise either at the tree or loop levels [28]. If R -parity is conserved, then the value of $\delta R_\pi^{\text{SUSY}}$ is negligible for current experimental reach [80] or requires very large mass splitting between the left-handed *sfermion* [28]. A *sfermion* is a hypothetical spin-0 super-partner particle (*sparticle*) of its associated fermion. The R -parity definition is $P_R = (-1)^{3B+L+2S}$, where S is spin, B is baryon number, and L is lepton number. All SM particles have R -parity of +1, while super-symmetric particles have R -parity of -1.


 Figure 2.7: Tree level RPV contributions to R^π [28].

If we consider R -parity violation (RPV) together with lepton number conservation violation, then the effects on $\delta R_\pi^{\text{SUSY}}$ are measurable at the tree level for the current PIENU experiment's precision [28]. Alternatively, if no deviation is found, new constraints could be set on MSSM. In the presence of R -Parity Violation (RPV) interactions, tree level exchanges of sfermions shown in Figure 2.7 lead to violations of lepton universality with violation of lepton number ($\Delta L = 1$) and no helicity suppression in the R^π . The magnitude of these tree level contributions is determined by both the sfermion mass and the parameters λ'_{11k} and λ'_{21k} , which are the coefficients in RPV interactions [28].

The RPV interactions are related to R_π as follows

$$\frac{\Delta R_\pi^{\text{RPV}}}{R_\pi^{\text{SM}}} = 2(\Delta'_{11k} - \Delta'_{21k}), \quad (2.21)$$

$$\Delta'_{i1k}(\tilde{f}) = \frac{\lambda'_{i1k}}{4\sqrt{2}Gm_{\tilde{f}}^2} \quad i = 1, 2, \quad (2.22)$$

where λ'_{11k} and λ'_{12k} are the parameters related to the RPV interaction for the decay into a positron or a muon respectively, $m_{\tilde{f}}$ is the mass of the exchange sfermion, and G is the Fermi constant. The allowed regions for λ'_{11k} and λ'_{12k} from precision measurements of electroweak parameters are shown in Figure 2.8, at the 95% confidence level [28]. The dark blue line encloses current constraints on these parameters using an old 1.0% precision PDG value of the branching ratio, $R_\pi^{\text{exp}} = 1.230(4) \times 10^{-4}$. The dashed red line shows the future expected experimental 0.1% precision from the PIENU experiment and the light green line shows the prospective impact of a future measurement of the proton weak-charge at Jefferson Lab [81].

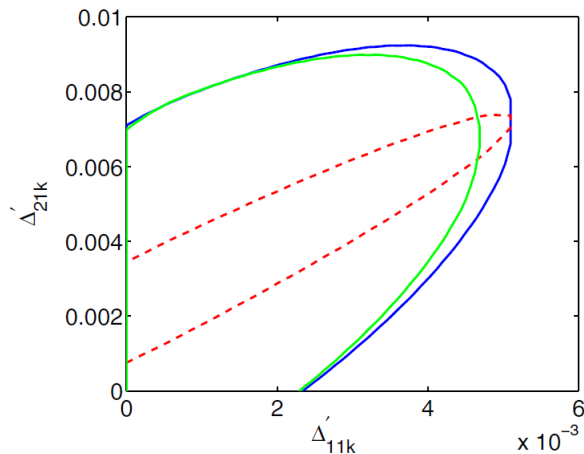


Figure 2.8: Present 95% C.L. constraints on RPV parameters Δ'_{11k} and Δ'_{21k} that enter R_π obtained from a fit to precision electroweak observables [28]. The dark blue contour shows the current constraints on these parameters (the interior is the allowed region). The dashed red line shows the contour when adding the future expected experimental precision (0.1%) from the PIENU experiment, assuming the same central value. The light green curve indicates the prospective impact of a future measurement of the proton weak charge at Jefferson Lab [81].

Charged Higgs Boson

Some SM extensions [82] [83], predict the existence of a charged Higgs doublet boson H^\pm . Assuming an H^\pm coupling constant of $g/2\sqrt{2}\lambda_{ud}$ to the pseudo-scalar current $\langle 0|\bar{d}(\gamma^5)u|\pi^+\rangle$ and $g/2\sqrt{2}\lambda_{l\nu}$ to the leptonic current $\bar{l}(1 - \gamma^5)\nu_l$, where g is the $SU(2)_L$ gauge coupling and λ is the chirality-breaking factor, we can access a deviation from the R_π^{exp} experimental measurement [24]:

$$1 - \frac{R^{\text{exp}}}{R^{\text{SM}}} = \frac{2m_\pi^2}{m_e(m_u + m_d)} \frac{m_W^2}{m_{H^\pm}^2} \lambda_{ud} \left(\lambda_{e\nu} - \frac{m_e}{m_\mu} \lambda_{\mu\nu} \right). \quad (2.23)$$

If we assume lepton universality for the electroweak coupling constants, i.e., $\lambda_{e\nu}/\lambda_{\mu\nu} = m_e/m_\mu$, then $R_\pi^{\text{Exp}} = R_\pi^{\text{SM}}$ in Eq. 2.23 and no experimental constraints can be reached. On the other hand, if the charged Higgs doublet couplings are $\lambda_{e\nu} \sim \lambda_{\mu\nu} \sim \lambda_{ud} \sim \alpha/\pi$ (where α is the electromagnetic coupling constant), then measuring the R_π^{exp} branching ratio at the 0.1% level will allow access to a relatively high mass to the charged Higgs,

$m_{H^\pm} \sim 400 \text{ GeV}$ [24].

Leptoquark

Beyond-SM frameworks postulate leptoquarks as particles carrying both lepton and baryon quantum numbers; therefore, they can act as mediators between quarks and leptons. Leptoquarks can be chiral or non-chiral, allowing them to couple to both left- and right-handed leptons and quarks. The $\pi^+ \rightarrow e^+ \nu_e$ decay set strong constraints on non-chiral leptoquarks with bounds on the mass M_{LQ} and couplings g_L, g_R of $M_{LQ}^2/g_L g_R \geq (100 \text{ TeV})^2$ [84]. If chiral components that couple left-handed particles are required, the pion decay can still set constraints on pseudo-scalar leptoquarks in a single representation. Assuming similar coupling as the strong interaction, the bound from the R_π branching ratio is $M_{LQ}/g \geq 12 \text{ TeV}$ [46].

2.3.3 Partial Compositeness

The existence of substructure for a particle previously considered elementary is referred to as “compositeness”. The Higgs boson represents an important case of not being an elementary particle, which drives the electroweak symmetry breaking obtaining a non-zero vacuum expectation value. In compositeness scenarios the Higgs boson is instead a pseudo-Nambu-Goldstone¹⁵ particle resulting from the formation of a condensate in a new strong interaction (a new “force”) [85]. Alternatively, *partial compositeness* [86] is a model to explain the fermion masses, where the standard model (SM) fermions mix with new composite fermions and become massive. Precise measurements of $\pi/K \rightarrow e\nu$ branching ratios give important constraints on the parameter space, since partial compositeness unavoidably leads to lepton flavour violation.

2.3.4 Heavy Neutrino

Neutrino mass is zero according to the SM; however, flavour-oscillation data indicate that at least two have non-zero values [87]. This is a clear sign of new physics. Their masses and their nature (e.g., are neutrinos their own anti-particles?) is an area of current research. In order to explain the relatively small observed neutrino masses and to resolve some experimental

¹⁵In particle and condensed matter physics, Goldstone bosons or Nambu-Goldstone bosons (NGBs) are bosons that appear necessarily in models exhibiting spontaneous breakdown of continuous symmetries.

2.3. Motivation Beyond the Standard Model

anomalies [88] observed at LSND and MiniBOONE, for example, the existence of additional neutrino states is hypothesized. The Neutrino Minimal Standard Model (ν MSN) [89] is an extension of the SM. This framework, in addition to the left-handed neutrinos ν_α ($\alpha = e, \mu, \tau$), postulates three additional right-handed “sterile” neutrinos. The right-handed neutrinos have zero electric, weak, and strong charges; therefore, they are called sterile. The (ν MSN) Majorana masses of the right-handed neutrinos are chosen to be below the electroweak scale, and via small Yukawa couplings, the ν MSN achieves the smallness of the first left-handed neutrino masses, consistent with the gauge symmetries and see-saw mechanism of the SM. According to ν MSN, the two more massive states of the sterile neutrinos are responsible for baryogenesis, and the lightest one can be a candidate for dark matter in the keV/c^2 range, since using a smaller Yukawa coupling would cause the the light-sterile neutrino lifetime to exceed the age of the universe. In the early universe sterile neutrinos are produced by their coupling with left-handed neutrinos.

Simple re-normalizable dark matter models addressing problems with small-scale structure formation of the universe [90] postulate a dark matter candidate that can couple to a sterile heavy neutrino via a new dark sector mediator. The model requires heavy neutrinos in the 100 MeV mass range and roughly 10 MeV dark matter particles. The same model has been systematically explored [91] for addressing dark matter annihilation and thermalization via interactions with heavy neutrinos. More generally, for k sterile neutrinos, the weak eigenstates ν_{χ_k} are related to the mass eigenstates ν_i by a unitary transformation matrix U_{li} , where

$$\nu_l = \sum_{i=1}^{3+k} U_{li} \nu_i, \quad (2.24)$$

with $l = e, \mu, \tau, \chi_1, \chi_2 \dots \chi_k$. In particular, sterile neutrinos with MeV/c^2 to GeV/c^2 masses can have measurable effects on meson decays that can be explored by precisely measuring their decay branching ratios or by searching for extra peaks in the energy spectrum of their leptonic two-body decays (e.g., $\pi, K, B \rightarrow l\nu$) [45]. The presence of any neutrino heavier than a few MeV will weaken the helicity-suppression mechanism and thus modify the R_π branching ratio. Thus, the PIENU experiment is sensitive to neutrinos below the pion mass range, i.e., 0 to 130 MeV, and particularly to those above 55 MeV.

2.3. Motivation Beyond the Standard Model

Below 55 MeV. The rate of the decay $\pi^+ \rightarrow e^+\nu_i$, where ν_i is a heavy neutrino, relative to the rate of the $\pi^+ \rightarrow e^+\nu_e$ decay, is given by [92]

$$\frac{\Gamma(\pi^+ \rightarrow e^+\nu_i)}{\Gamma(\pi^+ \rightarrow e^+\nu_e)} = |U_{ei}|^2 \rho_e, \quad (2.25)$$

where U_{ei} is the mixing parameter between ν_e and ν_i , and the kinematic factor is

$$\rho_e = \frac{\sqrt{1 + \delta_e^2 + \delta_i^2 - 2(\delta_i + \delta_e + \delta_i\delta_e)}}{\delta_e(1 - \delta_e)^2} \times \delta_i + \delta_e - (\delta_i - \delta_e)^2. \quad (2.26)$$

with $\delta_e = m_e^2/m_\pi^2$, $\delta_i = m_{\nu_i}^2/m_\pi^2$, and the massive neutrino mass m_{ν_i} is restricted by the two-body decay mechanism to be

$$m_{\nu_i} = \sqrt{m_\pi^2 - 2m_\pi E_{e^+} + m_e^2}. \quad (2.27)$$

The presence of a massive neutrino will modify the branching ratio

$$\begin{aligned} R_{\text{exp}} &= \frac{N(\pi \rightarrow e\nu) + N(\pi \rightarrow e\nu_M)}{N(\pi \rightarrow \mu \rightarrow e)} \\ &= R_{\text{SM}} + \frac{N(\pi \rightarrow e\nu_M)N(\pi \rightarrow e\nu)}{N(\pi \rightarrow e\nu)N(\pi \rightarrow \mu \rightarrow e)} \\ &= R_{\text{SM}} + |U_{ei}|^2 \rho_e R_{\text{SM}}, \end{aligned} \quad (2.28)$$

leading to

$$|U_{ei}|^2 = \frac{r - 1}{\rho_e - 1}, \quad (2.29)$$

where $r = R_{\text{exp}}/R_{\text{SM}}$. Thus, the limits on the mixing matrix $|U_{ei}|^2$ can be calculated as a function of neutrino mass m_{ν_i} .

Above 55 MeV. In the case of the $\pi^+ \rightarrow e^+\nu_e$ decay, heavy neutrino states with masses below the pion m_π can be searched for with a peak search on the decay lepton energy spectrum. In particular, leptonic two-body decays like $\pi^+ \rightarrow e^+\nu_e$ have a fixed kinematics which results in a precise final state energy for the lepton, given the pion four-vector. In the case of the PIENU experiment, the pion is at rest and therefore the lepton energy was fixed by energy-momentum conservation

$$E_{e^+} = \frac{m_\pi^2 + m_e^2 - m_\nu^2}{2m_\pi}. \quad (2.30)$$

2.3. Motivation Beyond the Standard Model

Near 55 MeV and above, the positron energy is low enough that an extra peak (sterile massive neutrino) would appear in the $\pi^+ \rightarrow e^+ \nu_e$ energy spectrum. Figure 2.9 shows the upper limit on $|U_{ei}|^2$ obtained through a search for extra peaks in PIENU data taken in 2009, compared with the limits from the previous PIENU experiment [3] [29].

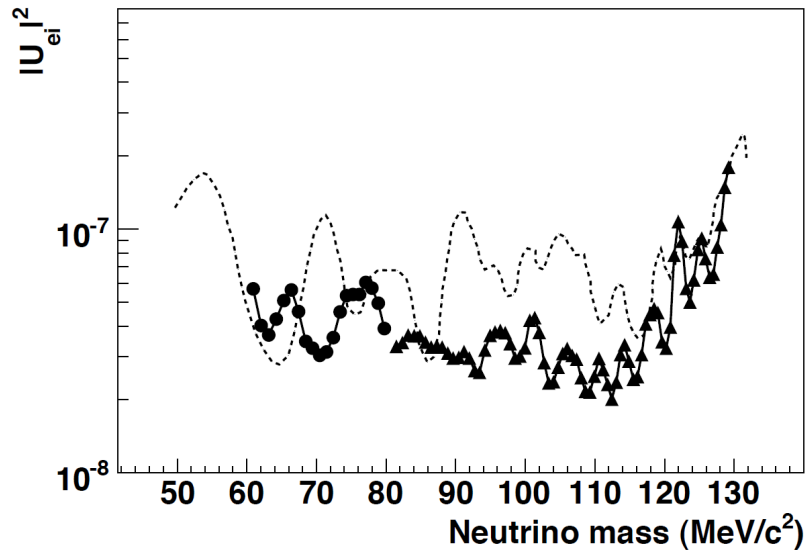


Figure 2.9: The 90% C.L. upper limit on the heavy-neutrino mixing parameter, as a function of its mass. The dashed line shows the result from the previous PIENU experiment [29], and the circles and triangles are the limits from a subset of PIENU data, published in 2011 [3]. The circles indicate a restricted angular region was used when constructing the $\pi^+ \rightarrow e^+ \nu_e$ energy spectrum.

Chapter 3

Experiment

3.1 Cyclotron and Beam-line

The PIENU experiment used a 520 MeV proton beam from TRIUMF's cyclotron with an average intensity up to $400 \mu\text{A}$, divided among four primary beam-lines. The cyclotron with a diameter of 18 m and main magnet weighing 4000 tons has an accelerating gradient provided by a 23.05 MHz 93 kV radio-frequency (RF) field and delivers 4-ns wide bunches every 43.4 ns with an intensity of $100 \mu\text{A}$ through the primary beam-line (BL1A). The proton beam was aimed at a 1cm-thick Beryllium production target **T1**¹⁶ located in the Meson Hall, as shown in Figure 3.1. The proton beam hitting **T1** produces several types of particles, such as photons, neutrons, protons, and pions, each with wide energy distribution. The secondary beam-line M13 delivers particles from the **T1** production target in vacuum to the PIENU detector. The M13 low energy beam-line (0-130 MeV/c) was tuned to select positively or negatively charged particles of momentum 75 MeV/c with a 1% spread. The final beam composition used for the PIENU detector was approximately 85% pion, 14% muon, and 1% positron [1].

The original M13 beam-line [93] begins from the BL1A at an angle of 135° from **T1** with a maximum angular acceptance of 29 mili-steradian. M13 is a low-momentum achromatic channel with -60° (**B1** magnet) and $+60^\circ$ (**B2** magnet) bends. M13 has a quadrupole¹⁷ doublet (**Q1-Q2**) between the production target and B1 for collecting pions, a quadrupole triplet (**Q3-Q4-Q5**) between the two bends, and a quadrupole doublet (**Q6-Q7**) downstream of **B2** for the F3 focal point. Figure 3.2 shows the location

¹⁶Note that the beam-line components in **bold** are not to be confused with the T1, B1, B2, or B3 scintillators from the PIENU detector.

¹⁷A quadrupole consist of groups of four magnets laid out so that in the planar multipole expansion of the field, the dipole terms cancel and where the lowest significant terms in the field equations are quadrupole. Quadrupole magnets are useful as they create a magnetic field whose magnitude grows rapidly with the radial distance from its longitudinal axis. This is used in particle beam focusing.

3.1. Cyclotron and Beam-line

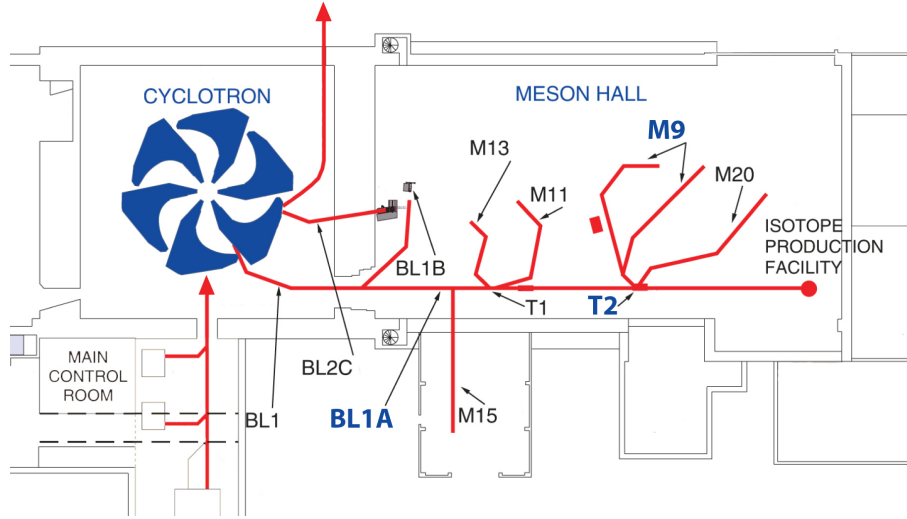


Figure 3.1: Schematic illustration of TRIUMF’s cyclotron, primary beam-lines, and Meson Hall’s secondary beam-lines [30].

of the M13 components. Before the beam-line extension, M13 had three foci: F1 between **B1** and **Q3**; F2 between **Q5** and **B2**; and F3 after **Q7**. Beam acceptance-defining slits SL0 are located just upstream of the first bending magnet **B1**, and there are momentum-defining slits SL1 and SL2 at F1 and F2, respectively. Around 10 cm downstream of SL1, two wheels hold different absorbers/slits.

By placing one of the absorber materials in the beam in combination with a collimator just before bending magnet **B3**, M13 works as an energy-loss based particle separator. In our case pions, muons, and positrons pass through a 1.45-mm-thick Lucite¹⁸ absorber; thus, owing to their different masses and energy deposited in the material ($\frac{dE}{dx}$), there is a sufficient momentum change to obtain a clean separation of the pions and positrons magnetically. Figure 3.3 (left) shows the pion and positron separation at F3. The data were taken in 2008 to verify the beam dynamics calculations performed with the REVMOC package [94] used for designing the beam-line [95]. The test setup consisted of a calorimeter named “Tina”¹⁹ and two plastic scintillators for triggering and particle identification via energy and

¹⁸Poly(methyl methacrylate) or PMMA. Lucite is one of the commercial names for this material, commonly referred to as acrylic.

¹⁹The calorimeter used in a previous experiment; see Section 1.2.1.

3.1. Cyclotron and Beam-line

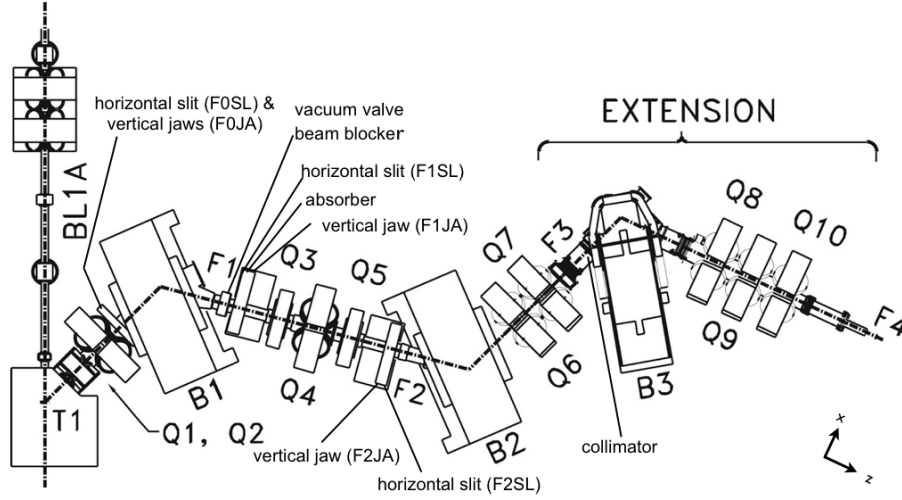


Figure 3.2: M13 channel with the extension [1]

time-of-flight (TOF) with respect to the cyclotron's radio frequency (RF) phase. In front of the calorimeter, there was a 3-layer wire chamber.

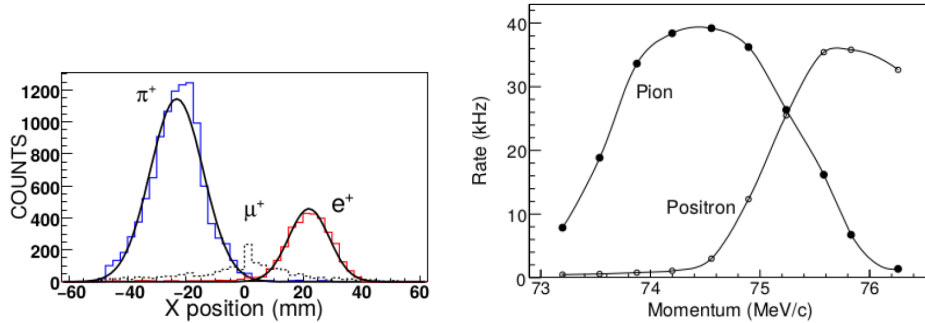


Figure 3.3: Left: Position distribution of π^+ , μ^+ , and e^+ at F3. The solid lines are Gaussian fits. Right: π^+ and e^+ rates at F4 as a function of the selected momentum [1]. The PIENU detector was placed at final focus point F4.

For reducing the statistical error on the branching ratio R_{π}^{exp} , a large sample of pion decays must be collected. By placing the calorimeter in the beam a larger acceptance is achieved. However, positrons in the beam can place severe limitations on data collection. The original M13 beam-line de-

3.1. Cyclotron and Beam-line

livered a pion beam with 25% contamination of positrons, which severely increased detector and trigger rates. Furthermore, in the 2008 test, with a two plastic scintillator setup, it was shown that after offline analysis cuts, 2% of positrons with respect to pions events remained in the data. Another background was identified in the form of neutrons and gamma rays from the beam-line (the source being the **T1** production target) that raised the energy of the $\pi^+ \rightarrow \mu^+ \nu_\mu \rightarrow e^+ \nu_e \bar{\nu}_\mu$ decay chain to $\pi^+ \rightarrow e^+ \nu_e$ energies adding another background [96]. All the previous considerations and experimental predictions pointed toward a modification of the M13 beam-line for dealing with these unacceptably high levels of beam background. Once it was verified that a clean separation between pions and positrons could be achieved, an extension of the beam-line was installed for further beam purification, as shown in Figure 3.2 and 3.4.

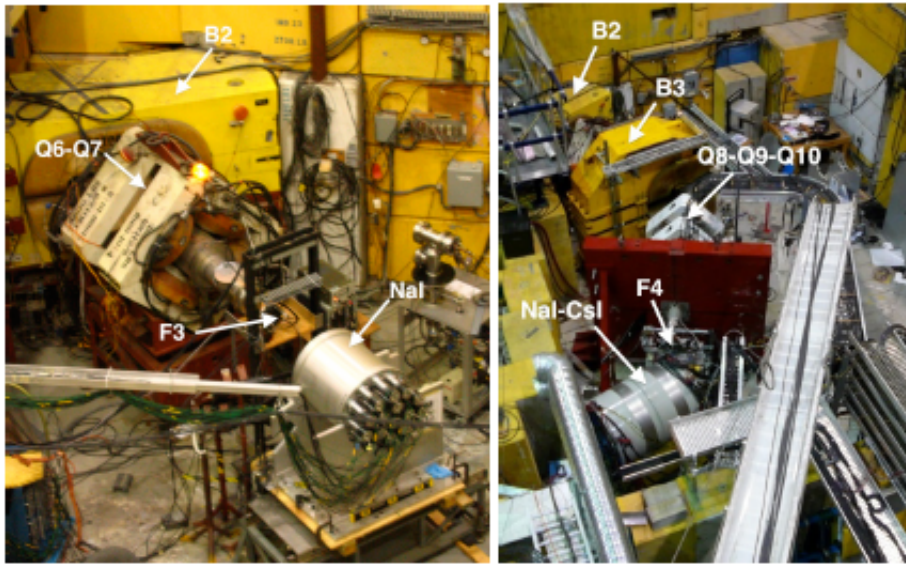


Figure 3.4: The end of the M13 beam-line, before (left) and after (right) the extension. Part of the detector was in place to measure the particle content of the beam.

3.1.1 Beam-line Extension

The extension starts at the F3 focus and consists of an additional -70° dipole (**B3**) and a 30 cm aperture quadrupole triplet (**Q8**, **Q9**, **Q10**) after

3.1. Cyclotron and Beam-line

B3. A 5-cm-thick lead collimator with a 3-cm square hole was placed at F3, blocking the spatially separated positrons. The beam-line extension defined a new focus, F4, 1.5 m after **Q10**, where the PIENU detector was placed. The **B3** magnet bent the beam for cleaning the electromagnetic radiation arising from the collimator. Figure 3.3 (right) shows the obtained particle rates as a function of the selected beam-line momentum. The rates were consistent with beam dynamics calculations, and it was demonstrated that the positron rate could be suppressed by a factor 60 with respect to the pion rate [1].

The momentum calibration of the beam-line is challenging to achieve with high accuracy, owing to the presence of fringe fields of the dipoles. Nevertheless, to obtain a proper calibration, we rely upon physics processes such as the endpoint of the muon decay spectrum $\mu^+ \rightarrow e^+\nu_e$ and the peak of the $\pi^+ \rightarrow e^+\nu_e$ decay. The positrons from the two chains come from the decays occurring in the primary target. Above 55 MeV/c, the primary source of positrons is γ pair production from $\pi^0 \rightarrow \gamma\gamma$ decays inside the primary target. The momentum distribution of these prompt positrons (with respect to the proton beam bunch) is nearly flat [97].

Instead, by selecting positrons delayed with respect to the primary beam RF structure, it is possible to eliminate the prompt background and observe pion and muon decays. Figure 3.5 (left) shows the result of the momentum scan where the endpoint of the muon decay and the peak of the $\pi^+ \rightarrow e^+\nu_e$ decay are clearly visible, this peak is used for calibration. In Figure 3.5 (right), it is shown that the delayed positrons have a time spectrum consistent with the pion decay time [1].

The beam-line was also tested with negative polarity, yielding a ratio of delayed to prompt positrons of $(3.4 \pm 0.4) \times 10^{-3}$, consistent with an estimate based on the yield ratio $N_{\pi^-}/N_{\pi^+} = 1/5$ in this energy region and the 1% fraction of pion decays in flight in which muons stop in the target [98]. The beam-line extension ended by going through a 20-cm-thick steel wall for shielding the experiment from the remaining γ and neutron backgrounds. The PIENU detector was attached to the end of the beam after the wall.

3.2. Detector

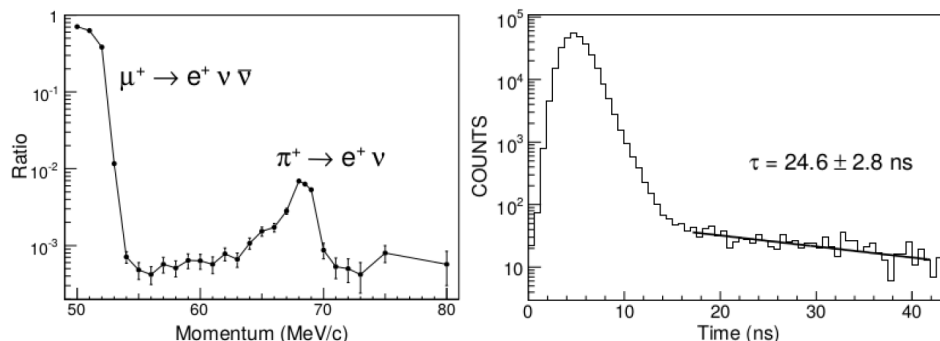


Figure 3.5: Left: Fraction of beam positrons as a function of the selected momentum. Right: Fit of the delayed component of the positrons time-of-flight showing consistency with the pion decay time [1].

3.2 Detector

The PIENU detector design has been reported in detail in Ref. [4]. Figure 3.6 shows a schematic of the detector that was conveniently designed as two main assemblies PIENU-1 and PIENU-2. PIENU-1 contains the detection, identification, and tracking capabilities for the incoming pion beam. In downstream order, the beam first passes through a pair of 3-layer wire chambers (WC1, WC2) that provide the beam profile. Then, the beam is degraded by two plastic scintillator counters (B1, B2), followed by two silicon-strip detectors (S1, S2), each of them with X-Y planes. Finally, the beam enters and stops in the target plastic scintillator (B3) where most of the pions will decay, and an isotropic positron “aura” will emerge. Decay positrons after B3 go into another double-sided silicon microstrip detector (S3) and a scintillator (T1) for positron timing.

PIENU-2, which follows PIENU-1, is contained inside a steel cylinder aligned with the beam-line to allow internal sub-detector rotation (along beam axis) capabilities for special positron runs to get the calorimeter’s energy response. PIENU-2 is a positron telescope with a 3-layer wire chamber (WC3) and a scintillator (T2) covering the front face of a NaI(Tl) calorimeter (Bina). To contain the electromagnetic shower produced, four rings made of 97 pure CsI crystals surrounded Bina. Veto scintillators were installed to cover the flanges for T2 (V2), and the calorimeter (V3). Table 3.1 summarizes the details of all the main detector components.

3.2. Detector

Table 3.1: Parameters for the PIENU detector [4].

Plastic scintillator counters					
Trigger counters	B1	B2	B3	T1	T2
Size in X (inner radius)	100 mm	45 mm	70 mm	80 mm	(0) mm
Size in Y (outer radius)	100 mm	45 mm	70 mm	80 mm	(171.45) mm
Size in Z	6.604 mm	3.07 mm	8.05 mm	3.04 mm	6.6 mm
Z position	-39.03 mm	-30.02 mm	0 mm	19.92 mm	72.18 mm
Photomultiplier model/ manufacturer	H3178-51 Hamamatsu	83112-511 Burle	XP2262B Photonis	83112-511 Burle	H3165-10 Hamamatsu
Photo-cathode diameter	34 mm	22 mm	44 mm	22 mm	10 mm
Veto counters			V1	V2	V3
Inner radius			40 mm	107.95 mm	177.8 mm
Outer radius			52 mm	150.65 mm	241.3 mm
Size in Z			3.175 mm	6.35 mm	6.35 mm
Photomultiplier model/ Photomultiplier manufacturer			H3164-10 Hamamatsu	H3165-10 Hamamatsu	
Photomultiplier photo-cathode diameter			8 mm	10 mm	
Tracking detectors					
Multi-wire proportional chambers	WC1		WC2	WC3	
Wire spacing			0.8 mm	2.4 mm	
Number of planes/wires/readout channels			3/120/40	3/96/48	
Active area diameter			96.0 mm	230.4 mm	
Cathode plane to anode wire spacing			1.6 mm	2.0 mm	
Anode wire diameter			15 μm		
Wire orientation			0°, +120°, -120°		
Silicon strip detector pair (X and Y oriented strips)			S1/S2/S3		
Active area			61 \times 61 mm ²		
Silicon strip pitch			80 μm		
Effective pitch after binding 4 strips			320 μm		
Number of planes/readout channels per plane			2/48		
Thickness (size in Z)			0.285 mm		
Separation between X and Y strip detectors			12 mm		
Electromagnetic calorimeter					
Crystal	NaI(T ℓ)		CsI		
Number used	1		97		
Energy resolution (FWHM) at 70 MeV	2.2%		10%		
Thickness (size in Z)	480 mm		250 mm		
Outer radius	240 mm		...		
Approximate width \times height for pentagon shaped CsI crystals	...		90 \times 80 mm ²		
Number of PMTs per crystal	19		1		
Hamamatsu PMT model (central PMT for NaI(T ℓ) was R1911-07)	R1911		R5543		
Photomultiplier photo-cathode diameter			76.2 mm		

3.2. Detector

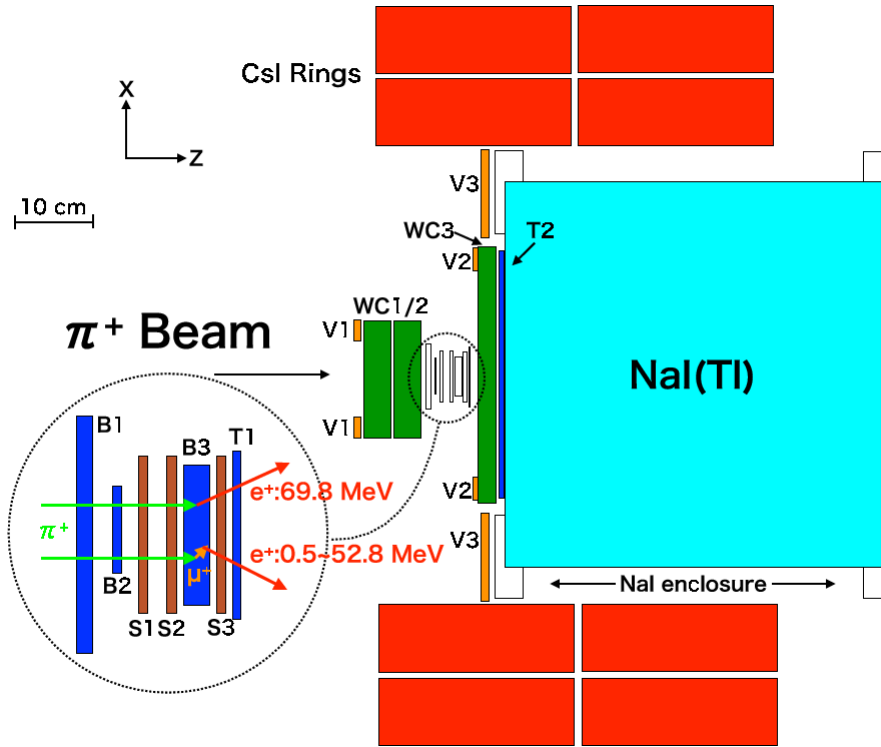


Figure 3.6: Schematic illustration of the PIENU detector [4]. The target region is magnified in the inset.

3.2.1 Scintillators

B1 and B2 are two square beam counters placed downstream of WC1 and WC2. Only B1 covers WC1 and WC2's full aperture. B1 and B2 were placed upstream close to B3 to select pions of their energy deposited (B2 is smaller than the target). B1 and B2 served to measure the time and energy loss for particle identification, and most importantly to improve the signal to noise ratio (Section 4.2.5). B3 is followed by the positron telescope counters T1 and T2. B3 and T1 were rotated with respect to B1 and B2 by an angle of 45° around the beam axis. T1 defines the timing of the decayed positrons with respect to the incoming pion time measured by B1. After B3, it is essential to have a compact assembly to maximize solid angle acceptance; therefore, T2 was placed directly in front of the NaI(Tl) calorimeter.

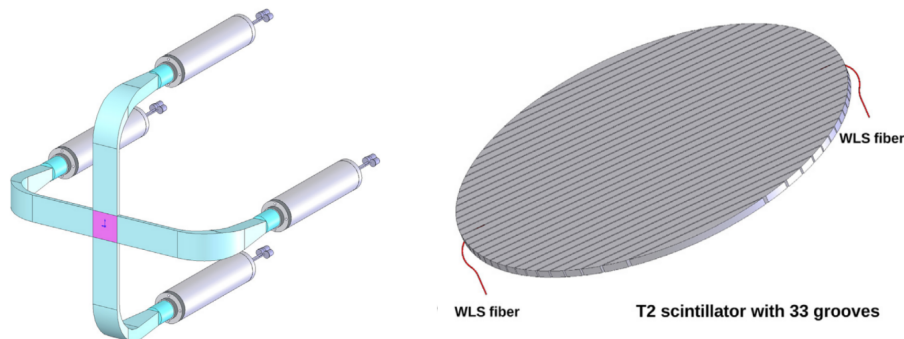


Figure 3.7: (Left) B1, (also B2, B3, and T1) plastic scintillator is read out with 4 PMTs (grey cylinders); Light was collected by four acrylic light guides (light green). (Right) Readout scheme with wavelength-shifting fibers of the T2 plastic scintillator.

The plastic scintillator counters were made of Bicron BC-408 (polyvinyl toluene) scintillator.²⁰ Each, except T2 and vetos, was read out by four PMTs through acrylic light guides. Owing to T2 and the veto's circular shape and limited space, they were read out by wavelength-shifting (WLS) fibers having a diameter of 1 mm (Kuraray Y-11). The schematic configuration of the scintillator readouts is showed in Figure 3.7.

3.2.2 Wire Chambers

Beam particles were tracked using WC1 and WC2. On the other hand, WC3 is part of the tracking devices for decay positrons and defines Bina's acceptance at the entrance of the calorimeter enclosure. The three wire chambers used for the PIENU detector were constructed similarly to the successful design from the E949 (TWIST) experiment [100]. Each wire chamber consisted of three wire planes rotated by an angle of 120° to each other to form an X-U-V assembly. The chambers used a gas mixture of 80% tetrafluoromethane (CF_4) and 20% isobutane (C_4H_{10}) at atmospheric pressure.

Figure 3.8 shows the assembly for WC1 and WC2. They had 120 wires in each of the three planes. For WC1-2, the effective pitch is 2.4 mm, and the total active diameter is 96 mm. Figure 3.9 (left) shows the assembly

²⁰Light output: 10240 photons/MeV, attenuation 380 cm, decay time 2.1 ns, and density 1.032 g/cm³ [99]

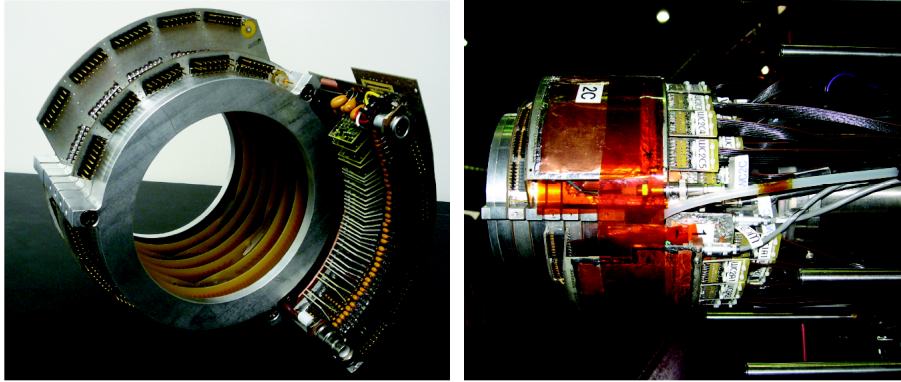


Figure 3.8: (Left) WC1/2 wire chamber plane and its preamplifier board. Each chamber consisted of three planes. (Right) WC1/2 after installation on the beam pipe [9].

for WC3, which has the same design; it only differs by being larger, with 96 wires for each of the three planes. For WC3, the effective wire pitch is 4.8 mm, and the total active diameter is 23.04 cm. Signals from the wires were fed in to a multi-hit TDC channel after preamplifiers and discriminators. The efficiency of every plane was measured to be larger than 99% for beam positrons.

3.2.3 Silicon Detectors

Each silicon detector (S1, S2, S3) had two planes (48 channels per plane) of strips to measure the X and Y coordinates, and each detector was a single-sided AC-coupled micro-strip device of the same type as the ones used in the ATLAS central tracker [31]. S1 and S2 were placed immediately upstream of B3, while S3 was placed immediately downstream of it to provide position and angle information of the incoming pion and the outgoing positron, respectively. Figure 3.9 (bottom-right) shows one visible plane from the S1 and S2 assembly; each plane of the silicon detector has an active volume of $61 \text{ mm} \times 61 \text{ mm} \times 285 \mu\text{m}$.

The strip pitch was $80 \mu\text{m}$, and as the PIENU experiment required a resolution of $300 \mu\text{m}$, the design was modified by binding four silicon strips to one read-out line. The read-out lines were interconnected with capacitors, and only every fourth line was read out by an amplifier. Figure 3.9 (top-right) shows a schematic of the silicon strip read-out. By adequately weighting the

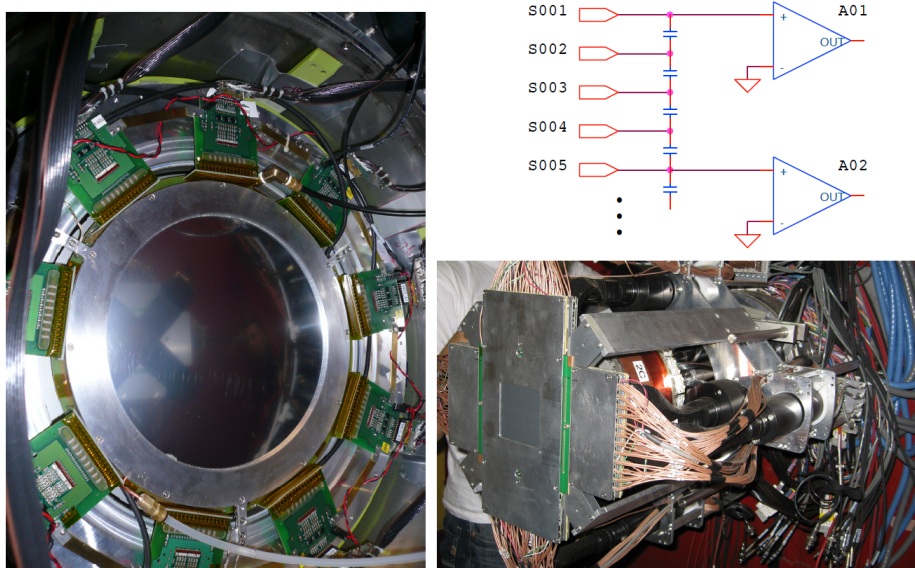


Figure 3.9: (Left) Image of the wire chamber WC3 placed in front of the NaI(Tl) calorimeter. (Right) S1 and S2 assembly on their support structure [9] [31].

channels that fire during an event, the capacitors form a charge division line to reconstruct amplitude and position. The signals were read out by VF48 60 MHz ADCs, where predefined thresholds for pulse-signal waveforms were adjusted to reduce the data size and to suppress channels with no hits. S1 and S2 were tuned for pions, and S3 thresholds were set lower to ensure that the efficiency for decay positrons for at least one plane was higher than 99%.

3.2.4 Bina

Figure 3.10 (left) shows the back side of PIENU's main calorimeter during PMT installation. It is a single crystal of Thallium-doped Sodium Iodide (NaI(Tl)) and it is the largest ever grown of this kind. The NaI(Tl) was obtained from the Brookhaven National Laboratory (Upton, NY, USA), where it was used by the LEGS collaboration [101] [102]. A reflective material was used to cover the surface of the crystal and it was enclosed in a 3-mm-thick aluminum enclosure having 19 circular quartz windows at the rear end. To minimize the amount of material crossed by the incoming particles, a 0.5-mm-thick aluminum front face was installed instead of the 3-mm enclosure.



Figure 3.10: (Left) Back side of the NaI(Tl) crystal on the test bench. (Right) The NaI(Tl) crystal and the 97 CsI crystals while the calorimeter was under construction [9].

On each circular window was mounted a Hamamatsu R1911 PMT having a diameter of 3 inches, except the centre PMT which is of type R1911-07. All PMTs used for Bina and the CsI crystals were wrapped with a μ -meter thin metal shield to reduce the cyclotron's 2 G fringe fields. Further, an optical simulation was performed with the software Detect2000 [103]. Results from simulations showed that light was uniformly reflected [104], and this was confirmed within 2% by bench tests with a ^{22}Na radioactive source [105].

3.2.5 CsI

To further contain radiative shower energy leakage and reduce uncertainty in the LET (discussed in Section 1.2), Bina was surrounded by a total of 97 pure CsI crystals, 25 cm in length (13.5 radiation length), with a pentagonal cross-section and around 9 radiation length radially (two layers). Figure 3.6 and 3.10(right) show how the CsI crystals were arranged in four concentric layers around the NaI(Tl) calorimeter. Layers are divided in an upstream and downstream part, each further divided into inner or outer part, forming a total of 4 rings [106]. CsI crystals and photo-tubes, obtained from BNL, had been used in the E949 experiment [107]; Hamamatsu R5543 PMTs [108] having a diameter of 3 inches PMT, are designed to operate in high parallel magnetic fields and used for the CsI crystals. As the pure CsI crystals are slightly hygroscopic, they were flushed continuously by nitrogen gas to maintain low humidity levels.

For light output and PMT gain performance traceability, each crystal had a $\text{YAlO}_3:\text{Ce}^{245}$ light pulser attached to it [109], to emit about 8 MeV equivalent 50 Hz light pulses with similar wavelength and pulse width as the CsI scintillation. Furthermore, to independently monitor the PMT gains without exciting the crystals, they were connected to a reference Xenon lamp via a merging quartz fiber to trigger the crystals at 2 Hz during data taking [110]. The Xenon lamp also sent pulses to seven reference PMTs (of the same type) enclosed in an incubator maintained at a constant temperature of 24.0 °C. Such external PMTs gave reference measurements for correcting the light-output changes of the Xenon-lamp that was located in an identical incubator. To obtain information on the light collection efficiency of the crystals, we compared data from both the $\text{YAlO}_3:\text{Ce}^{245}$ and the Xenon lamp. The instability of the light yield from the Xenon lamp was measured to be less than 1%.

3.2.6 Tracking

The PIENU tracking system consists of three subsystems that can provide particle positions and angle information of a track in three dimensions. Our first “tracker” (Trk1) uses both of the beam wire chambers WC1 and 2, the second tracker (Trk2) uses the first two silicon detectors S1 and 2, and the third tracker (Trk3) joins S3 and WC3. Trk1 provides six position measurements (6 wires), while Trk2 provides four (2 x-y planes) and Trk3 five (1 x-y and 3 wires). Figure 3.11 shows a schematic of the tracking devices and the different track topologies, i.e., pion decay-at-rest (πDAR), muon decay-at-rest (μDAR), pion decay-in-flight (πDIF), and muon decay-in-flight (μDIF).

Trk3 is used for tracking decay positrons entering the calorimeter, and therefore, it defines the acceptance radius (A_R). To suppress pion decays in flight, Trk1 and Trk2 can be used for detecting pion decays before the target. Further suppression and removal of background events can be achieved by matching the tracks from Trk1 and Trk2 with the positron tracks from Trk3 and checking if the decay vertex lies within the target (Z_v). Some track topologies are as follows.

- $\pi^+ \rightarrow e^+\nu_e$: The pion stops in the target and decays directly to a positron.
- $\pi\text{DAR} \rightarrow \mu\text{DIF}$: In $\pi^+ \rightarrow \mu^+\nu_\mu \rightarrow e^+\nu_e\bar{\nu}_\mu$ decay, the muon decays in flight in the target. These events are a problem because the muon

3.2. Detector

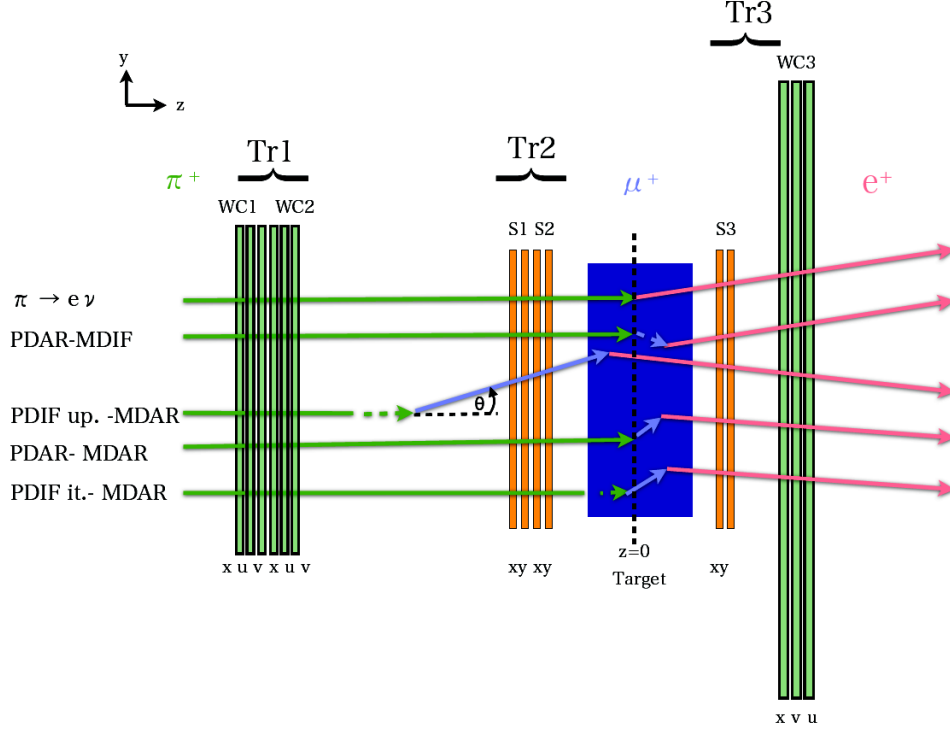


Figure 3.11: Schematic of the tracking devices, the $\pi^+ \rightarrow e^+ \nu_e$ signal, and the different decay-in-flight backgrounds (the sizes are not to scale). π DAR $\rightarrow \mu$ DIF: In $\pi^+ \rightarrow \mu^+ \nu_\mu \rightarrow e^+ \nu_e \bar{\nu}_\mu$ decay, the muon decays in flight in the target. π DIF upstream of target (“up.”) $\rightarrow \mu$ DAR: The pion decays in flight before entering the target. Part of these decays can be detected by tracking through the kink variable (K_θ). π DAR $\rightarrow \mu$ DAR: Both the pion and the muon in the $\pi^+ \rightarrow \mu^+ \nu_\mu \rightarrow e^+ \nu_e \bar{\nu}_\mu$ channel decay at rest in the target. π DIF inside target (“it.”) $\rightarrow \mu$ DAR: Pion decay-in-flight in the target and muon decay at rest. The “u” orientation of a WC plane corresponds to a rotation of $+60^\circ$ while “v”= -60° .

energy can boost the LE positrons into HE events. Such a topology has the same timing distribution as the direct $\pi^+ \rightarrow e^+ \nu_e$ decay. These events cannot be detected and separated from the $\pi^+ \rightarrow e^+ \nu_e$ events; therefore, a correction is needed. Such correction will be discussed in Section 6.3.

- π DIF upstream of target (“up.”) $\rightarrow \mu$ DAR: The pion decays in flight

3.2. Detector

before entering the target. Part of these decays can be detected by tracking through the kink variable (K_θ), shown in Figure 3.11.

- π DAR \rightarrow μ DAR: Both the pion and the muon in the $\pi^+ \rightarrow \mu^+ \nu_\mu \rightarrow e^+ \nu_e \bar{\nu}_\mu$ channel decay at rest in the target.
- π DIF inside target (“it.”) \rightarrow μ DAR: Pion decay-in-flight in the target and muon decay at rest.

From Geant4 calculations, the probabilities of decays in flight (DIF) with respect to the decays at rest (DAR) for the $\pi^+ \rightarrow \mu^+ \nu_\mu \rightarrow e^+ \nu_e \bar{\nu}_\mu$ events are: about 0.6% for π DIF up. \rightarrow μ DAR; and 0.6% for π DIF it. \rightarrow μ DAR. Figure 3.12 shows the kink angle K_θ distribution of π DAR events and π DIF events obtained with simulations. The probability of both π DIF \rightarrow μ DIF is negligible.

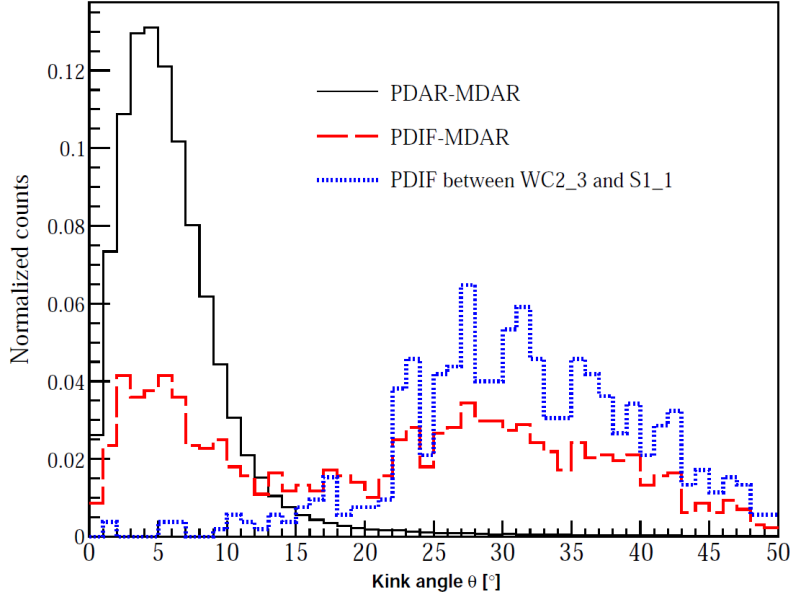


Figure 3.12: Simulation of the kink angle K_θ for different pion decay modes.

Track definition

The goal is to find an algorithm for calculating the track parameters of charged particles traversing three or more planes. The tracking algorithm

3.2. Detector

is described in [111], where without magnetic fields, tracks are straight lines parameterized as

$$\begin{aligned}x &= x_0 + v_x t, \\y &= y_0 + v_y t, \\z &= z_0 + v_z t.\end{aligned}\tag{3.1}$$

The reference frame is the center of target B3, defined as point $\{x_0, y_0, z_0\}$ where z -axis points downstream, x -axis goes horizontally and y -axis vertically. The point $\{x, y, z\}$ is for the position of the particle at a given time t , with velocity vector $\vec{v} = \{v_x, v_y, v_z\}$. The number of parameters is six; however, only four are independent. We can choose $z_0 = 0$ and set a normalization for the vector \vec{v} . Choosing $v_z = 1$ gives $\vec{v} = \{t_x, t_y, 1\}$, where $t_x = v_x/v_z$ and $t_y = v_y/v_z$. With these choices, and $z = t$, we get the new parameterization

$$\begin{aligned}x &= x_0 + t_x z, \\y &= y_0 + t_y z.\end{aligned}\tag{3.2}$$

The parameterization choice is convenient, as the particles are mainly going in one direction, which we choose to be the beam direction z , and the parameters x_0 and y_0 identify the point where the track intersects the plane at $z = 0$ (the center of the target). A drawback of the chosen parameterization is that it is not able to describe lines parallel to the xy plane, but this situation is not relevant in this case.

Track Fitting

The measurement of one hit in a tracking detector plane corresponds ideally to one wire chamber wire or to a silicon detector channel, for which the position is known. In reality, more wires or strips can be active and the tracking software used only “hits”, which were consistent with the correct trigger timings. Consider now a coordinate system uv in a tracker’s plane (z is fixed), where the axis u is orthogonal to the wires/strips. In this way, the coordinate u is proportional to the wire/strip number. With rotation, it is possible to transform the uv system to the xy system of the experimental hall, as we know the fixed angles for each plane. In addition, every track has a χ^2 function, which is the squared deviation of the tracks from the measurements, weighted with the errors in each measurement.

Tracking Quantities

For defining the acceptance and suppress the $\pi^+ \rightarrow \mu^+ \nu_\mu \rightarrow e^+ \nu_e \bar{\nu}_\mu$ background in the suppressed spectrum,²¹ the following variables were constructed:

- **Acceptance Radius:**

$$A_R = \sqrt{(t_x z_{WC3} + x_0)^2 + (t_y z_{WC3} + y_0)^2}, \quad (3.3)$$

where z_{WC3} was the location of the centre of WC3 along the beam direction z.

- **Kink angle:**

$$K_\theta = \arccos \frac{t_{xA} t_{xB} + t_{yA} t_{yB} + 1}{\sqrt{(t_{xA}^2 + t_{yA}^2 + 1)(t_{xB}^2 + t_{yB}^2 + 1)}}, \quad (3.4)$$

where the track A was reconstructed by Trk1, while the track B was reconstructed by Trk2.

- **Z-vertex (π stopping position in target B3):**

$$Z_v = \frac{(x_{0A} - x_{0B})(t_{xA} - t_{xB}) + (y_{0A} - y_{0B})(t_{yA} - t_{yB})}{(t_{xA} - t_{xB})^2 + (t_{yA} - t_{yB})^2}, \quad (3.5)$$

where track A was reconstructed by Trk2 and track B by Trk3.

3.3 Final Detector Assembly

The final detector assembly is shown in Figures 3.13, and 3.14. Additional technical drawings are shown in Appendix F. PIENU-1 was mounted to the beam pipe and PIENU-2 enclosed by a steel cylinder was mounted on a supporting structure on wheels which were guided by rails to ensure correct alignment to PIENU-1. This flexible system allowed removing of the PIENU-1 assembly to enable rotation for PIENU-2 with respect to the beam axis for investigation of the calorimeter response to a positron beam at different entrance angles. This information is crucial for the determination of the $\pi^+ \rightarrow e^+ \nu_e$ LET. Following the 2009 data-taking, it was observed that

²¹In the calorimeter, the low energy tail from the $\pi^+ \rightarrow e^+ \nu_e$ energy distribution is buried under the $\pi^+ \rightarrow \mu^+ \nu_\mu \rightarrow e^+ \nu_e \bar{\nu}_\mu$ energy. The $\pi^+ \rightarrow \mu^+ \nu_\mu \rightarrow e^+ \nu_e \bar{\nu}_\mu$ events can be suppressed with specialized cuts to access just the $\pi^+ \rightarrow e^+ \nu_e$ distribution.

temperature variations in the experimental hall resulted in gain variations in the PMTs. Therefore, a temperature-controlled enclosure housing for the detector was constructed to maintain temperatures at 20°C within $\pm 0.5^\circ\text{C}$ to keep the gain variations within acceptable limits.

3.4 Data Acquisition System

3.4.1 Trigger

The PIENU trigger (full diagram in Appendix E) system was assembled using NIM²² modules for the most part. The trigger logic was designed for two main functions; physics and detector calibration data. Figure 3.15 shows a schematic of the PIENU trigger diagram. Particle identification for the incoming beam composed mainly of pions is made by requiring a trigger coincidence between beam counters B1, B2, and target scintillator B3, and proper energy cuts in B1-B2 to ensure a pion particle. Such coincidence is called pion signal. If needed, beam muons or positrons could be selected for sub-detector calibration. Positrons from either $\pi^+ \rightarrow e^+\nu_e$ or $\pi^+ \rightarrow \mu^+\nu_\mu \rightarrow e^+\nu_e\bar{\nu}_\mu$ decays downstream from target (B3) are detected with a T1-T2 counter coincidence, which defines the decay-positron-signal. A pion-decay-positron-signal coincidence within the time window of -300 ns to 540 ns with respect to the pion stop in target B3 (t_0) is the basis of the trigger logic. We call such events “PIE” events.

We used three main trigger configurations for normal physics data taking, named: *Prescale*, *Early* and *TIGC aka BinaHigh* trigger; we call them physics triggers,

- *Prescale*: As $\pi^+ \rightarrow \mu^+\nu_\mu \rightarrow e^+\nu_e\bar{\nu}_\mu$ events dominate $\pi^+ \rightarrow e^+\nu_e$ events by four orders of magnitude, a *Prescale* unbiased trigger selects only 1/16 of PIE events. The PIE events include $\pi^+ \rightarrow e^+\nu_e$ events as well, thus an event can have more than one trigger tag.
- *Early*: As the pion has a very short decay time relative to the muon, 26 ns vs. 2.2 μs , respectively, around 70% of the $\pi^+ \rightarrow e^+\nu_e$ decay positron events can be selected in an early time window, 6 ns to 46 ns

²² The Nuclear Instrumentation Module (NIM) standard defines mechanical and electrical specifications for electronics modules used in experimental particle and nuclear physics. The concept of modules in electronic systems offers enormous advantages in flexibility, interchange of instruments, reduced design effort, ease in updating and maintaining the instruments.

3.4. Data Acquisition System

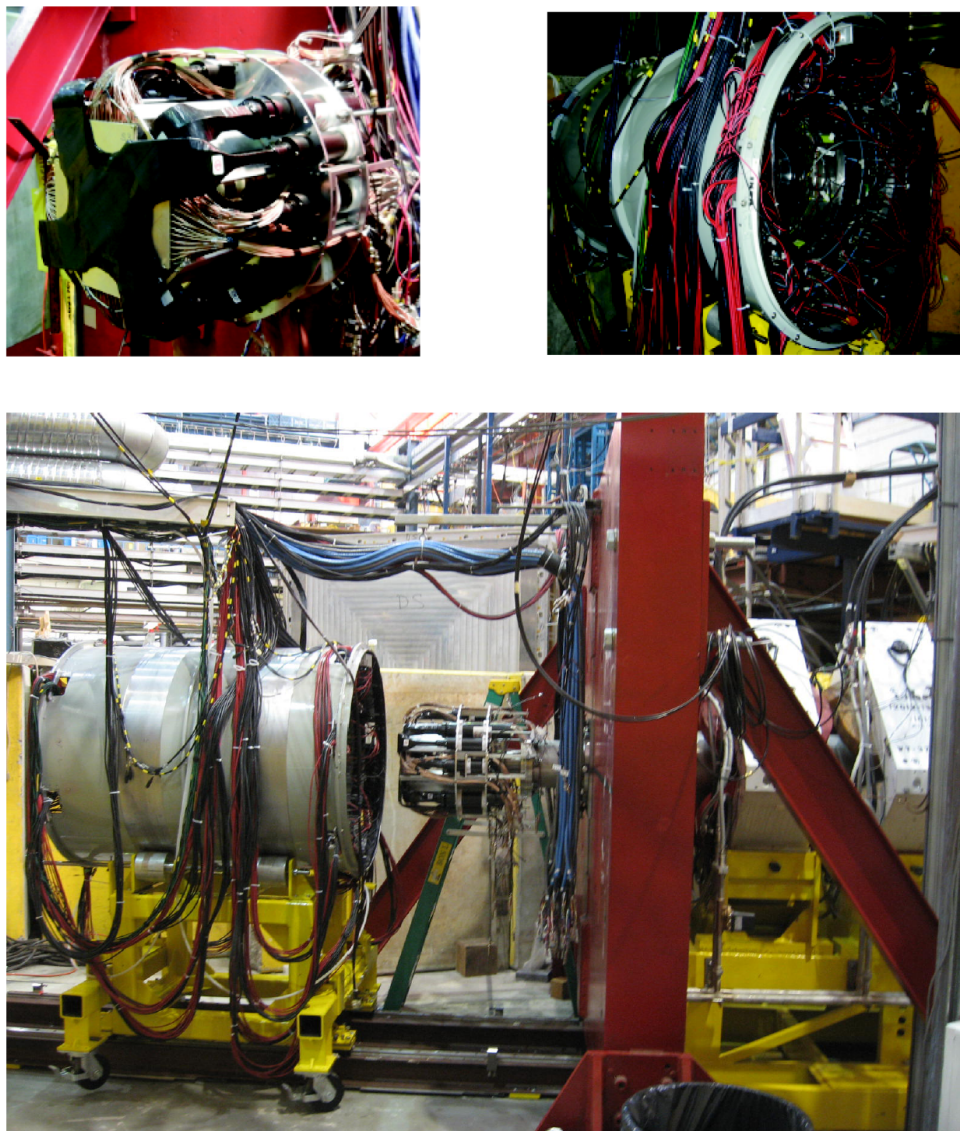


Figure 3.13: Bottom: Beam goes from right \rightarrow left. The PIENU detector and beam-line after the last bending magnet, showing the steel wall used for radiation shielding. Top-Left: PIENU-1 assembly of scintillators, wire-chambers, and silicon detectors. Top-Right: PIENU-2 detector calorimeter assembly, image from [9].

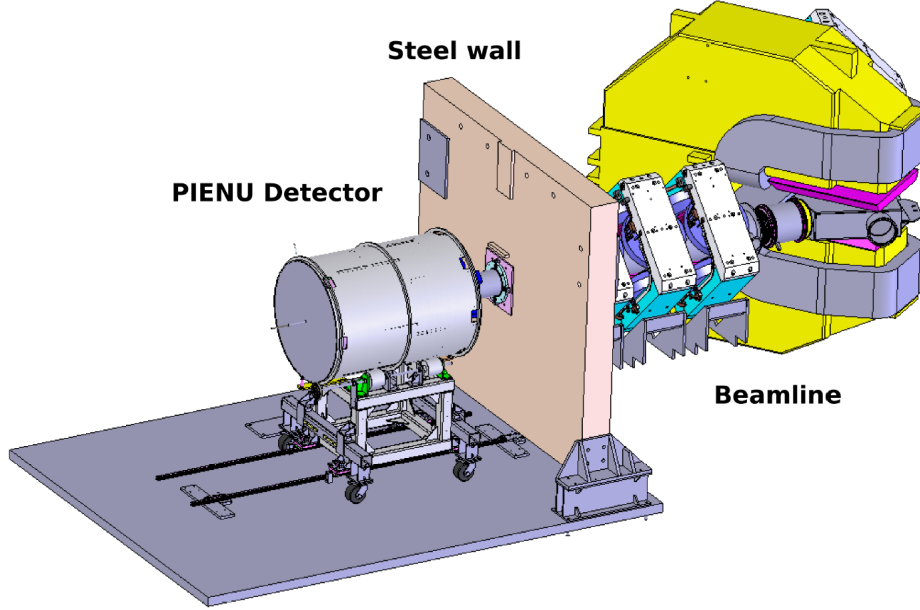


Figure 3.14: Beam-line-Detector CAD drawing [9].

after pion stop time t_0 . We used such *Early* trigger configuration to enhance those events.

- *TIGC or BinaHigh*: Another $\pi^+ \rightarrow e^+\nu_e$ event enhancer is the *TIGC or BinaHigh* trigger. It selects events that have a high energy deposit in the calorimeters (Bina and CsI rings). The energy (TIGC) threshold is set at the upper edge of the $\pi^+ \rightarrow \mu^+\nu_\mu \rightarrow e^+\nu_e\bar{\nu}_\mu$ spectrum. This trigger selects nearly all the $\pi^+ \rightarrow e^+\nu_e$ events (with the exclusion of the tail events which extend below the TIGC threshold).

The other three triggers *Cosmic*, *Xe-lamp*, and *Beam-Positron* were used for calibration and data quality checks.

- *Cosmic*: The Cosmic trigger selected cosmic-ray events. Mostly high energy cosmic muons were selected by the requirement of a high-energy deposit in the CsI outer layer or the coincidence of inner and outer layers. A prescaling factor of 16 is applied to reduce the rate of this trigger. These events are used for the calibration of the CsI calorimeter as it is the only detector not directly exposed to the beam. This trigger

3.4. Data Acquisition System

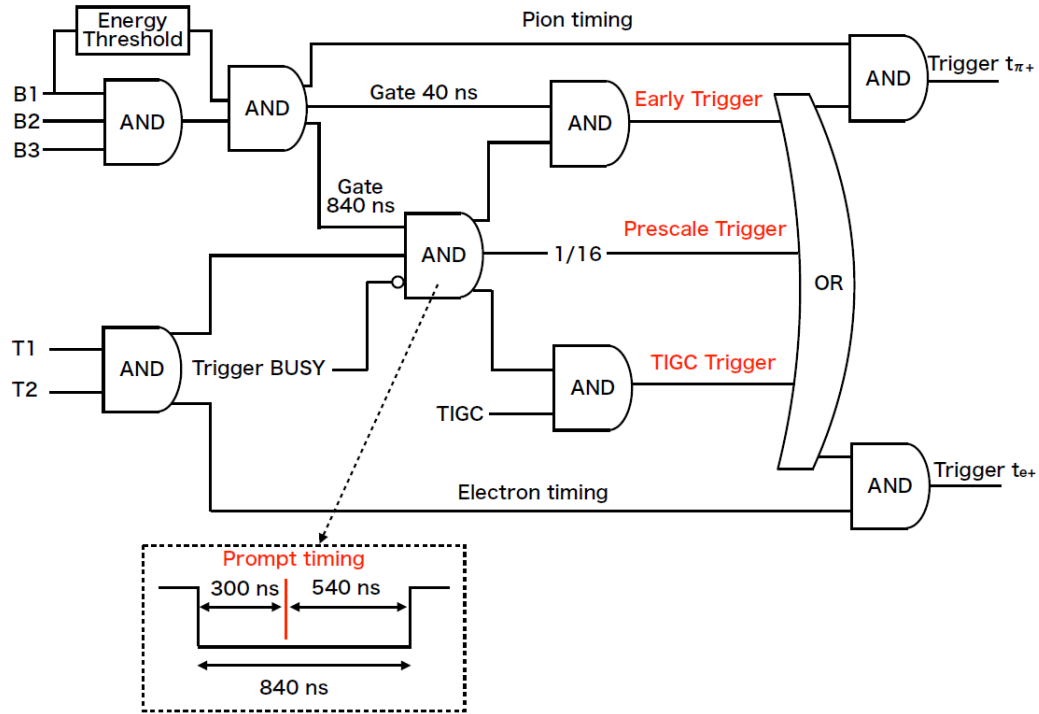


Figure 3.15: Schematic of the trigger diagram for the three physics triggers. The rates of the triggers are listed in Table 3.2. Image from [18].

provides an energy calibration for the crystals as well as the monitoring of the crystal and PMT gains.

- *Xe-lamp*: The Xe lamp provided flashes to all the CsI crystals (Xe trigger) for monitoring PMT variations. This lamp was triggered by a pulse generator twice in a second.
- *Beam-Positron*: The beam positrons are accepted by this trigger with pre-scaling by a factor of 32. Beam positron trigger was used for the Bina and plastic scintillators calibration.

During a typical data taking run, all six triggers were used, and several of them could be triggered at the same time. To distinguish the associated trigger types to a particular event, the trigger logic pulses were also recorded

3.4. Data Acquisition System

with a multi-hit Time-to-Digital Converter (TDC) named VT48²³. The rates of the triggers are listed in Table 3.2. The total trigger rate was about 600 Hz. The trigger signal made by any of the six triggers enabled measurement of the pion (t_{π^+}) and the positron (t_{e^+}) timing. These latched signals triggered the data acquisition. t_{e^+} was used for the trigger of the VME²⁴ modules (VF48 and VT48)²³, while t_{π^+} triggered the COPPER²³ board data acquisition. Details of those modules will be described in the next section.

Table 3.2: Rates for all triggers [4].

Trigger	Rate (in Hz)
Pion stop in Target	5×10^4
<i>Physics Triggers</i>	
Early trigger	160
TIGC trigger	170
Prescale trigger	240
<i>Other Triggers</i>	
Cosmic trigger	15
Beam Positron trigger	5
Xe lamp trigger	2
Total Trigger	~ 600

3.4.2 Boards

COPPER

PIENU featured a 500 MHz Flash-ADC system, named *The COmmon Pipelined Platform for Electronics Readout* (COPPER) ([4], [15] and [112]). It was used for all plastic scintillators; B1, B2, B3, T1, and T2. COPPER was initially designed for the Belle experiment at KEK. The main COPPER board was a 9U-size VME board. The significant advantage of the system was its onboard data processing capability featuring a CPU able to host

²³Details in Section 3.4.2.

²⁴ VMEbus (Versa Module Europa bus) is a computer bus standard widely used today in particle physics. It is physically based on Eurocard sizes, and connectors (DIN 41612), but uses its own signaling system.

3.4. Data Acquisition System

LINUX on board to allow data suppression with embedded software. One COPPER board had four frontend digitization modules called “FINESSE” (Figure 3.16). Each frontend can receive two analogue inputs, and the back-end data process was handled on the COPPER main board; therefore, each COPPER board can receive a total of eight signals to digitize.

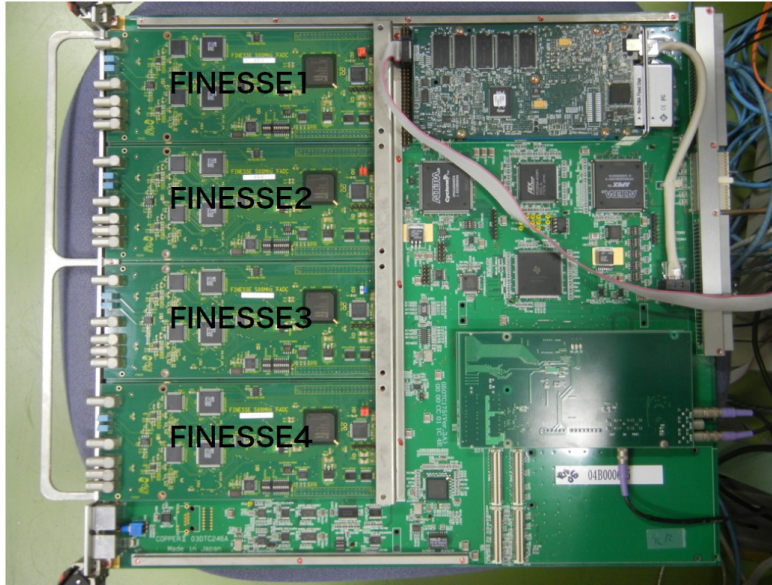


Figure 3.16: Picture of main COPPER board mounted with four FINESSE modules.

Each FINESSE card had four 250-MHz Fast-Analogue-to-Digital-Converters (FADC) devices that were driven in alternating phases to realize 500-MHz sampling. The gain of these two synchronized FADCs were monitored and adjusted on a run-by-run basis using beam particle signals to be able to sample the signal at 500 MHz correctly. Figure 3.17 shows the digitized waveform from a PMT obtained with COPPER. The PIENU experiment used 4 COPPER boards to digitize the signals coming from the 23 PMTs of all plastic scintillators and a few other additional signals.

The FINESSE cards were driven and synchronized by a 250 MHz **Clock Distribution** module by providing gate, reset, and busy signals to the boards. A General Purpose Input Output (**GPIO**) module developed by

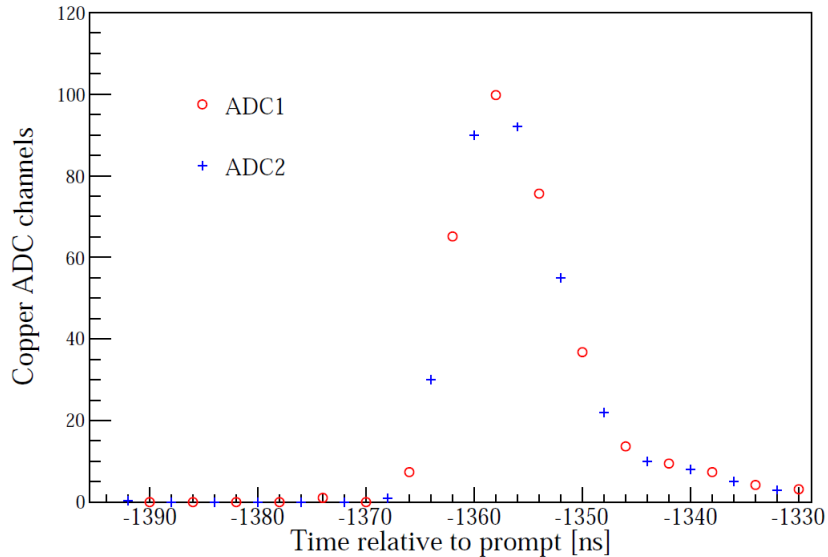


Figure 3.17: A waveform digitized by COPPER. The red circles and blue crosses show the digitization of each 250 MHz ADCs, which produce a 500 MHz waveform.

KEK provided gate and reset signals into Clock Distributor module. Additionally, GPIO module received the busy signal from COPPER boards and provided it to the trigger logic, and received the trigger signal from the trigger logic to distribute it to the COPPER system. In short, GPIO is the interface between the COPPER system and the trigger. The time window of the signals recorded by COPPER covers approximately $8\mu\text{s}$ ($1.35\mu\text{s}$ after and $7.75\mu\text{s}$ before the trigger timing) to be able to detect pre and post-pile up particles. Data below a certain threshold was suppressed to reduce the amount of data except for a given region around detected peaks to be able to record pedestals. For the PIENU experiment, the dynamic range of the FADC was set from -950 mV to 50 mV .

VF48

The VF48 is a 60 MHz flash-ADC with 10 bits and a dynamic range of $\pm 250\text{ mV}$. VF48 is a 6U-size VME module designed at the University of Montreal in 2004 [113]. All the Bina and CsI PMT signals, as well as all the silicon detectors channels, were read out by VF48 modules. A total of 404 channels (NaI: 19, CsI: 97, Silicon: 288) were read out by 10 VF48 modules.

3.4. Data Acquisition System

All VF48 modules received a 20-MHz clock signal provided by the TIGC module. This clock is multiplied internally to reach 60 MHz. Owing to the large number of channels we needed further data suppression. The full waveform is recorded with zero-suppression only with the following logic: if two subsequent samples have a pulse height difference higher than a given threshold. Except for Bina signals which were always recorded, but to a reduced rate of 30 MHz since the waveforms were $1.3 \mu\text{s}$ long. In order to suppress electronic noise the data suppression threshold for the CsI channels was set at 2 MeV, while it was 0.2 MeV for S1 and S2, and 0.1 MeV for S3. The number of samples recorded by the VF48 is different for each detector: 40 (666 ns), 40 (1333 ns) and 70 (1162 ns) samples are recorded for the CsI, Bina, and Silicon channels, respectively.

TIGC

The Tigress Collector (TIGC) is a VME module built and developed by the University of Montreal and TRIUMF for the TIGRESS experiment at TRIUMF [114]. This module allows on-the-fly summing of VF48 signals before the read-out. Every 250 ns, the highest sample of each waveform of all CsI and Bina channels went to TIGC, which then sums them and compares it to a predefined threshold. Before the sum, a multiplicative factor was applied to take into account the different gains of the two detectors. For 2010 and 2011 the TIGC threshold was set to be about 2 MeV below the $\pi^+ \rightarrow \mu^+ \nu_\mu \rightarrow e^+ \nu_e \bar{\nu}_\mu$ energy upper edge. For 2012 the TIGC threshold was lowered. A TIGC trigger is issued if a threshold is passed in coincidence with a valid pion-positron-decay signal, enabling the readout. TIGC also provided the synchronized clock to all the VF48 modules.

VT48

VT48 multi-hit TDC modules were used to read out the Wire Chamber wires, logic signals from PMTs after discrimination, and some trigger logic signals. VT48 is a single width VME 6U-size module [115] designed at TRIUMF in 2006 for the KOPIO experiment [116]. The VT48 module uses the AMT3 chip [117] which was initially developed for reading out ATLAS muon detectors channels. An onboard 25-MHz clock is multiplied to achieve 0.625 ns resolution. All VT48s are fed with an external 25-MHz clock to synchronize each of the modules. One board can read out 48 channels for up to $20 \mu\text{s}$. In 2012, two channels were read out with the full-time window to detect long lifetime backgrounds, while the other channels were read out with

3.4. Data Acquisition System

MIDAS experiment "pienu"			Fri Dec 14 14:19:11 2012 Refr:60		
<div style="display: flex; justify-content: space-between;"> Stop Pause ODB CNAF Messages ELog Alarms Programs History Config Help </div>					
monitor					
VME0_settings VME1_settings B1_Setpt B2_Setpt B3_Setpt Shifts Cameras Histos Operators Runlog HV_PIENU HVBertan					
Run #82584	Running	Alarms: On	Restart: Yes	Data dir: /home/pienu/online/data	
Start: Fri Dec 14 14:03:40 2012			Running time: 0h15m31s		
Equipment	FE Node	Events	Event rate[/s]	Data rate[MB/s]	Analyzed
Vme0	feVme0@lxpienu01.triumf.ca	86890	105.8	0.467	N/A
Vme1	feVme1@lxpienu02.triumf.ca	87085	107.3	0.576	N/A
Copper1	feCopper01@copper1	86908	107.7	0.071	N/A
Copper2	feCopper02@copper2	86849	107.7	0.038	N/A
Copper3	feCopper03@copper3	87085	108.3	0.055	N/A
Copper4	feCopper04@copper4	87018	103.5	0.025	N/A
Copper5	feCopper05@copper5	86864	107.7	3.202	N/A
EB	Ebuilder@pienu01.triumf.ca	87018	88.4	3.675	N/A
PostAmp	PostAmp@pienu01.triumf.ca	0	0.0	0.000	N/A
u_Beam	fe3hp@pienu01.triumf.ca	0	0.0	0.000	N/A
NMR	fenmr@pienu01.triumf.ca	0	0.0	0.000	N/A
Epics	feepics@pienu01.triumf.ca	0	0.0	0.000	N/A
M13DVM	fem13dvm@pienu01.triumf.ca	0	0.0	0.000	N/A
GASDVM	fegasdvm@pienu01.triumf.ca	0	0.0	0.000	N/A
ScalerN	feScalerN@lxpienu03.triumf.ca	0	0.0	0.000	N/A
LRS1440	FeLrs1440@pienu01.triumf.ca	0	0.0	0.000	N/A
RunLog	feRunLog@pienu01.triumf.ca	0	0.0	0.000	N/A
QOD	feqod@pienu02.triumf.ca	0	0.0	0.000	N/A
Temperature	FeTemperature@pienu01.triumf.ca	90	0.0	0.000	N/A
scbertan	scbertan@lxpienu03.triumf.ca	0	0.0	0.000	N/A
Channel	Events	MB written	Compression	GB total	
run82584.mid.gz	86976	1170.957	67.7%	116315.892	
Lazy Label	Progress	File Name	# Files	Total	
Dcache	0 %	run82581.mid.gz	20206	0.0 %	

Figure 3.18: Web interface of the MIDAS data acquisition system. All the VME modules were integrated and easily controlled via this interface.

an 8.0 μ s window before the trigger signal to reduce dead-time. However, because of the delay induced by the TIGC decision time, the trigger signal arrives in those latter channels at the middle of the VT48 recording window; this means that signals up to 4.0 μ s before and after the trigger time were read out. The PIENU experiment employed eleven VT48 modules.

3.4.3 Software

The PIENU data acquisition system consisted of three VME crates. Two VME crates were used for the VF48 and VT48 modules while the third was used for **Slow Control** modules and COPPER boards with a processor on each board. The slow control modules recorded many quantities such as the high voltage of PMTs, pressure of WC gas, magnet NMR, and other similar hardware to monitor the data-taking conditions. Collection of the data was

done via the **MIDAS** data acquisition system [118] which incorporates an integrated slow control system with a fast on-line database (ODB) and a history. To ensure scalability, MIDAS was designed to integrate multiple data sources from multiple computers through a TCP/IP network. The PIENU DAQ system made use of this advantage of MIDAS to integrate all the VME modules. The MIDAS server computer could be controlled via a web interface; see Figure 3.18. All the information and errors from the DAQ modules were displayed on the web page. MIDAS also controlled programs to make on-line histograms for the data quality check during data-taking.

3.5 Data-taking History and Milestones

The PIENU datasets contain four years of data, taken between 2009 and 2012, with around 5M $\pi^+ \rightarrow e^+\nu_e$ events. A summary of the data taking history and milestones is presented in Table 3.3. The DAQ system was set to record runs containing approximately 300k events at an incident pion rate of 50–60 kHz in around 10-min-long MIDAS files of about 1.8-GB in size. The MIDAS files or “raw” data had to be processed with the PIENU analysis framework to produce ROOT [119] “tree” files of about the same size. After all cuts from the analysis, each run had approximately 150 $\pi^+ \rightarrow e^+\nu_e$ “clean” events depending on the beam rate and hardware configuration. The PIENU proposal was approved by TRIUMF in 2005, the PIENU detector was designed in 2006, concept tested with the M9 beam-line in 2007, and the full detector constructed and fully tested with M13 beam-line in 2008.

3.5.1 2009

During 2009, the first stable runs with physics data were recorded. The dataset was divided as Run I and Run II, with about 1 M and 0.5 M clean $\pi^+ \rightarrow e^+\nu_e$ events respectively. As the digital module “TIGC” was not yet installed, a discriminator for BinaHigh triggers (high-energy events) was used to determine the pulse height of the sum of the NaI(Tl) and CsI PMTs. The analogue sum of the PMTs was recorded without gain correction, leading to unstable trigger conditions and potential loss of $\pi^+ \rightarrow e^+\nu_e$ events. In this period, the trigger for recording cosmic rays in coincidence with the CsI rings to calibrate them properly was not yet available. The CsI ring calibration was attempted using the external Xenon lamp/trigger and the internal $\text{YAlO}_3:\text{Ce}^{245}$ crystals, but such an attempt was inadequate. Such constraints limited the usability of the data to initial measurements of the detector response with special positron beam setup and exotic neutrino search in the

$\pi^+ \rightarrow e^+\nu_e$ energy spectrum. Preliminary results for massive neutrino analysis of the 2009 dataset were disseminated in the Ph.D. thesis of K. Yamada [15] and published in ref. [3], and the beam-line design and performance was published in ref. [1].

3.5.2 2010

The final trigger configuration was available starting 2010. The dataset was divided as Run III and Run IV with about 2 M and 0.4 M clean $\pi^+ \rightarrow e^+\nu_e$ events, respectively. However, the CsI PMTs were out of timing in Run III; therefore, no CsI information is available. Thus, the largest source of systematic error in the experiment, the estimated uncertainty in the low-energy tail of the measured $\pi^+ \rightarrow e^+\nu_e$ energy spectrum, was larger by approximately a factor of 2 for Run III. Run IV was the first high-quality data with all triggers and detector capabilities available. An initial analysis of Run IV was presented in the Ph.D. thesis of C. Malbrunot [16] which after further investigation resulted in the first publication of an improved value of the branching ratio [5]. Furthermore, the calorimeter design and performance was published in ref. [2]. The branching ratio uncertainty reached 0.24% precision with similar contributions from statistics and systematics; an improvement by a factor of 2 over the previous measurements was achieved.

3.5.3 2011

During 2011, an improved measurement of the response function of the detector was taken. This special set of runs replaces the 2009 special runs. Physics data were taken and named Run V with about 0.5 M clean $\pi^+ \rightarrow e^+\nu_e$ events. Preliminary results of the analysis of the 2011 dataset were published in the Ph.D. thesis of S. Ito [18].

3.5.4 2012

The 2012 dataset represents the largest and most easily usable high quality data recorded. Physics data were taken and named Run VI with around 2 M clean $\pi^+ \rightarrow e^+\nu_e$ events. At the start of this run, the energy threshold of the TIGC trigger was lowered, to ensure that no $\pi^+ \rightarrow e^+\nu_e$ decays were being missed. This resulted in additional $\pi^+ \rightarrow \mu^+\nu_\mu \rightarrow e^+\nu_e\bar{\nu}_\mu$ events causing TIGC triggers. As these events are not used in the analysis, the number of events per run is around 1.5 times lower in 2012 compared with 2010 and

2011. Preliminary results of the analysis of the 2012 dataset were published in the Ph.D. thesis of T. Sullivan [19].

3.5.5 Full analysis

The full analysis, including all datasets for the PIENU branching ratio, is currently in progress. The current analysis presented in this thesis is blinded, but includes the highest quality data portion available: Run IV, V and VI with a total around 3M $\pi^+ \rightarrow e^+\nu_e$ events. From this point forward Run IV, V and VI will be addressed, respectively as the 2010, 2011 and 2012 datasets. The massive neutrino search in the $\pi^+ \rightarrow e^+\nu_e$ energy spectrum including all 5M events from the PIENU datasets was recently published [11], and more collateral studies are being considered for publication, including the detector's energy response, an exotic neutrino decay $\pi \rightarrow \mu\nu$ search in the scintillator target (B3), a search for 3-body decays $\pi \rightarrow e\nu M$ where M is a Majorana [120] in the positron energy spectrum, and finally, an analysis on direct muon capture in zirconium for a special set of muon runs.

3.5. Data-taking History and Milestones

Table 3.3: Run history and milestones of the PIENU experiment.

Year	Month	Events	Run Range
2005	Dec.	Proposal approved by TRIUMF	
2006/07		Detector designed and prototyped in Meson Hall	
2008	May	Beam test in M13	
	Oct.	M13 beam channel extension completed	
	Oct.-Nov.	Test in M13 with most of the detectors	
2009	May	PIENU detector completed	5365
	May-Sep.	Run I (1 M $\pi^+ \rightarrow e^+\nu_e$)	5365–19123
	Oct.-Dec.	Run II (0.5 M)	19126–25751
	Nov 26	Lineshape tests	26021–26244
	Nov	Lineshape measurements	26245–26955
		Beam-line NIM paper published [1]	
2010	March	Temperature controlled enclosure completed	
	Apr.-Sep.	Run III (2 M)	29412–45780
	Oct.-Dec.	Run IV (0.4 M)	49669–52003
		Calorimeter NIM paper published [2]	
2011	Aug.	Systematic studies with beam	
	Sept-Oct.	Lineshape measurements	54879–56496
	Nov.	Run V (0.5 M)	57420–61179
		Neutrino Analysis for 2009’s data-sets published [3]	
2012	Apr.-Dec.	Run VI (2 M)	62492–81560
	Dec.	Special Runs for systematic Studies	81566–82489
2015		Detector NIM paper published [4]	
		2010’s Run IV R_π^{exp} analysis [5]	
2018		Massive neutrino in $\pi^+ \rightarrow e^+\nu_e$ spectrum, all datasets [11]	
Ongoing		Massive Neutrino search $\pi \rightarrow \mu\nu$ in target (B3)	
		$\pi \rightarrow e\nu M$ search [120]	
		Direct muon capture in Zirconium [17]	
		Detector’s energy response	
		Final R_π^{exp} publication (short version)	
		Final R_π^{exp} publication (long version)	

Chapter 4

Analysis

4.1 Variable Extraction and Calibration

4.1.1 Run Selection

The 2012 data-set range goes from run #62000 to 82000, a total of ~ 20000 runs. The Midas (Section 3.4.3) log was checked for any DAQ system related errors, and high-voltage wire-chamber planes trips. Run durations outside the normal range were excluded; the type of excluded runs were periods with no beam, pure cosmic rays data taking periods, or special beam test conditions. Additionally, the electronic run logs were manually inspected to exclude bad runs due to DAQ errors, rack temperature outside working conditions, or any other special condition not appropriate for the analysis. After the run selection, there are 13211 good runs available for analysis. For the 2011 and 2010 data-set, the suggested lists were taken from [18] and [5] respectively.

4.1.2 Scintillators

Each scintillator has four PMTs read out (except T2 read out with wavelength-shifting fibers) by the 500-MHz COPPER system (See Section 3.4.2). Before the extraction of charge and pulse-height variables, the pedestal is subtracted from the waveforms. The gain correction factors for each ADC pair are monitored and adjusted on a run-by-run basis based on pulse-height from the physics trigger signals. The pedestal procedure is calculated as the mean of the distribution of the first three samples of the waveforms over an entire run, thus is insensitive to random signal pulses that may change the level of baseline for each ADC (COPPER and VF48).

To automatically correct the gain against fluctuations, beam pion (for B1 and B2) and beam muon (for B3 and T1) energy distributions are used on a run-by-run basis. The strong position dependence of signals in T2 because of the Wavelength Shifting Fibers (WLSF) geometry calls for gain calibration

4.1. Variable Extraction and Calibration

with decay positrons from the $\pi^+ \rightarrow \mu^+ \nu_\mu \rightarrow e^+ \nu_e \bar{\nu}_\mu$ decay chain selecting their entrance with WC3. The energy calibration is based on the amount of energy deposited by a minimum ionizing particle along the known amount of material of each scintillator (Polyvinyltolulene) using the PDG value and verified with an MC (Geant4) including the corresponding Birks' correction [121]. All scintillators had the Birks' correction applied. The light yield per path length is generally proportional to the the energy loss per path length: $dY/dx \propto dE/dx$. Birks law takes into account saturation and quenching effects with the correction

$$dY/dx = S \frac{dE/dx}{1 + k_B(dE/dx)}, \quad (4.1)$$

where S is the scintillation efficiency and k_B the Birks constant (which is typically of the order 10^{-1} – 10^{-2} mm/MeV).

Figure 4.1 shows charge variables with different integration times. The “prompt” signal and timing is defined as a “simultaneous” coincidence between B1 and T1. The main trigger²⁵ enables the pion-decay-positron signal “PIE” when there is a coincidence between the pion signal timing t_{π^+} and positron timing t_{e^+} within an 840 ns window, specifically 300 ns before and 540 ns after prompt. The COPPER system records $-6.4 \mu\text{s}$ prior and $1.35 \mu\text{s}$ after the prompt, for a total integration window of $7.75 \mu\text{s}$. The main trigger timing $t = -1.35 \mu\text{s}$ corresponds to the pion timing $t_{\pi^+} = 0 \mu\text{s}$ or prompt time. The signal-region is defined within $-3.5 < t < 0 \mu\text{s}$, and the pre-region (pileup detection) from $-7.75 < t < -3.5 \mu\text{s}$.

The number of hits in each region (NSig, NPre) were identified by a hit-finding algorithm based on the highest point before a drop. In the signal-region, the charge $Q[i]$ of each hit is obtained by integrating the pulse between -20 and $+20$ ns around the pulse peak; nominally in target B3 a $\pi^+ \rightarrow \mu^+ \nu_\mu \rightarrow e^+ \nu_e \bar{\nu}_\mu$ decay $Q[i=0]$ is a pion, $Q[i=1]$ a muon and $Q[i=2]$ a positron. Similarly, wider integration windows are available as $Qw[i]$ with -20 ns to $+80$ ns and $Qww[i]$ with -20 ns to $+600$ ns around the pulse peak. Additionally, $Qfull[i]$ is integrated in the whole 7.75 ns window. The time of the peak point (t), the pulse height of the peak point (PH), and the charge deposits (Q , Qw , and Qww) were recorded as array variables. For example, if three hits (NSig = 3) were found in the signal region, the time, pulse height, and charge deposit were respectively stored as $t[3] = \{t_{0th}$,

²⁵Section 3.4.1

4.1. Variable Extraction and Calibration

t_{1st}, t_{2nd} , $PH[3] = \{PH_{0th}, PH_{1st}, PH_{2nd}\}$, and $Q[3] = \{Q_{0th}, Q_{1st}, Q_{2nd}\}$. In the pre-region, the charge $Pre.Q[i]$ variable stores the pulse between -20 and $+20$ ns around the peak and $Pre.Qw[i]$ similarly stores a pulse between -20 and $+80$ ns. The pre-region charge variables ($Pre.Q$, $Pre.Qw$), their peak point times and pulse heights were also stored in the array.

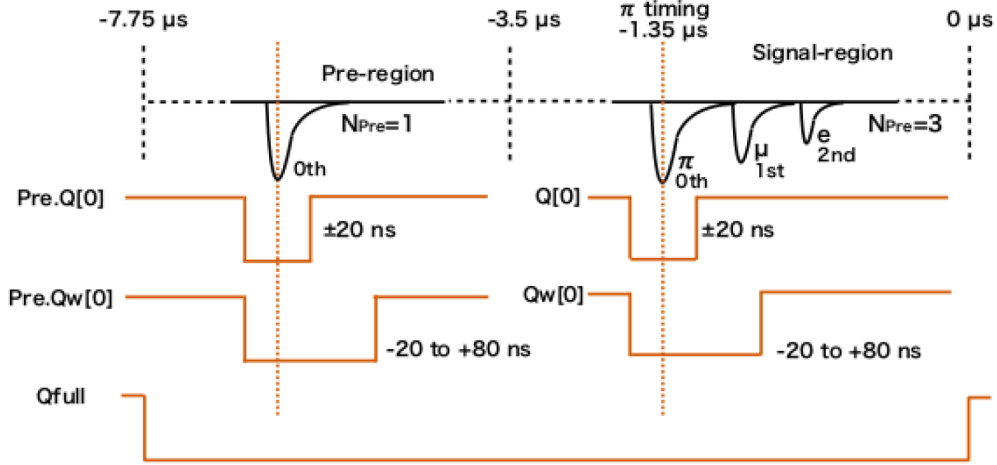


Figure 4.1: COPPER's signals timing. Image from [18].

4.1.3 Silicon Detectors and Calorimeter

The VF48 was used for the silicon detectors, Bina, and CsI crystals, integrating typically -300 ns to 540 ns ($\sim 1 \mu s$ window) with respect to prompt. The COPPER pedestal methodology was used for VF48, but different integration ranges were used: Q : $t_{hit} - 5 < t < t_{hit} + 5$ samples, Qw : $t_{hit} - 10 < t < t_{hit} + 10$ samples, and Qww : $t_{hit} - 10 < t < t_{hit} + 25$ samples. Hits are identified by a hit finding algorithm; the charge, pulse height, and time are recorded for each hit. The number of samples recorded by the VF48 is different for each detector: 40 (666 ns), 40 (1333 ns), and 70 (1162 ns) samples for the CsI, Bina, and silicon channels, respectively. Information on the charge deposited before (Q_{pre} : $t_{hit} - 15 < t < t_{hit} - 5$ samples) and after (Q_{pos} : $t_{hit} + 5 < t < t_{hit} + 15$ samples) the pulse is also stored in the tree.

Silicon Detectors

The extraction of the charge deposited and the position of the hit in the silicon is more complex owing to the charge division circuit. Hits on adjacent strips are clustered. For each cluster, the two strips with the highest charge (Q: $t_{hit} - 128 < t < t_{hit} + 128$ ns) are tagged (they will be called “high-strips” in the rest of this thesis). Amplitudes of the two high strips are compared to estimate the position of the hit with a resolution of $\sim 95 \mu\text{m}$.²⁶ The time of the hit is the average of the time recorded in the high strips weighted by their respective charge. The number and size (how many strips were hit) of clusters are also recorded.

A calibration pulser was connected to the amplifiers of all silicon detector channels. Run by run, a correction factor is calculated from the pulser taking a specific run as a reference. In total, 288 correction factors corresponding to all the silicon detector channels are calculated every run. This calibration procedure corrects only changes in the amplification electronics and is therefore not sensitive to changes in the silicon detector itself. The energy scale calibration is expected to change because of temperature fluctuations, voltage fluctuations, or degradation in the silicon due to radiation damage. Voltages and temperatures in the area were recorded for every run in order to make corrections off-line if needed. Such residual fluctuations could be identified and corrected during the offline analysis. The energy calibration is based on the amount of energy deposited in the “high-strips” by a minimum ionizing particle traversing a silicon wafer. As for other detectors, this energy calibration factor has been calculated from PDG data and checked against MC predictions.

NaI(Tl) Crystal “Bina”

Bina uses the same pedestal procedure as COPPER’s scintillators. For every event, hits found within the $1 \mu\text{s}$ window around prompt are fitted for all 19 NaI PMTs. The amplitude, time, χ^2 , and the value of the fitted pedestal are recorded in the tree. The energy in Bina for all years was calibrated by using long charge-integrated variable Q_{ww} and the pulse-height (PH) from VF48 in order to reduce the pileup effect. The energy calibration in Bina is based on the total energy deposited in the detectors downstream

²⁶ This resolution is reached if at least two strips are fired. It corresponds to the resolution on the readout strip ($1.28\text{mm}/\sqrt{12}$) divided by four. If only one strip is hit, the resolution is $1.28\text{mm}/\sqrt{12}=0.37 \text{ mm}$.

of the target by the $\pi^+ \rightarrow e^+\nu_e$ events. The total energy should be equal to 70.3 MeV: the positron kinetic energy is 69.3 MeV, plus the 0.511 MeV mass of the positron and 0.511 MeV mass of the electron with which the positron is annihilated. The energies recorded by S3, T1, and T2 amount to ~ 2.5 MeV, while the mean energy deposited in the target (~ 1 MeV) and in the front aluminum face (0.22 MeV) of Bina are obtained from MC (dependent on average pion stopping position). The sum of all these energies is used to fix the energy calibration for the NaI(Tl) calorimeter. As for other detectors, this energy calibration factor has been calculated from PDG data and checked against MC predictions.

CsI Crystals

As the CsI crystals are not directly exposed to the beam, they are calibrated using cosmic rays. A cosmic ray trigger was operated in parallel to the other triggers, enabling a new calibration every 20 runs (needed to collect sufficient statistics). The peak due to the passage of minimum ionizing cosmic muons in each crystal was compared with the energy deposit predicted by a simulation made using the CRY package [32]. CRY generated cosmic-rays at the altitude (sea level) and at the geographic coordinates of the PIENU experiment, and the resulting particles are injected in the Geant4 simulation of the detectors. The charge deposit in each CsI crystal was converted to the energy deposit by using a multiplicative factor f

$$f = \frac{\Delta E_{\text{MC}}^{\text{Cosmic}}}{\Delta Q_{\text{Data}}^{\text{Cosmic}}} \frac{Q_{\text{Data}}[\text{Xe}_{\text{ref}}]}{Q_{\text{Data}}[\text{Xe}]}, \quad (4.2)$$

where $\Delta E_{\text{MC}}^{\text{Cosmic}}$ is the peak position of the energy deposit obtained by MC, $\Delta Q_{\text{Data}}^{\text{Cosmic}}$ is the charge deposit from the Cosmic trigger, $Q_{\text{Data}}[\text{Xe}_{\text{ref}}]$ is the reference charge of Xe lamp (Section 3.4.1) trigger event, and $Q_{\text{Data}}[\text{Xe}]$ is the charge of Xe lamp trigger event for each run. The precision of the energy calibration in the calorimeters (NaI plus CsI) is at least 0.1 MeV. In Figure 4.2, the comparison between simulation and the data is shown. The peak positions vary up to 20% in energy with the position of the crystal in the detector, but they are well emulated in MC. The energy deposited by minimum ionizing particles in a single CsI crystal is ~ 50 MeV.

4.1.4 Wire-chambers

The VT48 was used for the wire chambers. The VT48 records hits in a window of $-3.6 \mu\text{s}$ and $+4.4 \mu\text{s}$ with respect to pion timing t_{π^+} . For the

4.1. Variable Extraction and Calibration

wire chambers, the wire hit indicates the spatial position of the hit. If two adjacent WC wires are fired the track is assumed to have passed in between the two wires giving a twice better position resolution. Based on the Wire Chamber (or Silicon detector) channels that fired, a track is reconstructed. In case of multiple hits for WCs (or clusters for Silicon), tracks are constructed with all possible combinations of hits. For each reconstructed track, the χ^2 , number of degrees of freedom, residuals, and position information are stored.

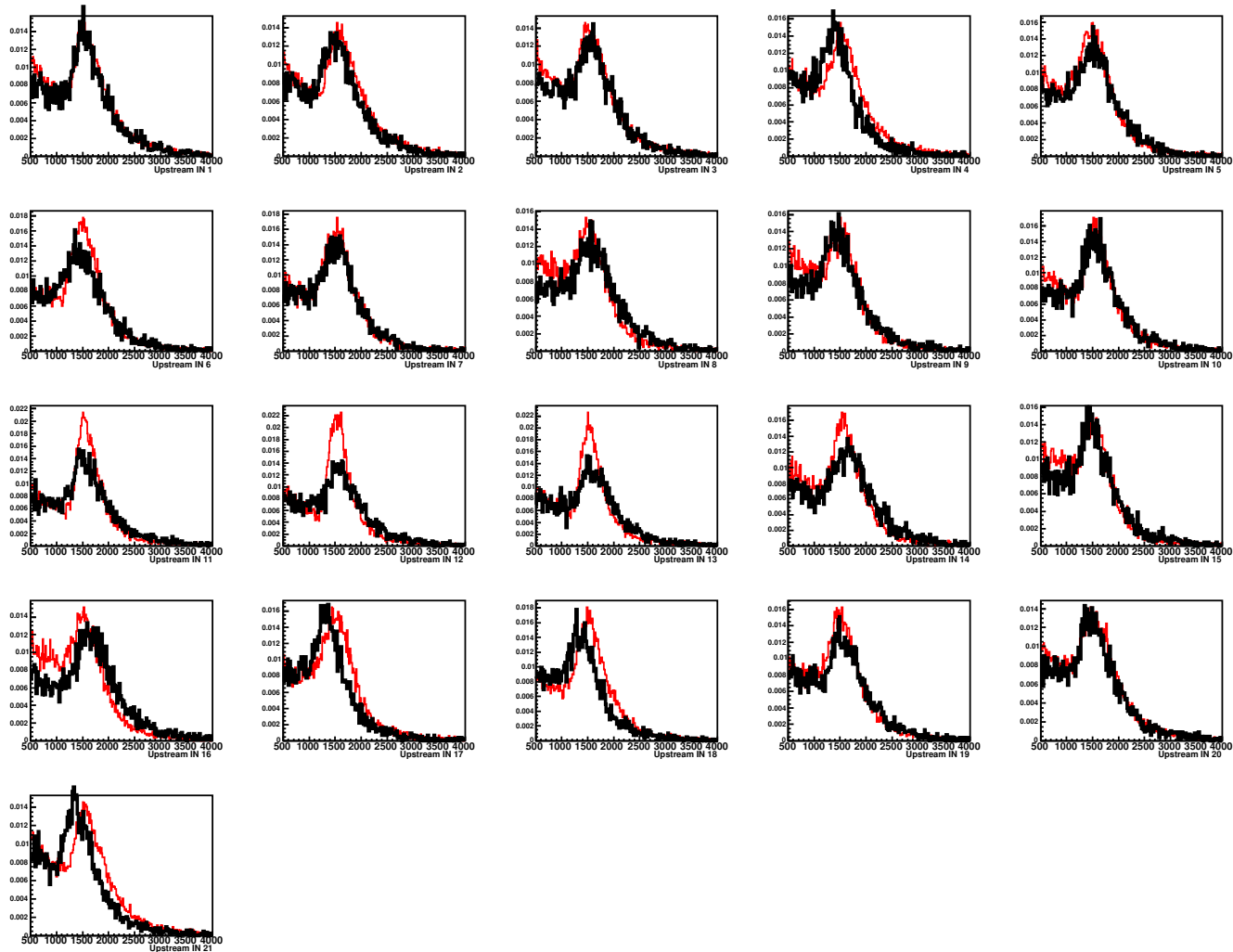


Figure 4.2: Comparison prior to calibration between data (black) taken with the cosmic ray trigger and an MC simulation (red) based on the CRY [32] simulation package. The spectra are relative to the 21 crystals in the inner-upstream CsI ring. Horizontal axes are ADC counts. The peak positions vary up to 20% in energy with the position of the crystal in the detector, but they are well emulated in MC. The energy deposited by minimum ionizing particles in a single CsI crystal is about 50 MeV. Image from [18].

4.2 Event Selection

In the following section the cuts are briefly described. In general, a pion needs to be selected from the incoming beam using scintillators for energy identification and wire chambers to restrict acceptance. Positron tracks are calculated from pions decaying in the center of target which then enter the calorimeter. Such events are checked for trigger timing consistency and pileup effects among the detector's scintillators, wire-chambers, silicon-detectors, and calorimeters. A summary of the selection cuts is presented at the end of this section (Section 4.2.5) accompanied by a cut flow shown in Table 4.1.

4.2.1 Pion Identification

Energy and Beam Acceptance. The energy information in B1 and B2 from the incoming beam identifies the type of particle. Figure 4.3(a) and 4.3(b) show the four main distributions from left to right, positrons, muons, pions, and two pions arriving at the same time. An energy cut window requirement is made for both B1 and B2 to select pions, 3.8 to 5.2 MeV, and 2.0 to 3.1 MeV, as shown in Figure 4.3(a) and 4.3(b). The 5.2 MeV energy cut in B1 trims out pileup and represents a non-negligible systematic uncertainty according to Ref. [122]. In the results Chapter 7, such uncertainty is tabulated in the final error budget for the final branching ratio. Furthermore, cuts on the beam profile in WC1 and WC2 (Figure 4.4) were applied to remove particles (mostly positrons and muons) from the beam halo. Beam profile restrictions for the 2012 dataset are -23 to 19 mm on the x-axis and -17 to 19 mm on the y-axis for both WC1 and WC2. The latter is a run dependent cut (see Table B.2).

Pileup in Scintillators. The waveforms digitized by COPPER in the plastic scintillators were used for reconstructing timing, studying energy deposits, and detecting the presence of multiple pulses generated by different particles (pileup). In principle, to reject pileup events, only single pulse (or "hit") events should be accepted, but we also need to account for the presence of additional pulses in the waveforms owing to optical reflections and electronic noise. The condition to reject only true pileup in B1, B2, and T1 was that each scintillator was required to have one hit in the signal

4.2. Event Selection

region is at least one PMT as follows,

$$\begin{aligned}
 & \{(N_{\text{Sig}}^{\text{B1.1}} = 1) \cup (N_{\text{Sig}}^{\text{B1.2}} = 1) \cup (N_{\text{Sig}}^{\text{B1.3}} = 1) \cup (N_{\text{Sig}}^{\text{B1.4}} = 1)\} \cap \\
 & \{(N_{\text{Sig}}^{\text{B2.1}} = 1) \cup (N_{\text{Sig}}^{\text{B2.2}} = 1) \cup (N_{\text{Sig}}^{\text{B2.3}} = 1) \cup (N_{\text{Sig}}^{\text{B2.4}} = 1)\} \cap \\
 & \{(N_{\text{Sig}}^{\text{T1.1}} = 1) \cup (N_{\text{Sig}}^{\text{T1.2}} = 1) \cup (N_{\text{Sig}}^{\text{T1.3}} = 1) \cup (N_{\text{Sig}}^{\text{T1.4}} = 1)\}. \quad (4.3)
 \end{aligned}$$

Where $N_{\text{Sig}}^{\text{B1.1}}$ stands for the number of hits for the first of four PMTs in scintillator B1 in the signal region (Figure 4.1), similarly for B2 and T1. On the other hand, requiring one hit on all PMTs gave an unacceptable number of signal events rejected with such tight requirements. Target B3 presents multiple hits from the decay of the pions; therefore, no hit requirements were made. The number of hits in T2 scintillator were not inspected since there is a position and energy dependence associated to the optic-fiber detector topology.

There are pulses in B1 and B2 that are too close in time to each other; thus, a hit-based pile-up rejection scheme would not work properly. Pile-up can be rejected using the ratio between the charge pulse area Q measured in a short time ($[-20, 20]$ ns) window over another one Q_w with longer integration time ($[-20, 80]$ ns). To optimize the beam pile-up rejection, the required condition was $0.75 \leq Q/Q_w \leq 1.05$ for each of B1 PMTs (Figure 4.5(a)) and $0.75 \leq Q/Q_w \leq 0.97$ for B2. The decay time variable is obtained with the time difference between B1 and T1. The time in B1 or T1 is calculated as the average of the time of the four PMTs. The time is extracted from a waveform fit. As all the PMTs are used, we require all B1 channels to have a good χ^2 to eliminate cases in which two pulses are very close to one another and therefore not detected as multiple hits by the hit finding algorithm.

B1 Timing and Trigger Consistency. The time consistency for the pion-signal (B1-B2-B3 coincidence) is verified by looping over all the hits of the B1 PMT. Figure 4.5(b) shows the trigger consistency cut window for a specific run period²⁷ with $-4399 \leq (\text{B1.Time} - \text{pion.trigger}) \leq -4380$ ns, time distribution without cuts in black, time distribution with all cuts in red (excluding cut being discussed), and cut values are shown in blue, with no normalization.

²⁷ Cut values for all run periods are available in Table B.2.

4.2.2 Pileup T1, and T2

Pion Trigger and T1-T2 Sync. For every PMT of T1, all the pulses are inspected. Only the pulse (for each PMT) that is closest to the pion-signal time is fitted. This requirement ensures that the fitted pulse is the first seen by the PMT after a pion stops in target B3. Events with additional pulses before the fitted one are discarded. Additionally, a coincidence of ± 20 ns is required between the T1 and T2 counters.

Proton Cut. The pion beam nuclear interaction with target B3 produced protons with energies up to ~ 100 MeV; this is due to pion absorption by nuclei. Since their large energy was deposited along the downstream counters, they were easily identified from the minimum-ionizing positrons. Figure 4.6 show the correlation between the minimum dE/dx in the downstream counters (S3, T1, T2) and energy deposit in the NaI. Because decay positrons could undergo Bhabha scattering in the counters to produce rather higher energy deposit, the minimum dE/dx in three counters was used for proton rejection.

T1 Prompt Time. Hits in T1 were rejected if an event was found to be in time coincidence (± 2 ns) with the pion time. This cut mostly kills beam positrons, muons, and protons. This cut also helps in rejecting events where an old-muon²⁸ decays from the target B3 and hits T1. Beam particles may open T1's gate waiting for the decay positron to effectively blind T1, thus the positron from the signal can be missed. This cut eliminates both prompt $\pi^+ \rightarrow \mu^+ \nu_\mu \rightarrow e^+ \nu_e \bar{\nu}_\mu$ and $\pi^+ \rightarrow e^+ \nu_e$ events. Such events are not required in our time spectrum analysis (Chapter 5) used to extract the branching ratio.

T1 Fake Pileup. For T1 pile-up, the one hit requirement in at least one of the PMTs does not address the presence of reflections and fluctuations (fake hits), raising the concern of preferentially rejecting earlier decay events and thus biasing the branching ratio. The identification of fake hits was achieved via the ratio of the full integrated charge over the pulse height of the triggering hit as a function of the pulse height. Figure 4.7 shows the fake hits and real pileup separated clearly into two bands; by only rejecting events where the ratio of integrated charge to pulse height is higher than the red line, only real pileup will be removed, and events with fake pileup will

²⁸Muon from a previous event.

be preserved. This protects the event being rejected by the pileup cut from depending on the positron decay time. The possible energy dependence was $< 1 \times 10^{-8}$ branching ratio units [7], thus negligible for our current level of precision.

4.2.3 Early Time

Pre-Pileup. The Pre-Pileup (Pre-PU) cut normally rejects events in a $-6.4 \mu\text{s}$ to $-2.2 \mu\text{s}$ window before the arrival of the pion ($-7.7 \mu\text{s}$ to $-3.5 \mu\text{s}$ window with respect to trigger time, see Figure 4.1). The implementation requires no hits in the Pre-PU window for all PMTs: B1, B2, and B3 to exclude pion pre-pileup, and T1 and T2 for positron pre-pileup.

Beam Muons and Multiple Pions. There is a muon selection logic for B1 connected to a special VT48 channel readout. With this signal, the presence of an extra incoming beam muon can be inspected up to $16 \mu\text{s}$ before the pion trigger signal. Events with hits in this channel up to $8.5 \mu\text{s}$ before and $1.25 \mu\text{s}$ after prompt were rejected, keeping events in a $0.1 \mu\text{s}$ window centered at prompt. These beam muons stop in T2, decay and may enter the calorimeter's time window. In this case, the energy they deposit in the calorimeters is added to that of the decay positron creating a pile-up event in the calorimeter, which was not detected by the scintillator counters. This cut reduces by a factor of two the level of beam muons. Similarly for the 2012 data taking period, in order to detect out-of-time pion structures there was an additional pion selection logic for B1 connected to a special VT48 channel readout. The same cut range was applied.

False Triggers. Certain processes (e.g., nuclear interactions, range straggling, low momentum pions, decays in flight) can enable false triggers. False triggers [123] occur, e.g., if the pion traverses only B1, and B2, and then stops before B3. Then, the target (B3) is fired by a positron from a pion which decayed upstream of the target. Such triggers can be seen by observing the event pulse time difference between the target and B1 ($B3_t - B1_t$) versus the total charge in the target ($B3_{charge}$). The false trigger cut space can be seen in Figure 4.8. The main distribution of positrons making false trigger can be separated at $(B3_t - B1_t) > 4 \text{ ns}$ and $B3_{charge} < 200 \text{ ADC}$ counts ($\sim 3 \text{ MeV}$). The three bands on the left represent pileup related to 4, 3, and 2 PMTs at 450, 300, and 150 ADC counts (10, 4, and 2 MeV), respectively. The main red blob in the center represents good beam pion events stopping in the center of target B3 and the blob's downward tail represents

pions barely entering B3, while the upward tail is pions stopping at the end of B3. This tail, and some of the few false positron triggers that go below 4 ns overlap representing a non-negligible systematic uncertainty according to Ref. [124]. In the results Chapter 7, such uncertainty is tabulated in the final error budget for final branching ratio.

4.2.4 Calorimeter Acceptance Radius A_R

To ensure that the decay positrons hit all the downstream counters, using track reconstruction (Section 3.2.6) the calorimeter acceptance radius (A_R) was defined using the radial distribution from the middle of WC3 (see Eq. 3.3 for definition). Thus, A_R is referred to as the track radius from WC3. Such a cut is shown in Figure 4.9 together with the acceptance cut. It is important to note that in order to keep Bhabha scattering events, there are no requirements on the number of tracks in the downstream tracker. For events with multiple tracks, the track with the minimum distance from the center is taken. The measured energy spectrum is highly dependent on the angle at which decay positrons enter the calorimeter assembly (NaI(Tl) and CsI). The choice of the cutoff value for A_R results from a trade-off between the increasing systematic error as the low energy tail of the $\pi^+ \rightarrow e^+\nu_e$ decay increases and the decreasing statistical error as more events are included at higher values of A_R . Considering these arguments, the radial cut was found²⁹ to be $A_R = 40$ mm for the full analysis using all combined data sets. Ideally we would like to make the acceptance as large as possible, but setting to $A_R = 90$ mm increases the systematic uncertainty in the branching ratio by a factor of 5 and almost a factor of 2 in the total (syst. and stat.) combined error.

4.2.5 Summary of Event Selection

About 90% of the events were removed by the event selection cuts discussed above. The major cuts were the pion energy cuts, the pileup cuts, and the pre pileup cuts. The combination of those three cuts rejected about 70% of all the events. The acceptance radius cut after all other cuts removed about 20% more of all the events. After all cuts have been applied we have about 11% at $A_R = 60$ mm or 7% at $A_R = 40$ mm left of all the events, which are used for the time spectrum analysis described in Chapter 5. Table 4.1 is a summary of the event selection cuts with the ratio of event

²⁹To be discussed in Chapter 7

reduction. A comprehensive list of cuts used for the analysis is shown in Table B.1, and run dependent cut values listed on Table B.2.

4.3 Energy Spectra

Only events that passed all cuts are selected to produce the histograms used for the time spectrum fit (Chapter 5) to obtain the blinded raw branching ratio R_{raw} . In nominal data-taking settings, a pion beam stops near the center of the target B3. The $\pi^+ \rightarrow \mu^+ \nu_\mu \rightarrow e^+ \nu_e \bar{\nu}_\mu$ energy spectrum is below 52 MeV. Events are separated in “high-energy” (HE), for which the sum of the energy deposited in the NaI and CsI ($E_{NaI+CsI}$) is larger than 52 MeV, and “low-energy” (LE) region otherwise ($E_{NaI+CsI} \leq 52$ MeV). The LE and HE threshold is called E_{cut} . The energy spectrum is shown in Figure 4.10 as the sum of NaI and CsI energies for all physics triggers combined after all event selection cuts. The branching ratio vs. E_{cut} was shown to be stable within ± 3 MeV (Chapter 7). The $\pi^+ \rightarrow e^+ \nu_e$ events are emitted isotropically from the center of the target with a kinetic energy of 69.3 MeV about 8 cm upstream of the front of the calorimeter’s face. Most positrons (about $E_{e^+} > 5$ MeV) traverse half of B3, and all of S3, T1, T2 and Bina’s aluminum face. Positrons on the beam’s axis traverse plastic scintillator, silicon, and aluminum depositing ~ 3.7 MeV on average. Thus the $\pi^+ \rightarrow e^+ \nu_e$ peak is at ~ 65.6 MeV as shown in Figure 4.10.

4.3.1 Monte-Carlo Calibration

A crucial step for the analysis was to match the scintillators and calorimeter’s energy scale to Monte-Carlo (MC). The sum of calibrated energies from scintillators B1, B2, B3, and the silicon detectors S1, and S2 is the Pion’s Total Energy,

$$E_{tot} = E_{B1} + E_{B2} + E_{B3} + E_{S1} + E_{S2}, \quad (4.4)$$

shown in Figure 4.11(a). As explained earlier in Section 1.2, the $\pi^+ \rightarrow e^+ \nu_e$ and $\pi^+ \rightarrow \mu^+ \nu_\mu \rightarrow e^+ \nu_e \bar{\nu}_\mu$ energy distribution peaks are about ~ 4 MeV apart. The black line represents the E_{tot} ’s “suppressed” energy, since a set of specialized cuts are used to enhance $\pi^+ \rightarrow e^+ \nu_e$ events, and suppress $\pi^+ \rightarrow \mu^+ \nu_\mu \rightarrow e^+ \nu_e \bar{\nu}_\mu$ i.e., Early triggers, $7 < \text{positron time} < 42$ ns, and kink angle (Section 3.2.6) < 12 degrees. The blue line is the opposite, E_{tot} ’s “late” energy uses Prescale triggers, and positron times greater than 100 ns. The red line represents MC’s E_{tot} ’s energy for $\pi^+ \rightarrow e^+ \nu_e$ events only. Figure 4.11(b) represents the “suppressed”, “late”, and MC’s $\pi^+ \rightarrow e^+ \nu_e$ energy

4.3. Energy Spectra

Table 4.1: Cut flow for event selection. The number of events before cuts is 2.027×10^9 for the 2012 dataset.

Cut	Events after each cut (%)
Blinding §1.3 and Integrity §3.4.2	99.33
Physics Triggers §3.4.1	99.25
Pion Energy §4.2.1	75.69
WC1,2's Halo	72.30
B1,2 PU	55.55
B1 Waveform	55.42
B1 prompt	55.40
Proton	54.07
TrCons	53.87
T1prompt	52.15
T1 fake PU	50.28
T1 Waveform	50.06
PionTrig §4.2.2	49.62
T1-T2 sync	49.59
Pre-PU §4.2.3	35.54
Beam Muons	34.30
Two Pions ^a	33.22
FalseTrig	33.20
Acceptance radius (A_R)§4.2.4	
$A_R = 60mm$	11.35
$A_R = 40mm$	6.60

^a Two pion detection only available for 2012 dataset.

4.3. Energy Spectra

in the calorimeter (Bina+CsI). Figure 4.11(c) both the “suppressed”, and “late” spectrum are shown with an extra cut in the pion total energy to select $\pi^+ \rightarrow e^+\nu_e$ events i.e., ± 1 MeV around E_{tot} ’s $\pi^+ \rightarrow e^+\nu_e$ peak. For all subplots in Figure 4.11, the “suppressed” (black) energy distribution was normalized to the MC’s (red) $\pi^+ \rightarrow e^+\nu_e$ peak, for proper comparison such normalization was used for the “late” (blue) spectrum as well. The alignment coefficient between data and MC was done to match the $\pi^+ \rightarrow e^+\nu_e$ peak in the calorimeter (Bina+CsI). The resultant alignment uncertainty of the scintillators’ total energy and the calorimeter’s peak to MC is below the calibration’s uncertainty 0.1 MeV.

Furthermore, also crucial is to check the alignment between the calorimeter’s energy for all physics triggers for all years (databases). All physics triggers were added together in the calorimeter energy distribution shown in Figure 4.10. In contrast, Figure 4.12, Figure 4.13, and Figure 4.14 show the calorimeter’s energy for *Early*, *Prescale*, and *TIGC* (physics) triggers (Section 3.4.1) respectively. For both, the integrated-charge (Q) and pulse-height (PH) calorimeter (NaI+CsI) based variables defined as,

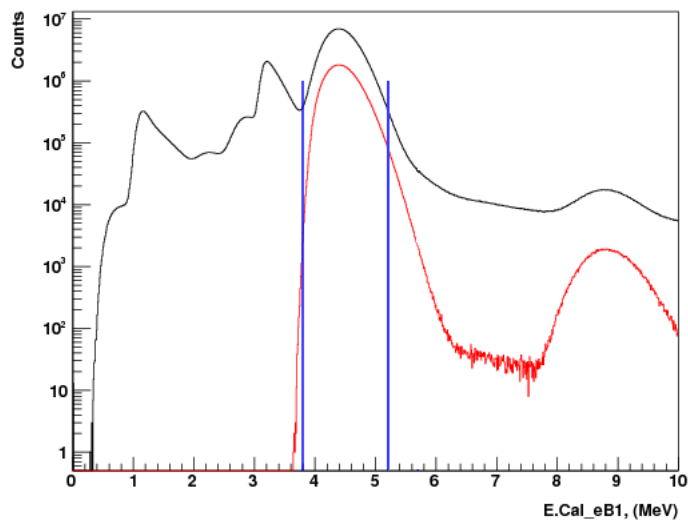
$$E_{\text{NaI+CsI}}^{\text{Q}} = E_{\text{NaI}}^{\text{Q}} C_{\text{NaI}}^{\text{Q}} + \sum_{i=1}^{97} E_{\text{CsI},i}^{\text{Q}} \quad (4.5)$$

and

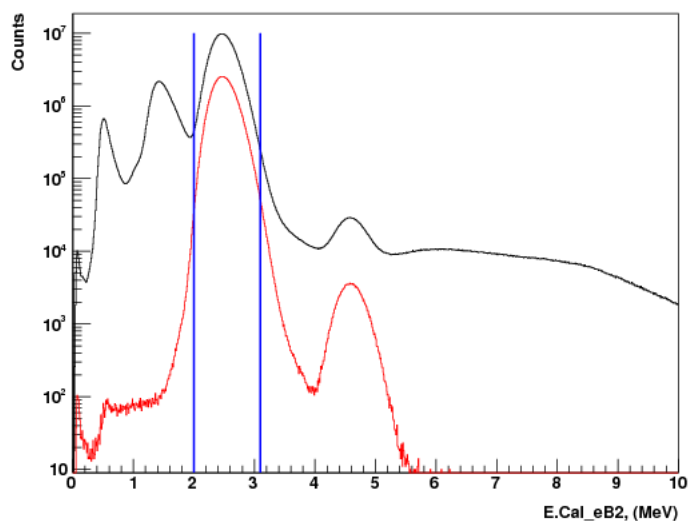
$$E_{\text{NaI+CsI}}^{\text{PH}} = E_{\text{NaI}}^{\text{PH}} C_{\text{NaI}}^{\text{PH}} + \sum_{i=1}^{97} E_{\text{CsI},i}^{\text{Q}}, \quad (4.6)$$

respectively. Where $E_{\text{NaI}}^{\text{Q}}$ is the calibrated NaI calorimeter Q based variable, $C_{\text{NaI}}^{\text{Q}}$ is the corresponding MC alignment coefficient, and $E_{\text{CsI},i}^{\text{Q}}$ is the calibrated energy of the i -th CsI crystal. Similarly goes for the PH superscripts. Note the CsI Q based energies are used in both cases. The coefficients can be found in the Appendices, in Table B.2. In each plot from Figure 4.12, 4.13, and 4.14 for the 2010, 2011, and 2012 energies were normalized to $\pi^+ \rightarrow e^+\nu_e$ peak. There is an improvement in pileup reduction on the PH versions over the Q, specifically fewer events in the low signal-to-background ratio region around E_{cut} (50 to 55 MeV), and after the $\pi^+ \rightarrow e^+\nu_e$ peak. Figure ??(bottom) shows how the different thresholds in the TIGC trigger across the datasets defines the “rising energy” between 30 and 45 MeV.

4.3. Energy Spectra



(a) Cut values for B1 scintillator



(b) Cut values for B2 scintillator

Figure 4.3: Pion Cut: B1 (top) and B2 (bottom) energy distribution without cuts in black, energy distribution with all cuts in red (excluding cut being discussed), and cut values are shown in blue. No normalization. Peaks from left to right in B1 (and B2): positrons at 1.1 (0.5), muons at 3.2 (1.5), pions at 4.5 (2.5), and two pions arriving at the same time at 9 (4.7) MeV.

4.3. Energy Spectra

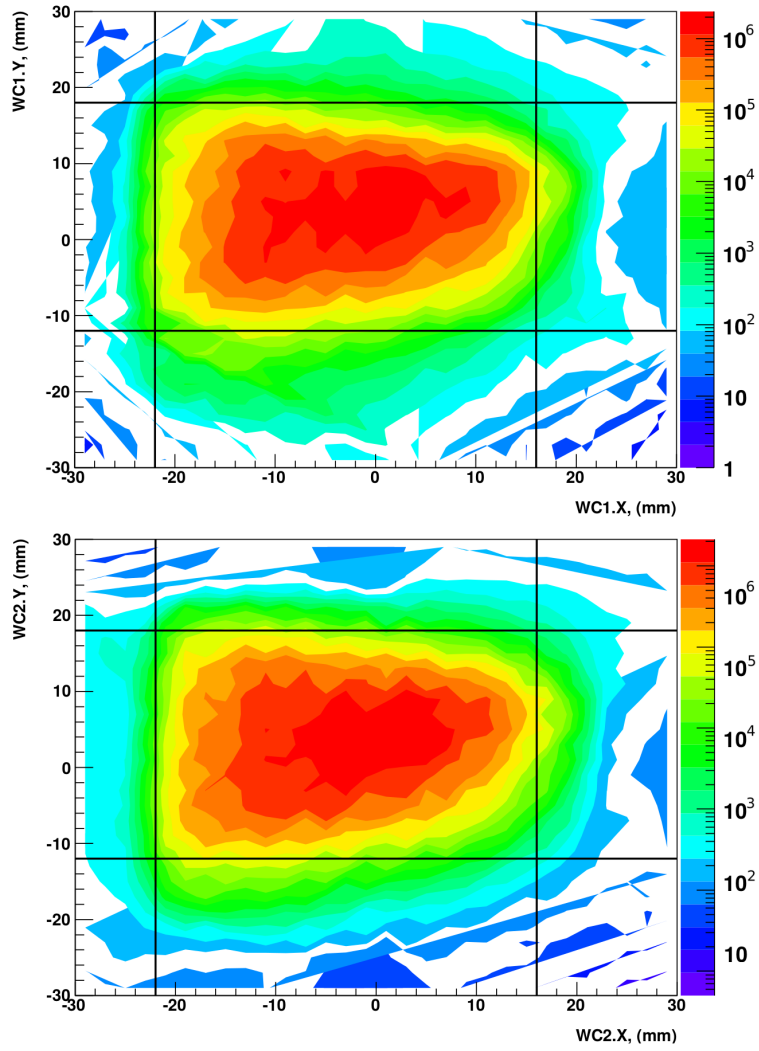
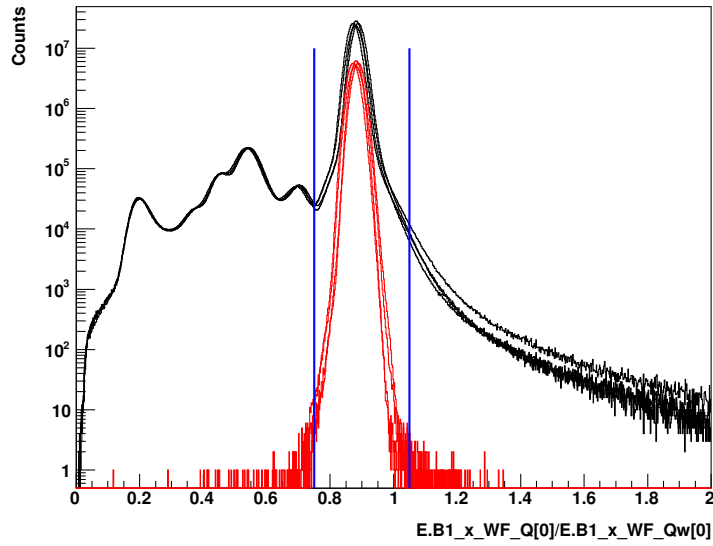
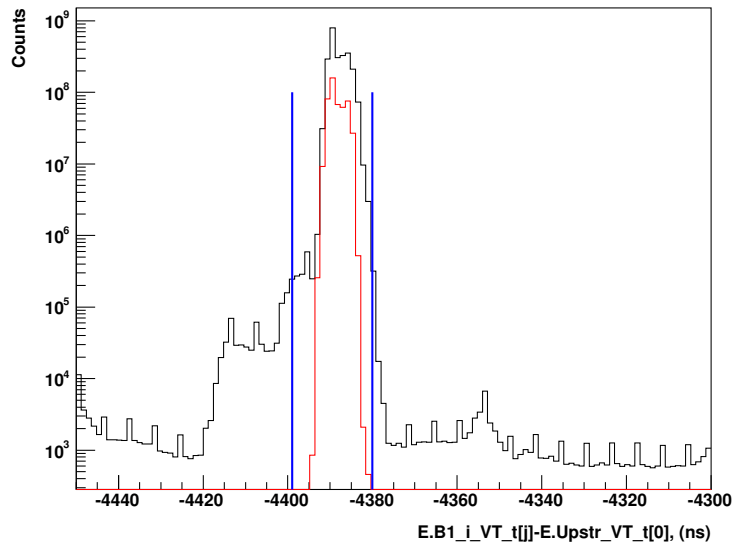


Figure 4.4: Acceptance for WC1 (top) and WC2 (bottom); beam halo is removed.

4.3. Energy Spectra



(a) B1 short gate / wide gate integrated charge



(b) B1 time minus pion trigger timing

Figure 4.5: Charge (top) and time (bottom) distributions without cuts in black, distributions with all cuts in red (excluding cut being discussed), cut values are shown in blue. No normalization. Top: B1 short gate/wide gate integrated charge. Bottom: Trigger Consistency Cut.

4.3. Energy Spectra

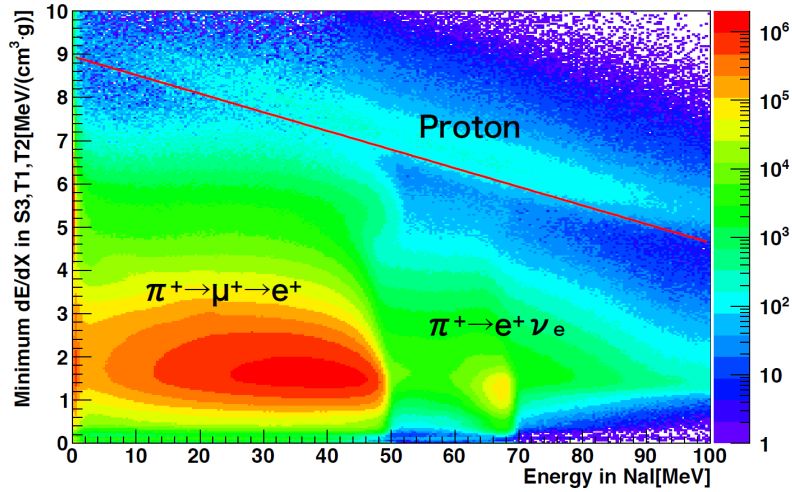


Figure 4.6: Energy in the NaI (Bina) versus minimum energy loss in the downstream counters. Protons are above the red line indicating the cut position. The red blob represents $\pi^+ \rightarrow \mu^+ \nu_\mu \rightarrow e^+ \nu_e \bar{\nu}_\mu$ events and the small yellow blob $\pi^+ \rightarrow e^+ \nu_e$ events.

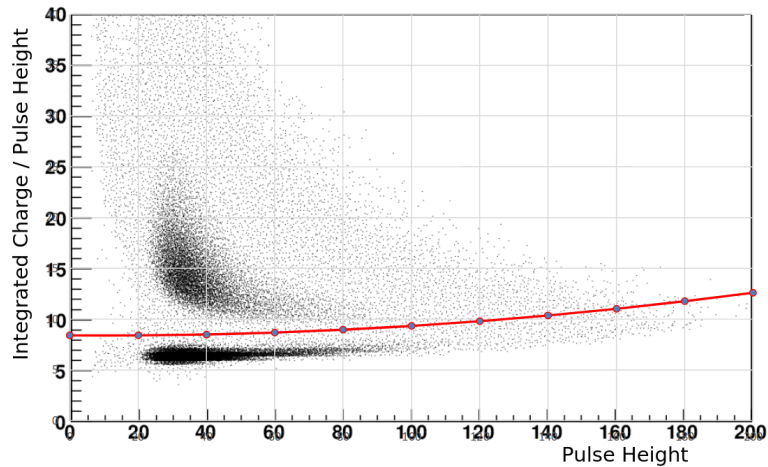


Figure 4.7: The ratio of integrated charge in the T1 PMTs to the fitted pulse height as a function of the fitted pulse height. The red line indicates the cut used to separate real pileup (above) from pileup due to fake hits (below).

4.3. Energy Spectra

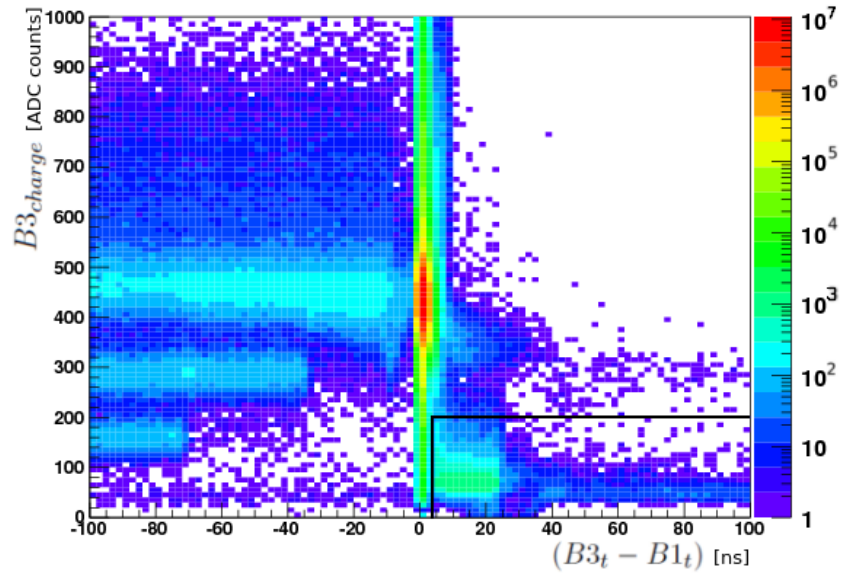


Figure 4.8: The false trigger cut rejects events when positrons from π DIF make false trigger. The positrons are found at $(B3_t - B1_t) > 4$ ns and $B3_{charge} < 200$ ADC counts (~ 3 MeV). The three bands on the left represent pileup related to 4, 3, and 2 PMTs at 450, 300, and 150 ADC counts (10, 4, and 2 MeV), respectively. The main red blob in the center represents good beam pion events stopping in the center of target B3 and the blob's downward tail represents pions barely entering B3, while the upward tail is pions stopping at the end of B3.

4.3. Energy Spectra

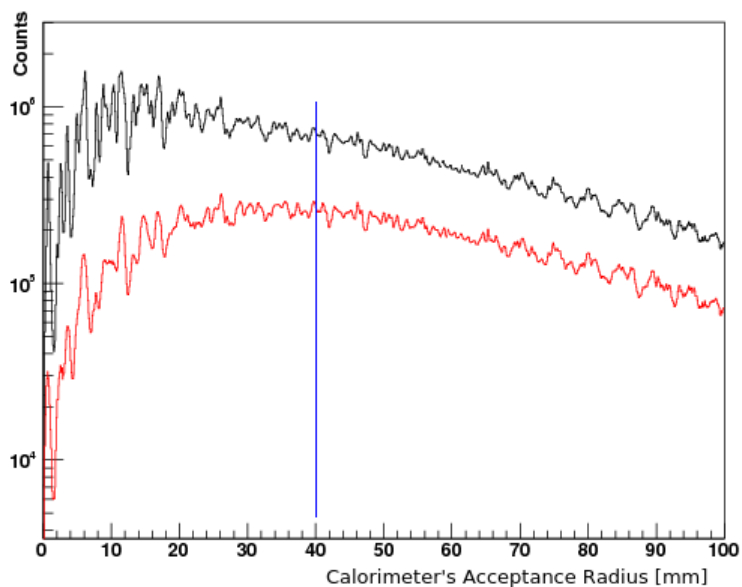


Figure 4.9: Calorimeter's acceptance radius (A_R) cut distribution without cuts in black, radius distribution with all cuts in red (excluding the cut being discussed), and cut value is shown in blue.

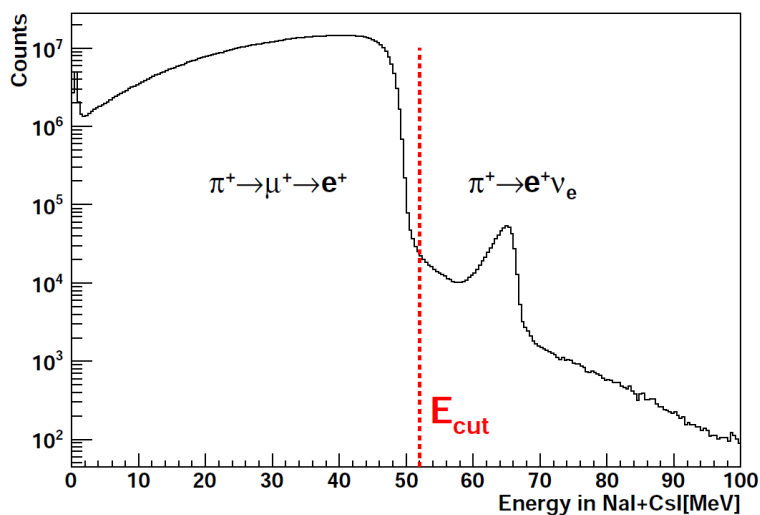


Figure 4.10: Combined energy spectrum of the NaI plus CsI detectors for the 2012 dataset. The vertical red line indicates $E_{cut} = 52$ MeV. The composition of the high energy tail beyond 70 MeV is due to pileup events.

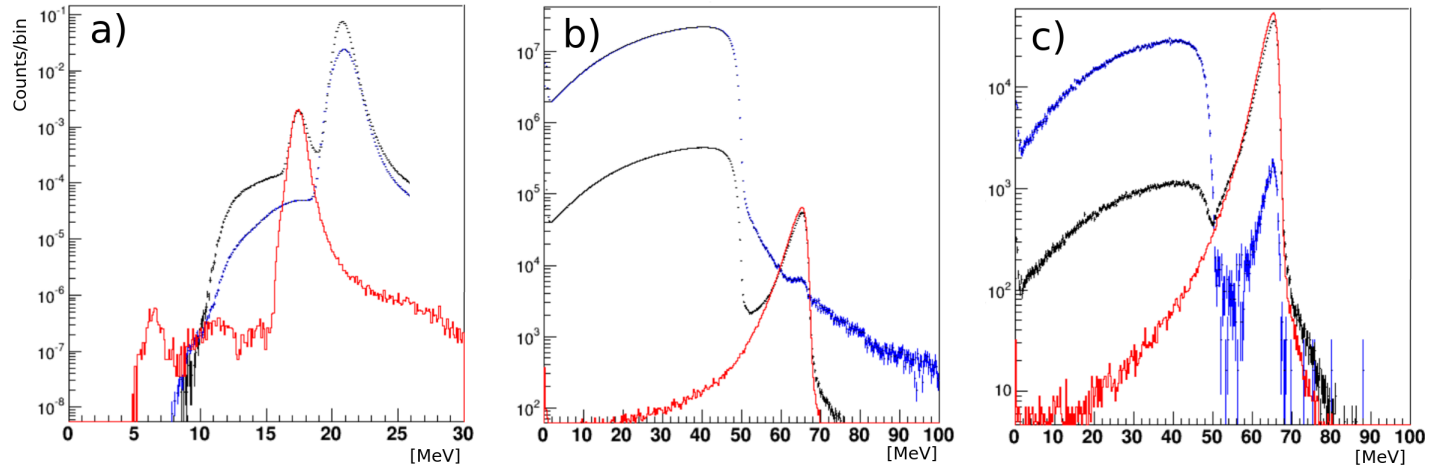


Figure 4.11: Alignment of scintillators and calorimeter’s energy scales to Monte-Carlo. a) E_{tot} ’s “suppressed” energy in black, E_{tot} ’s “late” energy in blue, and MC’s E_{tot} energy for $\pi^+ \rightarrow e^+\nu_e$ events only in red. b) Calorimeter’s “suppressed” energy in black, “late” energy in blue, and MC’s for $\pi^+ \rightarrow e^+\nu_e$ events only in red. c) Calorimeter’s “suppressed” and “late” energy with E_{tot} ’s cut to select $\pi^+ \rightarrow e^+\nu_e$ events. For all subplots the “suppressed” (black) energy distribution was normalized to the MC’s (red) $\pi^+ \rightarrow e^+\nu_e$ peak, for proper comparison such normalization was used for the “late” (blue) spectrum as well. The alignment coefficient between data and MC was done to match the $\pi^+ \rightarrow e^+\nu_e$ peak in the calorimeter (Bina+CsI). The resultant alignment uncertainty of the scintillators’ total energy and the calorimeter’s peak to MC is below the calibration’s uncertainty 0.1 MeV. The normalization for each subplot (left, center, and right) was done independently, thus the vertical axes between subplots don’t match, i.e., E_{tot} ’s plots were normalized to 1, and the calorimeter’s energies to the total number of events.

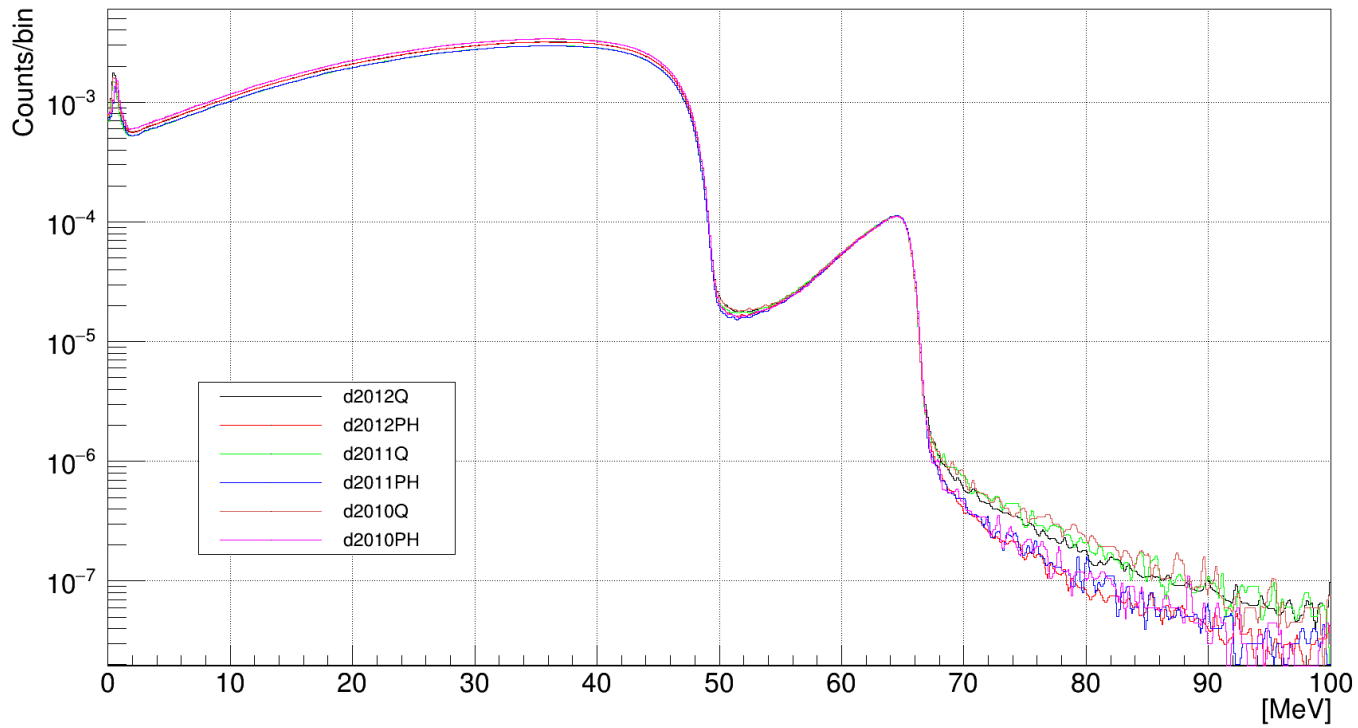


Figure 4.12: Early triggers for all years including charge-integration (Q) and pulse-height (PH) calorimeter (NaI+CaI) energy based variables defined by Eq. 4.5 and Eq. 4.6. The three datasets (2010, 2011, and 2012) make two groups in the tail above 70 MeV, in such region all three PH versions have less pileup than the Q version group.

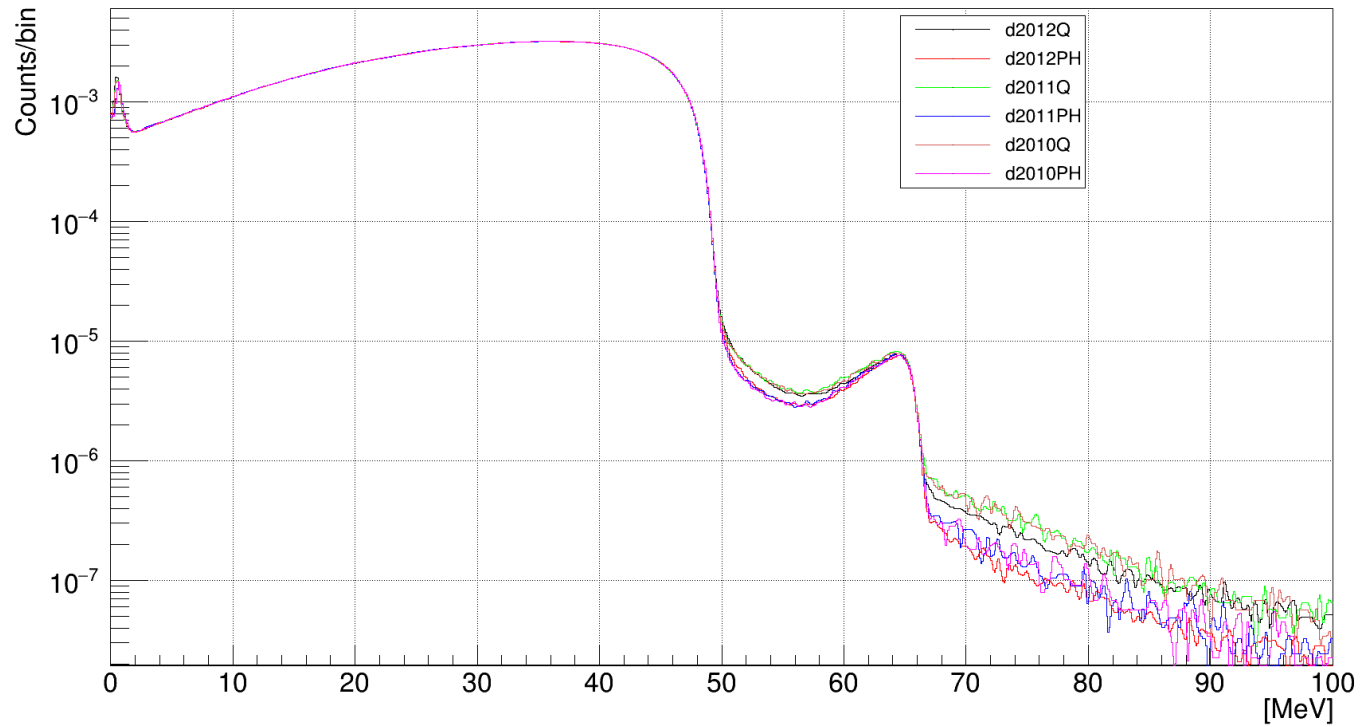


Figure 4.13: Prescale triggers for all years including charge-integration (Q) and pulse-height (PH) calorimeter (NaI+CaI) energy based variables defined by Eq. 4.5 and Eq. 4.6. The three datasets (2010, 2011, and 2012) make two groups in the tail above 70 MeV, in such region all three PH versions have less pileup than the Q version group.

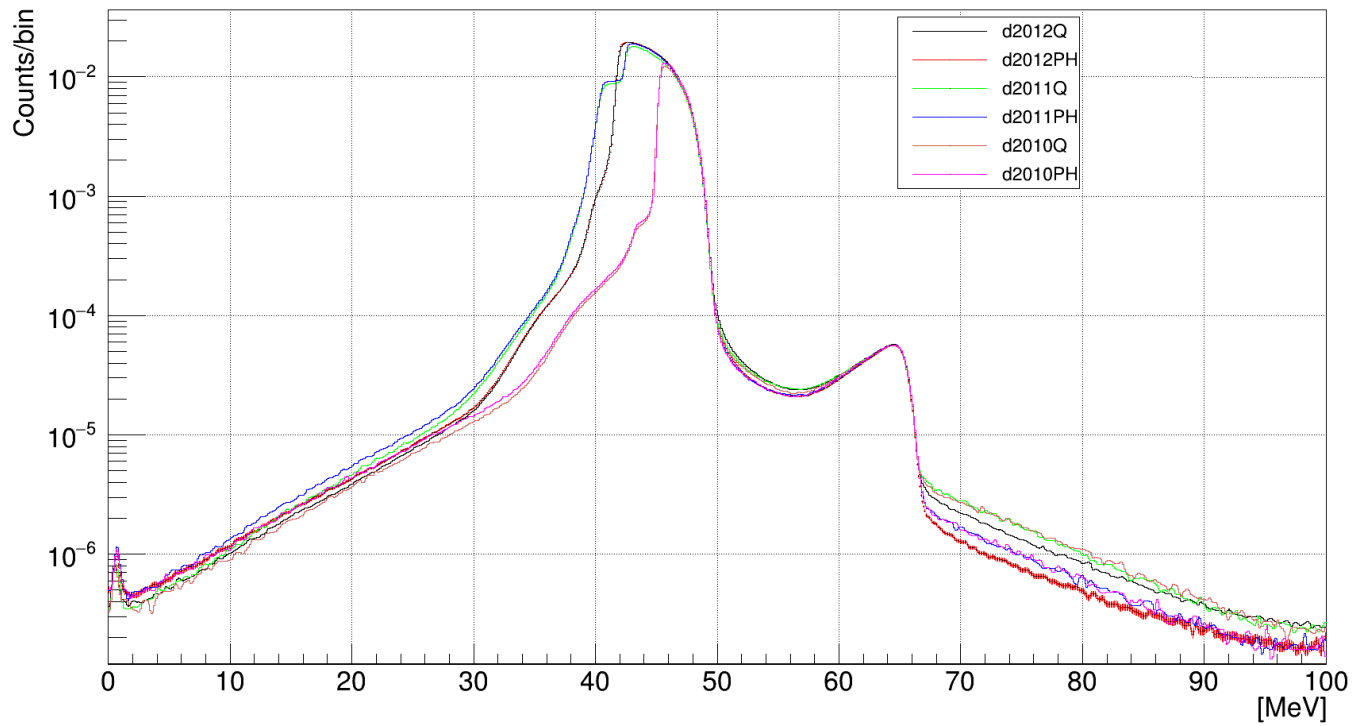


Figure 4.14: TIGC triggers for all years including charge-integration (Q) and pulse-height (PH) calorimeter (NaI+CaI) energy based variables defined by Eq. 4.5 and Eq. 4.6. The three datasets (2010, 2011, and 2012) make two groups in the tail above 70 MeV, in such region all three PH versions have less pileup than the Q version group.

Chapter 5

Time Spectrum

5.1 Construction

The time spectrum (TS) is constructed from the decay pion time and positron time. The time was obtained on the basis of the time difference average of fitted pulses between B1 and T1 scintillators for all four PMTs as follows,

$$T_{\text{pos}} = \frac{1}{4} \sum_{i=1}^4 (t_{\text{Fit}}^{\text{T1},i} - t_{\text{Fit}}^{\text{B1},i}). \quad (5.1)$$

Where $t_{\text{Fit}}^{\text{B1},i}$ refers to the time from B1's first fitted pulse from the i -th PMT, similarly for T1 with $t_{\text{Fit}}^{\text{T1},i}$. Signals, background functions, and processes to construct the TS will be explained later in this chapter. Only “physics” trigger (TIGC, Early or Prescale) events (section 3.4.1) are included and all “calibration” triggers (cosmic, beam-positrons, Xe-lamp) are omitted. Only events which passed all cuts are selected to produce the histograms used for the TS fit to obtain the blinded raw branching ratio. Events are separated into “high-energy” (HE), for which the sum of the energy deposited in the NaI and CsI ($E_{\text{NaI+CsI}}$) is larger than 52 MeV, and “low-energy” (LE) ($E_{\text{NaI+CsI}} \leq 52$ MeV) regions. The LE and HE threshold is called E_{cut} nominally at 52 MeV.

The LE and HE region are associated with $\pi^+ \rightarrow \mu^+ \nu_\mu \rightarrow e^+ \nu_e \bar{\nu}_\mu$ and $\pi^+ \rightarrow e^+ \nu_e$ decays respectively. Events in the HE region were required to have fired the *TIGC* trigger. Events in the LE region were triggered by the *Early* trigger in the early time window while the rest of the events were *Prescale*. Outside the boundaries of the early time region, the Prescale events were added 16 times³⁰ to the spectrum and the errors on each time bin were scaled accordingly. The Early trigger efficiency was $\sim 100\%$. There were no distortions observed at the boundary between Prescaled and Early

³⁰ As $\pi^+ \rightarrow \mu^+ \nu_\mu \rightarrow e^+ \nu_e \bar{\nu}_\mu$ events dominate $\pi^+ \rightarrow e^+ \nu_e$ events by four orders of magnitude, a *Prescale* unbiased trigger selects only 1/16 of PIE events. See Section 3.4.1 for more detail.

5.1. Construction

events. The addition of Early to the Prescaled events reduced the statistical uncertainty in the raw branching ratio by 10%. The implementation to generate the TS for LE and HE events is the Algorithm 5.1.

```

1 | bool Bhigh = E.Cal_eBina * C[year] + E.Cal_CsISum >= 52;
2 | bool Blow  = E.Cal_eBina * C[year] + E.Cal_CsISum < 52;
3 |
4 | // tsH and tsL: time spectrum histogram for HE and LE
5 | if( ALLCUTS ){ //apply all standard cuts
6 |
7 |     // Fill histogram with E.Tpos (T1-time - B1-time)
8 |     // TIGC trigger ONLY in HE,
9 |     if( Bhigh && E.BinaHTrig_VT_N>0) H.Fill( tsH ,E.Tpos ,1.0 );
10 |    // PreScale (P) and Early (E) trigger ONLY in LE
11 |    if( Blow ){
12 |        if( E.PreScaleTrig_VT_N>0 || E.EarlyTrig_VT_N>0 ){
13 |            if( E.EarlyTrig_VT_N>0) H.Fill( tsL ,E.Tpos ,1.0 );
14 |            else H.Fill( tsL ,E.Tpos ,16.0 ); // if P, weight*16
15 |        }
16 |    }
17 | }

```

Algorithm 5.1: Time Spectra Algorithm.

The charge-integrated (Q) based TS is populated with T_{pos} , using $E_{\text{NaI+Csl}}^{\text{Q}}$ (Eq. 4.5) to distinguish between LE and HE events. On the other hand, the pulse-height (PH) based TS uses $E_{\text{NaI+Csl}}^{\text{PH}}$ (Eq. 4.6). The LE and HE TS are labeled as “tsL” and “tsH” for the 2012 dataset shown in Figure 5.1 and 5.2 respectively. The raw TS with the selected good runs list and only data integrity checked out from the DAQ system is labeled “raw”, orange and black for PH and Q respectively. Level 1 TS with “Pion Identification” plus previous cuts from Section 4.2.1 is labeled “L1”, violet and red for PH and Q. Level 2 TS with “Pileup T1, and T2” plus previous cuts from Section 4.2.2 is labeled “L2”, light-blue and yellow for PH and Q. The final TS with the “Early Time and Acceptance” plus previous cuts from Section 4.2.3 and 4.2.4 is labeled “clean”, dark-green and navy-blue for PH and Q. There is no clear differences between the PH and Q version on the LE TS on the other hand the PH version of the HE TS is clearly less receptive to pile-up. The ~ 44 ns structures in the raw TS are due to beam pileup from the cyclotron’s RF which are eliminated from the analysis with event selection discussed in Section 4.2; therefore they do not affect the branching ratio.

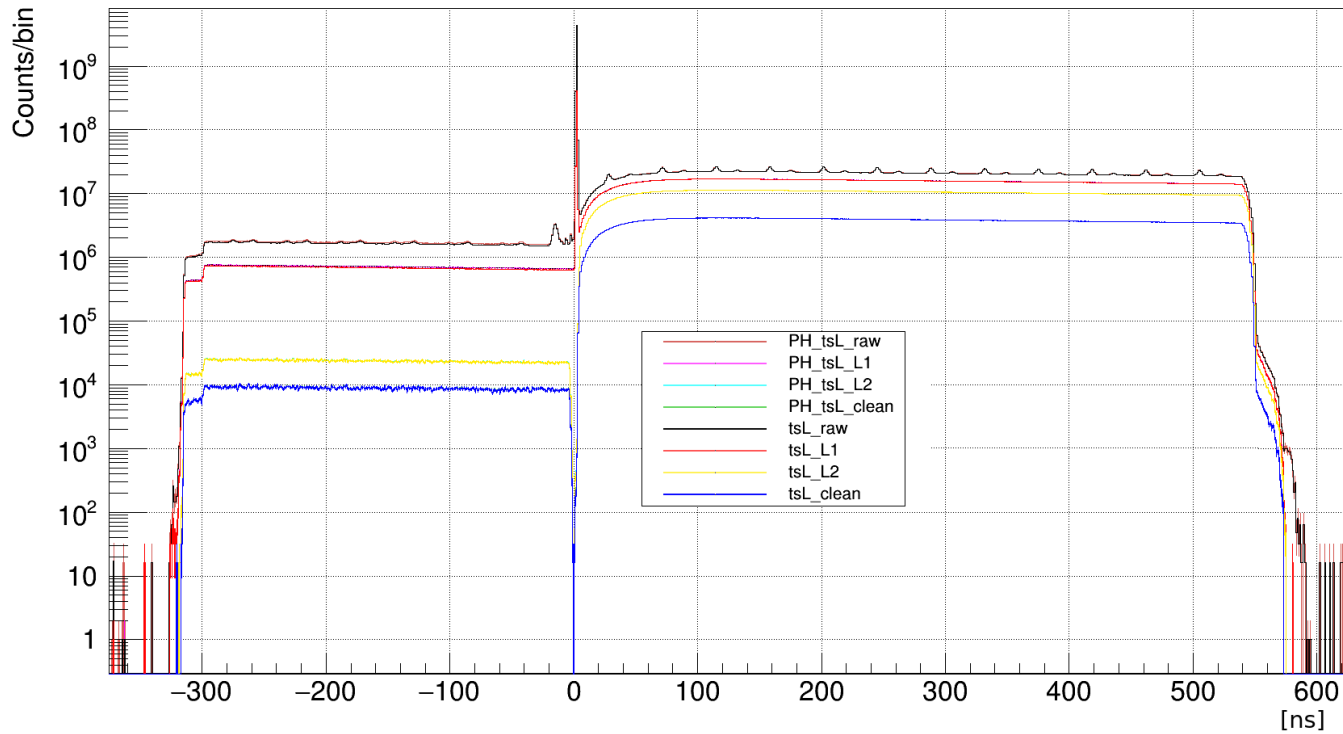


Figure 5.1: 2012 Dataset - Low-Energy (LE) Time-Spectrum (TS), T_{pos} for $E_{\text{NaI+CsI}} < E_{\text{cut}}$: Using the pulse-height “PH” $E_{\text{NaI+CsI}}^{\text{PH}}$ and charge-integrated “Q” $E_{\text{NaI+CsI}}^{\text{Q}}$ calorimeter based variable to construct the LE TS “tsL”. Overlaying TS with different levels of cuts: The “raw” (orange and black) spectrum (no cuts), “L1” (violet and red) with “Pion Identification” cuts, “L2” (light-blue and yellow) with “Pileup T1, and T2” cuts, and the final “clean” (dark-green and navy-blue) TS with “Early Time and Acceptance” (All) cuts. See Section 4.2 for discussion on cuts. The PH and Q versions overlap.

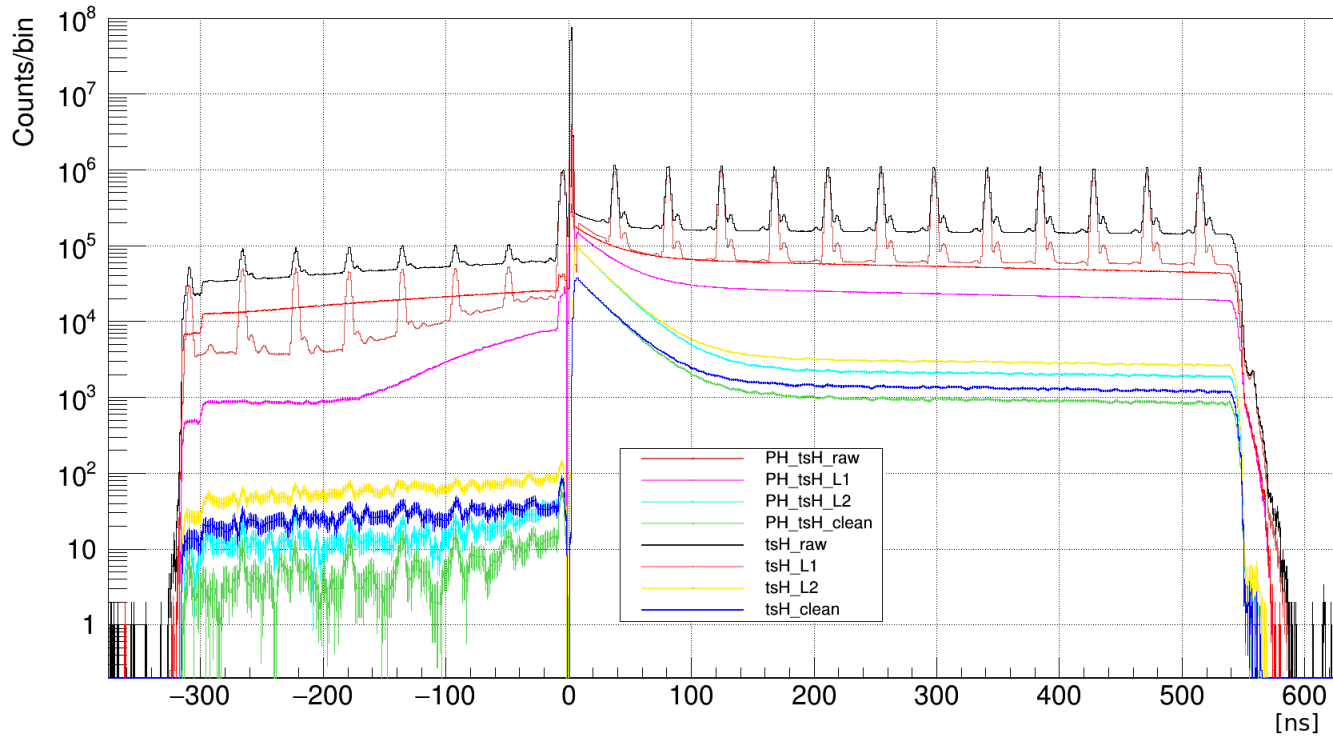


Figure 5.2: 2012 Dataset - High-Energy (HE) Time-Spectrum (TS), T_{pos} for $E_{\text{NaI+CsI}} \geq E_{\text{cut}}$: Using the pulse-height “PH” $E_{\text{NaI+CsI}}^{\text{PH}}$ and charge-integrated “Q” $E_{\text{NaI+CsI}}^{\text{Q}}$ calorimeter based variable to construct the HE TS “tsH”. Overlaying TS with different levels of cuts: The “raw” (orange and black) spectrum (no cuts), “L1” (violet and red) with “Pion Identification” cuts, “L2” (light-blue and yellow) with “Pileup T1, and T2” cuts, and the final “clean” (dark-green and navy-blue) TS with “Early Time and Acceptance” (All) cuts. See Section 4.2 for discussion on cuts. The PH version is shown to be less sensitive to pileup compared to the Q based branching ratio.

5.2 Signal and Background

Prompt events from the HE (Figure 5.2) and LE (Figure 5.1) TS at $t = 0$ ns refers to beam pions (after selection cuts from Section 4.2) stopping in the center of scintillator target B3. The negative time region reflects the level of background in the positive region. Before detailing the fit functions used, we will briefly describe the different signals backgrounds present in each spectrum. Each signal and background will be presented as a probability distribution function and its amplitude. The amplitudes can be either a fixed or a free parameter.

5.2.1 Signals

The low and high energy regions are mostly associated with $\pi^+ \rightarrow \mu^+ \nu_\mu \rightarrow e^+ \nu_e \bar{\nu}_\mu$ and $\pi^+ \rightarrow e^+ \nu_e$ events, respectively. The two-way leakage of events from one region to another will be described later in this chapter. The time probability distribution functions (PDFs) for the signals in the LE and HE time spectra are given by Eq. 5.2 and Eq. 5.3, respectively. Both signals are only valid for positive times,

$$\mathcal{E}_{\pi \rightarrow \mu \rightarrow e}(t) = \frac{\exp(-\frac{t}{\tau_\mu}) - \exp(-\frac{t}{\tau_\pi})}{\tau_\mu - \tau_\pi}, \quad (5.2)$$

$$\mathcal{E}_{\pi \rightarrow e}(t) = \frac{\exp(-\frac{t}{\tau_\pi})}{\tau_\pi}. \quad (5.3)$$

To introduce time resolution effects each signal was convoluted with a Gaussian kernel $\mathcal{G}'(t) = \frac{1}{\sqrt{2\pi\sigma^2}} \exp(-\frac{t^2}{2\sigma^2})$; this technique was used in the previous experiment [25]. The signals with time resolution effects are,

$$\mathcal{E}'_{\pi \rightarrow \mu \rightarrow e}(t, \sigma) = \int_0^\infty \mathcal{E}_{\pi \rightarrow \mu \rightarrow e}(x) \mathcal{G}'(t-x) dx = \frac{\mathcal{R}(t, \sigma, \tau_\mu) - \mathcal{R}(t, \sigma, \tau_\pi)}{2(\tau_\mu - \tau_\pi)} \quad (5.4)$$

$$\mathcal{E}'_{\pi \rightarrow e}(t, \sigma) = \int_0^\infty \mathcal{E}_{\pi \rightarrow e}(x) \mathcal{G}'(t-x) dx = \frac{\mathcal{R}(t, \sigma, \tau_\pi)}{2\tau_\pi}, \quad (5.5)$$

where $\mathcal{E}'_{\pi \rightarrow \mu \rightarrow e}(t, \sigma)$ and $\mathcal{E}'_{\pi \rightarrow e}(t, \sigma)$ are the signals with time resolution σ effects included, term $\mathcal{R}(t, \sigma, \tau) = \exp(\frac{\sigma^2 - 2\tau t}{2\tau^2}) \text{erfc}(\frac{\sigma^2 - \tau t}{\sqrt{2\sigma\tau}})$, and $\text{erfc}(t)$ is the complementary error function.³¹ The time difference between scintillators

³¹ The complementary error function is defined as $\text{erfc}(t) = \frac{2}{\sqrt{\pi}} \int_t^\infty e^{-x^2} dx$.

B1 and T1 used to determine t was measured to have resolution $\sigma = (0.3 \pm 0.1)$ ns. The effects of including the time resolution are further discussed in Section 7.1.

5.2.2 Pion Decay-In-Flight and Muon from Previous Event (Old-muon) in Target B3

Only two backgrounds remain at a non-negligible level in the LE time spectra after all selection cuts: pion decay-in-flight (π DIF) for positive times and old-muons³² in target B3 for positive and negative times. Both have the same probability distribution function as shown in Eq. 5.6.

$$\mathcal{E}_{\mu \rightarrow e}(t) = \frac{\exp(-\frac{t}{\tau_{\mu}})}{\tau_{\mu}}. \quad (5.6)$$

For negative times, the spectrum is mainly old-muons (muon from previous event) coming from beam muons or decayed from beam pions which stopped in the target or surroundings materials. Such beam contribution is replenished every 43 ns thus should be a flat component to the time spectrum TS. However, an early time rejection cut (Section 4.2.3) of $8.5 \mu\text{s}$ before the prompt ($t < 0$) means no beam particles can add to the background, thus the remaining background follows an exponential decay with the muon lifetime. The old-muon component is also contaminating the positive region. For positive times, the spectrum is mainly signal $\pi^+ \rightarrow \mu^+ \nu_{\mu} \rightarrow e^+ \nu_e \bar{\nu}_{\mu}$ events, more specifically π DAR $\rightarrow \mu$ DAR (Section 3.2.6). A non-negligible fraction of π DIF $\rightarrow \mu$ DAR (about 2% of π DAR $\rightarrow \mu$ DAR) is present in the spectrum. This π DIF background starts at $t = 0$ and decays with the muon lifetime. π DIF events are only included in the fit if the decay muon stops before T1, if it stops in T1 or beyond, the event is prompt and thus outside the fitting range.

5.2.3 T1 Double Pulse Resolution.

Following the discussion of the T1 pileup cut from Section 4.2.2, the case when two hits occur within T1's double pulse time resolution is not taken into account; therefore, this should be modeled into the time spectrum fit as a background. Let ΔT be the time for two positrons to pass through T1 sufficiently close together in time, where the waveforms will overlap, and only a single hit is recorded. Case A, defined as $\mathcal{F}_{2A}(t)$ (Eq. 5.7) is when T1

³²A muon from a previous event.

5.2. Signal and Background

is triggered by a positron from an old-muon decay in positive and negative times. This means the real pion gives signal in B1 but an old-muon hits T1 before the true positron. The positron from old-muon is followed only in positive time by a positron from a primary pion event. Such a case is modeled as the product of the old-muon probability distribution function (Eq. 5.6) and the probability that the $\pi^+ \rightarrow \mu^+ \nu_\mu \rightarrow e^+ \nu_e \bar{\nu}_\mu$ positron (Eq. 5.2) will emerge within ΔT :

$$\mathcal{F}_{2A}(t) = \begin{cases} 0 & t < -\Delta T \\ \mathcal{E}_{\mu \rightarrow e}(t) \int_0^{t+\Delta T} \mathcal{E}_{\pi \rightarrow \mu \rightarrow e}(y) dy & -\Delta T < t < 0 \\ \mathcal{E}_{\mu \rightarrow e}(t) \int_t^{t+\Delta T} \mathcal{E}_{\pi \rightarrow \mu \rightarrow e}(y) dy & t > 0. \end{cases} \quad (5.7)$$

Case B, defined as $\mathcal{F}_{2B}(t)$ (Eq. 5.8) is the opposite and is therefore modeled as the product of the $\pi^+ \rightarrow \mu^+ \nu_\mu \rightarrow e^+ \nu_e \bar{\nu}_\mu$ shape and the probability of old-muon decaying within ΔT as follows:

$$\mathcal{F}_{2B}(t) = \begin{cases} 0 & t < 0 \\ \mathcal{E}_{\pi \rightarrow \mu \rightarrow e}(t) \int_t^{t+\Delta T} \mathcal{E}_{\mu \rightarrow e}(y) dy & t > 0. \end{cases} \quad (5.8)$$

ΔT is a fixed value and the extraction procedure is to plot the time difference between the first and second hits for each PMT. Then, each distribution is fitted on the edge to a step function with Gaussian resolution (Eq. 5.9) as shown in Figure 5.3. The average of the four tubes is $\Delta T = 15.7$ ns and the shape with this value is shown in Figure 5.4(a):

$$\frac{1}{2} \left\{ 1 + \operatorname{erf} \left(\frac{t - \Delta T}{\sqrt{2}\sigma} \right) \right\}, \quad (5.9)$$

where $\operatorname{erf}(t)$ is the error function, also called the Gauss error function.³³

³³ The error or Gauss error function is defined as $\operatorname{erf}(t) = \frac{2}{\sqrt{\pi}} \int_0^t e^{-x^2} dx$.

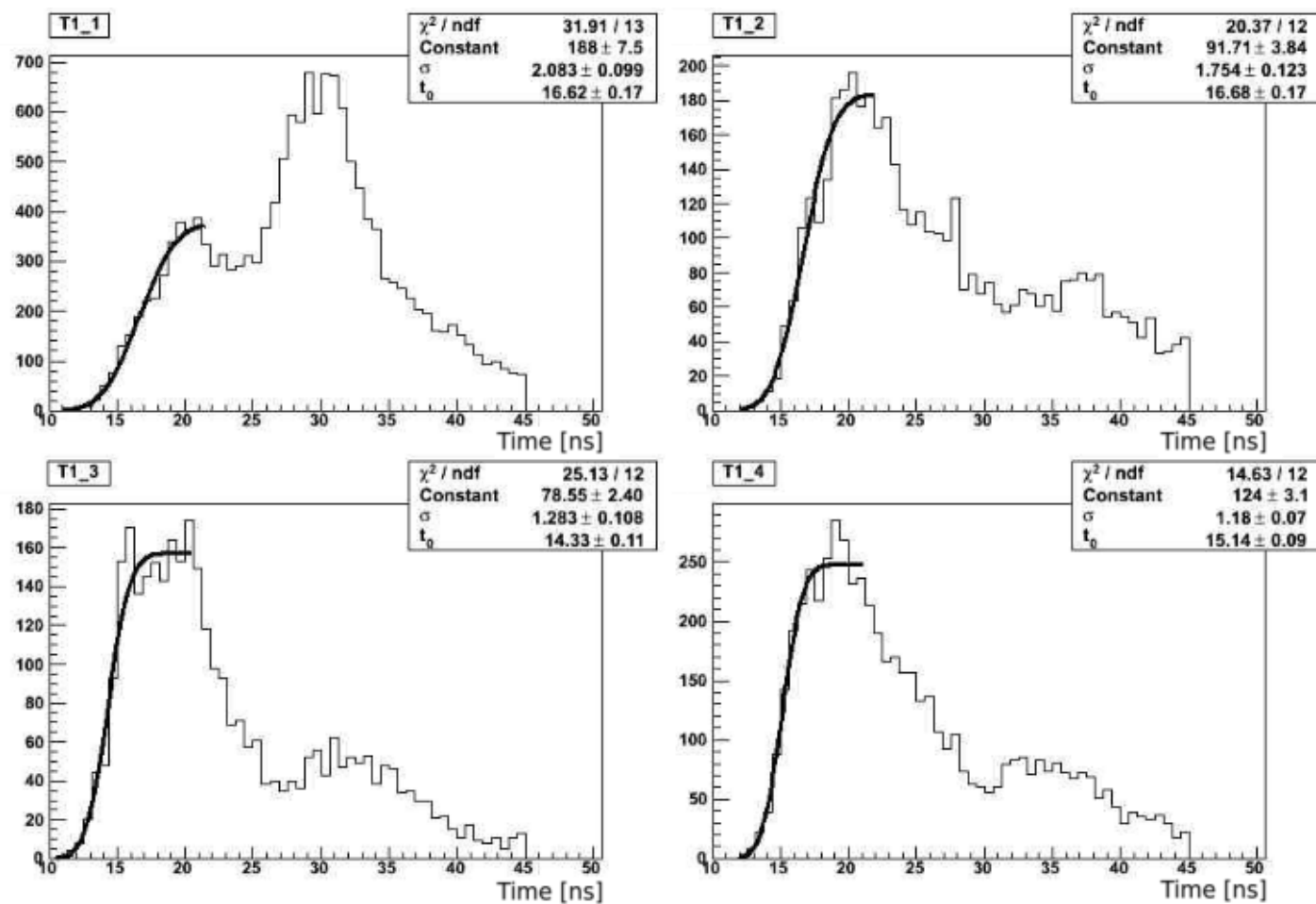
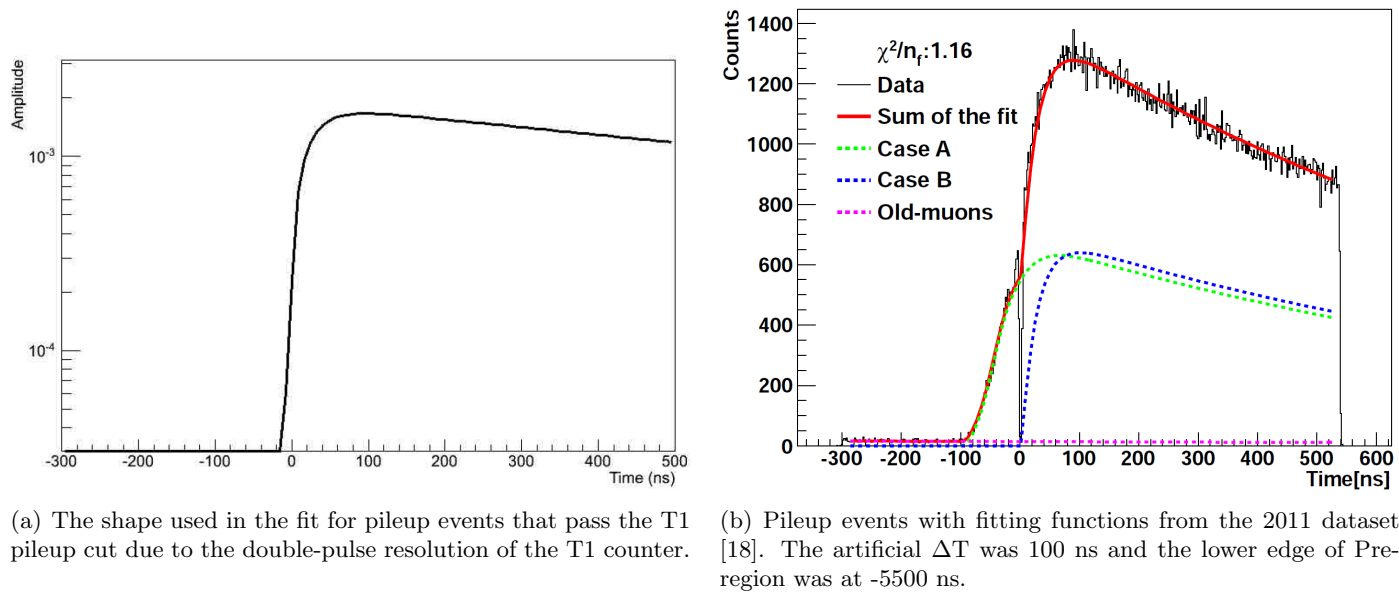


Figure 5.3: The time difference between subsequent hits in each T1 PMT. The leading times are fitted with an error function. The peak around 30 ns is due to an after-pulse hit at a characteristic time after the real hit.

5.2. Signal and Background

The effect of pileup coming within the double pulse resolution time in T1 was estimated by artificially increasing the double pulse resolution time ΔT in the data up to 100 ns. This is done by rejecting events in T1 after initial pulse. Figure 5.4(b) shows the time spectrum of the pileup events for the case of 100 ns double pulse resolution. The time distribution of the pileup events was fitted to the Eqs. 5.7 ($\mathcal{F}_{2A}(t)$), 5.8 ($\mathcal{F}_{2B}(t)$), and 5.6 ($\mathcal{E}_{\mu \rightarrow e}(t)$). The amplitudes of $\mathcal{F}_{2A}(t)$ and $\mathcal{F}_{2B}(t)$ should be the same magnitude, therefore a common amplitude for the fitting parameter was used for the fit, $\mathcal{F}_2(t) = \mathcal{F}_{2A}(t) + \mathcal{F}_{2B}(t)$.

The amplitude (number of events) of $\mathcal{F}_2(t)$ is obtained from the time spectrum pileup events vs. different artificial double pulse time resolutions (ΔT) are shown in Figure 5.5(a,b,c,d, and e) for increasing pre-pileup windows -7500, -6500, -5500, -4500, and -3500 ns from *trigger time* (Figure 4.1) as upper edge respectively and lower edge is fixed at -7750 ns. The plots are fitted to a quadratic curve and the fitted functions evaluated at $\Delta T = 15.7$ ns to extract the amplitude (absolute values of the intercepts) for each pre-pileup window. As shown in Figure 5.5(f), the extracted amplitudes are correlated to the number of old-muon events in the LE region for each pre-pileup window. The points are fitted to a line; the slope (f') and y-intercept (y_f) are obtained. Finally the amplitude (f) for T1 resolution ($\mathcal{F}_2(t)$) is normalized as $f = f'c + y_f$, where c is the number (amplitude) of old-muons events in the LE region (Eq. 5.6) independent from the pre-pileup window. The c amplitude is a free parameter to be found with the time spectrum technique to be discussed in Section 5.3. For the 2012 dataset, the values of f' and y_f were extracted and found to be independent of acceptance radius A_R at $f' = (4.08 \pm 0.22) \times 10^{-4}$ and $y_f = 803$. Such values were used globally for all datasets since the 2012 dataset is the most significant, statistically.



(a) The shape used in the fit for pileup events that pass the T1 pileup cut due to the double-pulse resolution of the T1 counter.

(b) Pileup events with fitting functions from the 2011 dataset [18]. The artificial ΔT was 100 ns and the lower edge of Pre-region was at -5500 ns.

Figure 5.4: a) T1 resolution function $\mathcal{F}_{2A}(t)$ evaluated with $\Delta T = 15.7$ ns. b) T1 resolution pileup events with artificial $\Delta T = 100$ ns.

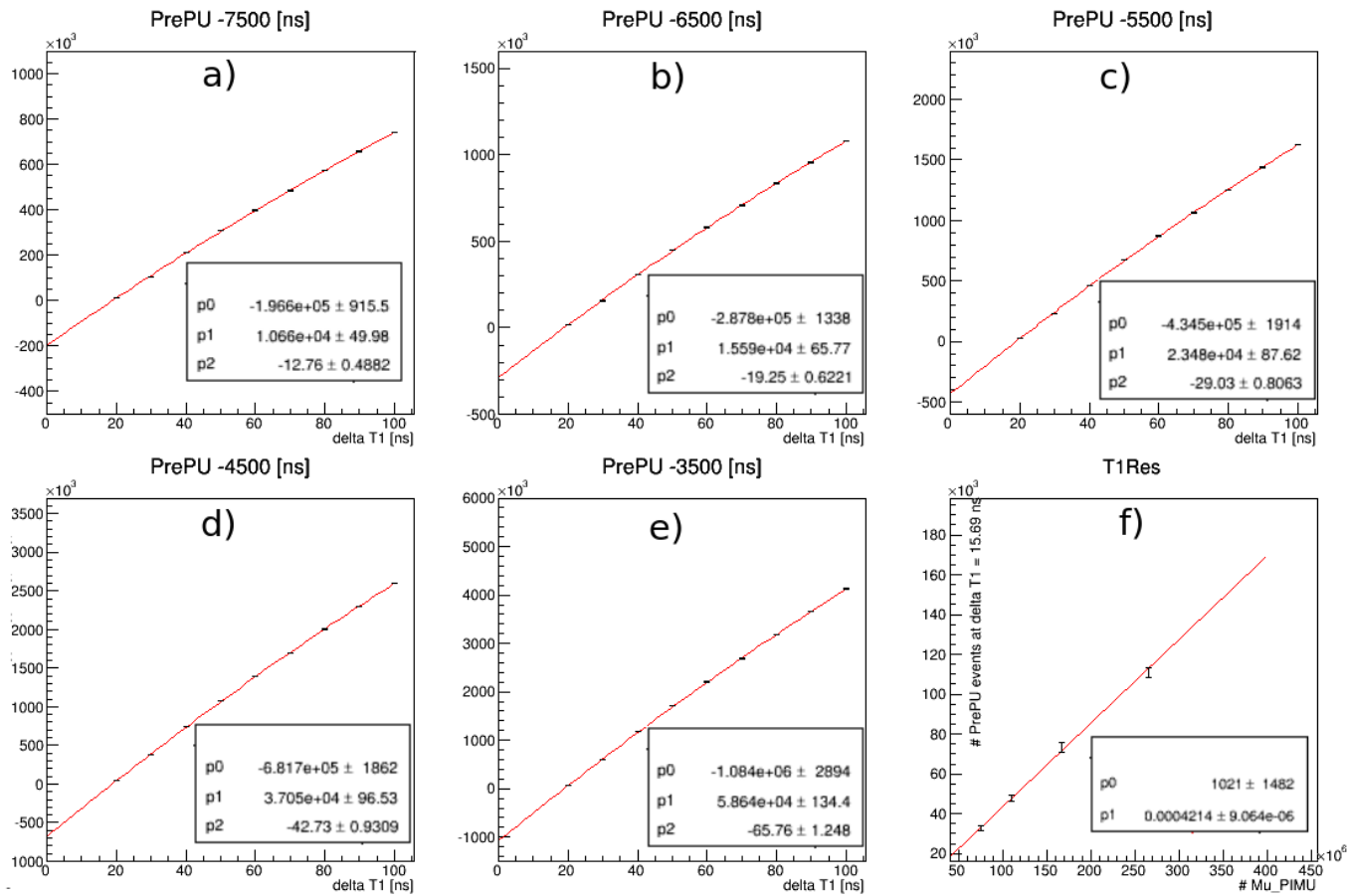


Figure 5.5: a, b, c, d, and e) Amplitudes of $\mathcal{F}_2(t)$ from 2012 dataset's pileup events vs. artificial T1 double pulse resolutions (ΔT) for different pre-pileup windows; points fitted with a quadratic curve. If the double pulse resolution time ΔT was zero, the amount of pileup would not be negative below 15.7 ns. f) Each intercept at $\Delta T = 15.7$ ns from subplots a) to e) is correlated to the number of old-muon events from the LE time region. See Section 5.2.3 for discussion.

5.2.4 Muon from Previous Event (Old-muon) No-T1-Hit

Another mechanism for an old-muon³⁴ pileup to appear in the HE region is when the positrons from a nominal event or from old-muons may enter the calorimeters without traversing the T1 counter. Geometrically, this is possible for muons in the target as there is some solid angle allowing such a trajectory to enter Bina or CsI without hitting T1. Since the positrons enter the calorimeter with no-T1-hit, the pileup cuts for T1 and T2 do not take care of a such case. Hence, when combined with a signal $\pi^+ \rightarrow \mu^+ \nu_\mu \rightarrow e^+ \nu_e \bar{\nu}_\mu$ event, the energy may get bumped up to the HE region.

As this background is HE (the LE component is negligible), the event is fired by a TIGC trigger that requires a sum of the Bina + CsI pulse height above a certain threshold in a 250 ns window. However, as the integration time for Bina energy calibration was 1 μ s, if the pileup and signal events are separated in time by more than the trigger time window, the calibrated energy could be above E_{cut} and a TIGC trigger would still not be present, meaning no trigger or event registered. This particular type of event was restricted when generating the MC shape for the time spectrum fit. The shape of the time spectrum for this background was obtained by Geant4 simulation using the waveform templates of the NaI and CsI detectors with the same pileup cut and trigger requirement as the data. Figure 5.6 shows the simulated time spectrum and it is represented in the HE region as $\mathcal{F}_1(t)$.

5.2.5 Radiative Pion Decay

If the decay positron was produced in association with a γ via $\mu^+ \rightarrow e^+ \nu_e \bar{\nu}_\mu \gamma$ the energy spectrum of the positron was altered, but the time dependence was not, and a separate shape is not required. In the other case, if the pion decayed radiatively to a muon as $\pi^+ \rightarrow \mu^+ \nu_\mu \gamma$, followed by $\mu^+ \rightarrow e^+ \nu_e \bar{\nu}_\mu$ decay, the measured energy could get boosted to the HE region above E_{cut} . The γ has the time of a pion decay and the positron has the muon decay time. The probability of this happening is dependent on the time difference between the γ and the positron entering the calorimeter; further, the TIGC trigger integration times comes into play just as in the Old-muon No-T1-Hit component described previously. If recorded in the calorimeter, the radiative γ will look like a pre-pileup event since it carries the time of the pion decay instead of the muon decay. Due to the long NaI pulse, the effect of such a pre-pileup in the HE region can persist long after

³⁴A muon from a previous event.

5.3. The Fitting Function

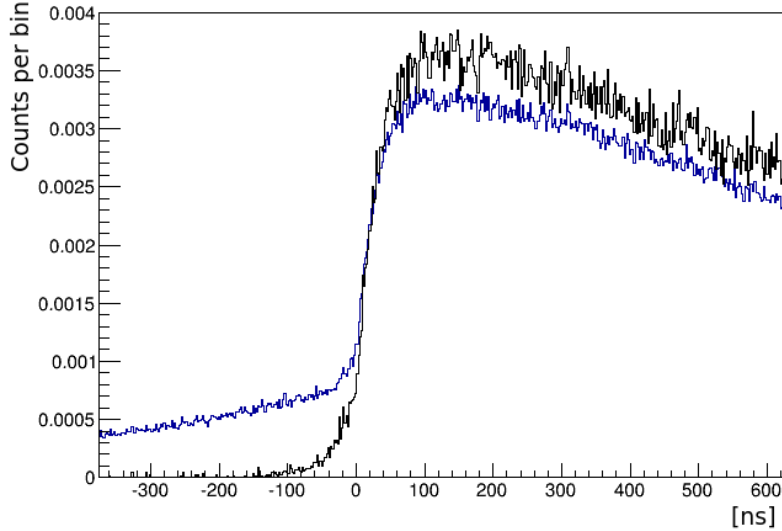


Figure 5.6: The shape used in the time spectrum fit from positrons entering the calorimeter, missing the T1-hit requirement. Integrated charge (Q) based in blue and pulse-height (PH) based in black.

the pion decay time. The CsI crystals have better time resolution than the NaI monolith, thus they can reject events with smaller time difference. The shape generated with Geant4 is shown in Figure 5.7, the contribution from NaI in red ($\mathcal{G}_1(t)$), CsI crystals in black ($\mathcal{G}_2(t)$), and the sum in blue ($\mathcal{G}(t)$). The fixed amplitudes from Geant4 are $d_1 = 3.62 \times 10^{-7}$, and $d_2 = 1.26 \times 10^{-7}$ for NaI and CsI crystals respectively. Thus, the amplitude for the total radiative pion decay component $\mathcal{G}(t)$ is $d = d_1 + d_2 = 4.88 \times 10^{-7}$.

5.3 The Fitting Function

The package MINUIT [22] is used over the time fitting function to fit all described signals and backgrounds and to extract the raw branching ratio R_π^{raw} . The current fitting limits are -290 to -20 and 10 to 520 ns in both HE and LE spectra. The gap from -20 to 10 ns is called prompt time. The T1 prompt cut from Section 4.2.2 kills beam positrons, muons, and protons, but the prompt region is excluded because of distortions to the time analysis owing to nuclear reactions which generate gamma rays, and pair production. In the time fit, $t = t' - t_0$, where t' is the measured time and t_0 is the offset

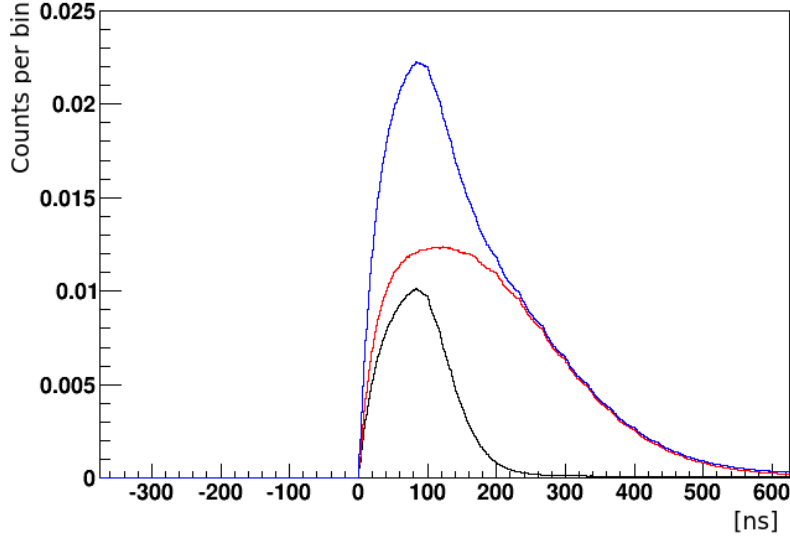


Figure 5.7: The shape used in the time spectrum fit for $\pi^+ \rightarrow \mu^+ \nu_\mu \gamma$ events. contribution from NaI in red, CsI crystals in black, and the sum in blue.

in the time spectrum (pion stop time in B3), which is included and fixed in the time spectrum fitting function. t_0 is determined by fitting the rising time from the time spectrum from a special set of muon runs (through-going particles). The pion stopping time t_0 was found to be 1.68 [16], 2.24 [18], and 2.15 [19] ns for 2010, 2011, and 2012 respectively. Although, the 2012 value was used for all datasets since its the most representative (statistically), the differences did not change the branching ratio result more than 1 [10⁻⁸] R units.

5.3.1 Time-Independent Addition of Energy

The low-energy time spectrum backgrounds are present in some portion in the HE time region as well. Time-independent mechanisms bump the energy of low-energy components and push events into high energy. Some of these LE events are promoted to the high-energy time spectrum due to poor energy resolutions of Bina and CsI crystals, cosmic rays, radiative muon decays $\mu^+ \rightarrow e^+ \nu_e \bar{\nu}_\mu \gamma$ in which the γ -ray increases the apparent positron energy, and pileup events in the calorimeter with a flat time distribution (e.g. due to neutrons coming from the production target). The free parameter r is the proportion of the low energy time spectrum that is present in the

5.3. The Fitting Function

high energy time spectrum. The fitting implements such a degree of freedom with a free parameter, namely r , present in both LE $\sim (1 - r)$ and HE $\sim r$.

5.3.2 Low-Energy Components

The major low-energy components are muon decays: $\pi^+ \rightarrow \mu^+ \nu_\mu \rightarrow e^+ \nu_e \bar{\nu}_\mu$, π DIF, and old-muons. There is also a negligible portion $\pi^+ \rightarrow e^+ \nu_e$ tail and μ DIF which both decay with the pion lifetime can be ignored in the low-energy time-spectrum fit [16]. The fitting function used in the low energy time spectrum ($\Phi_{LE}(t)$) is shown in Eq. 5.10, where \mathcal{H} is the Heaviside function, τ_μ and τ_π are the muon and pion lifetimes, (a) is the total number of $\pi^+ \rightarrow \mu^+ \nu_\mu \rightarrow e^+ \nu_e \bar{\nu}_\mu$ events, $(1 - r)$ is a correction for the loss of LE events that are boosted to HE, (b) is the LE amplitude of the π DIF shape, and (c) is the LE amplitude of the old-muon background. The overall LE fitting function is,

$$\Phi_{LE}(t) = \mathcal{H}(t) \left[\underbrace{a(1-r)\mathcal{E}_{\pi \rightarrow \mu \rightarrow e}(t)}_{\text{LE signal}} + \underbrace{b\mathcal{E}_{\mu \rightarrow e}(t)}_{\text{LE } \pi\text{DIF}} \right] + \underbrace{c\mathcal{E}_{\mu \rightarrow e}(t)}_{\text{LE old-muon from Tg}}. \quad (5.10)$$

5.3.3 High-Energy Components

The fitting function used in the high energy time spectrum ($\Phi_{HE}(t)$) shown in Eq. 5.11 consists of all of the shapes previously discussed. The rest of the parameters are as follows: R_π^{raw} for the raw branching ratio before corrections, $(a \times r)$ represents the boosted LE $\pi^+ \rightarrow \mu^+ \nu_\mu \rightarrow e^+ \nu_e \bar{\nu}_\mu$ events to HE, (b') for HE amplitude of the pion decay-in-flight shape, (c') for HE amplitude of the old muon background, (d) for HE amplitude of radiative pion, (e) for HE amplitude of the old-muon with No-T1-Hit, (f) for HE amplitude of T1 resolution. The correlation between π DIF decays and old-muon decays was significant; therefore, parameter b' was scaled to the amplitude of π DIF in the low-energy region, i.e. $b' = rb$. The parameter $C_{\mu\text{DIF}}$ was the corrected amplitude for μ DIF events in the target, which will be discussed in Section 6.3. The HE fitting function is,

$$\Phi_{HE}(t) = \mathcal{H}(t) \left[a \left\{ \underbrace{(R_\pi^{raw} + C_{\mu\text{DIF}})\mathcal{E}_{\pi \rightarrow e}(t)}_{\text{HE signal}} + \underbrace{d\mathcal{G}(t)}_{\text{Radiative Pion}} + \underbrace{r\mathcal{E}_{\pi \rightarrow \mu \rightarrow e}(t)}_{\text{LE signal}} \right\} \right. \\ \left. + \underbrace{b'\mathcal{E}_{\mu \rightarrow e}(t)}_{\text{HE } \pi\text{DIF}} \right] + \underbrace{c'\mathcal{E}_{\mu \rightarrow e}(t)}_{\text{HE Old-muon from B3}} + \underbrace{e\mathcal{F}_1(t)}_{\text{Old-muon No-T1-Hit}} + \underbrace{f\mathcal{F}_2(t)}_{\text{T1 Resolution}}. \quad (5.11)$$

5.3.4 Fit Parameters

Results from the time spectrum fitting for the three data taking periods are shown in Table 5.1. The first column shows the fit parameters, and the first row shows the datasets. The errors are statistical only as obtained by the MINUIT [22] fit, and the parameters marked as fixed were kept fixed during the fit. The total number of low-energy events is labeled N_{LE} , and the total number of high-energy events is N_{HE} .

The parameter amplitudes for the $\pi^+ \rightarrow \mu^+ \nu_\mu \rightarrow e^+ \nu_e \bar{\nu}_\mu$ events “a”, the π DIF “b”, and the LE old-muon component “c” are consistent within error for integrated-charge (Q) and pulse-height (PH) based R_π for each year, but increases from 2010 to 2011, and from 2011 to 2012. The increase in “a”, “b”, and “c” throughout the years is expected when comparing the size of each dataset. The only inconsistency is “b” being slightly lower in 2011 compared to 2010. This could be explained by fact the of parameter “b” and t_0 being degenerate. As mentioned earlier in section 5.3, t_0 is slightly lower in 2010 than in 2011. The 2012’s t_0 value was used for all datasets since it is the most representative (statistically); the differences did not changed the branching ratio result more than $1 [10^{-8}] R_\pi^{raw}$ units.

The amplitude for the amount of LE events being boosted to HE “r” is larger for the Q compared to PH versions. This is expected since PH should be less sensitive to pile-up events responsible to push LE events to HE regime. The errors in the R_π^{raw} reflect the magnitude of the data samples collected in the three periods. The amplitudes for old-muon (c’) parameters in HE spectra are consistent with zero for the Q version datasets: within 1σ for all three years. The amplitudes (c’) for the PH versions are all larger than any Q version. The largest (events) dataset 2012-PH has the largest amplitude, and the smaller dataset 2010-PH has the smallest. The amplitude for the amount of old-muon no-T1-hit (e) events is larger for the Q calorimeter based branching ratio compared to the PH version. The largest (events) dataset 2012 (Q or PH) has the largest amplitude, and the smaller dataset 2010 (Q or PH) has the smallest.

The total χ^2 over the total degrees of freedom ($\chi^2/d.o.f.$) is larger for the PH versions. This is mainly due to the ~ 44 ns structures in the HE $t < 0$ region in the PH version due to beam pileup from the cyclotron’s RF. These events in such region causes distortions in the time spectrum and inflates the total $\chi^2/d.o.f.$ Such distortions and pile-up at negative times are negligible for positive times, and do not affect the branching ratio. An alternative could be introducing a ~ 44 ns cyclic term in the fitting function to improve the fit.

Table 5.1: Results from the timing spectra for the three data-taking periods, presented for both integrated-charge (Q) and pulse-height (PH) calorimeter variables. The exact fit values are truncated for a more compact presentation. The errors are statistical only as obtained by the MINUIT [22] fit, and the parameters marked as fixed were kept fixed during the fit. The errors in the R_{π}^{raw} reflect the magnitude of the data samples collected in the three periods. The acceptance radius used was $R_A = 40$ mm, and the nominal range for our fitting function (FF) for both high- and low-energy time spectra is from -290 to 520 ns, excluding prompt events from -20 to 10 ns. Using 1 ns bins for the time spectrum, the total degrees of freedom (*d.o.f.*) are 1557 .

Parameter ↓, Dataset →	2012 (PH)	2012 (Q)	2011 (PH)	2011 (Q)	2010 (PH)	2010 (Q)
N_{LE} [10^8] “Total Low-Energy events” §5.3.2	1.323	1.323	0.424	0.424	0.301	0.301
N_{HE} [10^6] “Total High-Energy events” §5.3.3	1.556	1.775	0.521	0.609	0.363	0.415
a [10^9] “ $\pi^+ \rightarrow \mu^+ \nu_{\mu} \rightarrow e^+ \nu_e \bar{\nu}_{\mu}$ ” §5.2.1	9.4502 ± 0.0020	9.4498 ± 0.0020	3.0441 ± 0.0011	3.0439 ± 0.0011	2.1252 ± 0.0009	2.1251 ± 0.0009
b [10^8] “ π DIF” §5.2.2	1.666 ± 0.014	1.665 ± 0.014	0.570 ± 0.008	0.569 ± 0.008	0.671 ± 0.007	0.671 ± 0.007
c [10^7] “LE’s old-muon” §5.2.2	1.811 ± 0.005	1.805 ± 0.005	1.555 ± 0.004	1.549 ± 0.004	1.073 ± 0.004	1.069 ± 0.004
r [10^{-4}] “boosted to HE” §5.3	2.126 ± 0.018	3.087 ± 0.018	1.914 ± 0.050	2.827 ± 0.053	2.028 ± 0.056	2.922 ± 0.050
R_{π}^{raw} [10^{-4}]	$1.2^{***} \pm 0.0014$	$1.2^{***} \pm 0.0014$	$1.2^{***} \pm 0.0025$	$1.2^{***} \pm 0.0026$	$1.2^{***} \pm 0.0030$	$1.2^{***} \pm 0.0031$
c' [10^3] “HE’s old-muon” §5.2.2	6.49 ± 0.27	1.28 ± 3.14	4.99 ± 0.24	1.72 ± 3.01	3.77 ± 0.21	1.44 ± 1.97
d [10^{-8}] “ $\pi^+ \rightarrow \mu^+ \nu_{\mu} \gamma$ ” §5.2.5	48.8 (fixed)					
e [10^4] “oldmuon-no-T1-hit” §5.2.4	5.85 ± 0.42	8.96 ± 0.54	4.64 ± 0.37	8.17 ± 0.51	2.41 ± 0.29	3.80 ± 0.34
f [10^{-4}] “T1Res” §5.2.3	4.08 (fixed)					
t_0 [ns] §5.3	2.15 (fixed)					
C_{μ DIF [10^{-7}] §6.3	2.406 (fixed)					
τ_{μ} [ns]	2197.03 (fixed)					
τ_{π} [ns]	26.033 (fixed)					
$\chi^2/d.o.f$ §5.3.4	1.19	1.13	1.08	1.06	1.00	1.07
HE $t < 0$	1.62	1.37	1.21	1.19	0.85	1.15
HE $t > 0$	1.14	1.09	1.04	0.99	1.05	1.10
LE $t < 0$	1.07	1.07	1.15	1.15	1.10	1.11
LE $t > 0$	1.13	1.13	1.07	1.07	1.01	1.01

5.3.5 Signal Overlay and Residuals

The fitted amplitudes superimposed in the LE ($\Phi_{\text{LE}}(t)$) and HE ($\Phi_{\text{HE}}(t)$) time spectrum for all datasets after all event selection cuts for the pulse-height (PH) and integrated-charge (Q) calorimeter based variables are shown in Figure 5.8, 5.10, 5.12, 5.14, 5.16, and 5.18 for 2012-PH, 2012-Q, 2011-PH, 2011-Q, 2010-PH, and 2010-Q respectively. The residuals (data - fit) for HE $t < 0$, HE $t > 0$, LE $t < 0$, and LE $t > 0$ are shown in Figure 5.9, 5.11, 5.13, 5.15, 5.17, and 5.19 for 2012-PH, 2012-Q, 2011-PH, 2011-Q, 2010-PH, and 2010-Q respectively.

The solid red line, dashed dark blue line, and dashed pink lines indicate $\pi^+ \rightarrow \mu^+ \nu_\mu \rightarrow e^+ \nu_e \bar{\nu}_\mu$, πDIF , and old-muon decays, respectively. The sum of the two LE backgrounds is shown as a solid green line. The high-energy (HE) spectrum is more complex than the low-energy (LE) spectrum: $\pi^+ \rightarrow e^+ \nu_e$ signal in red, $\pi^+ \rightarrow \mu^+ \nu_\mu \rightarrow e^+ \nu_e \bar{\nu}_\mu$ events in blue (boosted from LE), pileup from T1's resolution in dashed red, positrons from $\pi^+ \rightarrow \mu^+ \nu_\mu \gamma$ radiative decay in dashed black, positrons from πDIF in dashed blue, positrons from old-muons coming from B3 in dashed pink, and decayed positron from old-muon-no-T1-hit component in dotted blue.

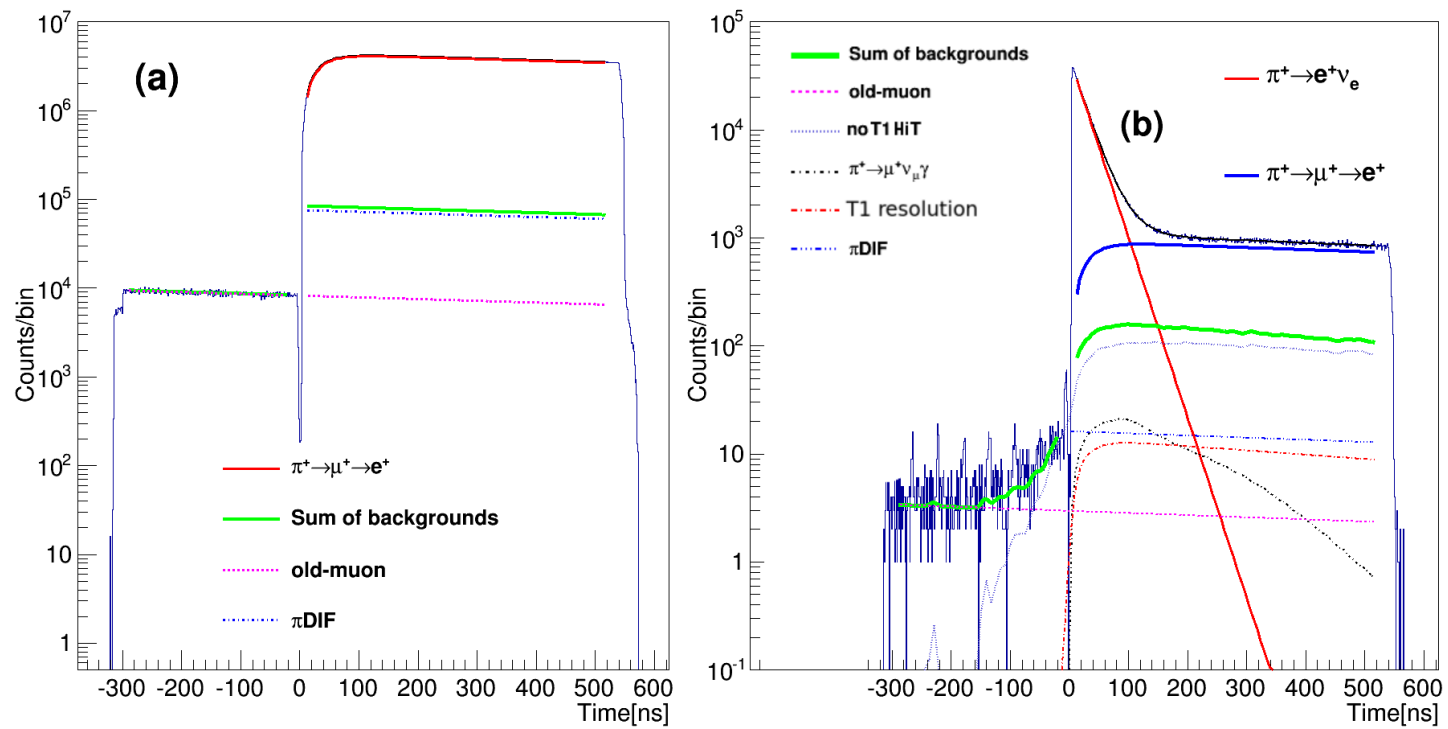


Figure 5.8: **Time Spectra for 2012 dataset pulse-height (PH) R_π based time fit.** Left: LE time spectrum on a logarithmic scale (black line). Right: HE time spectrum on a logarithmic scale (black line).

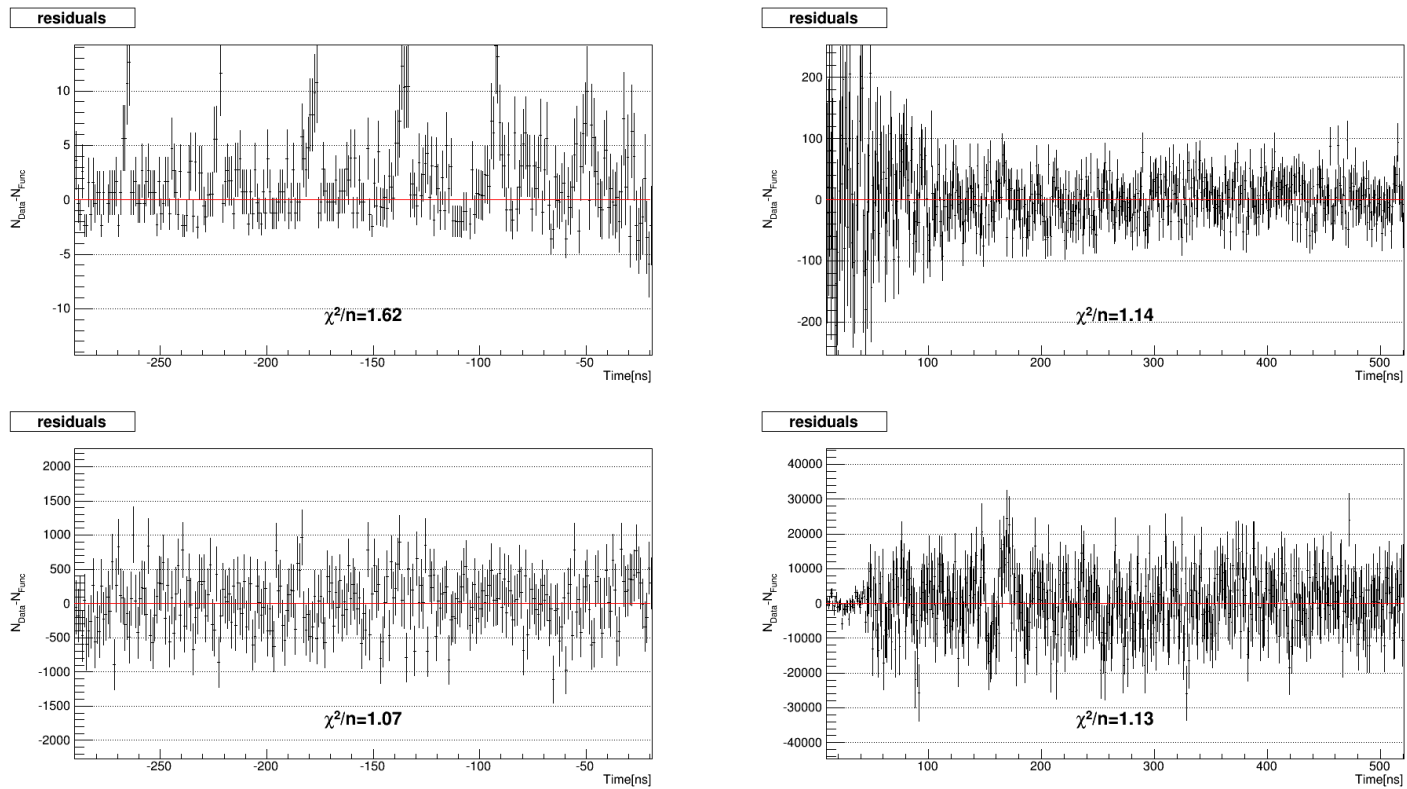


Figure 5.9: **Residuals (data - fit) for 2012 dataset pulse-height (PH) R_π based time fit.** Top-Left: HE, negative times. Top-Right: HE, positive times. Bottom-Left: LE, negative times. Bottom-Right: LE, positive times.

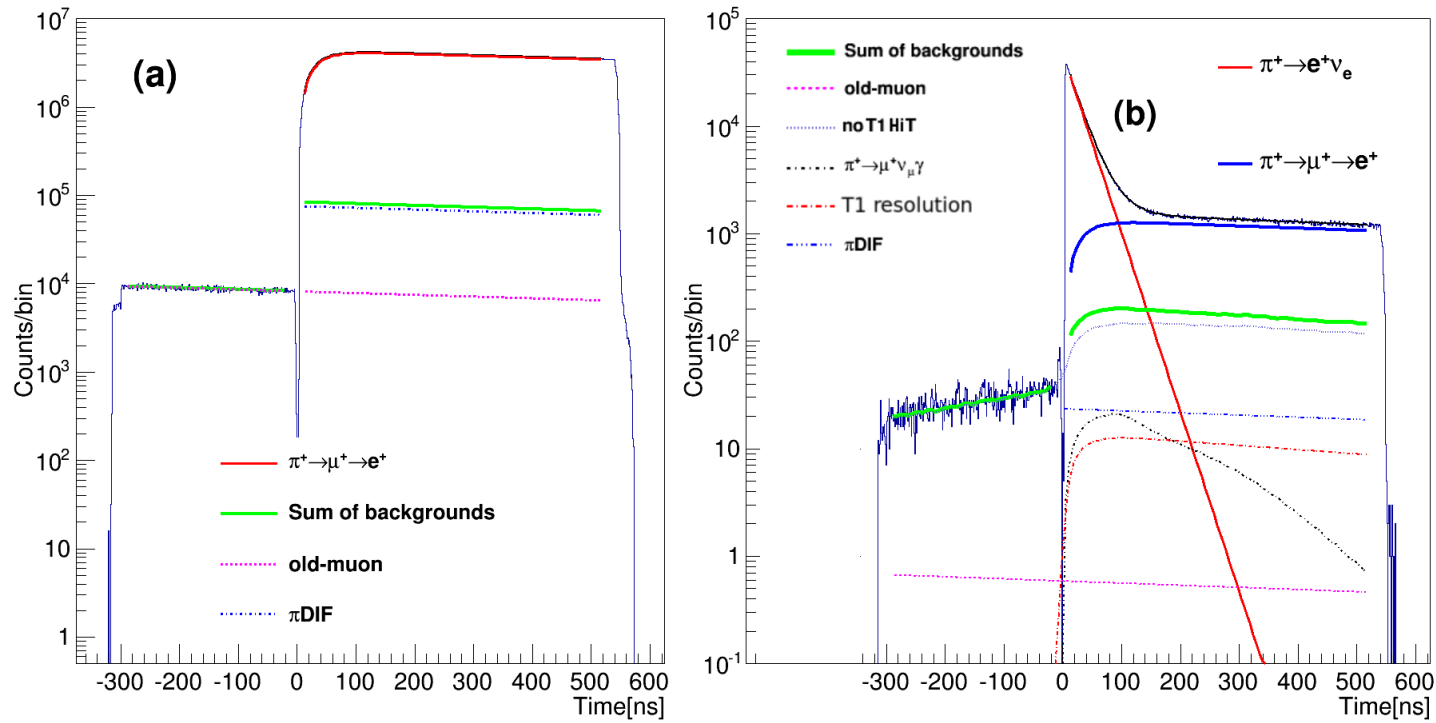


Figure 5.10: **Time Spectra for 2012 dataset integrated-charge (Q) R_π based time fit.** Left: LE time spectrum on a logarithmic scale (black line). Right: HE time spectrum on a logarithmic scale (black line).

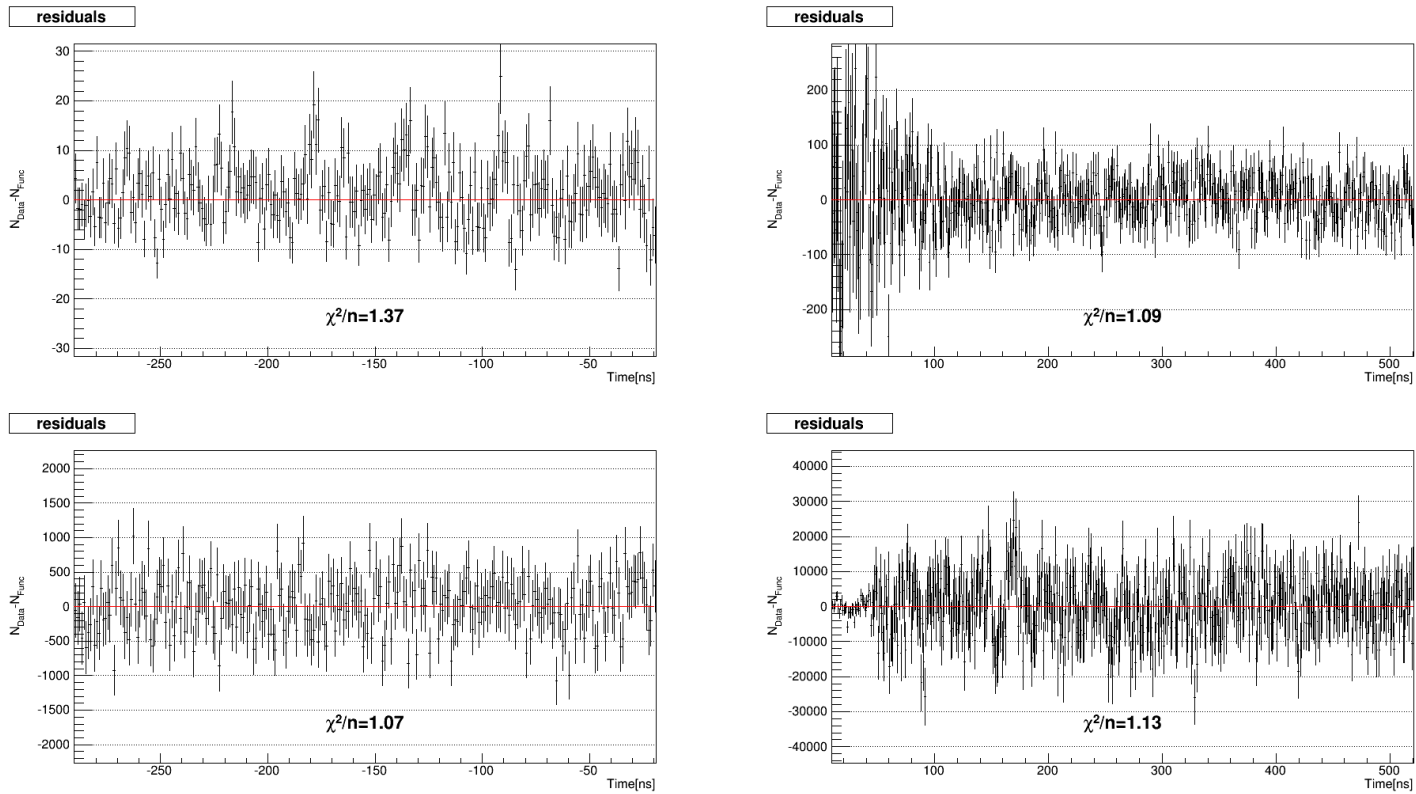


Figure 5.11: Residuals (data - fit) for 2012 dataset integrated-charge (Q) R_π based time fit. Top-Left: HE, negative times. Top-Right: HE, positive times. Bottom-Left: LE, negative times. Bottom-Right: LE, positive times.

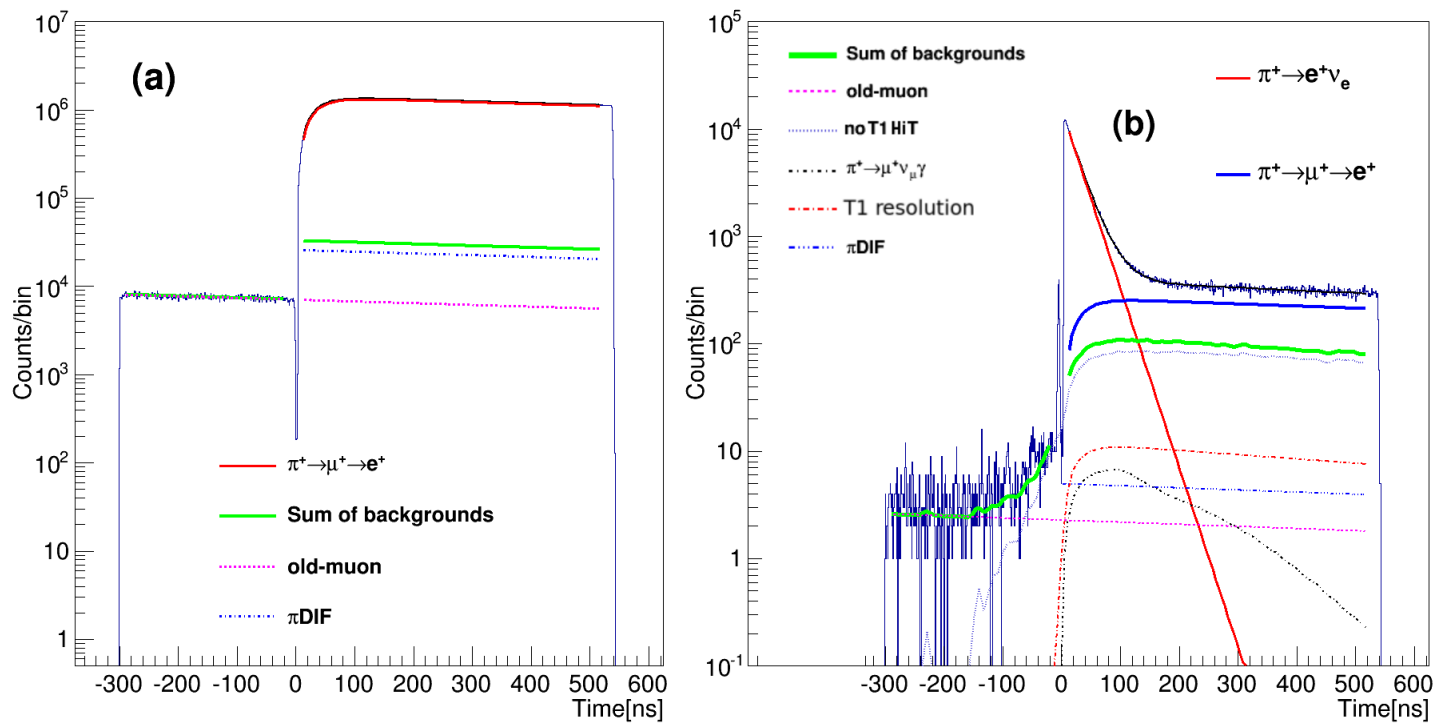


Figure 5.12: **Time Spectra for 2011 dataset pulse-height (PH) R_π based time fit.** Left: LE time spectrum on a logarithmic scale (black line). Right: HE time spectrum on a logarithmic scale (black line).

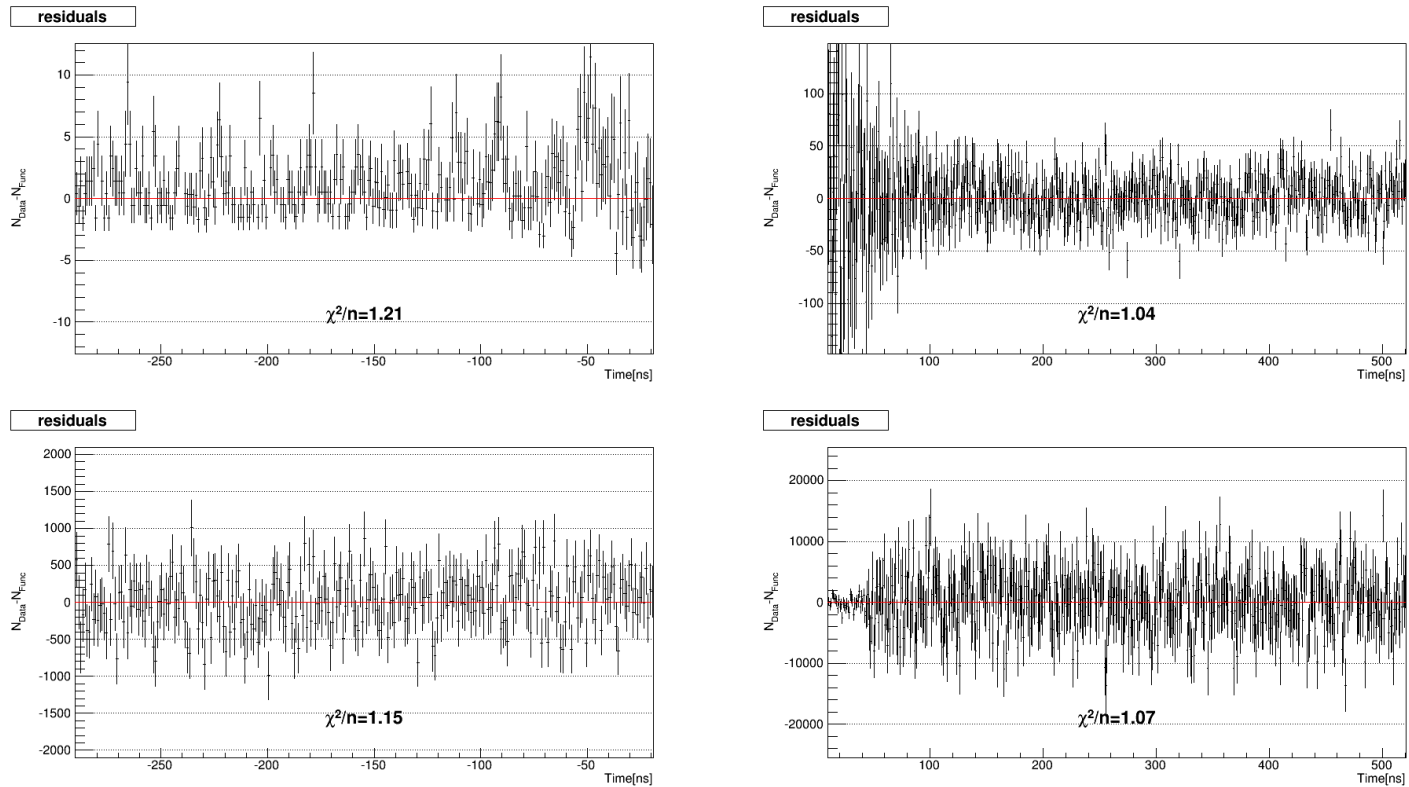


Figure 5.13: **Residuals (data - fit) for 2011 dataset pulse-height (PH) R_π based time fit.** Top-Left: HE, negative times. Top-Right: HE, positive times. Bottom-Left: LE, negative times. Bottom-Right: LE, positive times.

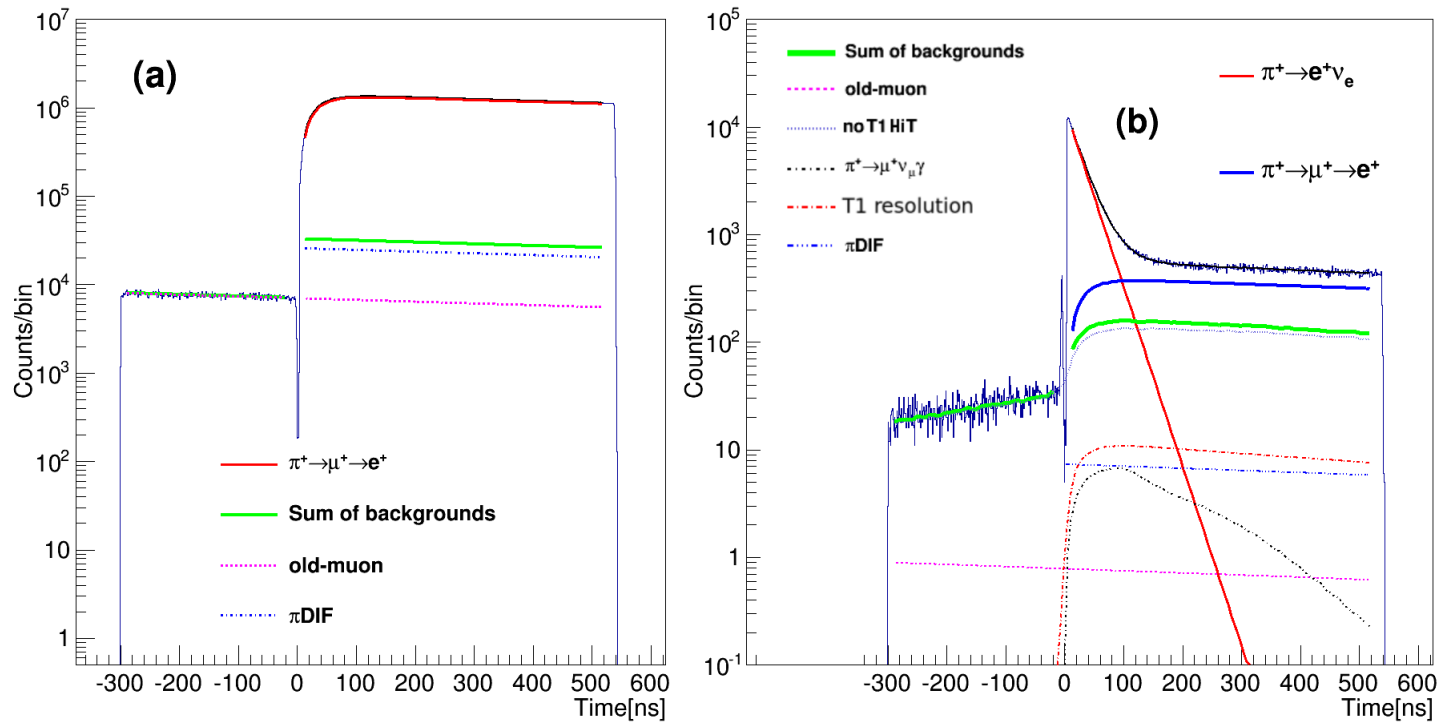


Figure 5.14: **Time Spectra for 2011 dataset integrated-charge (Q) R_π based time fit.** Left: LE time spectrum on a logarithmic scale (black line). Right: HE time spectrum on a logarithmic scale (black line).

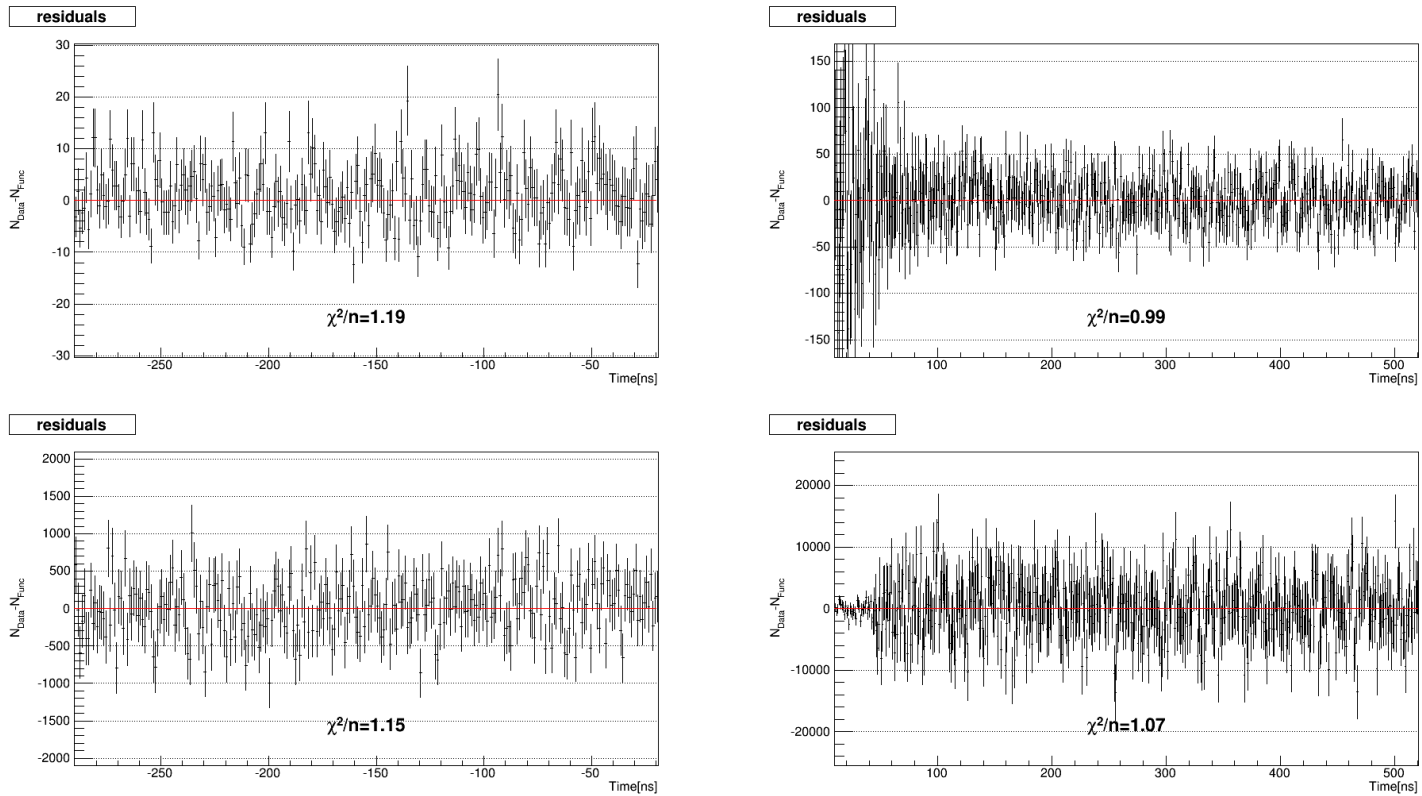


Figure 5.15: **Residuals (data - fit) for 2011 dataset integrated-charge (Q) R_π based time fit.** Top-Left: HE, negative times. Top-Right: HE, positive times. Bottom-Left: LE, negative times. Bottom-Right: LE, positive times.

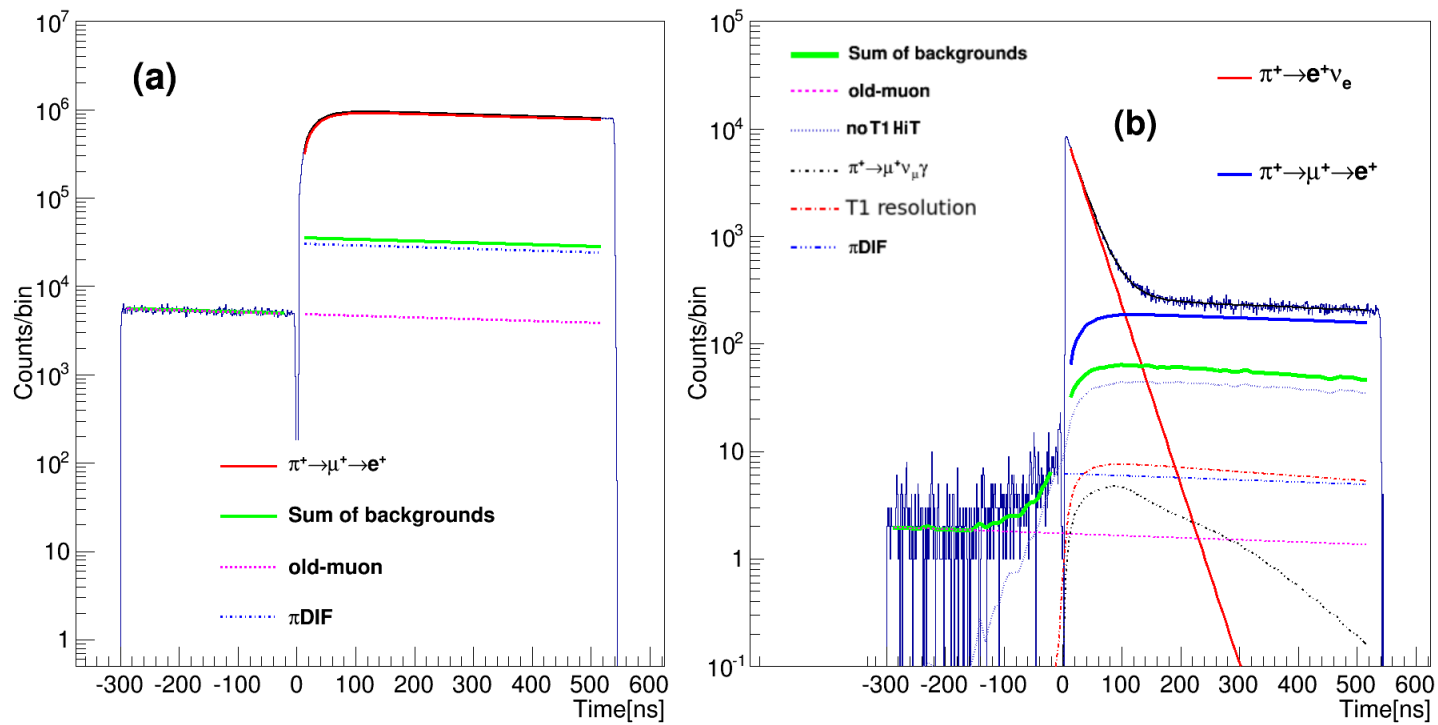


Figure 5.16: Time Spectra for November 2010 dataset pulse-height (PH) R_π based time fit. Left: LE time spectrum on a logarithmic scale (black line). Right: HE time spectrum on a logarithmic scale (black line).

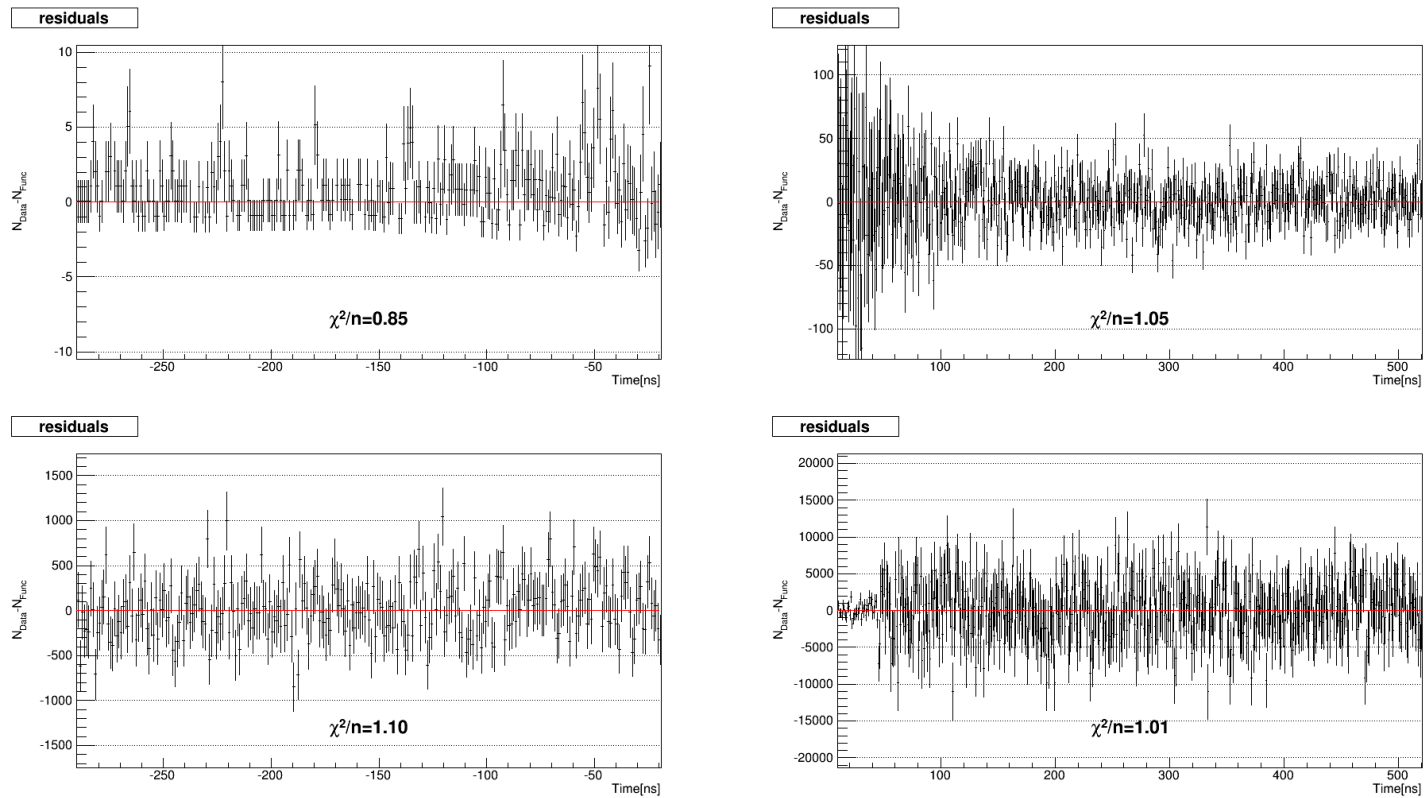


Figure 5.17: Residuals (data - fit) for November 2010 dataset pulse-height (PH) R_π based time fit. Top-Left: HE, negative times. Top-Right: HE, positive times. Bottom-Left: LE, negative times. Bottom-Right: LE, positive times.

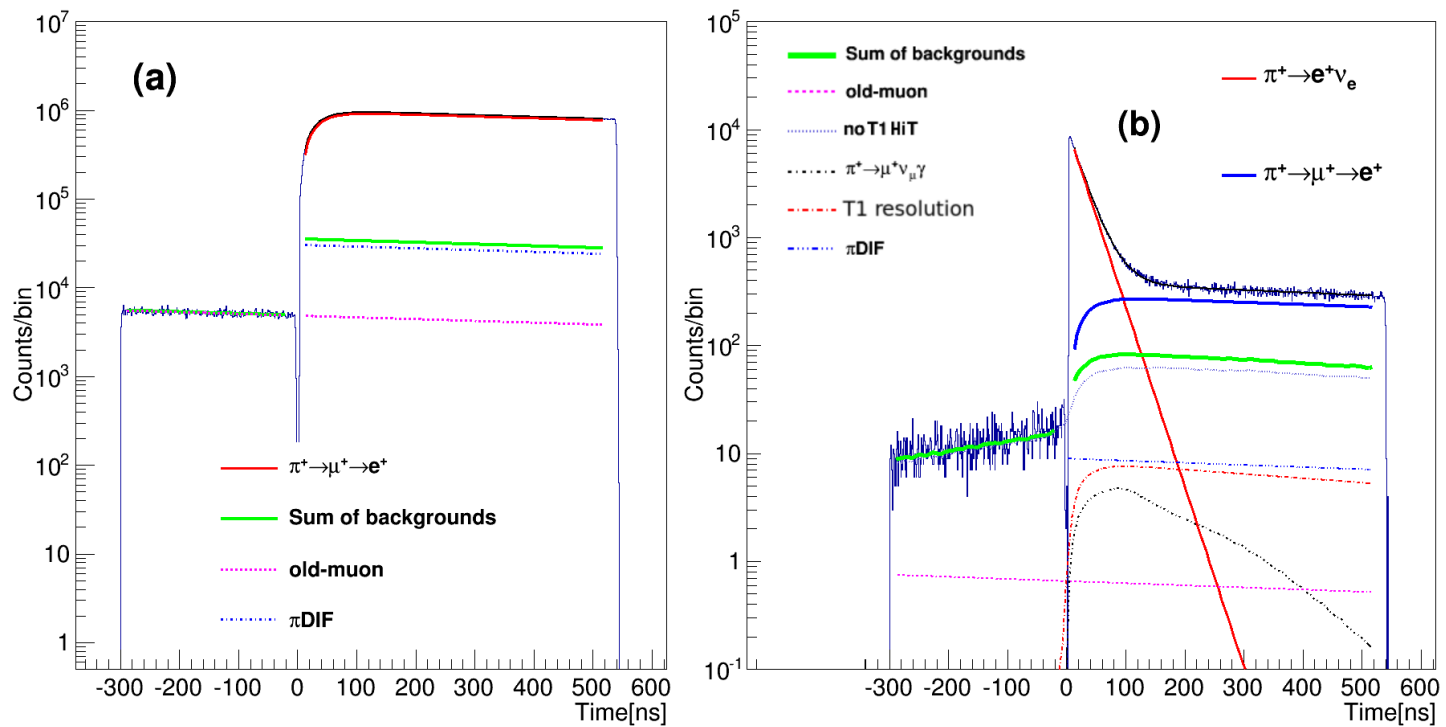


Figure 5.18: **Time Spectra for November 2010 dataset integrated-charge (Q) R_π based time fit.** Left: LE time spectrum on a logarithmic scale (black line). Right: HE time spectrum on a logarithmic scale (black line).

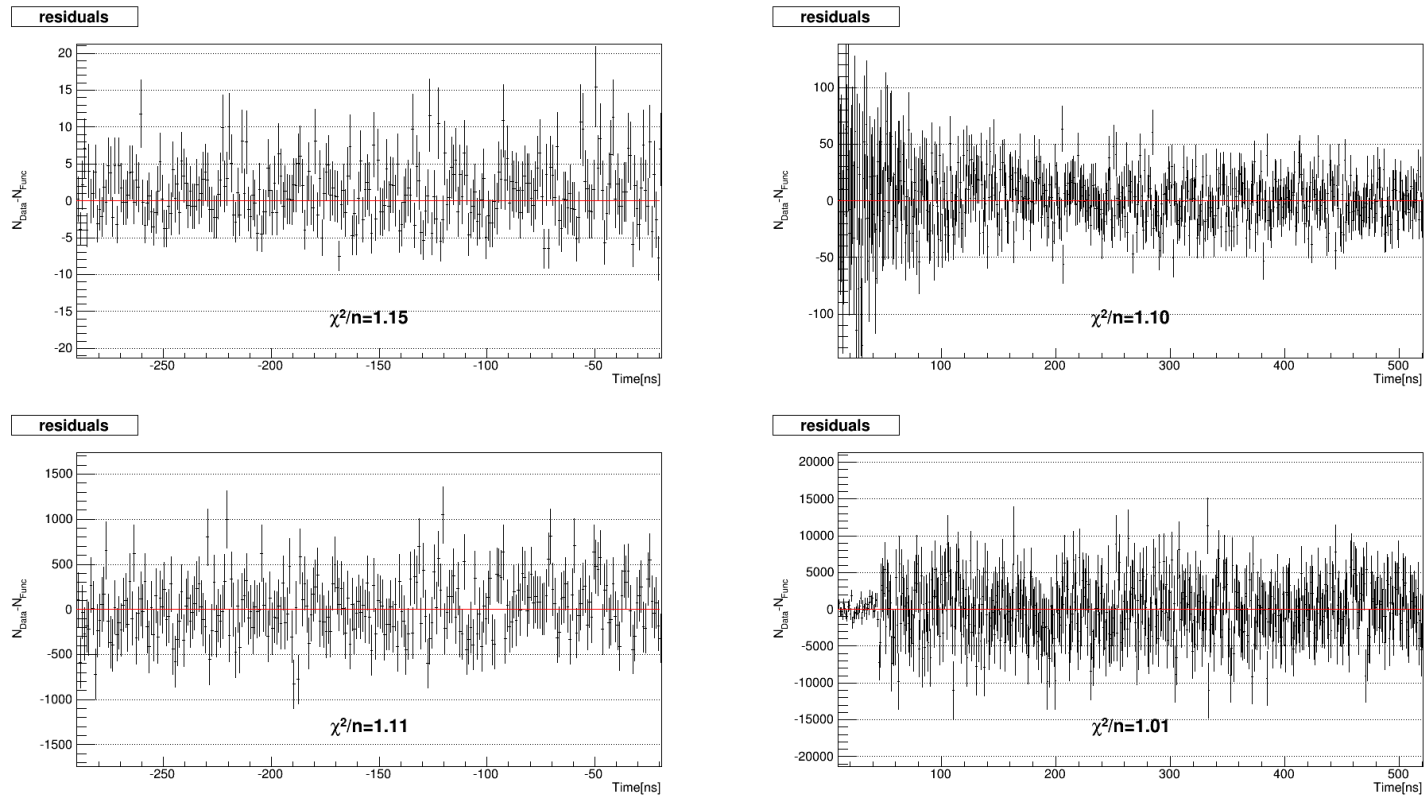


Figure 5.19: **Residuals (data - fit) for November 2010 dataset integrated-charge (Q) R_π based time fit.** Top-Left: HE, negative times. Top-Right: HE, positive times. Bottom-Left: LE, negative times. Bottom-Right: LE, positive times.

Chapter 6

Corrections

The raw branching ratio R_{π}^{raw} needs to be corrected for the calorimeter's low energy tail from the $\pi^+ \rightarrow e^+\nu_e$ events buried under the $\pi^+ \rightarrow \mu^+\nu_{\mu} \rightarrow e^+\nu_e\bar{\nu}_{\mu}$ energy distribution (C_T) §6.1, the calorimeter's energy-dependent acceptance (C_{Acc}) §6.2, the effect of muons decaying in flight ($C_{\mu DIF}$) §6.3, and the energy-dependent effects in the determination of the timings between the two decay modes (C_{t0}) §6.4. All of them are multiplicative corrections to R_{π}^{raw} , except the additive $C_{\mu DIF}$ which is embedded in the high energy time spectrum fitting function (Equation 5.11). In this chapter all corrections are described.

6.1 Calorimeter's Low Energy Tail

The Low Energy Tail (LET) from the $\pi^+ \rightarrow e^+\nu_e$ energy spectrum arises mainly due to electromagnetic shower leakage and energy loss upstream of the calorimeter. Another small contribution arises from photo-nuclear interactions within Bina. $N(E)$ is defined as the $\pi^+ \rightarrow e^+\nu_e$ energy spectrum and the tail fraction T is defined as the proportion of this spectrum below the cutoff energy $E_{cut} = 52$ MeV over all events:

$$T = \frac{\int_0^{E_{cut}} N(E)dE}{\int_0^{\infty} N(E)dE}. \quad (6.1)$$

The raw branching ratio obtained from the fit (Section 5.3) is thus related to the actual branching ratio by $R_{\pi} = R_{\pi}^{raw}/(1 - T)$, then we can define the multiplicative LET correction as,

$$C_T = \frac{1}{1 - T}. \quad (6.2)$$

There are two different methods used to obtain the tail fraction. The first one is called the *Response Function Measurement*: a 70 MeV positron beam imitating $\pi^+ \rightarrow e^+\nu_e$ decay positrons in the calorimeter (Bina+CsI)

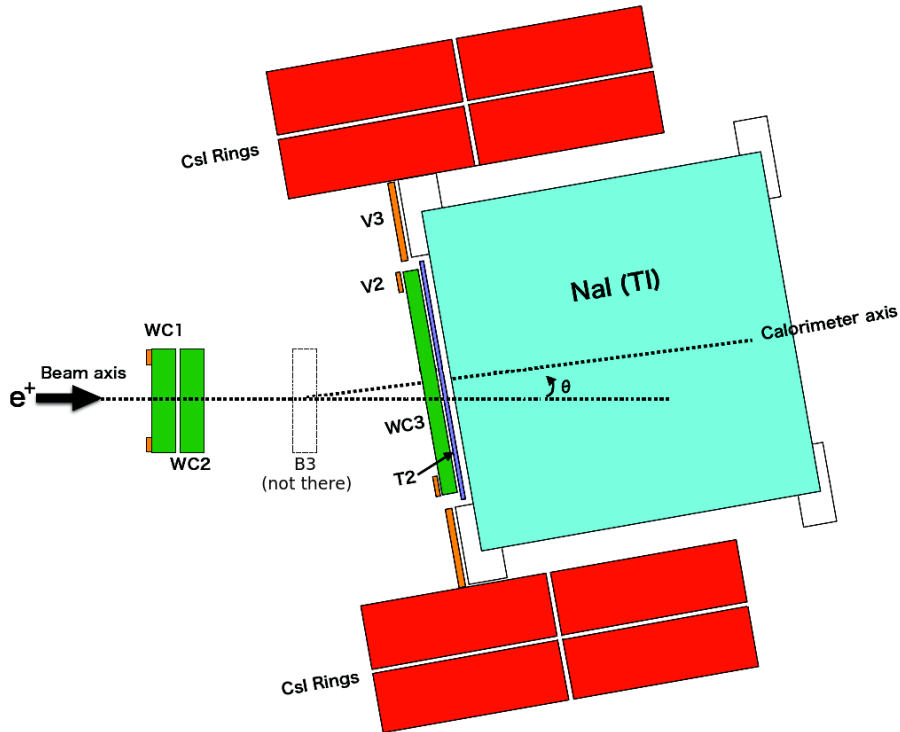


Figure 6.1: Schematic drawing of the detector setup for special positron runs, showing rotating angle θ between the beam and calorimeter.

is injected at several angles (Figure 6.1) to measure the proportion of the spectrum below E_{cut} directly. This method was initially referred to as an *upper-limit* because of the potential for the positrons to scatter in the beam-line, giving an intrinsic low momentum tail coming from the beam-line. The *Response Function Measurement* method was originally described in detail [19] with updates [126] and [127] including the proper photo-nuclear cross section scaling, better cuts, and a 3.2-mm layer of powdered aluminum oxide (Al_2O_3) on the front face of Bina missing from the previous analysis [5]. Currently, we can reproduce the simulated tail fraction T at several angles (Figure 6.1) from the 70 MeV positron beam data to a level of precision that is sufficient to keep us within our precision goals. Figure 6.2 shows the agreement between MC³⁵ and data corresponding to angle 0.0° , i.e., no

³⁵All MC is Geant4 based unless stated otherwise.

6.1. Calorimeter's Low Energy Tail

rotation. The disagreement between data and MC above 68 MeV is due to pileup being deactivated in the simulation, resulting in the difference to the right of the main peak. The nature of the negligible deactivated pileup in the MC is mainly due to out of time beam muons and beam pions, which does not affect the peak location in MC (Appendix C). The small to null disagreement below 35 MeV is also a pileup effect negligible for our level of precision. The normalization is to the total number of events. The sets of cuts used to clean the positron beam data are described in Appendix C. The peaks at 58 and 50.5 MeV are due to photo-nuclear interactions. Using MC, it was determined that they were caused by either one or two neutrons being emitted from iodine and escaping Bina [2]. Such agreement validates our positron beam MC and gives us confidence to use the *Response Function Measurement* to calculate the true tail fraction directly from our nominal $\pi^+ \rightarrow e^+\nu_e$ MC. Section 6.1.1 discusses the agreement to the tail for all available angles, the uncertainties for the positron data, nominal $\pi^+ \rightarrow e^+\nu_e$ data, and MC.

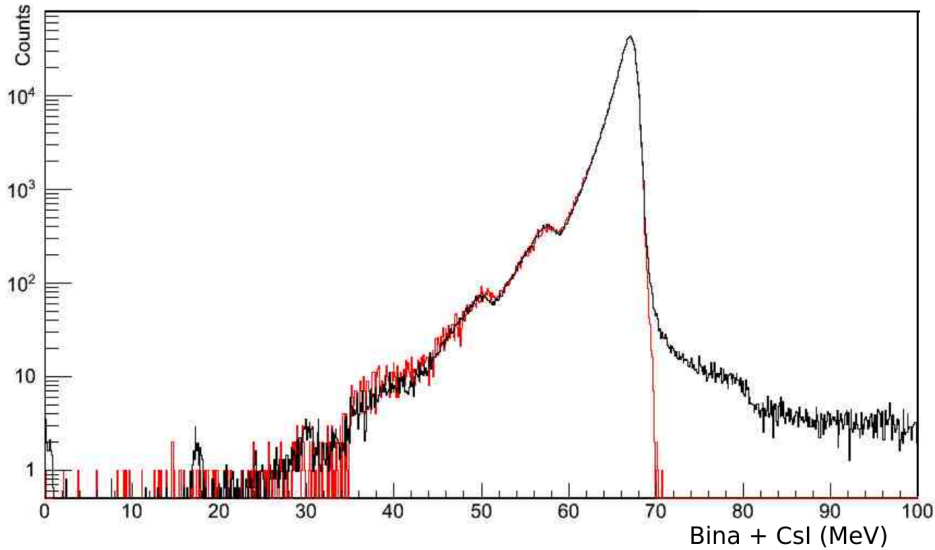


Figure 6.2: The energy spectrum from a 70 MeV positron beam parallel to the crystal axis. Data is shown in black and simulation is shown in red. The histograms are normalized to have the same total number of events.

The second method to calculate T was done similarly to what the previous generation experiment did to estimate the tail fraction (Section 1.2.1) by suppressing $\pi^+ \rightarrow \mu^+\nu_\mu \rightarrow e^+\nu_e\bar{\nu}_\mu$ events with specialized cuts from the energy spectrum itself to uncover the positrons from the $\pi^+ \rightarrow e^+\nu_e$ events, also called the *suppressed spectrum*. This approach assumes that the $\pi^+ \rightarrow e^+\nu_e$ tail is negligible at very low energies, which leads to a slight over-subtraction of $\pi^+ \rightarrow \mu^+\nu_\mu \rightarrow e^+\nu_e\bar{\nu}_\mu$ events from the measured energy spectrum. Thus, the *suppressed spectrum* results in an underestimation of T ; therefore, we refer to it as the *lower limit*. The *lower limit* was described in detail in [18]. At a previous point of the analysis, the upper and lower limits were combined to give the best estimate of T , but as the *Response Function Measurement* gives the best estimate of T , such combination is no longer needed. In this section, we present a brief description of the tail fraction estimate and the possible intrinsic tail coming from the beam-line.

6.1.1 Response Function Measurement

Since the calorimeter is finite, additional energy will be lost owing to electromagnetic (EM) shower leakage (mainly via Bremsstrahlung and pair production until the initial positron runs out of energy) and a small contribution from photo-nuclear interactions within Bina [2]. If sufficient energy escaped from the calorimeter, the measured energy of a $\pi^+ \rightarrow e^+\nu_e$ event could fall below E_{cut} , putting the event in the tail or low energy (LE) region. The positron's shower leakage is dependent on the entrance angle because the amount of material in the path of the beam changes resulting in a varying tail fraction T . The beam-line settings were adjusted to produce a 70 MeV positron beam (collimator and absorber were removed) to measure the calorimeter's response function by rotating it from the beam reference at several angles as shown in Figure 6.1. In order to geometrically allow rotation of the calorimeter against the beam axis, material was removed for the positron beam configuration: B1, B2, S1, S2, B3, S3, and T1 were removed, leaving only the wire chambers, T2, and the calorimeter. This reduces the momentum and position divergence of the positron beam and allows for more accurate measurement of the crystal response.

We confidently rely on Geant4 MC for the contribution to the tail fraction T due to energy loss upstream of the calorimeter, as energy loss in the material is well understood and reproduced with Geant4 [52]. As the average energy loss for $\pi^+ \rightarrow e^+\nu_e$ positrons in B3, T1, and S3 is 1.7 MeV, this meant that the effective value of E_{cut} for the response function measurement

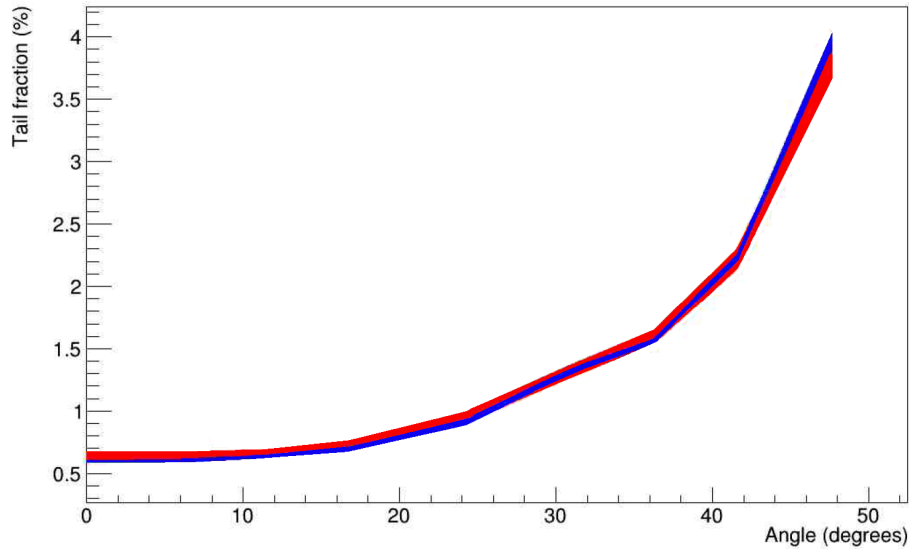


Figure 6.3: Tail fraction below 53.7 MeV vs angle for the positron data (blue) and MC (red), equivalent to the 52 MeV cutoff in the $\pi^+ \rightarrow e^+\nu_e$ data. The 1σ error band for the tail fractions in data and MC overlap at all angles.

was 53.7 MeV compared to its value for the $\pi^+ \rightarrow e^+\nu_e$ case at 52.0 MeV in the nominal pion beam configuration, thereby shifting the peak of the energy spectrum. Positron beam data was first obtained in 2009 and later again in 2011 with higher quality. Only the 2011 positron beam data was used for the tail fraction calculation, with subsets of data for each angle: 0.0, 6.0, 11.8, 16.5, 20.9, 24.4, 30.8, 36.2, 41.6, and 47.7 degrees with an accuracy of 0.1 degrees. The angles of 41.6 and 47.7 degrees correspond to the calorimeter's acceptance radius A_R (Section 4.2.4) equal to 50 and 60 mm, respectively. Figure 6.3 shows the tail fraction below 53.7 MeV (equivalent to the 52 MeV cutoff in the $\pi^+ \rightarrow e^+\nu_e$ data) vs. angle for the positron data (blue) and MC (red).

Uncertainty. The 1σ error bands for the positron beam tail fractions in data and MC from Figure 6.3 overlap at all angles. The seven sources of systematic uncertainties are: the energy calibration (± 0.1 MeV), the photo-nuclear cross section scaling constant (1.1 ± 0.1), the muon correction (Appendix C), the angle between the crystal axis and the incident positron

6.1. Calorimeter's Low Energy Tail

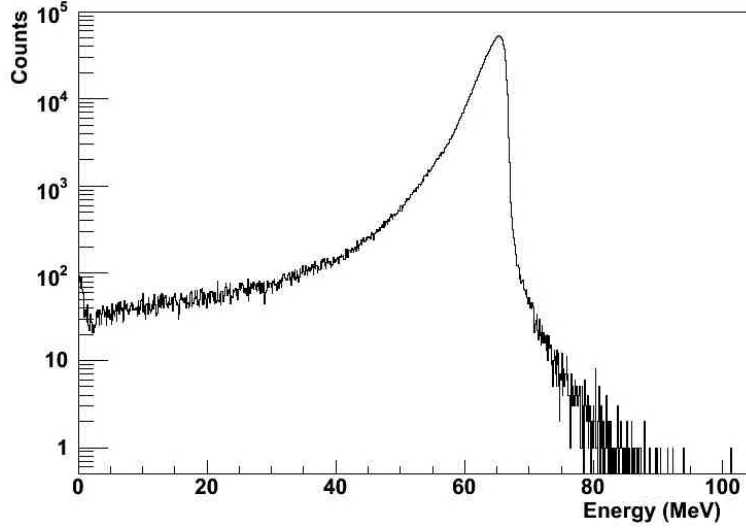


Figure 6.4: Simulated Bina+CsI spectrum from $\pi^+ \rightarrow e^+ \nu_e$ decay including radiative components and events that underwent Bhabha scattering in the target.

Table 6.1: Low energy tail fraction (T) percentage for nominal pion beam configuration as a function of the maximum acceptance radius A_R with $E_{cut} = 52$ MeV, and as a function of E_{cut} with $A_R = 60$ mm.

Max A_R [mm]	Tail fraction T [%]	Stat. Error [%]	Syst. Error [%]
30	2.140	0.023	0.028
40	2.540	0.020	0.045
50	3.030	0.019	0.068
60	3.580	0.018	0.095
70	4.220	0.018	0.115
80	4.960	0.018	0.154
90	5.850	0.019	0.198
E_{cut} [MeV]			
50	2.780	0.016	0.063
51	3.130	0.017	0.076
52	3.580	0.018	0.095
53	4.140	0.020	0.116
54	4.850	0.021	0.142
55	5.740	0.023	0.173

6.1. Calorimeter's Low Energy Tail

beam ($\pm 0.1^\circ$), the centre of rotation of the crystal array (± 0.25 mm), the beam momentum (0.5%), and the beam divergence.³⁶ As our MC effectively reproduces the energy spectrum and tail fraction for all angles from the positron beam configuration, we are now confident to calculate the nominal pion beam tail fraction from our nominal $\pi^+ \rightarrow e^+\nu_e$ validated MC.

The systematic error in the $\pi^+ \rightarrow e^+\nu_e$ tail is different from the systematic error in the Response Function Measurement (RFM) tail. The error from the $\pi^+ \rightarrow e^+\nu_e$ tail shares two items from the RFM: energy calibration (± 0.1 MeV), and photo-nuclear scaling (1.1 ± 0.1). The photo-nuclear cross section scaling was done within experimental uncertainty [128]. There is an additional geometrical error coming from the uncertainty in the WC3 position (± 1 mm). Figure 6.4 shows the MC generated $\pi^+ \rightarrow e^+\nu_e$ energy spectrum in the calorimeter (Bina + CsI), including radiative components and events that underwent Bhabha scattering in the target B3. The cuts applied are energy deposit > 0.1 MeV in T1 and T2, pion decay at rest within the target, B1 energy between 3.8 and 5.2 MeV, and B2 energy between 2.0 and 3.1 MeV. The tail fraction is simply the number of counts below 52 MeV divided by the total number of counts; the value obtained with acceptance radius $A_R < 60$ mm is 3.58% with $\pm 0.05\%$, $\pm 0.05\%$, and $\pm 0.07\%$ uncertainty from the calorimeter energy calibration, photo-nuclear scaling, and WC3's position, respectively. In the same order, the value for $A_R < 40$ mm is $2.54\% \pm 0.03\% \pm 0.02\% \pm 0.02\%$. The tail correction for $A_R < 40$ mm has better uncertainty than $A_R < 60$ mm. Ten MC trees of one million events each were used for this result. Table 6.1 shows the tail fraction as a function of the maximum calorimeter's acceptance radius A_R and the E_{cut} energy.

Photo-nuclear interactions. The agreement between data and MC for all the tail fraction measurements from the positron data does not suggest by itself that low-energy beam positron contamination is negligible. In principle a low-energy tail in the beam could be masking some disagreement between MC and data. Thus, we need some way of validating that the agreement between data and MC for all the tail fraction measurements from the positron data is insensitive to the low-energy beam positron contribution. As shown in Ref. [127] this was done by selecting events from the positron beam data

³⁶ In electromagnetism, especially in optics, beam divergence is an angular measure of the increase in beam diameter or radius with distance from the optical aperture or antenna aperture from which the beam emerges.

6.1. Calorimeter's Low Energy Tail

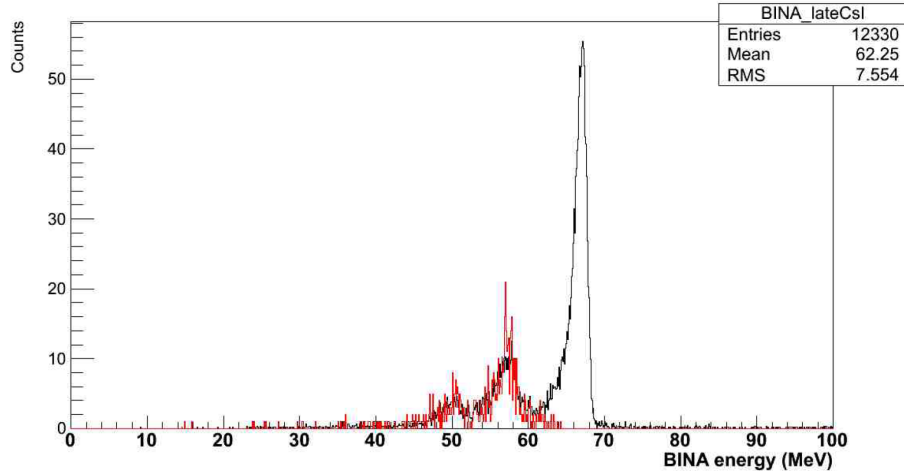


Figure 6.5: The BINA spectrum for events with a late hit (450 to 670 ns) in CsI. Data in black, MC in red. The two photo-nuclear peaks are enhanced.

with a late hit (450 to 670 ns) in CsI and looking for MC agreement; a reasonable fraction of the delayed neutrons produced in photo-nuclear interactions that escape Bina will deposit their energy in CsI [2]. The majority of CsI hits are at ~ 3 ns. Figure 6.5 shows the BINA spectrum in data and MC, for events with a delayed hit in CsI, with the photo-nuclear cross section scaled by 1.1. 0° data is used, where the shower leakage is smallest and thus the photo-nuclear peaks are best defined. Such agreement says that photo-nuclear effects are simulated properly, which suggest the low-energy beam positron contamination is not present. Additionally, an independent G4beamline simulation was implemented for the M13 beam-line channel to generate from production target (**T1**) through beam-line components the plausible positron contamination at focus point F4 (target B3). Such contamination was shown to be negligible for different beam-line configurations as shown in [6], and [20]. Section 6.1.2 will describe this attempt.

6.1.2 Beam-line's Intrinsic Tail

This section briefly explores the intrinsic positron low-momentum tail distribution coming from TRIUMF's M13 beam-line used for the PIENU experiment. This is relevant because of the potential for the positrons to scatter in the beamline, giving an intrinsic low momentum tail coming from the beam-line, as we assume such contribution is negligible it could mask a

6.1. Calorimeter's Low Energy Tail

portion of the low-energy tail due to the detector's energy leakage. This intrinsic beam positron low-momentum tail events cannot be excluded by cuts from the nominal pion beam analysis since the positron beam detector configuration only uses the wire-chambers, T2 scintillator, and the calorimeters. The approach is to simulate the production of the beam, transport through all beam-line components and spatial-energy distributions at the final focus point (F4) using the specific MC tool G4beamline [129]. Previous work on how positron distributions affect the experiment can be found in [130] and [131]. There was a set of special experimental runs to obtain the PIENU detector's response where the beam-line components were adjusted to obtain 75 and 70 MeV/c positron beams corresponding to runs #54880 and #81633 (Table D.1). Both configurations were tested with MC. Appendix D describes how the beam production target **T1** and beam-line components were implemented in the simulation, including the results of the simulation, comparison with run data, and systematic tests.

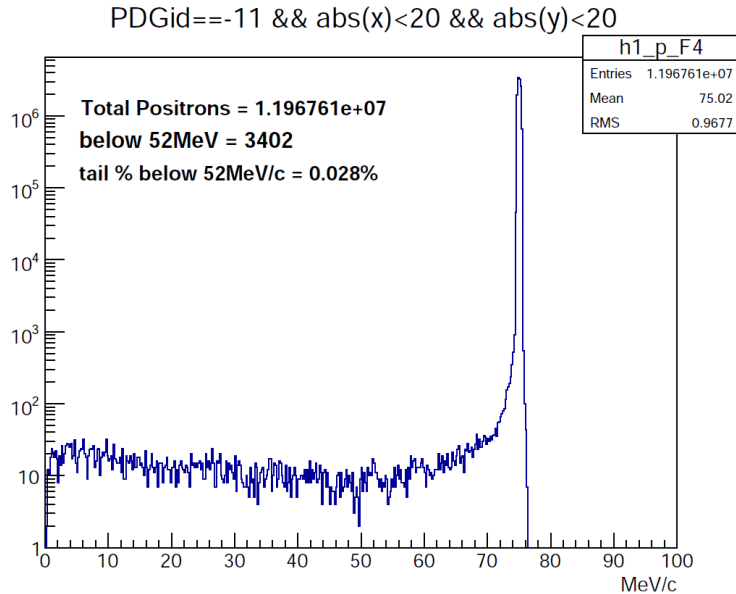


Figure 6.6: Positron momentum distribution at F4 (target B3), for the 75 MeV/c positron beam (run #54880).

The M13-beam-line output at F4 generated by G4beamline is shown in Figure 6.6 representing the positron beam-line configuration intrinsic mo-

6.1. Calorimeter's Low Energy Tail

momentum distribution. The momentum distributions at F4 include a square cut of ± 20 mm to exclude the beam halo similarly to beam cuts discussed for nominal pion data and positron data input into the calorimeter. The momentum vs. angle (between X and Z coordinates) distributions at F4 is shown in Figure 6.7 with a square cut of ± 20 mm. As F4's square cut is relaxed, the intrinsic beam contribution rises but such events can be safely ignored since their angle distribution does not point directly to the calorimeter; the maximum angle to enter the calorimeter is roughly 57 degrees corresponding to an acceptance radius $A_R = 90$ mm. The possibility for these excluded halo beam events or any others to reach the calorimeter by scattering with the beam-line's exit foil or air in between was not included in the simulation. After taking into consideration all settings and systematics mentioned in this section and appendix D, we set an upper limit to the Beam-line's contribution to the tail fraction T_{beam} at $(2.8 \pm 0.5) \times 10^{-4}$. The two different positron beam-line settings, 75 and 70 MeV/c beams show negligible differences in T_{beam} as shown in Table 6.2.

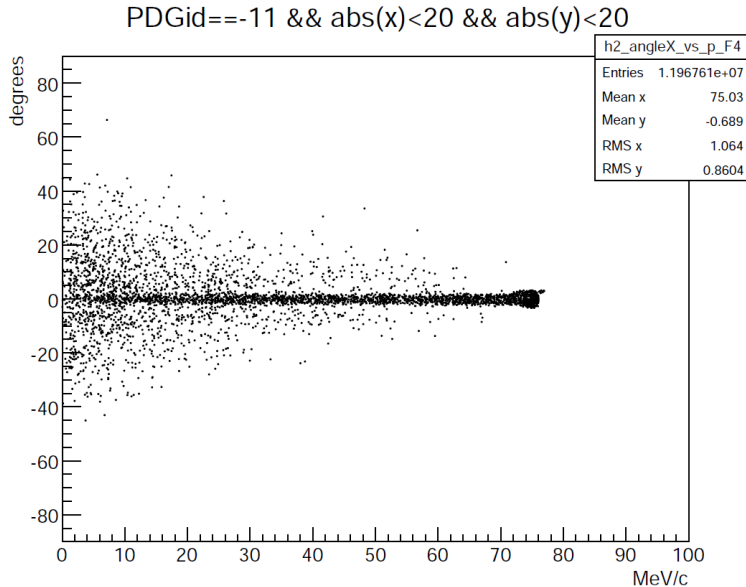


Figure 6.7: Positron momentum vs. angle distribution at F4 (target B3), for the 75 MeV/c positron beam (run #54880).

6.2. Acceptance

Table 6.2: Upper limit to beam-line’s contribution to tail fraction (T_{beam}) percentage.

T_{beam} [%]	Error [%]	Condition
0.028	< 0.005	75 MeV/c positron beam, 10^{10} simulated events, run #54880
0.027	0.005	70 MeV/c positron beam, 10^8 simulated events, run #81633

6.2 Acceptance

To first order, the detector’s acceptance for the $\pi^+ \rightarrow e^+\nu_e$ and $\pi^+ \rightarrow \mu^+\nu_\mu \rightarrow e^+\nu_e\bar{\nu}_\mu$ decays is the same, as they are both measured with the same detector and time interval. In second order, two effects may change the acceptance ratio: the extra spread in the starting position distribution of the decay positron caused by the $\mathcal{O}(1\text{ mm})$ distance traveled within target by the 4.1 MeV muon, and energy dependent interactions upstream of Bina. Figure 6.8(left) shows a cut on the full combined datasets of the total energy seen by the sum of B1, B2, B3, S1, and S2. This sum was defined as the pion total energy (E_{tot}) in Eq. 4.4. B3 used a longer (100 ns) integration window with respect to the branching ratio analysis. This choice allowed to integrate also the muon energy deposit. Because of the presence of the muon, the $\pi^+ \rightarrow \mu^+\nu_\mu \rightarrow e^+\nu_e\bar{\nu}_\mu$ decay deposits more energy in B3 with respect to the $\pi^+ \rightarrow e^+\nu_e$ decay. The E_{tot} distribution is used to identify LE and HE events in the pion stopping position distribution (Z_v) previously defined in Section 3.2.6. Figure 6.8(right) shows the pion stopping distribution for the combined datasets for both decay types.

Although, Z_v and E_{tot} parameters were not used to select events in the nominal analysis, it served as a diagnostic measure for beam momentum changes. It also turned out be a good complementary cut to separate the $\pi^+ \rightarrow e^+\nu_e$ and $\pi^+ \rightarrow \mu^+\nu_\mu \rightarrow e^+\nu_e\bar{\nu}_\mu$ energy distribution in the calorimeters. In Figure 6.9(a) the average peak position after all event selection cuts for 2010 in black, 2011 in red, and 2012 in blue are 0.2, -0.3, and 0.2 mm respectively. The different Z_v are due to beam momentum changes throughout the years as shown in Figure 6.9(b) and 6.9(c) for 2010 and 2012 respectively. On the other hand the 2011 dataset had an overall shift not because beam momentum change but due to an extra piece of material left near target B3 for a special set of runs for direct muon capture [17].

6.2. Acceptance

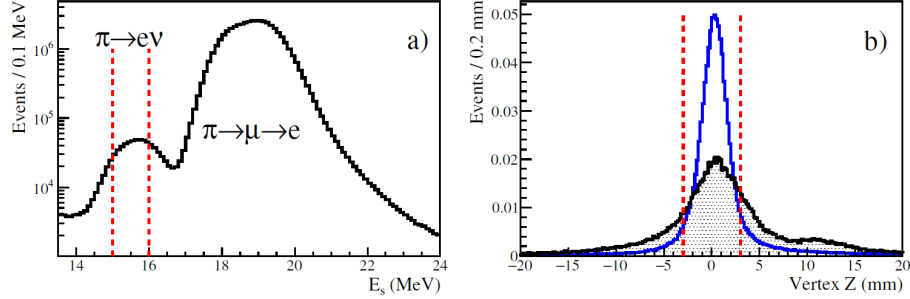


Figure 6.8: Left: Sum of the energies in B1, B2, S1, S2, and B3. Right: Z-vertex for events with positron energy $E_{cut} < 52$ MeV (shaded histogram) and $E_{cut} > 52$ MeV (blue full line). The two distributions are normalized to the same number of events, and cuts applied are indicated by the red vertical dashed lines. Image from [11].

Processes such as multiple Coulomb scattering, Bhabha scattering, and pair production occurring in the materials traversed by the decay positrons are energy dependent. As the two decay modes have different energy distributions, a small change in the acceptance is expected. Furthermore, the three main data-taking periods from 2010, 2011 and 2012 had slightly different input beam momenta and detector geometry. The beam differences may alter the pion stopping position; therefore, the correction may change. As all related processes are well-understood electromagnetic physics, the acceptance correction was estimated with MC independently for all three periods. A total of 10^9 events for each decay mode and data-taking period were simulated and the correction factor

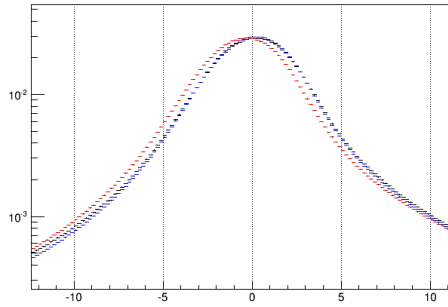
$$C_{Acc}(A_R) = \frac{N(\pi^+ \rightarrow \mu^+ \rightarrow e^+, A_R)}{N(\pi^+ \rightarrow e^+ \nu_e, A_R)} \quad (6.3)$$

was calculated. N is the number of events for the specified decay channel in the detector's energy spectrum (Bina+CsI) for a maximum value of the radius A_R . The branching ratio is corrected as,

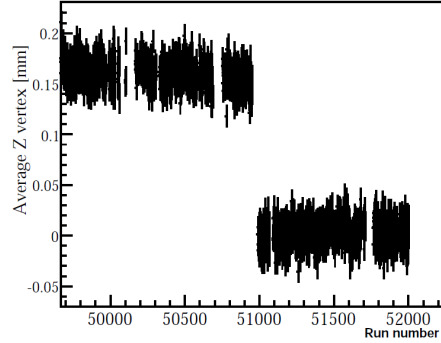
$$R_\pi = R_\pi^{raw} \times C_{Acc}. \quad (6.4)$$

The results are shown in Figure 6.10 for the 2012 dataset, the most significant data-taking period. It was found that the small differences in beam momentum and geometry in our datasets are negligible concerning acceptance correction C_{Acc} at our level of precision. The systematic error on C_{Acc}

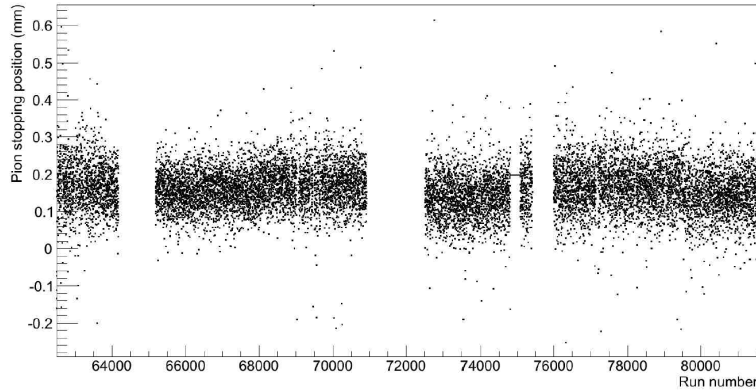
6.2. Acceptance



(a) The pion stopping position within target B3 or Z vertex (Z_v). The averages peak after all event selection cuts for cuts for 2010 in black, 2011 in red, and 2012 in blue are 0.2, -0.3, and 0.2 mm respectively.



(b) Z_v vs. run number for the 2010 dataset [16].



(c) Z_v vs. run number for the 2012 dataset [19].

Figure 6.9: The pion stopping position Z_v distribution from data.

was obtained by varying several parameters in the simulation: the position and width of the pion stopping distribution (Z_v), the positions and thicknesses of various detectors, and the trigger thresholds in T1 and T2. All the uncertainties, both statistical and systematic are at the 10^{-8} level and are therefore negligible for the branching ratio error budget. The acceptance correction for various A_R values is shown in Table 6.3. The change in the

6.3. Muon Decay in Flight

acceptance correction with different E_{cut} values is negligible at our level of precision.

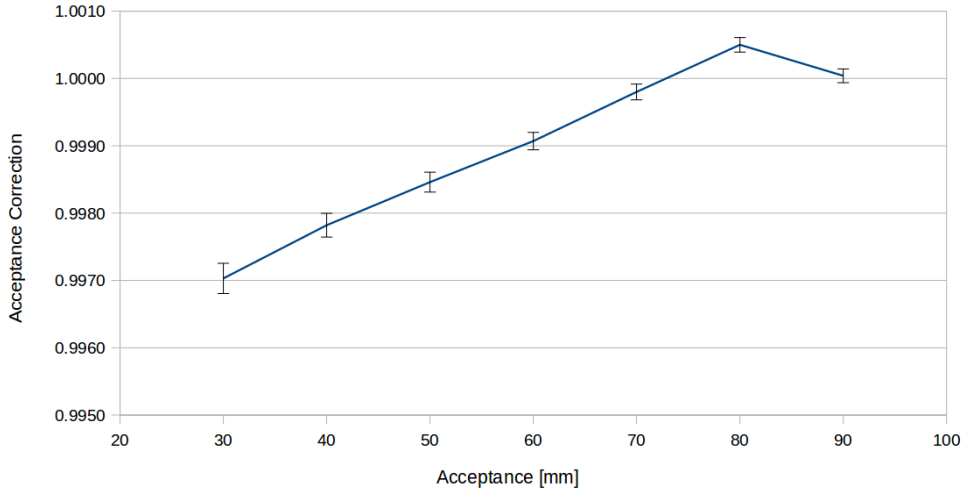


Figure 6.10: Acceptance correction C_{Acc} as a function of the A_R radius for the 2012 dataset. Error bars are only statistical.

Table 6.3: Acceptance correction C_{Acc} for different A_R values.

Max A_R (mm)	Correction C_{Acc}	Stat. Error
30	0.99703	0.00023
40	0.99782	0.00018
50	0.99846	0.00015
60	0.99907	0.00013
70	0.99980	0.00012
80	1.00050	0.00011
90	1.00004	0.00010

6.3 Muon Decay in Flight

The 4.1 MeV muons coming from the pion beam stopping in the centre of target B3 can decay in flight (μ DIF) inside the target. These events are a problem because the μ DIF kinetic energy can boost the LE positrons

above E_{cut} . Such a topology has the same timing distribution as the direct $\pi^+ \rightarrow e^+\nu_e$ decay. These events cannot be detected and separated from the $\pi^+ \rightarrow e^+\nu_e$ events; therefore, a correction is needed. The MC simulation shown in Figure 6.11(a) indicates that the decay time distribution of such DIF muons that were not at rest in the target is approximately flat between 0 and 19 ps. The probability of a muon decay in flight can be estimated as

$$1 - e^{-\frac{\tau_{\mu DIF}/\gamma}{\tau_{\mu}}} = 8.3 \times 10^{-6}. \quad (6.5)$$

Where $\gamma = 1/\sqrt{1-v^2/c^2} = 1.039$ for the muon kinetic energy $T_{\mu} = 4.1$ MeV, $\tau_{\mu DIF}$ is the time that the muon travels before it stops, about 19 ps. Typically decays in flight will have lost some energy, but the muon's 19 ps flight path is too short to lose a significant amount of kinetic energy T_{μ} . The proportion of these events above $E_{cut} = 52$ MeV and $A_R < 40$ mm was estimated to be 2.90% (Figure 6.11(b)), giving a total correction factor $C_{\mu DIF} = 0.0290 \times 8.3 \times 10^{-6} = 2.406 \times 10^{-7}$ for this case. Taking into account the level of agreement in the measured energy spectra between Monte-Carlo and data for both $\pi^+ \rightarrow \mu^+\nu_{\mu} \rightarrow e^+\nu_e\bar{\nu}_{\mu}$ events and the positron beam, the relative error on the proportion of the spectrum above 52 MeV is on the order of a few percent, resulting in an uncertainty on the correction of less than 10^{-8} . The error on $C_{\mu DIF}$ is negligible for our level of precision measurement. The values for different A_R and E_{cut} values are in Table 6.4. The additive correction $C_{\mu DIF}$ was embedded in the high energy time spectrum fitting function (Equation 5.11).

6.4 t_0

The starting point of the time spectrum analysis is t_0 . The timing of the positron signal from the main decays $\pi^+ \rightarrow e^+\nu_e$ and $\pi^+ \rightarrow \mu^+\nu_{\mu} \rightarrow e^+\nu_e\bar{\nu}_{\mu}$ is calculated by fitting the waveforms from the T1 scintillator. If the shape of the waveform depends on the positron energy, the extracted time can be energy-dependent, thereby affecting the branching ratio. To investigate this effect, special muon runs at 62 MeV/c making the muons stop at the centre of target B3, then the time spectra for different energy regions were constructed and t_0 was obtained by fitting the edge with a step function with Gaussian resolution. The correction used for this global analysis was obtained using data runs from 2011. The multiplicative correction was $C_{t_0} = 1.0006 \pm 0.0003$ [18]. As the error is only due to statistics, further precision could be achieved using more runs from the 2012 dataset. For the moment, the 2011 value is used for all datasets.

6.4. t_0

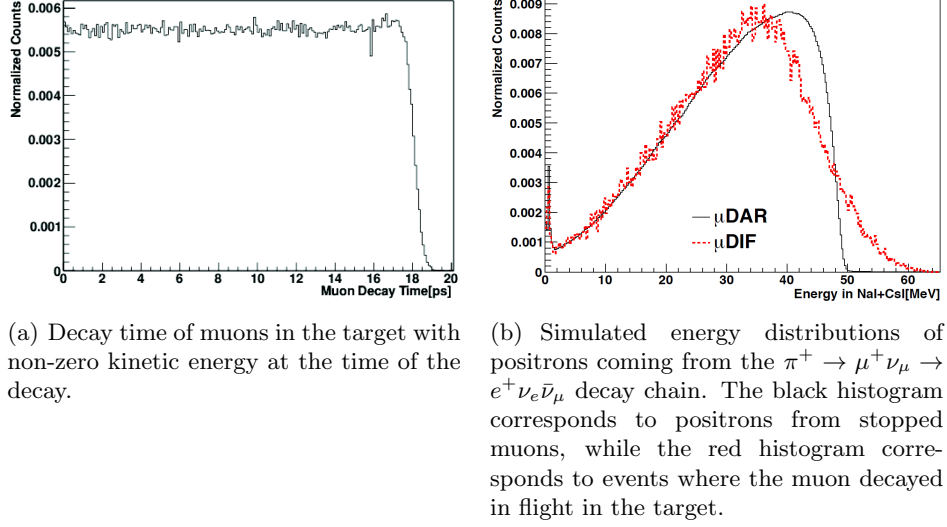


Figure 6.11: Time and energy spectra for μ DIF.

Table 6.4: Muon decay in flight correction $C_{\mu DIF}$ for different E_{cut} and A_R values.

Max A_R (mm)	Correction $C_{\mu DIF}$
30	2.533E-7
40	2.406E-7
50	2.219E-7
60	2.071E-7
70	1.937E-7
80	1.826E-7
90	1.727E-7
E_{cut} (MeV)	for $A_R < 60$ mm
50	3.374E-7
51	2.655E-7
52	2.071E-7
53	1.560E-7
54	1.175E-7
55	0.852E-7

Chapter 7

Results

Results from the branching ratio analysis are presented in this chapter. The previous two chapters described the fitting technique of the time spectra for the extraction of the raw branching ratio and its corrections. In this chapter, the results of the fits are reported together with the (blinded) corrected results for the branching ratio. The simultaneous fit to the high-energy and low-energy timing spectra allowed for the extraction of the raw branching ratio (R_π^{raw}), which had to be corrected with the corrections described in the previous chapter for obtaining the final branching ratio R_π^{exp} .

At the time of writing, the analysis is in its final stages and the data blinding has not been removed yet. The first analysis of the 2010 dataset has already been published [5], with an outdated event selection analysis and a different procedure for estimating the LET. For this thesis, we present the results of an improved re-analysis of the 2010 data combined with the results for the 2011 and 2012 datasets. Before results (and unblinding the data), some crucial tests on the R_π stability are presented in this chapter, i.e., branching ratio versus bin size, pileup time windows, acceptance (A_R), and high energy threshold (E_{cut}).

7.1 Stability and Systematic Errors

In general, all sensitivities of the branching ratio against other parameters were calculated following standard methodology [23], which were used to assign systematic errors by varying the parameters within reasonable ranges. Each particular case will be discussed in the rest of this section. The branching ratio difference (ΔR) and the uncorrelated statistical error (Δe) between two different branching ratio calculations is defined as,

$$\Delta R \pm \Delta e = (R - R') \pm \sqrt{|e_{\text{stat.}}^2 - e'_{\text{stat.}}|^2} \quad (7.1)$$

where e_{stat} is the raw statistical error from the test point and e'_{stat} from the anchor or nominal point to be tested against, with ΔR being the branching

ratio difference from the test point R and anchor R' . The uncorrelated statistical error (Δe) between two different branching ratio calculations is defined as $\sqrt{|e_{\text{stat.}}^2 - e'_{\text{stat.}}{}^2|}$ to show how much statistical difference there is between the two. Normally the errors are summed in quadrature, i.e., $\sqrt{e_{\text{stat.}}^2 + e'_{\text{stat.}}{}^2}$, but we are interested in difference between two different branching ratio calculations not in adding errors from the same calculation. For the rest of the chapter all quoted branching ratio changes are in 10^{-8} units for simplicity, unless specified otherwise.

7.1.1 Fit Tests

The shapes derived from MC were modified to assess the dependence of the R_{π}^{raw} on them. Additional background shapes were included in the fit for checking the sensitivity of the R_{π}^{raw} to small unaccounted backgrounds. The shapes tested were a flat background, and a faster ($\tau_{\mu}/2$) decay time component. The R_{π}^{raw} must be stable against changes in the fit conditions. The fit results were tested by changing the fitting range, bin width, and time resolution effects.. The stability of the R_{π}^{raw} was checked when the parameters of the fit were changed. This includes changing the pion and muon lifetimes, the contribution of the radiative decay, and the variation of t_0 . Results are shown in Table 7.1.

Time Resolution Effects: The fitting function nominally uses the probability distribution functions (PDFs) $\mathcal{E}_{\pi \rightarrow \mu \rightarrow e}(t)$ (Eq. 5.2) and $\mathcal{E}_{\pi \rightarrow e}(t)$ (Eq. 5.3) for the $\pi^+ \rightarrow \mu^+ \nu_{\mu} \rightarrow e^+ \nu_e \bar{\nu}_{\mu}$ and $\pi^+ \rightarrow e^+ \nu_e$ signals, respectively. In order to test the effects of including the time resolution (σ) from the scintillators (B1 and T1) from which the timing signal is extracted, the PDFs are replaced by $\mathcal{E}'_{\pi \rightarrow \mu \rightarrow e}(t, \sigma)$ (Eq. 5.4) and $\mathcal{E}'_{\pi \rightarrow e}(t, \sigma)$ (Eq. 5.5). The time difference between B1 and T1 has the time resolution of $\sigma = (0.3 \pm 0.1)$ ns. Figure 7.1 shows ΔR vs time resolution (σ) where the x -axis is the time resolution from the scintillators in ns and the y -axis is in ΔR units, with zero change representing 2012(PH)'s nominal analysis result for $\sigma = 0$ ns. The uncorrelated statistical error is zero for all points since there is no change in statistics for this test. The blue solid line represents the 2012 dataset pulse-height (PH) based branching ratio. The blue dashed line represents the actual time resolution from the scintillators. Since time resolution effects are negligible for the branching ratio to our level of precision, i.e., $\Delta R < 1$ change. Eq. 5.2 and 5.3 have been used for the PDFs.

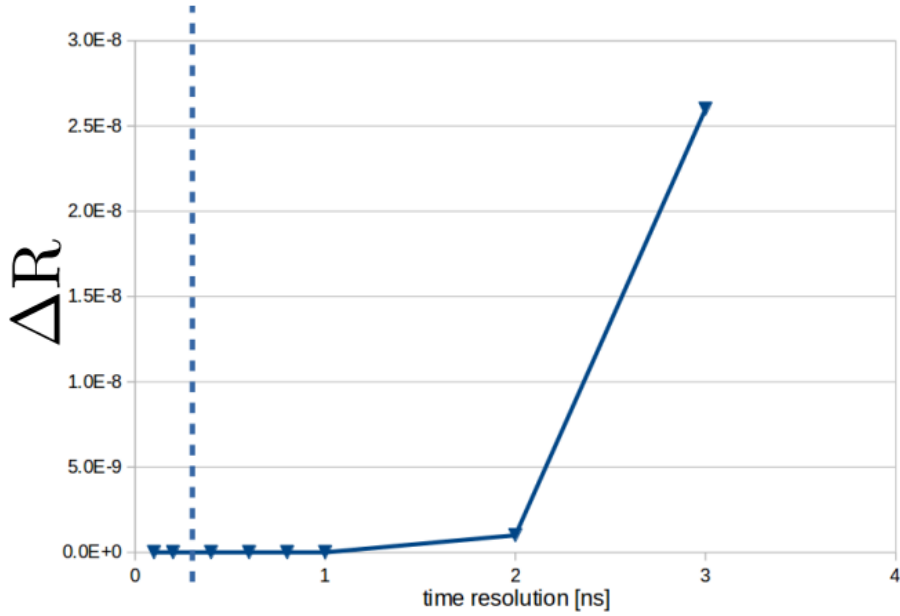


Figure 7.1: Change in the branching ratio ΔR vs time resolution: The x -axis is the time resolution from the scintillators. The y -axis is in ΔR units, with zero change representing 2012(PH)’s nominal analysis (without time resolution effects). The uncorrelated statistical error is zero for all points since there is no change in statistics for this test. The blue solid line represents the 2012 dataset pulse-height (PH) based branching ratio. The blue dashed line represents the actual time resolution from the scintillators (B1 and T1) from which the timing signal is extracted. The change in the branching ratio ΔR is $< 1 [10^{-8}]$ for time resolutions < 2 ns. Since the time difference between B1 and T1 has the time resolution of $\sigma = (0.3 \pm 0.1)$ ns the time resolution effects are negligible for the branching ratio to our level of precision.

Triggers: The variation of the R_{π}^{raw} between the time spectrum with only the Prescale trigger and the combined triggers was $\Delta R < 1 [18]$, i.e., below our precision goal. The combined triggers improved the statistics by 10%.

Fitting Range: The nominal range for our fitting function (FF) for both high and low energy time spectra is from -290 to 520 ns, excluding prompt events from -20 to 10 ns. In order to test the stability of the FF, these values were shifted. Ideally, the FF should report no change in the raw branching

7.1. Stability and Systematic Errors

ratio (R_{π}^{raw}) within uncorrelated statistical error, since such shifts effectively do change the level of statistics in the analysis. All R_{π}^{raw} are changes either of 1σ deviation or are at the level of $\Delta R < 1$, thus not significant to our level of precision. This is shown in Table 7.1, where the bottom limit goes from -290 to -250 ns, the bottom prompt limit from -20 to -30 ns, the top prompt limit from 10 to 8 ns, and the top limit from 520 to 490 ns.

Lifetimes: Nominally, both the muon and pion lifetimes (LT) in the fitting function (FF) are fixed to PDG values. Ideally, the FF should find both LTs at PDG values and report no change in the raw branching ratio (R_{π}^{raw}) within the uncorrelated statistical uncertainty. As shown in Table 7.1, when lifetimes are set free for the 2012 charge-integration (Q) based R_{π}^{raw} there is a change of 1.4 ± 3.7 ns (0.4σ variation) in the muon LT, no change in the pion LT, and a change in $\Delta R \pm \Delta e$ of 5.0 ± 18.3 (0.3σ variation). Such variations for the muon LT, pion LT, and $\Delta R \pm \Delta e$ when the LT parameters are set free on the fitting function are acceptable since the changes are consistent with zero, thus there is no need to add a systematic error to the final error budget. The other datasets behave similarly.

Fixed Parameters: Nominally, the amplitude of $\pi^+ \rightarrow \mu^+ \nu_{\mu} \gamma$ and T1 resolution background energy distributions are fixed in the fitting function (FF). To test their sensitivity to the FF, $\pi^+ \rightarrow \mu^+ \nu_{\mu} \gamma$ was varied by $\pm 20\%$ and the T1 resolution by $\pm 50\%$. The results are shown in Table 7.1. For $\pi^+ \rightarrow \mu^+ \nu_{\mu} \gamma$ there is a change in the raw branching ratio of about $\Delta R = \pm 3$ for all three datasets in both the integration-charge (Q) and pulse-height (PH) branching ratio calorimeter based variables. The uncertainty of $\pi^+ \rightarrow \mu^+ \nu_{\mu} \gamma$ is also $\pm 20\%$ [18], thus a global systematic uncertainty of ± 3 is assigned to the experiment. The uncertainty of the T1 resolution is only $\pm 10\%$, therefore after proper weighting all errors fall to either below 1σ deviation from error or at a level $\Delta R < 1$ change in R_{π}^{raw} . The fixed pion stopping time (t_0) in target B3 was extracted to be 2.15, 2.24, and 1.68 ns for 2012, 2011 and 2010 respectively ([19], [18], [16]); thus t_0 was shifted ± 1 ns to cover such uncertainty; such changes were found to be $\Delta R < 1$ change in R_{π}^{raw} . It was observed that the changes in t_0 are compensated by the πDIF parameter from the FF. This is expected since t_0 is degenerate with πDIF parameter. The error in the muon decay in-flight correction ($C_{\mu\text{DIF}}$) used in the FF is negligible [18], thus there is no systematic error to report here.

Old-muon No-T1-Hit MC shape: The old-muon time distribution described in Section 5.2.4 and shown in Figure 5.6 was generated with Geant4 Monte Carlo. In order to test the sensitivity to the raw branching ratio (R_{π}^{raw}) the shape was binned to 1, 2, 3, and 4 ns and shifted ± 1 ns independently from the time spectra, Table 7.1 shows the non-negligible deviations ΔR of 3.5, 5.4, 2.6, and 3.5 units for the 2011-PH, 2011-Q, 2010-PH, and 2010-Q datasets.

Other backgrounds: Table 7.1 shows tests for additional background shapes included in the fit for checking the sensitivity of R_{π}^{raw} to small unaccounted for backgrounds. Activating a flat component (due to time-independent backgrounds) shows a negligible deviations for the 2012-PH and 2012-Q datasets, but there are non-negligible deviations ΔR of -3.9, -3.5, -4.7, and -4.5 units for the 2011-PH, 2011-Q, 2010-PH, and 2010-Q datasets. On the other hand when a double μ lifetime (falling twice as fast) as $\mathcal{E}_{\mu \rightarrow e}(2t)$ (Eq. 5.6 evaluated with $2t$) time spectra is enabled, there is no significant change in R_{π}^{raw} .

Pre-pileup: Nominally as discussed in Section 4.2.3, no hits are allowed in the scintillators before the arrival of the pion (pre-region). An important diagnostic test was the stability of the R_{π}^{raw} as more pileup is allowed in the trigger window. This test shows how robust and precise is the PIENU time spectrum analysis to identify and model pileup correctly. Toward this end, the PrePileup (PrePU) window identified by the PrePileup Cut was varied. This cut normally rejects events in a $-6.4 \mu\text{s}$ to $-2.2 \mu\text{s}$ window before the arrival of the pion ($-7.7 \mu\text{s}$ to $-3.5 \mu\text{s}$ window with respect to trigger time, as shown in Figure 4.1). The rejection window was varied in B1, B2, B3, T1, and T2 scintillators to be sensitive to both sections, before and after the pion to lepton vertex. The dependence of the R_{π}^{raw} from the PrePU window width was studied.

Figure 7.2 shows the stability of the charge-integration (Q) and pulse-height (PH) based ΔR vs. PrePU window for the 2010 (yellow), 2011 (orange) and 2012 (blue) datasets. The x -axis is the PrePU window in ns units. The y -axis is in ΔR change units, with zero change representing 2012(PH)'s nominal analysis (PrePU cut enabled). The error bars on each point represent the uncorrelated statistical error between the point in question and the nominal point with the error bars going up when there is a statistical increase and down otherwise. For comparison, the horizontal dashed black

lines both at the same distance from nominal represent the raw statistical error from the 2012 dataset. PrePU is allowed in from left to right, the point at $-7,500$ ns trigger time ($-7.5 \mu\text{s}$) is the closest to the nominal prePU cut, therefore as the inclusion window is relaxed further right, there is an increase in statistics. When the window is completely relaxed at $-3,500$ ns trigger time ($-3.5 \mu\text{s}$) it is equivalent to not applying the PrePU cut.

The PH versions are better than Q-based branching ratios, and it is also clear that both versions of 2012 are better than the rest. The χ^2 values for 2010 and 2011 shown in the bottom of Figure 7.2 do increase as the pre-pile-up window is relaxed to the right. The 2012 data advantage is the extra detection mechanism for out of time pions and related pileup as described in Section 4.2.3. The branching ratio varies considerably as pileup is added to the spectrum, indicating the presence of an incorrect shape or missing component in the time spectrum fit. However, the impact on the branching ratio monotonically becomes negligible especially for the 2012 dataset (both Q and PH versions) as the cut approaches its nominal value. Since the 2012 dataset is the most significant statistically, no systematic error was included in the final branching ratio.

Binning: The fitting function uses 1-ns bins for the nominal analysis. Ideally the raw branching ratio (R_{π}^{raw}) should be independent of the bin size within a reasonable range. Figure 7.3 shows ΔR change vs. bin size from 1 to 8 ns bins for all three datasets in both the integration-charge (Q) and pulse-height (PH) based R_{π}^{raw} . The ΔR change is stable within 1 to 8 ns binning. The χ^2 values are best when the fitting function uses 1-ns bins and grows monotonically for greater binning, as shown in Figure 7.3. The negligible ΔR variations with different bin sizes may be due to different sampling rates from different DAQ hardware components. No systematic error was applied for this effect.

Table 7.1: Stability tests and systematic errors from the fit, following standard methodology [23]. Non-negligible deviations are in red. See Section 7.1.1 for discussion. Units in the branching ratio change are ΔR [10^{-8}], with uncorrelated errors unless specified otherwise.

$\Delta R \pm \Delta e$ [10^{-8}]	2012(PH)	2012(Q)	2011(PH)	2011(Q)	2010(PH)	2010(Q)
Stability tests						
Fitting range, t						
positive limit: 520 \rightarrow 490	0.1 ± 0.7	0.5 ± 0.7	-1.5 ± 1.2	-0.3 ± 1.3	-1.0 ± 1.5	0.2 ± 1.6
prompt positive: 10 \rightarrow 8	-2.9 ± 4.1	-2.9 ± 4.3	2.4 ± 7.4	2.2 ± 7.6	8.9 ± 8.9	9.3 ± 9.1
prompt negative: $-20 \rightarrow -30$	0.1 ± 0.1	0.0 ± 0.1	0.2 ± 0.2	0.2 ± 0.3	0.1 ± 0.2	0.1 ± 0.2
negative limit: $-290 \rightarrow -250$	0.0 ± 0.0	-0.1 ± 0.1	0.0 ± 0.0	0.0 ± 0.3	0.0 ± 0.1	0.0 ± 0.1
Lifetimes						
$\Delta R, \tau_\mu$ and τ_π free	4.6 ± 18.1	5.0 ± 18.3	-38.9 ± 38.2	-47.1 ± 38.8	8.8 ± 46.3	1.3 ± 47.0
$\tau_\mu^{fit} - \tau_\mu^{PDG}$ [ns]	1.4 ± 3.7	1.4 ± 3.7	-6.8 ± 6.4	-8.2 ± 6.4	1.3 ± 7.7	-1.8 ± 7.7
$\tau_\pi^{fit} - \tau_\pi^{PDG}$ [ns]	0.0 ± 0.0	0.0 ± 0.0	0.1 ± 0.0	0.1 ± 0.0	0.0 ± 0.0	0.0 ± 0.0
Systematic errors from sensitivities						
Fixed Parameter						
$\pi \rightarrow \mu\gamma$ ($\pm 20\%$)	$\pm 3.2 \pm 0.0$	$\pm 2.9 \pm 0.0$	$\pm 3.1 \pm 0.0$	$\pm 2.8 \pm 0.1$	$\pm 3.1 \pm 0.0$	$\pm 2.8 \pm 0.0$
T1 resolution ($\pm 50\%$)	$\pm 1.0 \pm 2.5$	$\pm 0.9 \pm 0.0$	$\pm 2.5 \pm 4.9$	$\pm 2.3 \pm 0.1$	$\pm 2.4 \pm 5.5$	$\pm 2.2 \pm 0.0$
T1's effective error [ΔR] ($\pm 10\%$ uncertainty)	0.2 ± 2.5	0.2 ± 0.0	0.5 ± 4.9	0.5 ± 0.1	0.5 ± 5.5	0.4 ± 0.0
Old-muon MC shape						
2 ns bin	-0.4 ± 0.0	-0.3 ± 0.1	-1.1 ± 0.1	-0.9 ± 0.2	-0.7 ± 0.1	-0.7 ± 0.1
3 ns bin	-0.5 ± 0.0	-1.0 ± 0.1	-1.0 ± 0.1	-2.8 ± 0.2	-0.1 ± 0.2	-1.8 ± 0.2
-1 ns shift	-1.1 ± 0.1	-1.2 ± 0.1	-2.6 ± 0.1	-3.3 ± 0.3	-1.9 ± 0.2	-2.2 ± 0.2
$+1$ ns shift	0.9 ± 0.1	1.1 ± 0.1	2.3 ± 0.3	3.2 ± 0.3	1.8 ± 2.5	2.1 ± 0.3
effective syst. error [ΔR]	0.0	0.0	3.5	5.4	2.6	3.5
Other backgrounds						
Flat component	-0.9 ± 0.5	-0.8 ± 0.5	-3.9 ± 1.5	-3.5 ± 1.6	-4.7 ± 1.8	-4.5 ± 1.8
$\mathcal{E}_{\mu \rightarrow e}(2t)$ (Eq. 5.6)	0.0 ± 0.0	0.0 ± 0.0	0.0 ± 0.1	0.2 ± 0.3	0.1 ± 1.3	0.2 ± 0.4

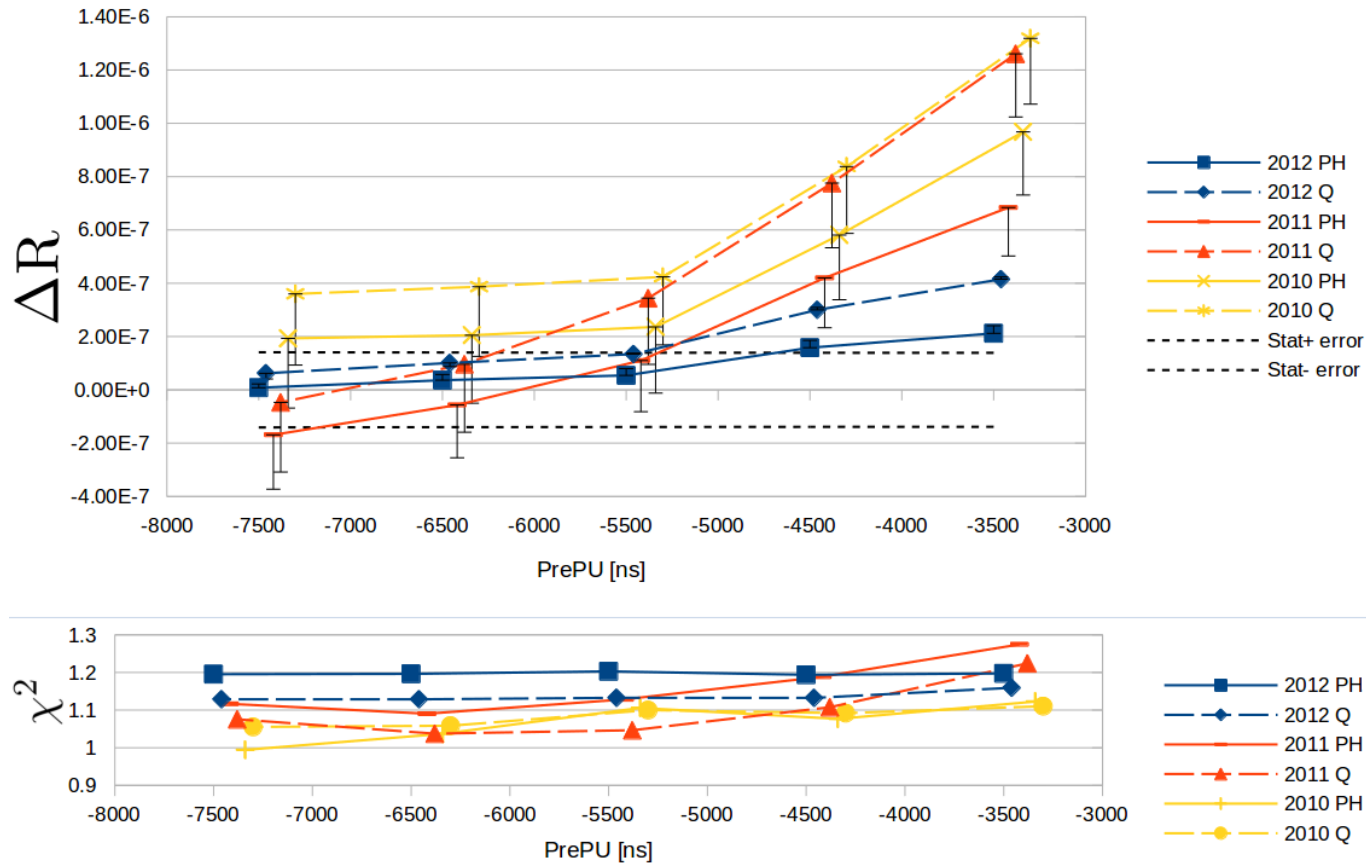


Figure 7.2: $\Delta R \pm \Delta e$ (Eq. 7.1) vs. PrePU: The x -axis is the PrePU window in ns units (Figure 4.1). The y -axis is in ΔR units, with zero change representing 2012(PH)'s nominal analysis (PrePU cut enabled), the error bars (Δe) on each point represent the uncorrelated statistical error between the point in question and the nominal point with the error bars going up, when there is a statistical increase, and down otherwise. The horizontal dashed black lines, both at the same distance from nominal, represent the raw statistical error from the 2012 dataset.

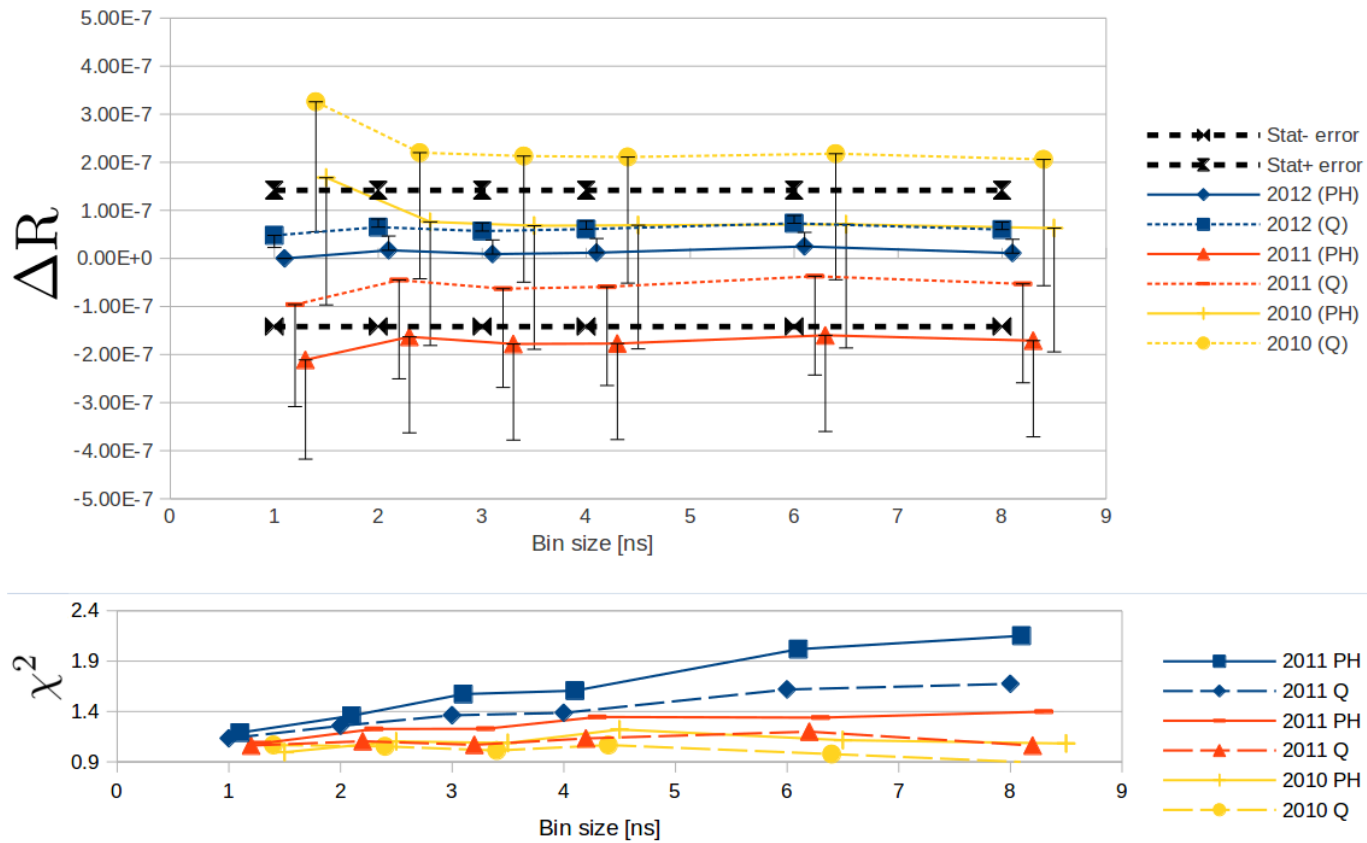


Figure 7.3: $\Delta R \pm \Delta e$ (Eq. 7.1) vs Bin size: The x -axis is the bin size in ns units. The y -axis is in ΔR units, with zero change representing 2012(PH)'s nominal analysis (binning 1 ns), the error bars (Δe) on each point represent the uncorrelated statistical error between the point in question and the nominal point with the error bars going up, when there is a statistical increase, and down otherwise. The horizontal dashed black lines, both at the same distance from nominal, represent the raw statistical error from the 2012 dataset.

7.1.2 LET tests

As the LET is the main correction for R_π , two tests involving it are particularly important. The LET changes if a different acceptance radius A_R is chosen, as well as a different energy threshold E_{cut} for separating the two energy regions. If R_π is calculated with different A_R and E_{cut} , a different LET correction has to be applied. If the LET-corrected R_π is stable against the change in A_R and E_{cut} , there is confidence that the LET is globally known. The stability of R_π with respect to variations of A_R and E_{cut} has already been demonstrated in the first published results [5]; here it is currently finalized for the other datasets.

Figure 7.4 shows the stability of the charge-integration (Q) and pulse-height (PH) based R_π vs. A_R for all datasets. The x-axis is the A_R value in mm units. The y-axis is in R_π (corrected) change units. The horizontal line at zero represents 2012(PH)'s analysis using anchor point with cuts $E_{\text{cut}} = 52$ MeV and $A_R = 60$ mm.³⁷ The error bars on each point represents the uncorrelated statistical error between the point in question and the anchor point with the error bars going up when there is a statistical increase and down otherwise. The dashed black lines both at the same distance from anchor represent the calorimeter's LET systematic error (Table 6.1). The bottom part of Figure 7.4 shows the total χ^2 from the fitting function for each point.

There is a slight but clear downward trend after $A_R > 60$ mm, although those point's statistical bars are within the LET's systematic error envelope. The calorimeter's response function measurement (Section 6.1.1) corrections as a function of acceptance (A_R) were confirmed against GEANT4 until $A_R = 60$ mm (effective maximum rotation angle for the calorimeter); for $A_R > 60$ mm the corrections are only GEANT4 predictions presented for completeness. It is also worth pointing out that χ^2 also grows monotonically as the acceptance A_R is relaxed. There is no A_R dependence, since points for both Q- and PH-based R_π are within statistical error from the systematic uncertainties envelope (Table 6.1) from the horizontal anchor.

³⁷ The nominal acceptance radius cut for this thesis is $A_R = 40$ mm. But for the LET tests the value of $E_{\text{cut}} = 52$ MeV and $A_R = 60$ mm was kept as the anchor comparison point for historical reasons, i.e., the 2010 dataset branching ratio publication [5] used 60 mm.

Figure 7.5 shows the stability of the charge-integration and pulse-height based R_π vs. high and low energy threshold (E_{cut}) for all datasets. The x -axis is the E_{cut} value in MeV units. The y -axis is in R_π change units. The horizontal line at zero represents the 2012(PH)'s analysis using an anchor point with cuts $E_{\text{cut}} = 52$ MeV and $A_R = 60$ mm. The error bars on each point represent the uncorrelated statistical error between the point in question and the anchor point with the error bars going up when there is a statistical increase and down otherwise. The horizontal dashed black lines both at the same distance from the anchor represent the calorimeter's LET systematic error. The bottom part of Figure 7.5 shows the total χ^2 of the fitting function for each point. There is no E_{cut} dependence, since points for both Q- and PH-based R_π are within the statistical error from the systematic uncertainties envelope (Table 6.1) from the horizontal anchor.

7.1.3 Charge- vs. Pulse-height-based R_π

The charge (Q) and pulse-height (PH) based R_π for 2012, 2011, and 2010 datasets can be compared in different stability and systematic tests shown in Figure 7.2 for R_π^{raw} change vs. PrePU, Figure 7.3 for R_π^{raw} change vs. binning, Figure 7.4 for R_π change vs. A_R , and Figure 7.5 for R_π change vs. E_{cut} . The Q-based R_π is consistently higher for all points. To assign a systematic error to the difference between Q and R, all points from the R_π vs. A_R and vs. E_{cut} were taken into account. Half of the average from the difference for each point was found to be 3.0, 4.2, and 5.9 [R_π^{raw}] units for 2012, 2011, and 2010, respectively. These differences are due to PH being less sensitive to pileup. Such non-negligible variations are included in the final error budget presented in the following section (Section 7.2).

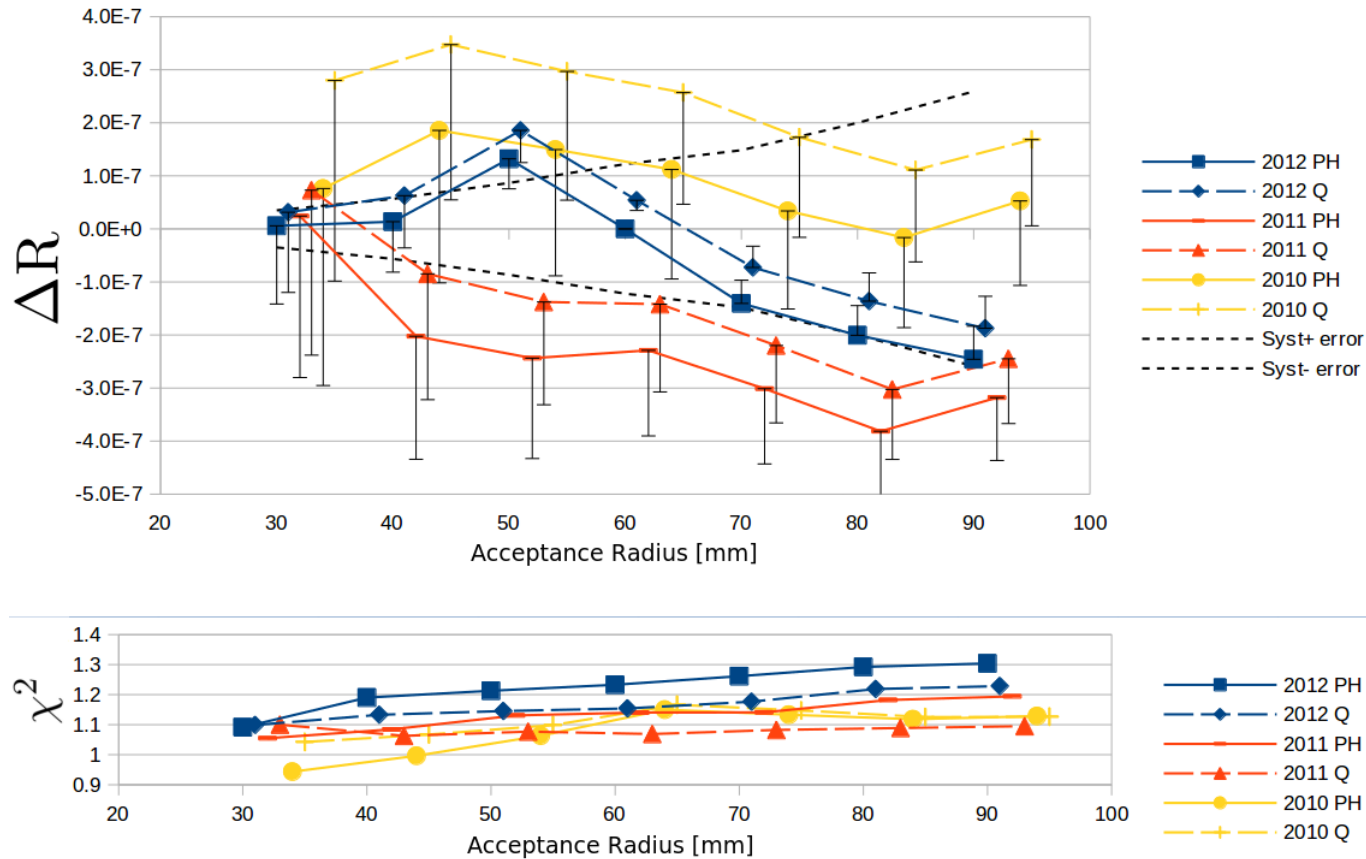


Figure 7.4: $\Delta R \pm \Delta e$ (Eq. 7.1) vs. A_R , Charge Integration and Pulse-height: The x -axis is the A_R value in mm units. The y -axis is in ΔR (corrected) units, with zero change representing 2012(PH)'s analysis using anchor point with cuts $A_R = 60$ mm and $E_{\text{cut}} = 52$ MeV, the error bars (Δe) on each point represent the uncorrelated statistical error between the point in question and the anchor point with the error bars going up when there is an statistical increase and down otherwise. The horizontal dashed black lines both at the same distance from anchor represent the calorimeter's LET systematic error. The bottom part shows the total χ^2 from the fitting function for each point.

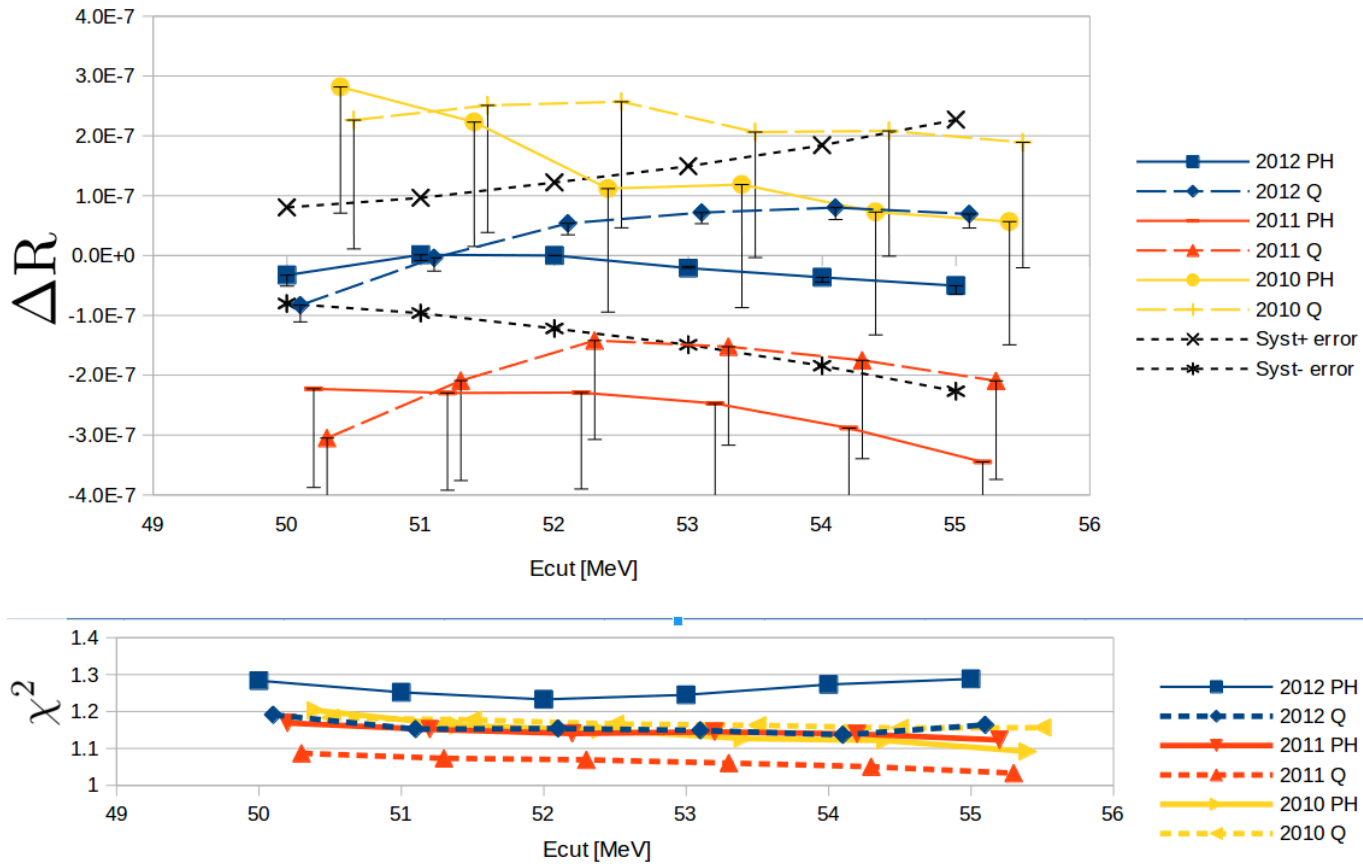


Figure 7.5: $\Delta R \pm \Delta e$ (Eq. 7.1) vs. E_{cut} , Charge Integration and Pulse-height: The x -axis is the E_{cut} value in MeV units. The y -axis is in ΔR units, with zero change representing 2012(PH)'s analysis using anchor point with cuts $A_R = 60$ mm and $E_{cut} = 52$ MeV, the error bars (Δe) on each point represent the uncorrelated statistical error between the point in question and the anchor point with the error bars going up when there is an statistical increase and down otherwise. The horizontal dashed black lines both at the same distance from anchor represent the calorimeter's LET systematic error. The bottom part shows the total χ^2 from the fitting function for each point.

7.2 Error Budget

All year-dependent and common errors are shown in Table 7.2. The first row is the header for the year-dependent systematic errors, the second row comes from the flat component test described in section 7.1.1, the third row old-muon shape (Section 5.2.4) test (Section 7.1.1), the fourth row is the assigned error for the differences between Q- vs. PH-based branching ratios (Section 7.1.3), and the fifth row is the quadrature sum of the previous three rows ($\sqrt{\Sigma_\alpha^2}$), which will be used as the total year-dependent systematic error in the final branching ratio calculation.

The sixth row displays the statistical uncertainties for each dataset for both PH- and Q-based R . The seventh row is the header for the common systematic uncertainties grouped in two categories, one for PH- and another for Q-based R . The eighth row corresponds to the $\pi \rightarrow \mu\gamma$ MC generated shape (Section 5.2.5) test (Section 7.1.1). The ninth and tenth rows are the systematic errors assigned to the pion energy (Section 4.2.1) and false trigger (Section 4.2.3) cuts, respectively. The eleventh row is the quadrature sum of the previous three rows ($\sqrt{\Sigma_\beta^2}$), which will be used as common systematic error in the final branching ratio calculation. Finally, the common statistical and systematic errors coming from the corrections (Chapter 6) are listed, specially the low energy tail, acceptance, and t_0 .

Table 7.2: Error budget in [10^{-8}] branching ratio units.

Dependent (syst)	2012(PH)	2012(Q)	2011(PH)	2011(Q)	2010(PH)	2010(Q)
Flat §7.1.1	0.0	0.0	3.9	3.5	4.7	4.5
Oldmuon-No-T1-Hit §7.1.1	0.0	0.0	2.5	4.2	1.9	2.8
PH vs. Q §7.1.3	3.0		4.2		5.9	
$\sqrt{\Sigma_\alpha^2}$	3.0	3.0	6.2	6.9	7.8	7.9
Statistics ($R_A = 40$ mm) §5.3.4	14	14	25	25	30	31
Common (syst)	(PH)			(Q)		
$\pi \rightarrow \mu\gamma$ §7.1.1	3.1			2.8		
Pion cut §4.2.1	3			5		
FalseTrig cut §4.2.3	3			3		
$\sqrt{\Sigma_\beta^2}$ ($R_A = 40$ mm)	5.2			6.4		
LET ($R_A = 40$ mm) §6.1	2 (stat), 5 (syst)					
Acceptance §6.2	2 (stat)					
C_{t_0} §6.4	3 (stat)					

7.3 Combination of Datasets

The three different datasets were collected in similar conditions, but differences are present besides the statistics collected. The differences do not allow for a global fit of all the data available. Therefore, the three branching ratios have to be combined after the separate fits to the timing spectra. In ref. [132], a procedure for combining the R_π is outlined. The raw branching ratios (R_π^{raw}) for each year with their respective statistical and systematic errors are $Y_i \pm \delta Y_i^{\text{st.}} \pm \delta Y_i^{\text{sy.}}$, labeling the data taking periods with the index $i = 1, 2, 3$ the 2010, 2011, and 2012, respectively. The dataset-dependent corrections with their uncertainties are $C_{ij} \pm \delta C_{ij}^{\text{st.}} \pm \delta C_{ij}^{\text{sy.}}$, labeling the multiplicative corrections with index $j = 1, \dots, J$.

In the present analysis there are no dataset-dependent corrections, but they are presented for completeness or for future use if needed. The dataset-independent (common) corrections with their uncertainties are $C_k \pm \delta C_k^{\text{st.}} \pm \delta C_k^{\text{sy.}}$, using index $k = 1, 2, 3$ for the LET (C_T), Acceptance (C_{Acc}), and t_0 (C_{t_0}), respectively. The common global systematic uncertainties are (see Section 7.1, and Table 7.2) $\pm \delta S = \sqrt{\Sigma S_\beta^2}$ with index $\beta = 1, 2, 3$ for $\pi \rightarrow \mu\gamma$, pion cut, and false trigger cut, respectively.

Defining the branching ratio for each year corrected for dataset-dependent corrections with uncertainties as $R_i \pm \delta R_i^{\text{st.}} \pm \delta R_i^{\text{sy.}}$ with index $i = 1, 2, 3$ for the 2010, 2011, and 2012, respectively,

$$R_i = Y_i \Pi C_{ij}, \quad (7.2)$$

$$\delta R_i = \sqrt{(R_i)^2 [(\delta Y_i / Y_i)^2 + \Sigma (\delta C_{ij} / C_{ij})^2]}. \quad (7.3)$$

Since there is no dataset-dependent correction, then $C_{ij} = 1$ and $\delta C_{ij}^{\text{st.}} = \delta C_{ij}^{\text{sy.}} = 0$ for all i and j , effectively making $R_i = Y_i$. The branching-ratio-weighted average with uncertainties before common corrections is $R_s \pm \delta R_s^{\text{st.}} \pm \delta R_s^{\text{sy.}}$, defined as,

$$R_s = \Sigma R_i w_i / \Sigma w_i, \quad (7.4)$$

$$\delta R_s = \sqrt{\Sigma (\delta R_i w_i / \Sigma w_i)^2}, \quad (7.5)$$

where the combined statistical plus systematic weight for each dataset is,

$$w_i = 1 / \{ (\delta Y_i^{\text{st.}})^2 + (R_i)^2 [(\delta Y_i^{\text{sy.}} / Y_i)^2 + \Sigma (\delta C_{ij}^{\text{st.}} / C_{ij})^2 + \Sigma (\delta C_{ij}^{\text{sy.}} / C_{ij})^2] \}. \quad (7.6)$$

7.3. Combination of Datasets

The final combined and weighted branching ratio, with uncertainties including global systematics, year-dependent, and year-independent corrections, is $R_f \pm \delta R_f^{\text{st.}} \pm \delta R_f^{\text{sy.}}$, defined as,

$$R_f = R_s \Pi C_k \pm \delta R_f^{\text{st.}} \pm \delta R_f^{\text{sy.}}, \quad (7.7)$$

$$\delta R_f^{\text{st.}} = R_s \Pi C_k \sqrt{(\delta R_s^{\text{st.}}/R_s)^2 + \Sigma(\delta C_k^{\text{st.}}/C_k)^2}, \quad (7.8)$$

$$\delta R_f^{\text{sy.}} = \sqrt{(R_s \Pi C_k)^2 ((\delta R_s^{\text{sy.}}/R_s)^2 + \Sigma(\delta C_k^{\text{sy.}}/C_k)^2) + \delta S^2}. \quad (7.9)$$

The combination of datasets is implemented in Table 7.3. The optimal acceptance cut (A_R) for the best combined statistical and systematic error was found to be 40 mm, giving a 0.12% precision measurement instead of 0.14% at 60 mm.

7.3. Combination of Datasets

Table 7.3: Combination of 2010, 2011, and 2012 datasets for $A_R = 40$ mm. The branching ratios for all datasets are still blinded. See Section 7.3 and Table 7.2 for nomenclature. The PH version was chosen over the Q based branching ratio since the global systematic error is (marginally) better.

	Value	Stat. error	Syst. error
$R^{\text{raw}}[10^{-4}]$ §5.3.4	Y_i	$\delta Y_i^{\text{st.}}$	$\delta Y_i^{\text{sy.}} = \sqrt{\Sigma_\alpha^2}$
2012 (PH)	1.2***	0.0014	0.0003
(Q)	1.2***	0.0014	0.0003
2011 (PH)	1.2***	0.0025	0.0006
(Q)	1.2***	0.0025	0.0007
2010 (PH)	1.2***	0.0030	0.0008
(Q)	1.2***	0.0031	0.0008
Common Corrections	C_k	$\delta C_k^{\text{st.}}$	$\delta C_k^{\text{sy.}}$
LET §6.1.1	1.0261	0.0002	0.0005
Acceptance §6.2	0.9978	0.0002	
t_0 §6.4	1.0006	0.0003	
Common systematics			S_l
$\sqrt{\Sigma_\beta^2}$ (PH)			0.0005
(Q)			0.0006
$R^{\text{final}}[10^{-4}]$			
2012 (PH)	1.2***	0.0015	0.0008
(Q)	1.2***	0.0015	0.0009
2011 (PH)	1.2***	0.0026	0.0010
(Q)	1.2***	0.0026	0.0011
2010 (PH)	1.2***	0.0030	0.0011
(Q)	1.2***	0.0031	0.0012
Weighted avg.	R_f	$\delta R_f^{\text{st.}}$	$\delta R_f^{\text{sy.}}$
(PH)	1.2***	0.0013	0.0008
(Q)	1.2***	0.0013	0.0009

7.4 Future prospects

7.4.1 Current PIENU experiment

The current dominant source of error is statistical, at 13 [10^{-8}] R_π units. Another set with about 3.5 M $\pi^+ \rightarrow e^+\nu_e$ events³⁸ is available from Run I (1 M), II (0.5 M), and III (2 M) collected from 2009 and prior to November 2010 which if added to the analysis could potentially bring down the statistical error below 10 [10^{-8}] R_π units. Those extra 3.5 M events are lower quality data because the CsI crystal information is not available, thus making the systematic error on the LET bigger. Additionally, the trigger was still a work in progress during the 2009 dataset, which could bring in extra systematic uncertainties. Also, all MC would have to be re-generated independently for those early datasets, since the pion stopping position was significantly different from the ones analyzed in this thesis. All corrections and shapes are dependent on the pion stopping position.

Another possibility is relaxing the acceptance A_R up to 60 mm, reducing the statistical error to around 10 [10^{-8}] R_π units using only Run IV, V and VI. However, it was verified that when $A_R = 60$ mm the systematic error from the LET inflates the total systematic error from the analysis from 8 [10^{-8}] R_π units to 14. If the uncertainty on the wire-chamber-3 (WC3) position along the beam axis currently at ± 1 mm is proved to be actually ± 0.5 mm, and the calorimeter energy uncertainty currently at 100 keV is reduced to 50 keV, the systematic error on the LET correction at higher angles will shrink, thus allowing events up to $A_R = 60$ mm without increasing the global systematic error. The implementation of the earlier datasets or the refinement of WC3 position and the calorimeter energy calibration uncertainty would improve the branching ratio measurement uncertainty from 0.12% to 0.10%, and if both are executed properly the analysis could access a measurement uncertainty of 0.09% or better.

7.4.2 Next generation PIENU

The next generation PIENU experiment would have to aim for a higher precision measurement goal close to the current theoretical calculation precision at 0.016%. To allow further experimental statistical precision while keeping the current stopping-pion technique, a higher number of $\pi^+ \rightarrow e^+\nu_e$

³⁸ The number of $\pi^+ \rightarrow e^+\nu_e$ events quoted for the rest of the chapter are for acceptance radius $A_R = 60$ mm.

7.4. Future prospects

events must be collected by running for longer periods of time, or a calorimeter setup with a bigger acceptance (currently around 20%) such as the 4π acceptance calorimeter used in the PEN experiment at PSI [51]. To allow further experimental systematical precision while keeping the current stopping-pion technique, the LET energy correction must be calculated to higher precision. The LET precision is limited by the detector geometric accuracy, calorimeter's photo-nuclear (PN) interactions Monte-Carlo calculation accuracy, and calorimeter's energy resolution. Therefore better machinery and assembly techniques for the detector's components, improved theoretical PN interaction Monte-Carlo implementations, and better energy resolution are required to reach a new level of systematic precision measurement.

Chapter 8

Limits on New Physics

8.1 The $\pi^+ \rightarrow e^+ \nu_e$ branching ratio

The *blinded*³⁹ branching ratio $R_\pi = \frac{\Gamma(\pi^+ \rightarrow e^+ \nu_e + \pi^+ \rightarrow e^+ \nu_e \gamma)}{\Gamma(\pi^+ \rightarrow \mu^+ \nu_\mu + \pi^+ \rightarrow \mu^+ \nu_\mu \gamma)}$ calculated for this thesis regarding the highest quality data available from PIENU’s datasets (Run IV, V and VI) with about 3 million $\pi^+ \rightarrow e^+ \nu_e$ events⁴⁰ collected between 2010 and 2012 is

$$R_\pi^{blind} = (1.2^{***} \pm 0.0013(\text{stat.}) \pm 0.0008(\text{syst.})) \times 10^{-4}. \quad (8.1)$$

For the 2012 dataset the total reduced $\chi^2/\text{d.o.f.}$ (where $\text{d.o.f.} = 1557$) is: 1.19, and 1.13 for the pulse-height (PH) and charge-integration (Q) based time spectrum analysis, from which the raw branching ratio is extracted; 1.08, 1.06, 1.00, and 1.07 for 2011; and 2010-November datasets. Although, the PH and Q analyses are consistent with each other, PH was chosen over the Q-based branching ratio for being less sensitive to pileup events. R_π^{blind} represents a *0.12% precision measurement*, a factor of 30 improvement from previous generation experiments [12] [13] and a factor 2 from a subset of data (Run IV) published [5] in 2015 as

$$R_\pi^{2015} = (1.2344 \pm 0.0023(\text{stat.}) \pm 0.0019(\text{syst.})) \times 10^{-4}. \quad (8.2)$$

Limits on new physics can be obtained starting from an upper limit to the branching ratio R_{UL} , which can be calculated for example with the Feldman-Cousins “unified approach” frequentist method [133] $(R_{\text{exp}} - R_{\text{SM}})/\sigma$ where R_{exp} is the measured branching ratio, σ the total error, and R_{SM} is the SM prediction. Consulting Table X of ref. [133], an upper limit can be obtained. For the published result R_π^{2015} , with a combined (statistical+systematic) error $\sigma = 0.003 \times 10^{-4}$, the upper limit at 95% confidence level is 1.67 standard deviations above the SM value

³⁹ If the blinding (Section 1.3) is to be removed from *this analysis*, the branching ratio will move within $\pm 0.5\%$.

⁴⁰ 3 million events when acceptance radius $A_R = 60$ mm.

$$R_{\text{UL}} = 1.2402 \times 10^{-4}. \quad (8.3)$$

For comparison, using the improved combined error from this thesis $\sigma = 0.002 \times 10^{-4}$, and the R_{π}^{2015} value for R_{exp} shrinks the upper limit to 1.2384×10^{-4} . New physics would not necessarily increase the branching ratio, it could also decrease it. Thus, a lower limit could be calculated similarly.

8.2 Lepton Universality

Lepton universality (LU) is the assumption that the W boson couples with the same strength to each lepton generation, i.e., $g_e = g_{\mu} = g_{\tau}$. If there is a difference in the couplings, we can quantify it with the three different coupling constants g_e , g_{μ} , and g_{τ} . In the case of the $\pi^+ \rightarrow e^+ \nu_e$ branching ratio we have $R_{\pi}^{\text{exp}} = (g_e/g_{\mu})^2 R_{\pi}^{\text{SM}}$ (see Section 2.3.1) where R_{π}^{exp} is the measured branching ratio and R_{π}^{SM} is the SM prediction. Since the yields depend on the square of the coupling constants, the measurement of the branching ratio is a particularly powerful test of LU. Using the published result of R_{π}^{2015} , a 0.24% precision measurement, the following result was obtained,

$$g_e/g_{\mu} = 0.9996 \pm 0.0012, \quad (8.4)$$

translating into a 0.12% precision of the lepton universality test. Using the current estimates for the errors from R_{π}^{blind} (0.12% precision) would improve the errors of the ratio of the coupling constants to ± 0.0006 , thus reaching a 0.06% precision test of LU.

This would make pion decay the most sensitive test of lepton universality, and improve the already stringent constraints on models attempting to explain the hints of possible lepton non-universality seen by the LHCb [71] [72] and BaBar [73] experiments. Essentially, the models must include the property that the mechanism that couples differently to the different generations be greatly enhanced for the third generation [77].

8.3 New Pseudo-scalar Interactions

The branching ratio is very sensitive to the presence of new pseudo-scalar interactions. By substituting the SM prediction and the value from the

estimated upper limit R_{UL} (Eq. 8.3) into the Eq. 2.20 gives

$$\frac{1.2402}{1.2352} - 1 \sim \left(\frac{1 \text{ TeV}}{\Lambda} \right)^2 \times 10^3, \quad (8.5)$$

which gives the estimate

$$\Lambda \sim 497 \text{ TeV}. \quad (8.6)$$

Thus, the mass scale of a new fundamental pseudo-scalar, with the same coupling strength to quarks and leptons as the weak interaction, must be $> 500 \text{ TeV}$ at 95% C.L. Using the upper limit derived with the improved estimated error raises the new pseudo-scalar interaction limit to $\Lambda = 621 \text{ TeV}$.

8.3.1 R-Parity violating SUSY

The relationship between R_π and the R-parity violating parameters Δ'_{11k} and Δ'_{21k} (see Section 2.3.2) is

$$\frac{\Delta R_\pi}{R_\pi^{\text{SM}}} = 2(\Delta'_{11k} - \Delta'_{21k}). \quad (8.7)$$

R_π itself does not provide any constraint on the size of Δ'_{11k} and Δ'_{21k} in the case where they are equal in value. According to Figure 2.8, a 0.1% level precision measurement of the branching ratio and in the extreme case where $\Delta'_{11k} = 0$ then Δ'_{21k} should be restricted to 0.002 ± 0.001 , at 95% C.L.

8.3.2 Charged Higgs Boson

As discussed in Section 2.3.2, if the coupling of the charged Higgs boson to leptons is proportional to the lepton mass, as with the SM Higgs boson, R_π is unaffected by the presence of a charged Higgs boson. However, if the coupling is independent of the lepton mass, this is no longer the case. Assuming couplings of the order $\lambda_{e\nu} \sim \lambda_{\mu\nu} \sim \lambda_{ud} \sim \alpha/\pi$ we have

$$m_{H^\pm} \sim \frac{m_\pi m_W \alpha}{\pi} \sqrt{\frac{2}{m_e(m_u + m_d)} \left(1 - \frac{m_e}{m_\mu}\right) \frac{R_{\text{SM}}}{R_{\text{SM}} - R_{\text{exp}}}}. \quad (8.8)$$

The limit at 95% C.L. for the upper limit R_{UL} (Eq. 8.3) is

$$M_{H^\pm} \geq 182 \text{ GeV}. \quad (8.9)$$

Using the upper limit derived with the improved estimated error raises the mass limit to $M_{H^\pm} \geq 227 \text{ GeV}$.

8.4 Search for Massive Neutrinos in the $\pi^+ \rightarrow e^+\nu_e$ Decay

Limits for massive neutrinos described in Section 2.3.4 below $50 \text{ MeV}/c^2$ can be set by using the Feldman-Cousins upper limit to the branching ratio R_{UL} at 95% C.L. and Equation 2.29,

$$|U_{ei}|^2 = \frac{R_{\text{UL}}/R_{\text{SM}} - 1}{\rho_e - 1}. \quad (8.10)$$

Thus, the limits on the mixing matrix $|U_{ei}|^2$ can be calculated as a function of neutrino mass m_{ν_i} . Figure 8.1 shows the 95% C.L. upper limit on the heavy-neutrino mixing parameter, as a function of its mass. The blue line shows the result from the derived branching ratio upper limit from a subset of PIENU data (Run IV) published [5] in 2015, i.e., a heavy neutrino mass m_{ν_i} of $50 \text{ MeV}/c^2$ has a limit of approximately 10^{-6} in the mixing parameter and the limit increases as m_{ν_i} goes to zero.

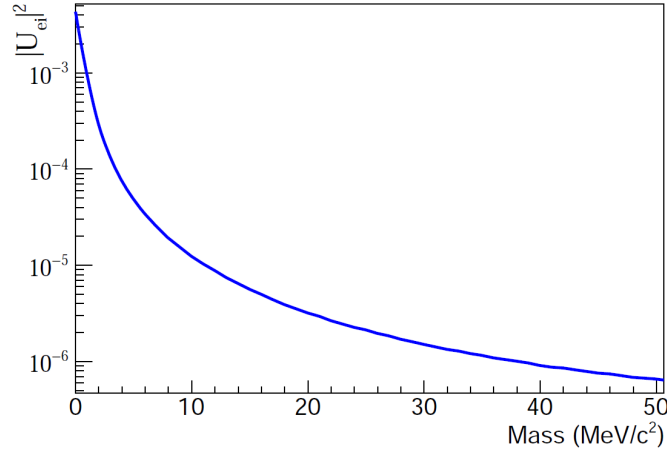


Figure 8.1: The 95% C.L. upper limit on the heavy neutrino mixing parameter, as a function of its mass. The blue line shows the result from the derived branching ratio upper limit from a subset of data (Run IV) published in 2015 [5].

Above 55 MeV , a search has been performed [11] for the mixing of heavy neutrinos coupled to electrons in the decay $\pi^+ \rightarrow e^+\nu_h$ using the full PIENU

8.5. Summary and Forward-looking for SM deviation scenarios

dataset, i.e., all runs from 2009 to 2012. No extra peaks due to heavy neutrinos were found in the positron energy spectrum as shown in Figure 8.2, resulting in upper limits set on the square of the mixing matrix elements $|U_{ei}|^2$ from 10^{-8} to 10^{-7} for neutrino masses in the range 60 to 135 MeV/ c^2 . See Figure 8.3. These results assume coupling to e^+ but are independent of assumptions about the nature of the heavy neutrino and are complementary to limits from neutrino-less double beta decay found in Ref. [134], which assume that massive neutrinos are Majorana in nature.

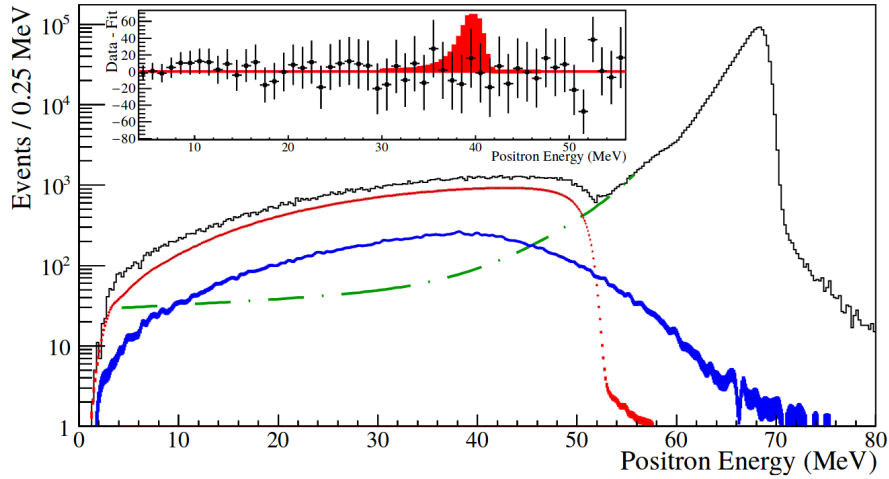


Figure 8.2: Background-suppressed $\pi^+ \rightarrow e^+ \nu_e$ positron energy spectrum (black histogram). Fitted components include muon decays in flight (thick blue line, from MC), $\pi^+ \rightarrow e^+ \nu_e$ (green, dot-dashed line, fit to MC), and $\pi^+ \rightarrow \mu^+ \nu_\mu \rightarrow e^+ \nu_e \bar{\nu}_\mu$ (red dashed line, from late-time data events). The insert shows the (rebinned) residuals (Data-Fit) with statistical error bars and the signal shape (massive neutrino search) in the case of $E_{e^+} = 40$ MeV and $|U_{ei}|^2 = 10^{-8}$ [11].

8.5 Summary and Forward-looking for SM deviation scenarios

In the scenario where the PIENU experiment gives a mild deviation from the SM result, what beyond-SM explanation is right for some future experiment? This thesis had already discussed direct access to Lepton Universality

8.5. Summary and Forward-looking for SM deviation scenarios

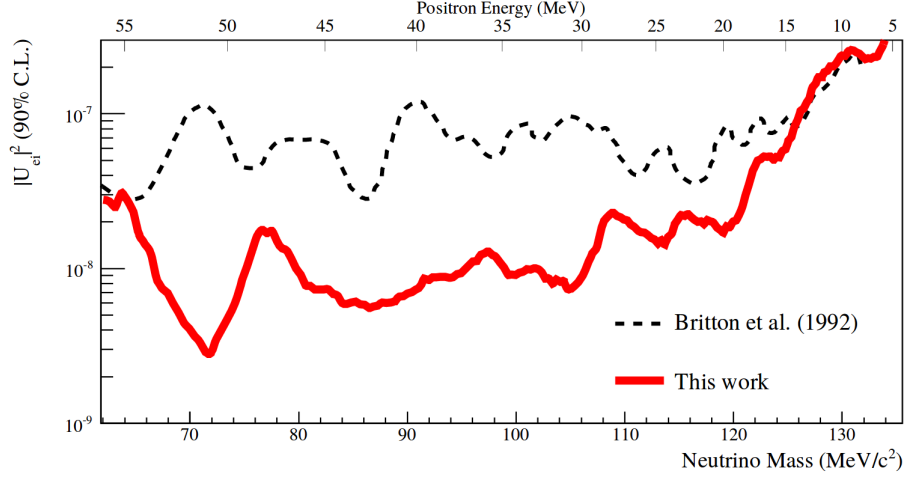


Figure 8.3: 90% C.L. upper limits on the square of the mixing matrix elements $|U_{ei}|^2$ of heavy neutrinos coupled to electrons (thick red line) regarding the full PIENU dataset, i.e., all runs from 2009 to 2012 [11]. The black dashed line shows the results from the previous generation PIENU experiment [29].

test of a first order weak interaction using the measured $\pi^+ \rightarrow e^+\nu_e$ branching ratio. There is also the search of massive neutrinos lighter than the π^+ in the $\pi^+ \rightarrow e^+\nu_e$ energy spectrum. Thus, the next generation PIENU experiment (see Section 7.4) would be a sensible test for beyond-SM deviations by delivering a higher precision $\pi^+ \rightarrow e^+\nu_e$ branching ratio measurement, i.e. $\mathcal{O}(0.01\%)$. On the other hand, a direct detection of a charged Higgs boson (H^\pm) is not within the capabilities of the current PIENU experimental technique. Nevertheless, the ATLAS collaboration has reported a search for charged Higgs bosons $H^\pm \rightarrow tb$ decay channel in proton-proton (pp) collisions at 8 TeV and $H^\pm \rightarrow \tau^\pm\nu_\tau$ of pp collision at 13 TeV in ref. [82] and [83], respectively. The $H^\pm \rightarrow tb$ search explored the H^\pm mass range from 200 to 600 GeV but no significant candidates were found. The $H^\pm \rightarrow \tau^\pm\nu_\tau$ search reported no evidence of a charged Higgs boson for the mass range 90–2000 GeV at a 95% confidence level. The ATLAS experiment at CERN is planning to keep looking for H^\pm bosons in higher energy collisions in the near future. In the case PIENU reports a small branching ratio SM deviation, the community could look to other experiments testing lepton universality to further restrict or allow beyond-SM theories.

Bibliography

- [1] A. Aguilar-Arevalo et al. (PIENU collaboration). High Purity Pion Beam at TRIUMF. *Nucl. Instrum. Methods Phys. Res., Sect. A*, 609:102–105, 2009.
- [2] A. Aguilar-Arevalo et al. (PIENU collaboration). Study of a large NaI(Tl) crystal. *Nucl. Instrum. Methods Phys. Res., Sect. A*, 621:188–191, 2010.
- [3] M. Aoki et al. (PIENU collaboration). Search for massive neutrinos in the decay $\pi \rightarrow e\nu$. *Phys. Rev. D*, 84:052002, 2011.
- [4] A. Aguilar-Arevalo et al. (PIENU collaboration). Detector for measuring the $\pi^+ \rightarrow e^+\nu_e$ branching fraction. *Nucl. Instrum. Methods Phys. Res., Sect. A*, 791:38–46, 2015.
- [5] A. Aguilar-Arevalo et al. (PIENU Collaboration). Improved measurement of the $\pi \rightarrow e\nu$ branching ratio. *Phys. Rev. Lett.*, 115:071801, 2015.
- [6] S. Cuen-Rochin. Tn30: Mc for positron tail in m13beam-line. Technical report, TRIUMF-PIENU’s internal documents, 2013.
- [7] S. Cuen-Rochin. Tn37: T1 single-multi pulse correction. Technical report, TRIUMF-PIENU’s internal documents, 2014.
- [8] S. Cuen-Rochin. Tn41: Master technote for 2010 analysis. Technical report, TRIUMF-PIENU’s internal documents, 2015.
- [9] Pienu webpage. <https://pienu.triumf.ca/>. Accessed: 2018.
- [10] S. Cuen-Rochin. Tn36: 2012 data. Technical report, TRIUMF-PIENU’s internal documents, 2014.
- [11] A. Aguilar-Arevalo et al. (PIENU collaboration). Improved search for heavy neutrinos in the decay $\pi \rightarrow e\nu$. *Phys. Rev.*, D97(7):072012, 2018.

Bibliography

- [12] G. Czapek, A. Federspiel, A. Flükiger, D. Frei, B. Hahn, C. Hug, E. Hugentobler, W. Krebs, U. Moser, D. Muster, E. Ramseyer, H. Scheidiger, P. Schlatter, G. Stucki, R. Abela, D. Renker, and E. Steiner. Branching ratio for the rare pion decay into positron and neutrino. *Phys. Rev. Lett.*, 70:17–20, 1993.
- [13] D. I. Britton, S. Ahmad, D. A. Bryman, R. A. Burnham, E. T. H. Clifford, P. Kitching, Y. Kuno, J. A. Macdonald, T. Numao, A. Olin, J-M. Poutissou, and M. S. Dixit. Measurement of the $\pi^+ \rightarrow e^+\nu$ branching ratio. *Phys. Rev. D*, 49:28–39, 1994.
- [14] S. Cuen-Rochin. First results from the PIENU experiment. In *17th Annual Meeting of the APS Northwest Section*, volume 61, May 12-14 2016. Penticton, British Columbia, Canada.
- [15] K. Yamada. *Search for massive neutrinos in $\pi^+ \rightarrow e^+\nu_e$ decay*. PhD thesis, Osaka University, 2010.
- [16] C. Malbrunot. *Study of $\pi^+ \rightarrow e^+\nu_e$ decay*. PhD thesis, The University of British Columbia, 2012.
- [17] D. vom Bruch. Studies for the PIENU Experiment and on the Direct Radiative Capture of Muons in Zirconium. M.Sc. thesis, The University of British Columbia, 2013.
- [18] S. Ito. *Measurement of the $\pi^+ \rightarrow e^+\nu_e$ Branching Ratio*. PhD thesis, Osaka University, 2016.
- [19] T. Sullivan. *A high-precision measurement of the $\pi \rightarrow e\nu$ branching ratio*. PhD thesis, The University of British Columbia, 2017.
- [20] R. Nuttall. Beamline Studies for the PIENU Experiment. B.Sc. thesis, The University of British Columbia, 2018.
- [21] M. Tanabashi *et al.* (Particle Data Group). Review of particle physics. *Phys. Rev. D*, 98:030001, Aug 2018.
- [22] F. James. Minuit function minimization and error analysis. Technical report, CERN Program Library Entry D 506.
- [23] R. Barlow. Systematic errors: Facts and fictions. In *Advanced Statistical Techniques in Particle Physics. Proceedings, Conference, Durham, UK, March 18-22, 2002*, pages 134–144, 2002.

Bibliography

- [24] D. A. Bryman, W. J. Marciano, R. Tschirhart and T. Yamanaka. Rare kaon and pion decays: Incisive probes for new physics beyond the standard model. *Annual Review of Nuclear and Particle Science*, 61:331–354, 2011.
- [25] D. I. Britton, S. Ahmad, D. A. Bryman, R. A. Burnham, E. T. H. Clifford, P. Kitching, Y. Kuno, J. A. Macdonald, T. Numao, A. Olin, J-M. Poutissou, and M. S. Dixit. Measurement of the $\pi^+ \rightarrow e^+\nu$ branching ratio. *Phys. Rev. Lett.*, 68:3000–3003, May 1992.
- [26] W. Loinaz et al. The NuTeV anomaly, lepton universality, and nonuniversal neutrino-gauge couplings. *Phys. Rev. D*, 70:113004, 2004.
- [27] Gregory Ciezarek, Manuel Franco Sevilla, Brian Hamilton, Robert Kowalewski, Thomas Kuhr, Vera Lth, and Yutaro Sato. A Challenge to Lepton Universality in B Meson Decays. *Nature*, 546:227–233, 2017.
- [28] M. J. Ramsey-Musolf, S. Su, and S. Tulin. Pion Leptonic Decays and Supersymmetry. *Phys. Rev.*, D76:095017, 2007.
- [29] D.I. Britton et al. Improved search for massive neutrinos in $\pi^+ \rightarrow e^+\nu$ decay. *Phys. Rev. D*, 46:R885–R887, 1992.
- [30] Triumf webpage. <https://www.triumf.ca/>. Accessed: 2018.
- [31] Y. Unno. ATLAS silicon microstrip detector system (SCT). *Nucl. Instrum. Meth.*, A511:58–63, 2003.
- [32] Nads: Cry simulation package for cosmics. <http://nuclear.llnl.gov/simulation/>, 2010.
- [33] H. Yukawa. On the Interaction of Elementary Particles I. *Proc. Phys. Math. Soc. Jap.*, 17:48–57, 1935. [Prog. Theor. Phys. Suppl.1,1(1935)].
- [34] C. M. G. Lattes, H. Muirhead, G. P. S. Occhialini, C. F. Powell. Processes involving charged mesons. *Nature*, 159:694–697, 1933.
- [35] Official website of the nobel prize. https://www.nobelprize.org/nobel_prizes/physics/laureates/. Accessed: 2018.
- [36] H. Yukawa. *Tabibito. English*. World Scientific, 1982.
- [37] S. Lokanathanand and J. Steinberger. Search for the β -decay of the pion. *J. Nuovo Cim*, 2(Suppl 1), 1955.

- [38] H.L. Anderson and C. Lattes. Search for the electronic decay of the positive pion. *Il Nuovo Cimento (1955-1965)*, 6:1356–1381, 1957.
- [39] C. S. Wu, E. Ambler, R. W. Hayward, D. D. Hoppes and R. P. Hudson. Experimental test of parity conservation in beta decay. *Phys. Rev.*, 105(4):1413–1415, 1957.
- [40] E. C. G. Sudarshan and R. E. Marshak. Chirality invariance and the universal fermi interaction. *Phys. Rev.*, 109(5):1860–1862, 1958.
- [41] R. P. Feynman and M. Gell-Mann. Theory of the fermi interaction. *Phys. Rev.*, 109(1):193–198, 1958.
- [42] T. Fazzini *et al.* Electron Decay of the Pion. *Phys. Rev. Lett.*, 1:247–249, 1958.
- [43] G. Impeduglia, R. Plano, A. Prodell, N. Samios, M. Schwartz, and J. Steinberger. β decay of the pion. *Phys. Rev. Lett.*, 1:249–251, Oct 1958.
- [44] H.L. Anderson *et al.* Branching Ratio of the Electronic Mode of Positive Pion Decay. *Phys. Rev.*, 119:2050–2067, 1960.
- [45] R. E. Shrock. General Theory of Weak Leptonic and Semileptonic Decays. 1. Leptonic Pseudoscalar Meson Decays, with Associated Tests For, and Bounds on, Neutrino Masses and Lepton Mixing. *Phys. Rev.*, D24:1232, 1981.
- [46] M. Leurer. A Comprehensive study of leptoquark bounds. *Phys. Rev.*, D49:333–342, 1994.
- [47] V. Cirigliano and I. Rosell. $\pi/K \rightarrow e\bar{\nu}_e$ branching ratios to $\mathcal{O}(e^2p^4)$ in Chiral Perturbation Theory. *JHEP*, 0710:005, 2007.
- [48] E. Di Capua, R. Garland, L. Pondrom, and A. Strelzoff. Study of the decay $\pi \rightarrow e + \nu$. *Phys. Rev.*, 133:B1333–B1340, 1964.
- [49] D. Bryman and C. Picciotto. Revised value for the $\pi \rightarrow e\nu$ branching ratio. *Phys. Rev. D*, 11:1337–1337, 1975.
- [50] D. A. Bryman, R. Dubois, T. Numao, B. Olaniyi, A. Olin, M. S. Dixit, D. Berghofer, J. M. Poutissou, J. A. Macdonald, and B. C. Robertson. New measurement of the $\pi \rightarrow e\nu$ branching ratio. *Phys. Rev. Lett.*, 50:7–10, 1983.

- [51] The PEN Collaboration. Precise measurement of the $\pi^+ \rightarrow e^+\nu$ branching ratio. psi proposal r-05-01. 2006.
- [52] S. Agostinelli et al. GEANT4: A Simulation toolkit. *Nucl. Instrum. Meth.*, A506:250–303, 2003.
- [53] J. R. Klein and A. Roodman. Blind analysis in nuclear and particle physics. *Annual Review of Nuclear and Particle Science*, 55(1):141–163, 2005.
- [54] P. F. Harrison. Blind analysis. *Journal of Physics G: Nuclear and Particle Physics*, 28(10):2679, 2002.
- [55] C. Burgess and G. Moore. *The Standard Model: A Primer*. Cambridge University Press, 2006.
- [56] G. D. Coughlan, J. E. Dodd, and B. M. Gripaios. *The Ideas of Particle Physics: An Introduction for Scientists*. Cambridge University Press, 3 edition, 2006.
- [57] R. P. Byron. *Particle Physics at the new Millenium*. Springer Verlag, 1996.
- [58] D. H. Perkins. *Introduction to High Energy Physics*. Cambridge University Press, 2000.
- [59] R. P. Feynman. *QED: The Strange Theory of Light and Matter*. Princeton University Press, new ed edition, 1988.
- [60] J. P. Ellis. TikZ-Feynman: Feynman diagrams with TikZ. *Computer Physics Communications*, 210:103–123, 2017.
- [61] M. E. Peskin and D. V. Schroeder. *An Introduction to Quantum Field Theory*. Westview Press, 1995.
- [62] T. Kinoshita. Radiative corrections to $\pi - e$ decay. *Phys. Rev. Lett.*, 2(11):477–480, 1959.
- [63] S. M. Berman. Radiative corrections to pion beta decay. *Phys. Rev. Lett.*, 1(12):468–469, 1958.
- [64] T. J. Goldman and W. J. Wilson. Radiative corrections to muon-electron universality in a gauge theory of charged-pion decay. *Phys. Rev. D*, 14(9):2428–2430, 1976.

Bibliography

- [65] W. J. Marciano and A. Sirlin. Theorem on π_{l2} Decays and Electron-Muon Universality. *Phys. Rev. Lett.*, 36(24):1425–1428, 1976.
- [66] W. J. Marciano and A. Sirlin. Radiative corrections to π_{l2} decays. *Phys. Rev. Lett.*, 71:3629–3632, 1993.
- [67] M. González-Alonso, J. Martin Camalich, and K. Mimouni. Renormalization-group evolution of new physics contributions to (semi)leptonic meson decays. *Physics Letters B*, 772:777–785, 2017.
- [68] Lusiani, A. Lepton universality and lepton flavour violation tests at the b-factories. *EPJ Web of Conferences*, 118:01018, 2016.
- [69] C. Lazzeroni et al. Test of lepton flavour universality in $K^+ \rightarrow l^+\nu$ decays. *Physics Letters B*, 698(2):105 – 114, 2011.
- [70] A. Pich. Tau Physics: Theory Overview. *Nucl. Phys. Proc. Suppl.*, 181-182:300–305, 2008.
- [71] R. Aaij et al. (The LHCb Collaboration). Test of lepton universality using $B^+ \rightarrow K^+l^+l^-$ decays. *Phys. Rev. Lett.*, 113(15):151601, 2014.
- [72] R. Aaij et al. (The LHCb Collaboration). Measurement of the ratio of branching fractions $\mathcal{B}(\overline{B}^0 \rightarrow D^{*+}\tau^-\overline{\nu}_\tau)/\mathcal{B}(\overline{B}^0 \rightarrow D^{*+}\mu^-\overline{\nu}_\mu)$. *Phys. Rev. Lett.*, 115(11):111803, 2015.
- [73] J.P. Lees et al (BaBar Collaboration). Evidence for an excess of $\overline{B} \rightarrow D^{(*)}\tau^-\overline{\nu}_\tau$ decays. *Phys. Rev. Lett.*, 109:101802, 2012.
- [74] R. Aaij et al. (LHCb Collaboration). Test of Lepton Flavor Universality by the measurement of the $B^0 \rightarrow D^{*-}\tau^+\nu_\tau$ branching fraction using three-prong τ decays. *Phys. Rev.*, D97(7):072013, 2018.
- [75] R. Aaij et al. (LHCb Collaboration). Test of lepton universality with $B^0 \rightarrow K^{*0}l^+l^-$ decays. *JHEP*, 08:055, 2017.
- [76] S. Bifani et al. Review of Lepton Universality tests in B decays. 2018.
- [77] F. Feruglio, P. Paradisi, and A. Pattori. Revisiting lepton flavor universality in b decays. *Phys. Rev. Lett.*, 118:011801, 2017.
- [78] O. U. Shanker. $\pi_{\ell 2}$, $K_{\ell 3}$ and $K^0 - \overline{K}^0$ Constraints on Leptoquarks and Supersymmetric Particles. *Nucl. Phys.*, B204:375–386, 1982.

Bibliography

- [79] B. A. Campbell and D. W. Maybury. Constraints on scalar couplings from $\pi^+ \rightarrow l^+ + \nu_l$. *Nucl. Phys.*, B709:419–439, 2005.
- [80] A. Masiero, P. Paradisi, and R. Petronzio. Probing new physics through mu e universality in $K \rightarrow l\nu$. *Phys. Rev.*, D74:011701, 2006.
- [81] R. Carlini, J.M. Finn, S.Kowalski, and S. Page, spokespersons. JLab Experiment E-02-020.
- [82] Georges Aad et al. Search for charged Higgs bosons in the $H^\pm \rightarrow tb$ decay channel in pp collisions at $\sqrt{s} = 8$ TeV using the ATLAS detector. *JHEP*, 03:127, 2016.
- [83] Morad Aaboud et al. Search for charged Higgs bosons decaying via $H^\pm \rightarrow \tau^\pm \nu_\tau$ in the τ +jets and τ +lepton final states with 36 fb^{-1} of pp collision data recorded at $\sqrt{s} = 13$ TeV with the ATLAS experiment. *JHEP*, 09:139, 2018.
- [84] M. Hirsch, H. V. Klapdor-Kleingrothaus, and S. G. Kovalenko. New low-energy leptoquark interactions. *Phys. Lett.*, B378:17–22, 1996.
- [85] D. B. Kaplan and H. Georgi. $SU(2) \times U(1)$ breaking by vacuum misalignment. *Physics Letters B*, 136:183–186, 1984.
- [86] F. Sannino, P. Stangl, D. M. Straub, and A. E. Thomsen. Flavor physics and flavor anomalies in minimal fundamental partial compositeness. *Phys. Rev. D*, 97:115046, 2018.
- [87] K. Abe et al. (T2K Collaboration). Measurements of neutrino oscillation in appearance and disappearance channels by the T2K experiment with 6.610^{20} protons on target. *Phys. Rev.*, D91(7):072010, 2015.
- [88] A. Aguilar-Arevalo et al. (MiniBooNE Collaboration). Event Excess in the MiniBooNE Search for $\bar{\nu}_\mu \rightarrow \bar{\nu}_e$ Oscillations. *Phys. Rev. Lett.*, 105:181801, 2010.
- [89] T. Asaka and M. Shaposhnikov. The nuMSM, dark matter and baryon asymmetry of the universe. *Phys. Lett.*, B620:17–26, 2005.
- [90] B. Bertoni, S. Ipek, D. McKeen, and A. E. Nelson. Constraints and consequences of reducing small scale structure via large dark matter-neutrino interactions. *Journal of High Energy Physics*, 2015(4):170, 2015.

Bibliography

- [91] B. Batell, T. Han, D. McKeen, and B. S. E. Haghi. Thermal Dark Matter Through the Dirac Neutrino Portal. *Phys. Rev.*, D97(7):075016, 2018.
- [92] R. E. Shrock. General theory of weak processes involving neutrinos. ii. pure leptonic decays. *Phys. Rev. D*, 24:1275–1309, 1981.
- [93] J. Doornbos. M13 a new low energy pion channel at triumf. Technical report, TRIUMF’s Internal Design Report, 1978.
- [94] C. Kost and P. Reeve. Tr-dn-82-28. Technical report, TRIUMF’s Internal Design Report, 1982.
- [95] J. Doornbos. Tn01 : Reduction of electron contamination in m13 with degrader. Technical report, PIENU Technical Report, 2006.
- [96] T. Numao. Pienu technote 07: Effects of positrons in the beam. Technical report, PIENU Technical Report, 2008.
- [97] C.J. Oram, J.B. Warren, G.M. Marshall, and J. Doornbos. Commissioning of a new low energy - at triumf. *Nuclear Instruments and Methods*, 179(1):95 – 103, 1981.
- [98] T. Numao, Yuri I. Davydov, J-M. Poutissou, T. C. Awes, V. Cianciolo, S. Berridge, W. Bugg, Yu. Efremenko, R. Gearhart, and S. Ovchinnikov. Search for free decay of negative pions in water and light materials. *Phys. Rev.*, D73:092004, 2006.
- [99] Saint gobain crystals. <http://www.crystals.saintgobain.com/>. Accessed: 2018.
- [100] R. S. Henderson et al. Precision planar drift chambers and cradle for the TWIST muon decay spectrometer. *Nucl. Instrum. Meth.*, A548:306–335, 2005.
- [101] G. Blanpied et al. $N \rightarrow \Delta$ Transition from Simultaneous Measurements of $p(\gamma \rightarrow, \pi)$ and $p(\gamma \rightarrow, \gamma)$. *Phys. Rev. Lett.*, 79:4337–4340, 1997.
- [102] V. Bellini et al. Polarized compton scattering from He-4 in the delta region. *Phys. Rev.*, C68:054607, 2003.
- [103] D. Laurendeau F. Cayouette and C. Moisan. Detect2000: an improved monte-carlo simulator for the computer aided design of photon sensing devices, 2003.

- [104] C. Malbrunot. Presentation: Bina optical simulation. Technical report, PIENU internal documents, 2008.
- [105] Ahmed Hussein A. A. Aguilar-Arevalo and Chlo Malbrunot. Tn08 : Testing and setting up bina using gamma ray calibration. Technical report, PIENU internal documents, 2008.
- [106] L. Doria. Tn11 : Installation of the csi calorimeter for the pienu experiment. Technical report, PIENU internal documents, 2009.
- [107] I. H. Chiang, E. Garber, T. Inagaki, K. Ino, S. Kabe, S. Kettell, M. Kobayashi, T. K. Komatsubara, Y. Kuno, K. K. Li, L. S. Littenberg, T. Morimoto, T. Nakano, K. Omata, T. Sato, T. Shinkawa, S. Sugimoto, K. Tauchi, A. Yamashita, and Y. Yoshimura. Csi endcap photon detector for a k^+ rarr; π^+ ν ; ν ; macr; experiment at bnl. *IEEE Transactions on Nuclear Science*, 42(4):394–400, 1995.
- [108] T. K. Komatsubara et al. Performance of fine mesh photomultiplier tubes designed for an undoped CsI endcap photon detector. *Nucl. Instrum. Meth.*, A404:315–326, 1998.
- [109] M. Kobayashi, T. Shinkawa, T. Sato, S. Sugimoto, M. V. Korzhik, A. A. Fedorov, and V. A. Kachanov. YAlO-3:Ce-Am light pulsers as a gain monitor for undoped CsI detectors in a magnetic field. *Nucl. Instrum. Meth.*, A337:355–361, 1994.
- [110] A. A. Aguilar-Arevalo. Tn10 : Stand-alone setup and testing of the Xe-flash tube monitoring system. Technical report, PIENU internal documents, 2008.
- [111] L. Doria. A tracking algorithm for the PIENU experiment. Technical report, PIENU internal documents, 2009.
- [112] Y. Igarashi, H. Fujii, T. Higuchi, M. Ikeno, E. Inoue, T. Murakami, Y. Nagasaka, M. Nakao, K. Nakayoshi, M. Saitoh, S. Shimazaki, S.Y. Suzuki, M. Tanaka, K. Tauchi, T. Uchida, and Y. Yasu. A common data acquisition system for high-intensity beam experiments. *IEEE Transactions on Nuclear Science*, 52(6):2866 –2871, 2005.
- [113] J.-P. Martin and P.-A. Amaudruz. A 48 channel pulse shape digitizer with dsp. *IEEE Transactions on Nuclear Science*, 53(3):715 – 719, 2006.

Bibliography

- [114] J.-P. Martin, C. Mercier, N. Starinski, C.J. Pearson, and P.-A. Amaudruz. The TIGRESS DAQ/Trigger System. *IEEE Transactions on Nuclear Science*, 55(1):84–90, 2008.
- [115] C. Ohlmann, TRIUMF, Vancouver, Canada. VT48 Rev.A, 48-Channel Time-to-Digital Module. User’s Manual, 2007.
- [116] Kopio web page. <http://www.hep.lancs.ac.uk/~athans/resinterests/KOPIO.html>.
- [117] Y. Arai. AMT-3 -ATLAS Muon TDC version 3 & AMT-2- User’s Manual, 2005.
- [118] S. Ritt and P. A. Amaudruz. The midas data acquisition system.
- [119] R. Brun and F. Rademakers. Root - an object oriented data analysis framework. *Proceedings AIHENP’96 Workshop, Lausanne, Sep. 1996, Nucl. Inst. and Meth. in Phys. Res. A 389 (1997) 81-86*.
- [120] C. E. Picciotto, S. Ahmad, D. I. Britton, D. A. Bryman, E. T. H. Clifford, P. Kitching, Y. Kuno, J. A. MacDonald, T. Numao, A. Olin, J.-M. Poutissou, J. Summhammer, and M. S. Dixit. Searches for Majoron production and other processes associated with $\pi \rightarrow e\nu$ decay. *Phys. Rev. Lett.*, 37:1131–1133, 1988.
- [121] J. B. Birks. *The Theory and Practice of Scintillation Counting*. Pergamon, 1964.
- [122] D. Mischke. Tn58: Pion cut. Technical report, PIENU internal documents, 2018.
- [123] T. Numao. Tn29: Distortion due to false triggers. Technical report, PIENU Internal Documents, 2013.
- [124] D. Mischke. Tn57: Discussion of false triggers. Technical report, PIENU internal documents, 2018.
- [125] S. Cuen-Rochin. Time resolution effects on data. Technical report, PIENU internal documents, 2019.
- [126] T. Sullivan. Tn54: New lineshape analysis. Technical report, TRIUMF-PIENU’s internal documents, 2017.
- [127] T. Sullivan. Tn59: Lineshape analysis. Technical report, TRIUMF-PIENU’s internal documents, 2018.

- [128] IAEA Photonuclear Data Library. <https://www-nds.iaea.org/photonuclear/>. Accessed: 2018.
- [129] T. J. Roberts and D. M. Kaplan. G4beamline simulation program for matter-dominated beamlines. In *2007 IEEE Particle Accelerator Conference (PAC)*, pages 3468–3470, 2007.
- [130] J. Doornbos. Tn01: Reduction of electron contamination in m13 with degrader. Technical report, TRIUMF-PIENU’s internal documents, 2006.
- [131] T. Numao. Tn07: Effects of positrons in the beam. Technical report, TRIUMF-PIENU’s internal documents, 2008.
- [132] R. Mischke. Formulae to combine years. Technical report, TRIUMF-PIENU’s internal documents, 2018.
- [133] G. J. Feldman and R. D. Cousins. Unified approach to the classical statistical analysis of small signals. *Phys. Rev. D*, 57:3873–3889, 1998.
- [134] A. de Gouvêa and A. Kobach. Global constraints on a heavy neutrino. *Phys. Rev. D*, 93:033005, 2016.

Appendix A

Time spectrum for $\pi \rightarrow \mu \rightarrow e$

The $\pi \rightarrow \mu \rightarrow e$ process is a decay chain composed by the two decays characterized by the decay times $\tau_\pi = 1/\lambda_\pi$ and $\tau_\mu = 1/\lambda_\mu$. The pion decays with a rate dN_π/dt given by

$$\frac{dN_\pi}{dt} = -\lambda_\pi N_\pi, \quad (\text{A.1})$$

where N_π is the number of pion at time t . Assuming that all the pions decay into muons, the formation rate of the muons equals the decay rate of the pions

$$\frac{dN_\mu}{dt} = +\lambda_\pi N_\pi. \quad (\text{A.2})$$

At the same time, the muons decay according to

$$\frac{dN_\mu}{dt} = -\lambda_\mu N_\mu. \quad (\text{A.3})$$

The overall change in the muon population is therefore given by

$$\frac{dN_\mu}{dt} = \lambda_\pi N_\pi - \lambda_\mu N_\mu. \quad (\text{A.4})$$

Assuming a known initial amount of pions N_π^0 and muons N_μ^0 , the solutions of Eq. A.4 is

$$N_\mu = N_\pi^0 \frac{\lambda_\pi}{\lambda_\mu - \lambda_\pi} (e^{-\lambda_\pi t} - e^{-\lambda_\mu t}) + N_\mu^0 e^{-\lambda_\mu t}. \quad (\text{A.5})$$

From the last result, assuming no initial muons present, the normalized $\pi \rightarrow \mu \rightarrow e$ time spectrum has a shape described by

$$f(t) = \frac{1}{\tau_\mu - \tau_\pi} (e^{-\frac{t}{\tau_\mu}} - e^{-\frac{t}{\tau_\pi}}), \quad (\text{A.6})$$

Where N is the total number of events.

Appendix B

Cuts for Pion Data

Table B.1: List of cuts.

Cut	Notes
Blinding §1.3	Activated
Integrity §3.4.2	Error signals from COPPER system cleared
Physics Triggers §3.4.1	Only Prescale, Early, and TIGC.
<i>Pion Identification §4.2.1</i>	
Pion Energy	B1 from 3.8 to 5.2 MeV, B2 from 2.0 to 3.1 MeV
WC1,2's Halo ^a	
B1,2 PU	Only one hit in one of four PMTs, $0.75 < Q/Q_w < 1.05$
B1 Waveform	B1 pulse fitting activated, $\chi^2 \geq 0$
B1 prompt	$-1380 < B1_t < -1340$ ns
TrCons ^a	
<i>Pileup After Target §4.2.2</i>	
PionTrig ^a	
T1-T2 sync	$abs(T1 - T2) < \pm 20$ ns
Proton	See Figure 4.6
T1prompt ^a	T1 hits within ± 2 ns of pion timing (t_{π^+})
T1 fake PU	See Figure 4.7
T1 Waveform	T1 pulse fitting activated, $\chi^2 \geq 0$
Post-PU ^b	Any VT48 hit with: $1335 < T1_t[i] - B1_t[j] < 1480$ ns, COPPER's fitted avg: $T1_{t,avg}[i] - B1_{t,avg}[i] > 420$ ns
<i>Early Time Pileup §4.2.3</i>	
Pre-PU	No hits in pre-region for B1, B2, B3, T1, and T2
Beam Muons and	No hits from 8000 to 16400 and
Two Pions ^c	16600 to 17850 ns (prompt at 16500).
FalseTrig	See Figure 4.8
Acceptance §4.2.4	$A_R < 40$ mm, See Figure 4.9

^a Year dependent, see Table B.2.

^b Only used for integrated charged (Q) based branching ratio.

^c Two pion detection only available for 2012 dataset.

Table B.2: Year dependent cut values.

Run# ↓, Cut →		WC1,2				TrCons, T1prompt		T1prompt				PionTrig			Bina's Alignment	
≥	<	x.L	x.H	y.L	y.H	p.L	p.H	av[0]	av[1]	av[2]	av[3]	t.1	t.2	t.low	(Q)	(PH)
	29000					-4399	-4380	11.2	13.1	11.8	13.1	1020	1040	-3797		
31000	42250	-22	16	-12	18	-4395	-4375	7.9	8.7	9.1	9.1				0.98298	0.99691
42250	54819					-4409	-4390	7.3	8.1	8.4	8.3	1030	1050			
45819	46816					-4410	-4380	2.9	3.7	3.9	3.8					
46816	47133					-4390	-4370	3.3	5.2	3.9	5.1	1020	1040			
47133	49005							7.2	9	7.8	9.1					
49005	52006					-4399	-4380	11.2	13.1	11.8	13.1					
57418	61179	-20	18			-4399	-4380	11.9	13.6	12.6	13.6	1010	1040		0.98086	0.99385
62491	70025	-23	19	-17	19	-4399	-4350	11.2	13.1	11.8	13.1	1000	1040	-3820	0.97953	0.99458
70025	81560					-4375	-4350	12.1	13.6	12.8	13.6					

Appendix C

Cuts for Positron Data

This appendix is complementary to the discussion of the Response Function Measurement described in Section 6.1.1. Details for event selection cuts to cleanse the 70 MeV positron beam for proper calorimeter response characterization and MC comparison are discussed here. Before any cuts, the raw calorimeter's response for the beam aligned with the crystal axis (0 degrees), is shown in Figure C.1(a) in black. The energy spectrum is structure rich as only the T2 scintillator was used for triggering, thereby allowing several types of events to be included.

The raw calorimeter's response shown in Figure C.1(a) (black) has rich structure: the peak at 1 MeV are events without hits in the wire chambers corresponding to the beam spot in the calorimeter. Such a pileup must be coming out backward from the calorimeter and not from the beam itself. The beam pions and muons are at 14 and 18 MeV, respectively. Using MC, it was determined that structure near 30 MeV appear to be pions decaying in flight. Photo-nuclear effects due to photons kicking out one or two neutrons are visible near 50 and 60 MeV. The main peak around 70 MeV is due to beam positrons. When a positron and pion arrive simultaneously, they form the peak near 78 MeV. The structure to the right of that peak is for a positron and muon arriving together. Finally, the peak around 130 MeV is due to two positron events. The last three structures composition is known for the correspondence of the peaks to the sum of individual particles in conjunction to the energy deposited in T2.

WC halo and timing. The beam's reconstructed x and y position distributions using WC12 tracker (section 3.2.6) are shown in Figure C.1(b) with red lines indicating the cut values. Events not due to beam particles must be excluded. The beam's halo needs to be trimmed out with the tracking information, leaving just the beam spot. The resultant energy spectrum is shown in Figure C.1(a) in red. Further suppressing for non-beam particles; the background was reduced by eliminating events with out-of-time hits in all three wire chambers; such a cut was implemented by

Appendix C. Cuts for Positron Data

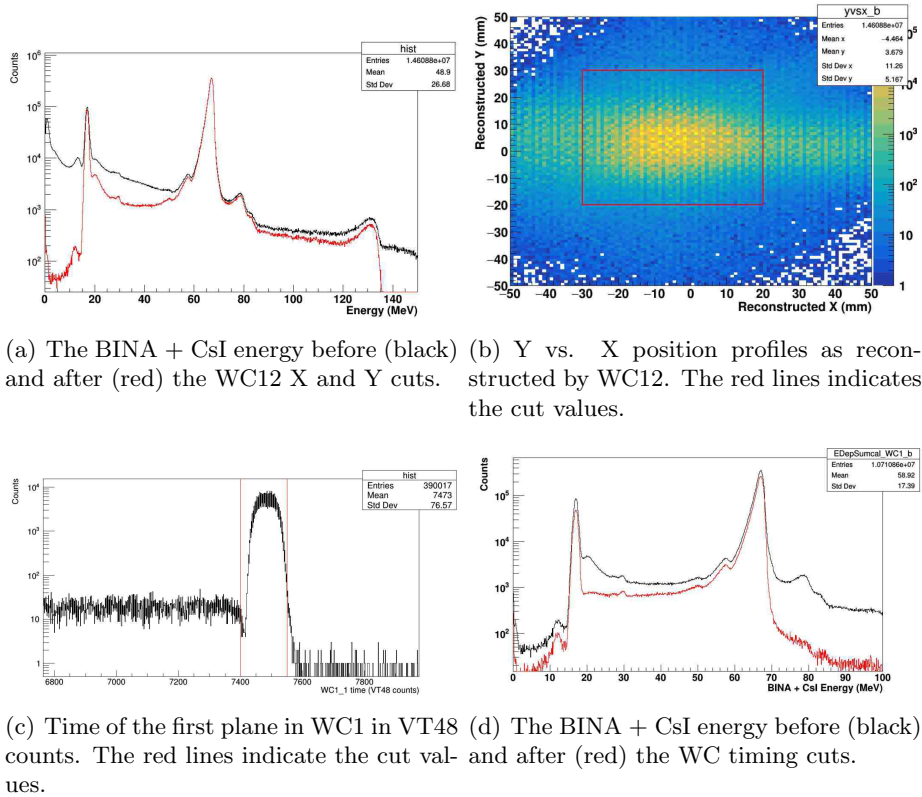


Figure C.1: The 0 degree positron energy spectrum cleaned through WC12 spatial and timing cuts.

keeping only the peak at ~ 7470 ADC counts (~ 4700 ns). The WC1 timing is shown in Figure C.1(c) with red lines indicating the cut values. Similar cuts were made in WC2 and WC3. Results for the WC timing cut are reflected in the energy spectrum, i.e., Figure C.1(d) in black before and red after the timing cut.

Muon correction. Following these cuts, the spectrum contained events due to beam positrons and beam muons. Assuming no shower leakage from the crystals, the total positron energy is the sum of the energy deposited in T2 and the energy deposited in the calorimeter (Bina+CsI). It is possible to remove beam muons completely using a cut on the energy deposited on the T2 scintillator, but this changes the tail significantly, as such a constraint removes some beam positrons with a direct dependence on the calorimeter

Appendix C. Cuts for Positron Data

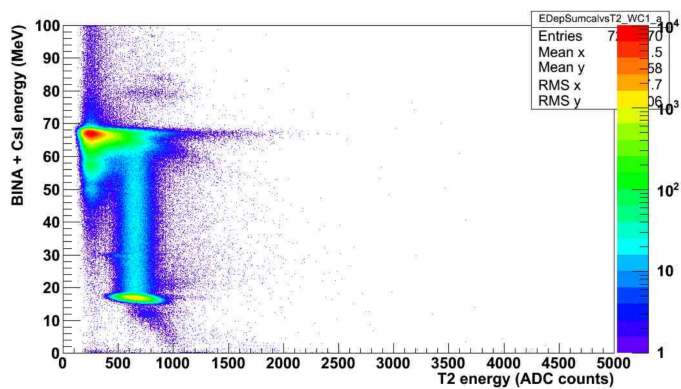


Figure C.2: The energy in Bina + CsI vs. the energy in T2. Blobs corresponding to positrons (~ 70 MeV), muons (~ 18 MeV), and pions (~ 14 MeV) can be clearly seen. There is also a structure around 30 MeV in Bina + CsI, with energy loss in T2 between positrons and beam muons. A similar structure appears in simulated pion events, from decays in flight.

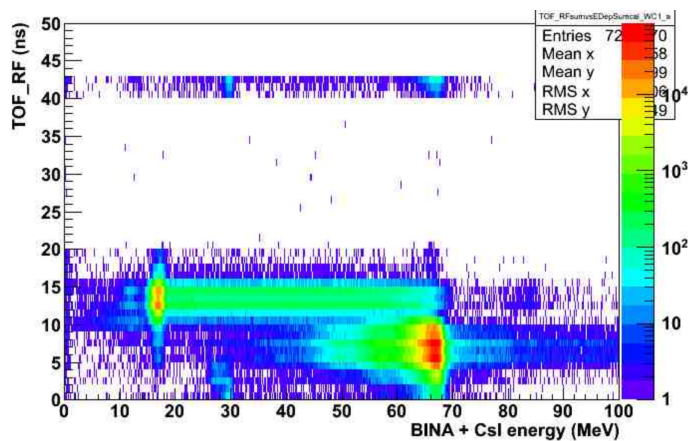


Figure C.3: The time of flight vs. the energy in BINA + CsI. Blobs corresponding to positrons and muons can be clearly seen. The region with essentially no events is due to the trigger condition excluding part of the RF window.

response, thereby introducing a bias to the response function measurement. Alternatively, the calorimeter vs. T2 energy distribution is shown in Figure C.2, which clearly identifies beam backgrounds below 35 MeV in Bina+CsI

Appendix C. Cuts for Positron Data

energy, where the positron tail is tiny, beam pions are at 14 MeV, beam muons are at 18 MeV, and π DIF are at 30 MeV. Implementation was carried out by removing events with more than 400 ADC counts in T2 and less than 35 MeV in Bina.

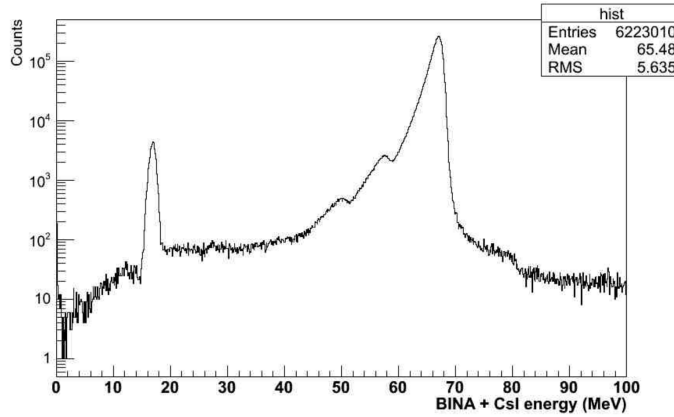


Figure C.4: The energy spectrum of positrons in BINA + CsI, selected by time of flight.

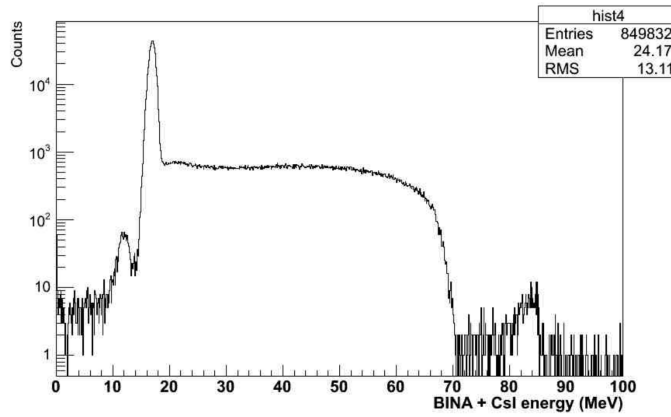


Figure C.5: The energy spectrum of muons in BINA + CsI, selected by time of flight.

The remaining muon trail above 35 MeV are events in which muons decayed within Bina's 1 μ s integration window. Such muons are identified with the RF time window vs. calorimeter energy distribution, as shown in Figure C.3. Muons are selected within 12 to 15 ns and positrons between 4 to 11 ns. The trigger was limited to a portion of the cyclotron's 43.3 ns RF window to record only where most positrons were present. The time region of 20 to 40 ns was not sampled as it contained mostly pions. The calorimeter's energy distribution after calorimeter vs T2 energy (Figure C.2) and calorimeter vs RF (Figure C.3) cuts is shown in Figure C.4 and Figure C.5, for positron and muon selection respectively. There is still a muon peak in the positron's spectrum but there is at best a negligible amount of positrons in the muon's distribution, as the near 70 MeV positron peak is gone. These conditions allow the muon spectrum to be subtracted from the positron spectrum and cleanse the muon contribution completely without compromising the response function. The procedure for muon subtraction is as follows:

- The muon spectrum is normalized to the muon peak from the positron spectrum.
- The T2 vs. calorimeter cut is applied to the positron spectrum.
- Set the muon spectrum to zero up to 35 MeV.
- Subtract the muon spectrum from the positron spectrum.

The result is shown in Figure 6.2 in black and the corresponding simulated spectrum is shown in red with the same cuts applied. There still are some muons left and π DIF in the positron spectrum, but it represents a negligible contribution to the tail fraction $< 0.01\%$.

Appendix D

Beam-line Simulation

TRIUMF's primary 520 MeV proton beam-line (BL1A) with $120 \mu\text{A}$ impulses on the *Be* production target apparatus shown in Figure D.1(a) with proton bunches of 4 ns width every 43 ns. Figure D.1(b) show the *Be* production target in detail. The cassette target consists of an oval tube or cassette measuring 18.8 mm by 11.3 mm, made from 0.25-mm-thick 316ELC stainless steel bent to shape, with 0.076-mm-thick 437 stainless steel windows welded at each end. The metal target is usually beryllium with a cross section of 14.7 mm by 5.1 mm, and it is held in the center of the tube by a wire frame. Cooling water enters the cassette near one end and leaves near the other end. The metal targets are completely immersed in the water inflow path at the entrance and exit faces and the sides.



(a) Full Frame



(b) Zoom on production target

Figure D.1: T1 production target apparatus for M13 beam extension.

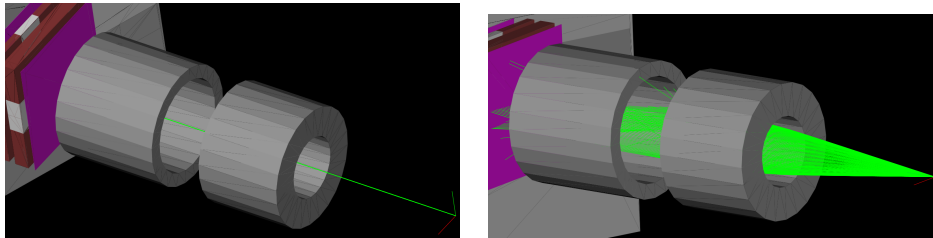
Beam-line settings. The two principal beam-line configurations simulated correspond to data run number #54880 and #81633. The main parameters are listed in Table D.1. Such runs were chosen as they represent different positron data taking periods for different years. The approach was to simulate their beam-line parameters and obtain the intrinsic positron tail

Appendix D. Beam-line Simulation

Table D.1: Beam-line’s settings for positron runs

Parameter	Run # 54880	Run # 81633
Positron beam mean momentum	75 MeV/c	70 MeV/c
Momentum spread σ_p	12 MeV/c	0.7 MeV/c
Beam origin spot size (Gaussian) $\vec{\sigma}$	(1.67, 1.67, 1.67) mm	(3.656, 3.133, 1.833) mm
Dipole field (B1,B2,B3)	(0.2138, -0.2307, 0.2808) T	(0.2077, -0.2077, 0.2630) T
Slit width (F0,F1,F2)	(102.4, 14.7, 30.0) mm	(120.0, 15.5, 30.4) mm

contribution, and validate MC by comparison with data. The implementation for run #54880 in the beryllium production target consisted of shooting a Gaussian positron beam from the origin ± 1.67 mm in the x, y, and z coordinates (99.7 % of the beams will be within a sphere having a radius of 10 mm). The beams had a mean momentum of 75 MeV/c and RMS momentum width 12 MeV/c to give a wide range of momentum as input to the M13 beam-line. These Gaussian beams were directed to the entrance of the beam-line from all angles within its acceptance cone. In Figure D.2(a), it can be seen how a Gaussian beam is directed to the center of the entrance of the beam-line, and in Figure D.2(b), how several beams are distributed within the acceptance cone. The implementation for run #81633 was carried out similarly by increasing the 10-mm-radius model three times, modifying the mean momentum to 70 MeV/c width 0.7 MeV/c (meaning different gradients for the quads and magnets), and different slit widths for focus points along the beams. Both implementations showed a negligible difference in the final beam intrinsic tail fraction.



(a) Gaussian beam aligned to beam-line main axis.

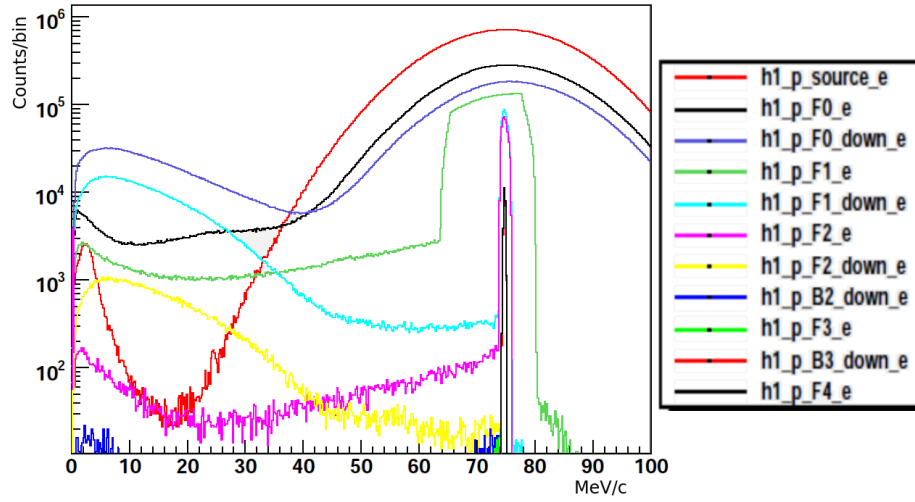
(b) Beam-line’s acceptance cone

Figure D.2: Beam input simulation

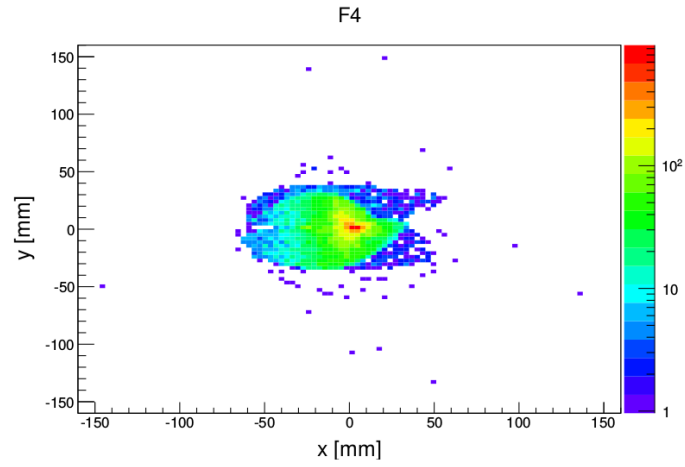
In Figure D.3(a), we can see the wide momentum range of the initial distribution (red) at the beginning of the beam and how the momentum distribution is affected after each beam component, and the final distribution (black) at focus point F4 with the corresponding beam spot in Figure D.3(b). Position profiles at F4 (target B3) for the x and y axes for run 54880 configured to a 75 MeV/c positron beam are shown in Figure D.4(c) and D.4(d) respectively, the F4 position profiles for x and y axis from G4beamline output with the same settings from run #54880 are shown in Figure D.4(a) and D.4(b) respectively. Position profiles at F4 for for x and y axis for run #81633 configured to a 70 MeV/c positron beam are shown in Figure D.5(a) and D.5(b) respectively, each plot has data (blue) and MC (red) overlay-ed. There are additional systematic tests and data comparisons with previous studies found in [6] and [20], including the number of events to determine the statistical accuracy, beam-line steering for beam spot matching (through additional data runs with similar beam-line settings), simulated magnetic field vs. implementation of measured magnetic field at bending magnets, and beam rotation. All of them were taken into account to set an upper limit to the intrinsic beam tail contribution.

Tail origin. As there is an interest in where the tail comes from, in this section, we show the results of tracing back the events in the tail of the positron momentum distribution at the final focus point F4. It was found that there is indeed a tail contribution coming from the beam scattering at several points on the beam-line. A common tail event comes from focus point F1 slit just after the first bending magnet B1. As shown in Figures D.6(a) and D.3(a)(green to light blue), the slit opening cleans low momenta from the positron beam but generates scattering, which will eventually contribute to the intrinsic beam momenta at the final focus point F4. Figure D.6(b) shows the x-axis position distribution after F1 slit; the events near the main distribution peak contribute to the tail.

Pion beam. Similarly, a pion beam was successfully simulated in accordance with pion data taking runs settings to evaluate and validate the beam-line's G4beamline MC implementation. Figures D.7(a) and D.7(b) show the main components of the beam simulation including the positron and pion beam settings, respectively. The implementation of the pion beam included additional components in the beam, a beam degrader after F1 to separate particles and allow pion selection further down the beam, and a collimator just before the third bending magnet as described in Section 3.1.



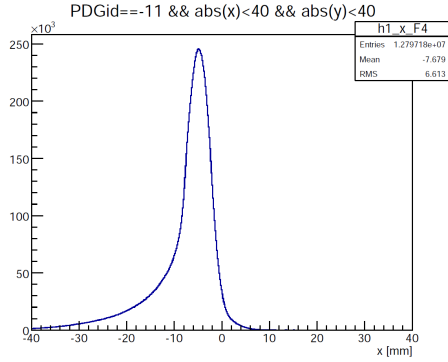
(a) Evolution of beam momentum



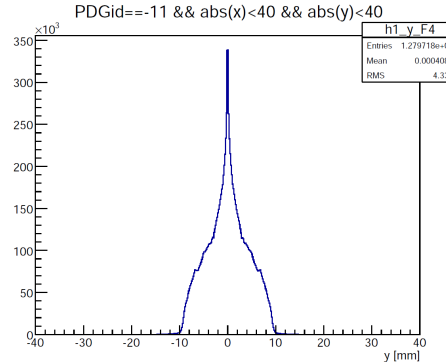
(b) Beam spot for final beam momentum at F4.

Figure D.3: Beam low momenta cleaning sequentially through different beam components and the final beam spot at F4.

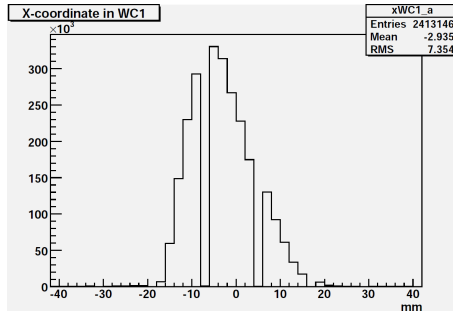
Appendix D. Beam-line Simulation



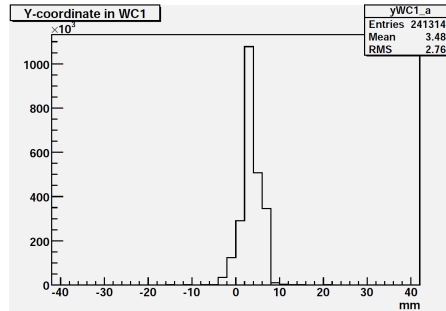
(a) X-axis position distribution in MC



(b) Y-axis position distribution in MC

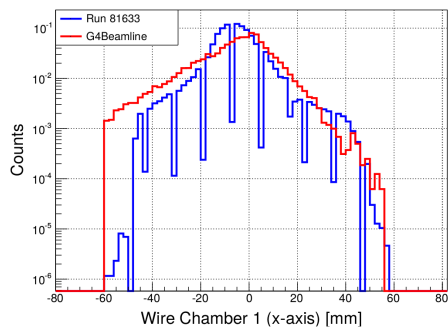


(c) X-axis position distribution in Data

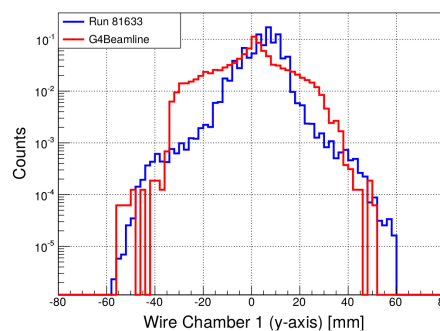


(d) Y-axis position distribution in Data

Figure D.4: Position profiles from MC and from positron run #54880 at F4.

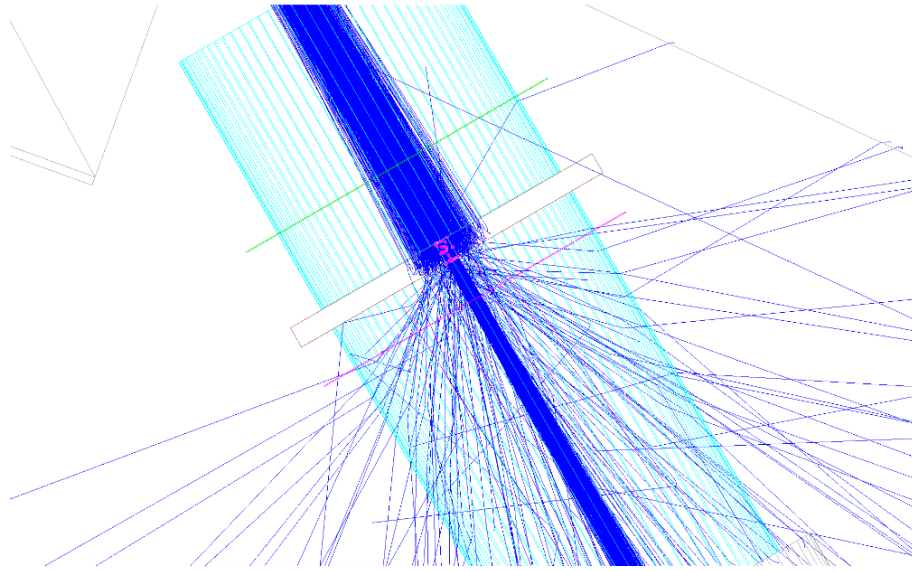


(a) X-axis position distribution

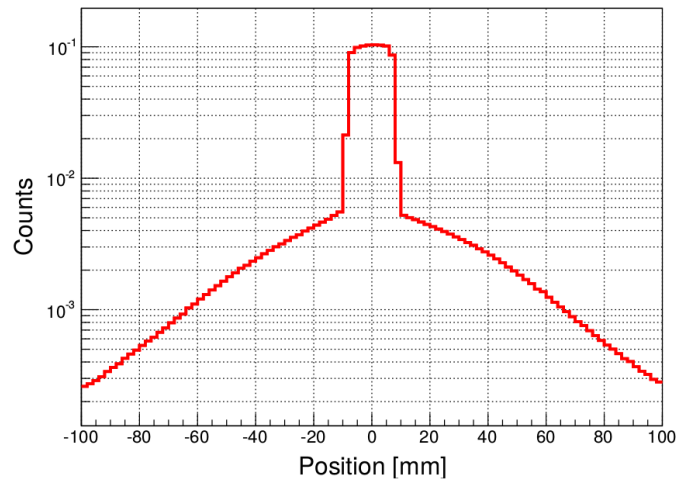


(b) Y-axis position distribution

Figure D.5: Position profiles from MC and from positron run #81633 at F4.

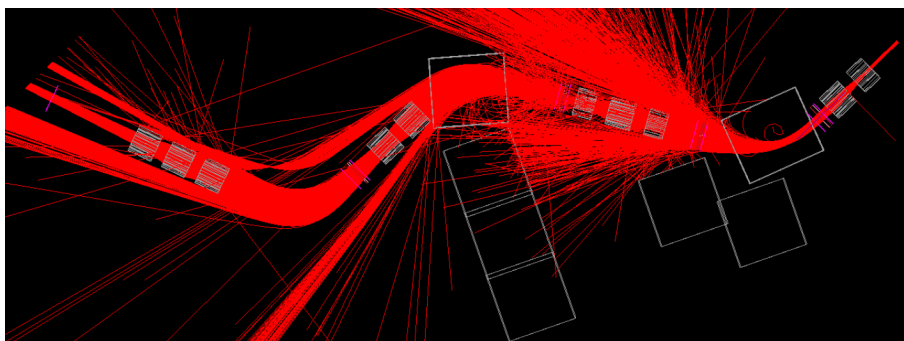


(a) Beam momenta cleanse

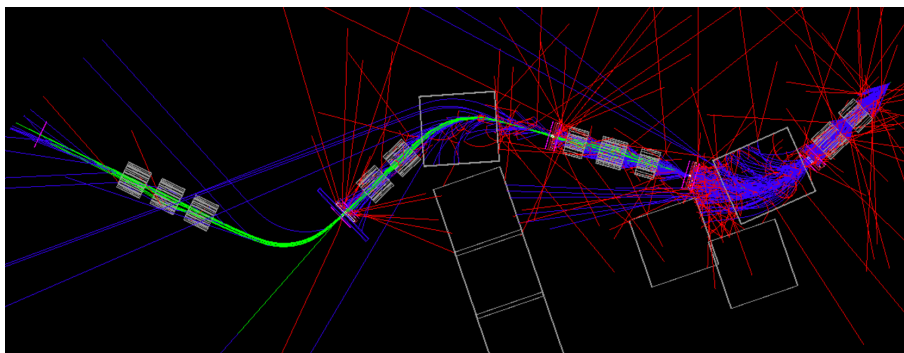


(b) Beam x-axis position distribution after F1's slit

Figure D.6: Focus point F1 slit simulation



(a) Positron beam simulation.



(b) Pion beam simulation. Pions in green, muons in blue, positrons in red.

Figure D.7: Aerial view of beam-line simulation including all main components. Please refer to Figure 3.2 for blueprint.

a) Right to Left: Starting from the **T1** production target 75 MeV width ± 12 MeV positrons (red) are isotropically simulated and go through the first two focusing quadrupoles **Q2**. Only a small solid angle is displayed. Positron passes horizontal slit (**F0SL**) and vertical jaws (**F0JA**) combo, then the first bending dipole steers the beam CW, then low momenta cleanse is done through **F1SL/JA**. Beam gets re-focused with three quads **Q3**, **Q4**, and **Q5**, enters another **F2SL/JA** to then get bended CC and further focused by quads **Q6** and **Q7**. Positrons enter the beam-line extension and positrons bend CW through dipole **B3** and final focusing is done with **Q8**, **Q9** and **Q10**.

b) Same configuration but in this case only pions (green) are produced initially. Muons (blue) and positrons are produced along each pion tree event but limited to one vertex. Additionally, a Lucite **absorber** is inserted after **F1SL** to separate the beam composition to enable magnetic selection of pions further downstream and finally a **collimator** at the beginning of the beam-line extension to filter the pions.

Appendix E

Trigger Diagram

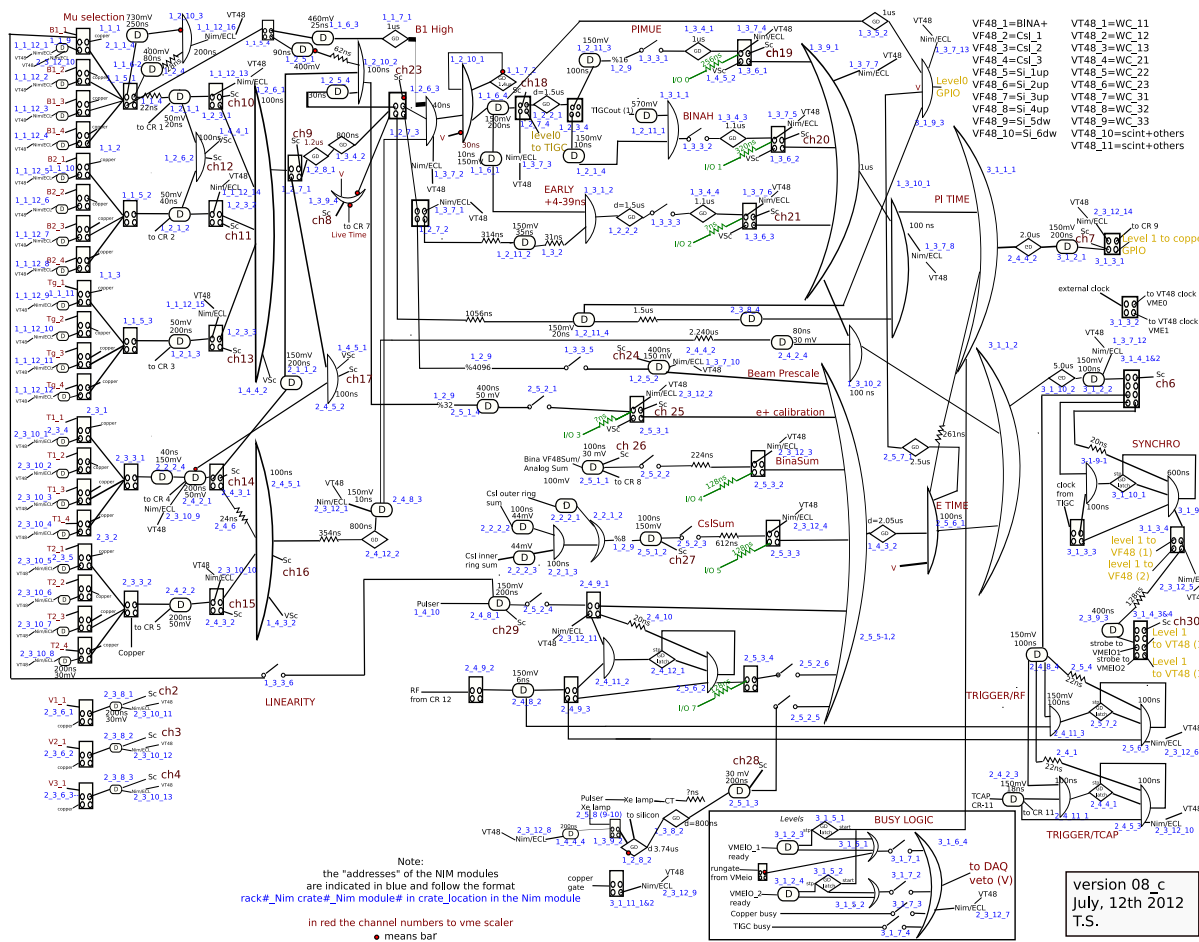


Figure E.1: Complete trigger diagram of the PIENU Experiment [19].

Appendix F

Technical Drawings

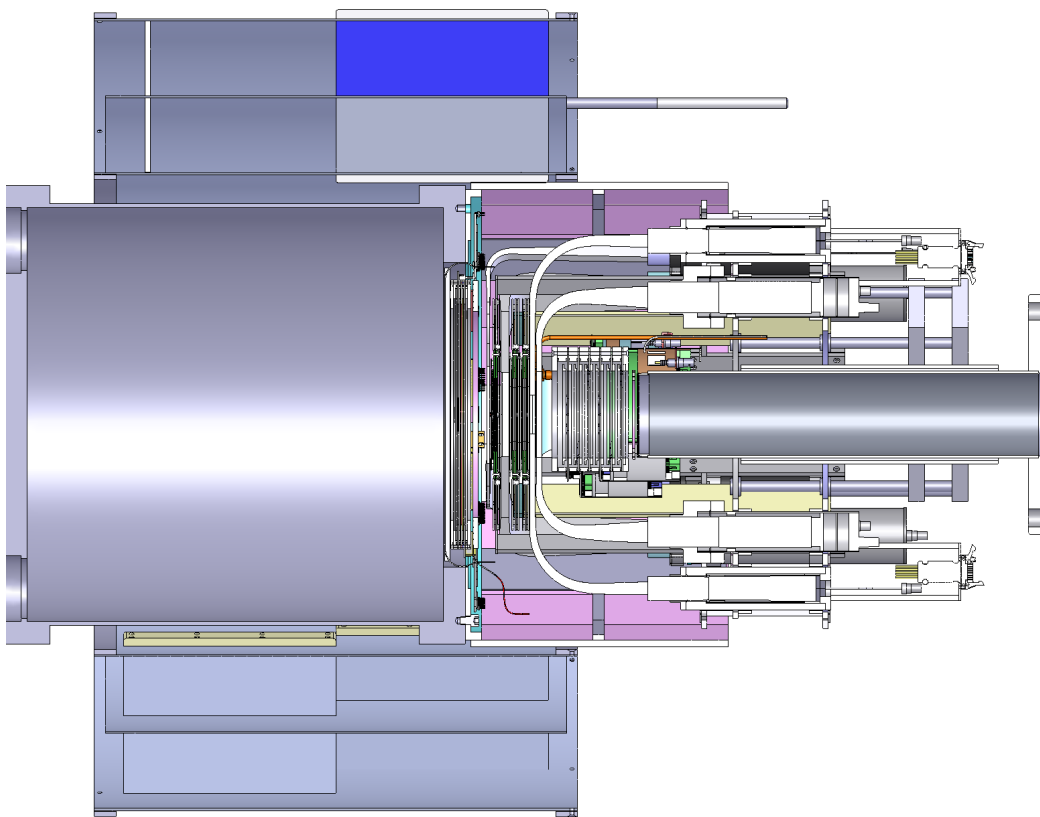


Figure F.1: Side view of the PIENU Detector. The pion beam comes from the right side.

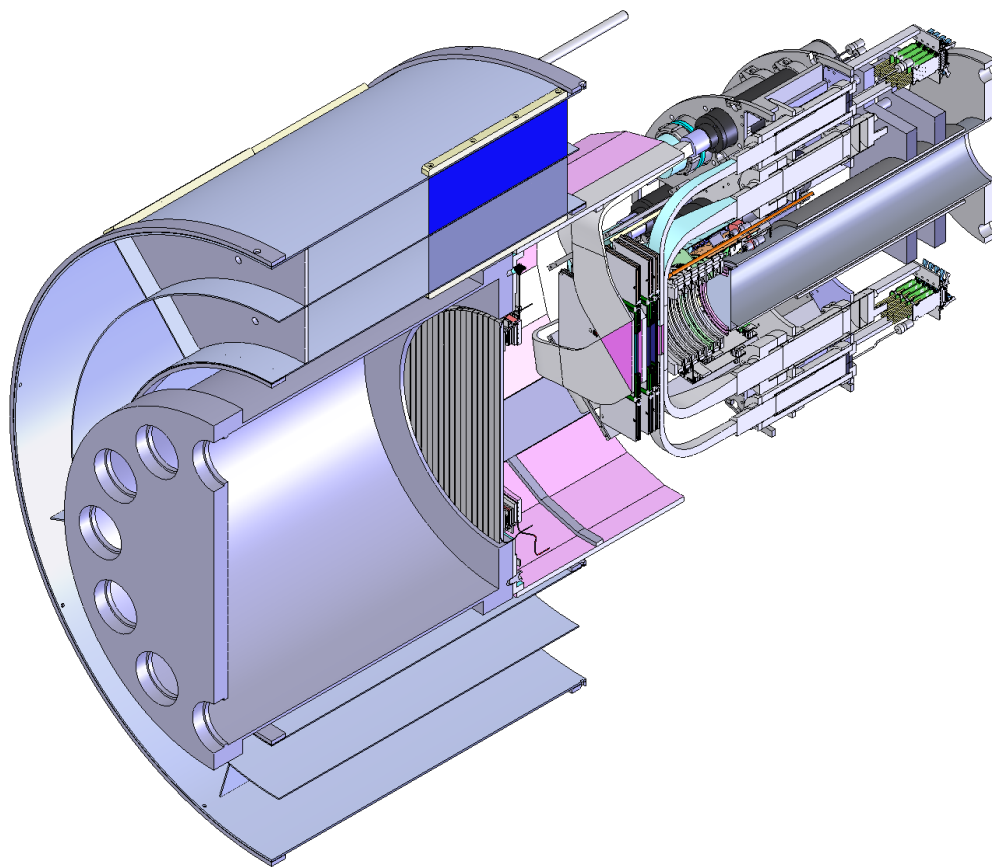


Figure F.2: Cross section of the PIENU Detector.

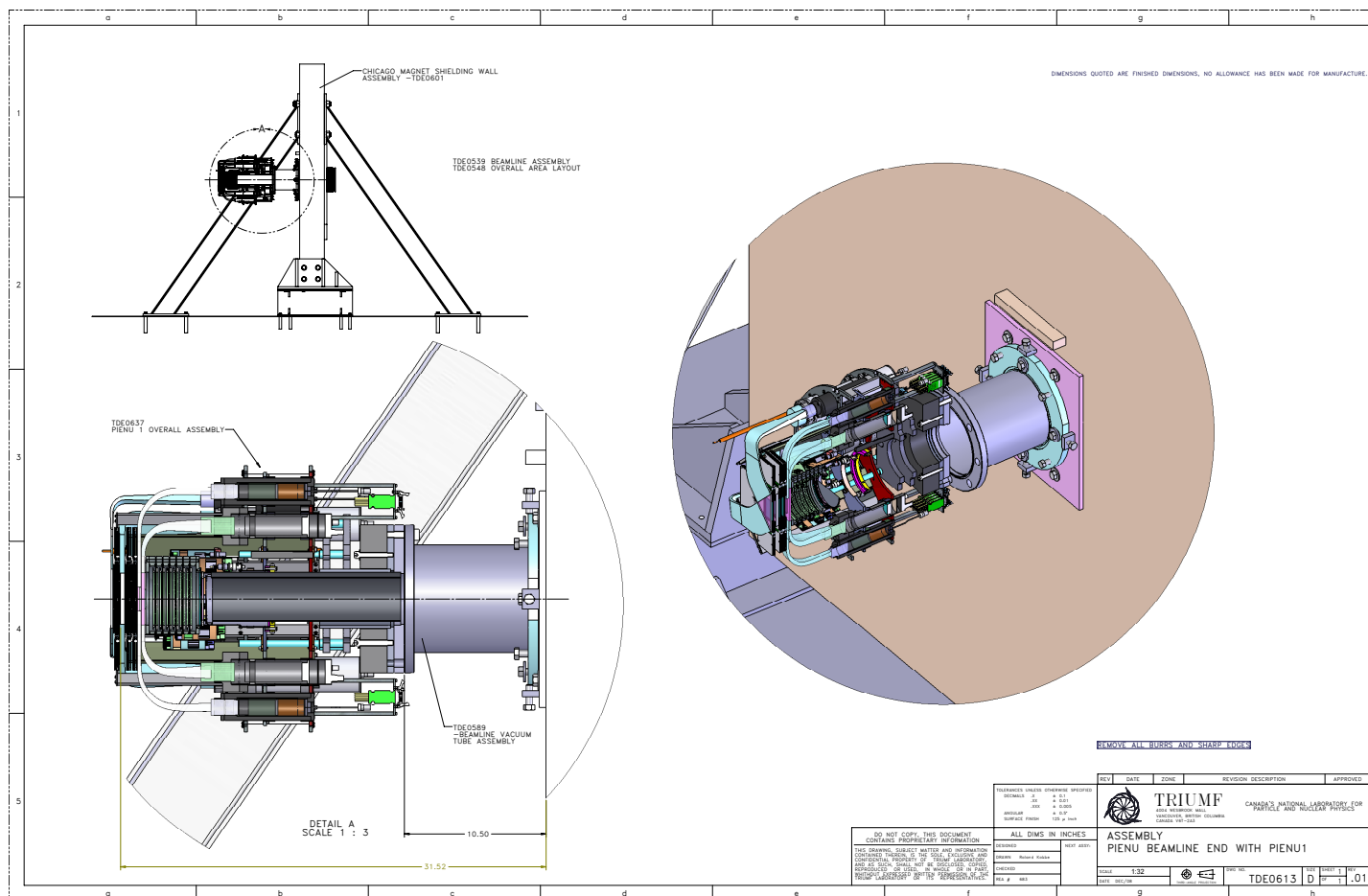


Figure F.3: The PIENU detector mounted to TRIUMF's M13 beam-line.